

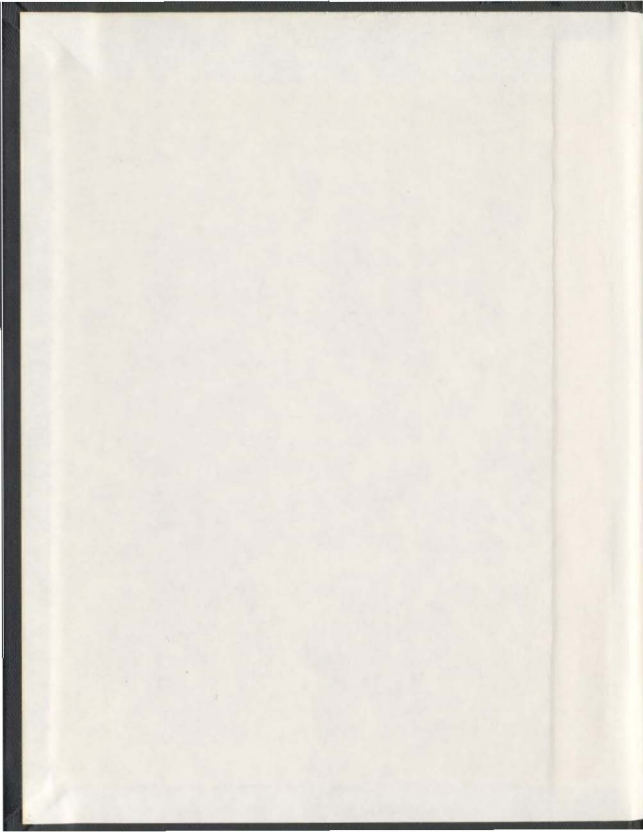
CENTRIFUGE MODELLING OF LARGE SOIL
DEFORMATION DUE TO ICE SCOUR

CENTRE FOR NEWFOUNDLAND STUDIES

**TOTAL OF 10 PAGES ONLY
MAY BE XEROXED**

(Without Author's Permission)

PAUL RICHARD LACH



001311



**CENTRIFUGE MODELLING OF LARGE SOIL
DEFORMATION DUE TO ICE SCOUR**

by

Paul Richard Lach, B.Sc., M.Sc.

**A thesis submitted to the School of Graduate Studies
in partial fulfilment of the requirements for
the degree of Doctor of Philosophy**

**Faculty of Engineering and Applied Science
Memorial University of Newfoundland**

April 1996

St. John's

Newfoundland

Canada

I learned this at least by my experiment : that if one advances confidently in the direction of his dreams, and endeavors to live that life which he has imagined, he will meet with a success unexpected in common hours. He will put some things behind, will pass an invisible boundary; new, universal, and more liberal laws will begin to establish themselves around and within him. If you have built castles in the air, your work need not be lost; that is where they should be. Now put the foundations under them.

Henry Thoreau, Walden

Abstract

Ice scouring occurs when drifting ice masses impinge upon and move through seabed sediments. It is a prevalent phenomenon over vast areas of the continental shelf regions of the Arctic Ocean and the Canadian east coast. This ice - seabed interaction represents a critical design consideration for marine pipelines associated with the production of offshore hydrocarbon reserves. Pipelines must be designed to accommodate loading transmitted by scour - induced soil deformation below the depth of ice intrusion in a safe and cost - effective manner. A rational design methodology must therefore incorporate a deterministic model which provides reliable predictions of the magnitude and extent of the soil displacements generated during a scouring event.

This dissertation describes experimental and numerical investigations undertaken to gain a better understanding of ice scouring effects on seabed soil. The experimental programme comprised a series of nine centrifuge model tests. In each test, an idealized scouring condition was simulated in an instrumented specimen of saturated clay to permit measurements of the stress and deformation fields developed in the soil, the contact pressures and resultant forces acting on the model ice feature, and the qualitative effects of scour on buried model pipeline segments. Test variables included the prescribed soil stress history, the attack angle and width of the model keel, and the scour depth attained for steady - state conditions. Centrifuge modelling was established as a valuable tool by which to obtain insight into the mechanics of the ice - soil interaction, and yielded quantitative data applicable to well - defined events. Soil displacement measurements exhibited variation which was dependent upon the initial state of the soil, and was also

influenced by differences in applied stress paths resulting from changes to boundary conditions in individual scouring events.

The finite element method was evaluated as a means for prediction of the soil response under idealized scouring conditions. The adopted two - dimensional numerical representation incorporated a finite strain formulation and the soil was modelled as a two - phase nonlinear elastic - plastic material. Preliminary verification of the numerical approach was provided through comparison of the analysis results with data acquired in representative centrifuge tests. Appropriate characterization of the effects of scouring required simulation of large movements associated with steady - state conditions, which imposed constraints on implementation of the analysis and discretization of the soil domain. The numerical representation provided adequate approximation of the effects of scouring for compressible soil behaviour, where an event was characterized by continuum distortion or flow, and volume change due to loss of material in the scour path was balanced primarily through compressive deformation beneath the incision.

Acknowledgements

I have had many positive and rewarding experiences over the duration of my programme of studies at the Memorial University of Newfoundland, and I wish to express my sincere appreciation to friends, colleagues, and mentors that have supported my endeavours in a variety of different ways. I have been fortunate to be involved with the Centre for Cold Ocean Resources Engineering during a period of tremendous growth of research activity and capability in the field of geotechnical engineering, which has been initiated, in large measure, through the efforts of my supervisor, Dr. Jack Clark. I am particularly indebted to Dr. Clark for his unwavering support and encouragement, and his genuine interest in my personal and professional development.

As my more recently appointed co - supervisor, Dr. Ryan Phillips has also had the unenviable task of wading through the detail of this relatively unwieldy document. I am grateful for his creative ideas, helpful advice, and constructive criticism, all of which have had considerable influence on the development of this research. Dr. Phillips was also involved directly in the experimental phase of the study, as the past manager of the Cambridge University Geotechnical Centrifuge Centre. I also wish to extend my thanks to Dr. Farrokh Poorooshasb, who introduced me to the concepts of centrifuge modelling, and provided enthusiastic guidance throughout the early stages, before his escape to more temperate climes. In addition, I wish to thank Dr. Gary Sabin for reviewing this work and the initial research proposal.

It was a privilege to be a visiting researcher at Cambridge University, and I am grateful to Professor Andrew Schofield and the technical and research staff at the

Geotechnical Centrifuge Centre for the provision of excellent facilities and invaluable technical assistance. Dr. Colin Smith deserves special thanks for his patient instruction on practical aspects of centrifuge testing, and his enlightened advice pertaining to design and implementation of the experiments. The contributions of the highly skilled and experienced centrifuge group, which included Messrs. Chris Collison, Steven Chandler, Neil Baker, Adrian Brand, John Chandler, Paul Ford, Ms. Susan Oliver, and Drs. Richard Dean and Jimmy James were greatly appreciated. Their cheerful disposition and enthusiasm also created a truly enjoyable atmosphere in which to work. I will always have fond memories of the time which I spent in England due to the kindness and hospitality which was shown to me by many new friends in the Cambridge Soil Mechanics group.

I was first introduced to the phenomenon of ice scouring through participation in field work undertaken as a part of the Lake Agassiz relict scour study initiated by Dr. Chris Woodworth - Lynas. I am grateful to Dr. Woodworth - Lynas, as a recognized authority, for passing on some of his many insights in relation to this fascinating area of research. More recently, I have benefited greatly from frequent discussions with my colleague and friend, Dr. K.S.R. Prasad, on computational aspects involved in simulation of the physical scouring process. I also wish to thank Mary Booton, Désirée King, and other staff members at C - CORE for the technical and moral support which they provided.

I was favoured to have distinguished teachers in Drs. James Graham, Len Domaschuk, and Donald Shields during my time spent as a student at the University of Manitoba. I wish to extend special thanks to them for presenting the subjects of soil

mechanics and geotechnical engineering in a challenging and stimulating fashion, which engaged my interest and ultimately influenced my chosen career path.

I wish to acknowledge the generous financial support which I have received through post - graduate Scholarships from the Natural Sciences and Engineering Research Council of Canada, and through a Fellowship provided by the Centre for Cold Ocean Resources Engineering. I also wish to thank the Association of Canadian Universities for Northern Studies for awarding the Polar Gas Studentship in Engineering Research in support of this work. The necessary funding to implement the experimental study was derived in part from the Government of Canada through the Natural Sciences and Engineering Research Council Strategic Grants entitled *An Integrated Investigation into the Processes of Ice Keel / Soil Interaction*, and *Quantification of Seabed Damage Due to Ice Scour*.

Finally, I wish to dedicate this dissertation to my parents, Christa and Edgar, for instilling in me a love of learning, and for their patience and encouragement throughout completion of the work described herein.

Table of Contents

Abstract	iii
Acknowledgements	v
List of Figures	xii
List of Tables	xxiv
List of Symbols	xxvi
Chapter 1	
Introduction	1
1.1 Background	1
1.1.1 Ice Scour	1
1.1.2 Marine Pipelines	5
1.2 Previous Work	10
1.3 Current Research	28
Chapter 2	
Physical Modelling	32
2.1 Introduction	32
2.2 Physical Models and Similarity	33
2.2.1 Soil Behaviour and Geotechnical Models	37
2.2.2 Centrifuge Modelling	40
2.3 Field Conditions for Ice Scouring	46
2.3.1 Arctic Sea Ice Scouring Regime	46
2.3.2 Eastern Canadian Iceberg Scouring Regime	54
2.4 Centrifuge Model Idealization	60

2.4.1	Materials Selection	60
2.4.2	Model Scouring Event	67
2.4.3	Model Pipeline Scaling	78
Chapter 3		
Experimental Devices and Procedures 83		
3.1	Introduction	83
3.2	Preparation of Clay Specimens	84
3.2.1	Laboratory Consolidation	84
3.2.2	Pore Pressure Transducers and Installation	86
3.2.3	Visual Techniques for Soil Deformation Measurement	90
3.3	Equipment and Instrumentation	98
3.3.1	Drive System	100
3.3.2	Model Iceberg	103
3.3.3	Regulation of Water Levels	113
3.3.4	Auxiliary Test Apparatus	114
3.4	Cambridge Geotechnical Centrifuge	118
3.5	Centrifuge Test Procedures	123
3.6	Site Investigation Procedures	129
Chapter 4		
Experimental Results 135		
4.1	Introduction	135
4.2	Experimental Programme	136
4.3	Centrifuge Test Results	140
4.3.1	Scour Test 01	141
4.3.2	Scour Test 02	162
4.3.3	Scour Test 03	180
4.3.4	Scour Test 04	183
4.3.5	Scour Test 05	199
4.3.6	Scour Test 06	214

4.3.7	Scour Test 07	231
4.3.8	Scour Test 08	245
4.3.9	Scour Test 09	263
Chapter 5		
	Numerical Analysis	281
5.1	Introduction	281
5.2	Finite Element Modelling	287
5.2.1	Geometric Nonlinearity	288
5.2.2	Material Nonlinearity	295
5.2.3	Boundary Nonlinearity	306
5.3	Implementation of Analysis	310
5.3.1	<i>In Situ</i> Stress State	310
5.3.2	Material Parameters	311
5.3.3	Model Development	321
5.3.4	Representation of Scouring Mechanisms	326
Chapter 6		
	Analysis Results and Discussion	332
6.1	Introduction	332
6.2	Analysis of Test 04	334
6.2.1	Input Conditions	334
6.2.2	Analysis Results	336
6.3	Analysis of Tests 05 / 09	369
6.3.1	Input Conditions	369
6.3.2	Analysis Results	371
6.4	Soil Deformation	402
6.4.1	Numerical Validation	402
6.4.2	Effects of Parameters	407
6.4.3	Summary of Experimental Data	415
6.5	Implications for Pipelines	420

6.5.1	Model Pipeline Results	420
6.5.2	Design Methodology	422
Chapter 7		
	Summary and Recommendations	430
7.1	Introduction	430
7.2	Physical Modelling	431
7.3	Numerical Analysis	435
7.4	Soil Deformation	444
7.5	Pipeline Response	449
7.6	Further Research	450
	References	454
Appendix A		
	Experimental Results	474
	Scour Test 01	475
	Scour Test 02	501
	Scour Test 04	525
	Scour Test 05	552
	Scour Test 06	577
	Scour Test 07	607
	Scour Test 08	629
	Scour Test 09	653
Appendix B		
	Resultant Force Calculation	679

List of Figures

1.1	500 kHz sidescan sonar image (swath width 75 m) showing scour features at 15 to 25 m water depth interval in Resolute Bay	3
1.2	An underwater view of a small ice island keel scouring into unconsolidated sediments	3
1.3	Plan and side elevation views of pipeline movement in a zone of large soil deformation beneath a scouring ice keel	10
1.4	Aerial photo of the study region near Lorette, Manitoba. Relict iceberg scour features appear as prominent white lines in cross-cutting patterns	13
1.5	Cross-section through large relict scour showing mapped shear planes and deformed bedding beneath the incision surface	13
1.6	Schematic of axial section through scouring ice keel and zones of soil deformation as defined by Palmer et al. (1989)	20
1.7	Soil deformation mechanisms during ice scouring. Top : Rupture surface due to passive or bearing capacity failure; Bottom : Shear dragging adjacent to ice keel or rupture surface	23
1.8	High-resolution sub-bottom profile showing cross-sections of two ice scours in stratified sediment	27
1.9	Schematic diagram of apparent sub-bottom scour disturbance, as exhibited on sub-bottom profile records	27
2.1	Limiting states of soil behaviour, shown in normalized effective stress space	39
2.2	Inertial stresses in centrifuge model correspond with gravity-induced prototype stresses	42
2.3	Variation of vertical stress with depth in centrifuge model	42
2.4	Elements of the ice scour problem	47
2.5	Top : Multi-year pressure ridge cross-section; Bottom : Geometric model of multi-year pressure ridge	50

2.6	Vertical force - deflection relationship for assumed failure mechanism and typical ice conditions	53
2.7	Top : Sediment - covered flat (keel) surface of an overturned iceberg; Bottom : Ice fragment embedded in iceberg - deformed seabed sediments	57
2.8	Comparison between baseline centrifuge model conditions and field data for Beaufort Sea clays. Left : Undrained shear strength profile; Right : Overconsolidation Ratio	67
2.9	Model iceberg geometry and parameters of the scour problem	70
3.1	Sectional view of laboratory consolidometer	87
3.2	Top : Schematic section of pore pressure transducer; Bottom : Diagram of transducer insertion into clay specimen	89
3.3	Top : Recharging hypodermic tubing with lead suspension; Bottom : Outline sketch of stages in lead trail insertion	95
3.4	Layout of pore pressure transducers, deformation markers, and model pipeline segments, shown in elevation and plan view	99
3.5	Sectional view of centrifuge test package	102
3.6	Baseline model iceberg configuration and instrumentation	105
3.7	Side elevation view of model iceberg used in Tests 01 and 02	106
3.8	Instrumented model icebergs used in Tests 07 and 08	110
3.9	Support apparatus for model shown in side and back elevation views	112
3.10	Plan view illustration of test package equipment and instrumentation	115
3.11	Components of the vane shear test device	117
3.12	Idealized sectional drawing of the Cambridge Geotechnical centrifuge	119
3.13	Schematic representation of data acquisition system	122
3.14	Pre - test view of completed package mounted on centrifuge	126
4.1	Top : Photograph of the model scour created in Test 01; Bottom : Plan view illustration of scour surface features	148

4.2	Top : Average cross - section surface profile for Test 01 scour; Bottom : Scour depth and berm elevation measurements plotted versus horizontal position	149
4.3	Test 01 pore pressure responses during event - transducer channels 01 to 08	150
4.4	Test 01 horizontal and vertical components of the resultant force plotted against model horizontal position	153
4.5	Test 01 model iceberg orientation and resultant force vectors	155
4.6	Top : Plan view drawing showing surface displacement vectors; Bottom : Average axial and lateral surface displacements versus distance from the scour axis	157
4.7	Test 01 initial / displaced plot of lateral grid shown in cross - section and plan view	159
4.8	Test 01 axial grid at final position of model iceberg; Top : Initial / displaced plot; Bottom : Displacement vector plot	160
4.9	Test 01 maximum vertical and horizontal components of soil displacement versus depth below scour base	161
4.10	Top : Plan view photograph of model scour created in Test 02; Bottom : Plan view drawing illustrating scour surface features	166
4.11	Top : Average cross - section surface profile for steady - state region of Test 02 scour; Bottom : Axial section plot of measured scour depths and berm elevations	167
4.12	Test 02 pore pressure responses during event - transducer channels 01 to 08	169
4.13	Test 02 horizontal and vertical components of the resultant force plotted against model horizontal position	171
4.14	Test 02 model iceberg orientation and resultant force vectors	173
4.15	Top : Test 02 plan view drawing of surface displacement vectors; Bottom : Average axial and lateral surface displacements versus distance from the scour axis	175

4.16	Test 02 initial / displaced plot of lateral grid at $x = -25$ shown in cross - section and plan view	177
4.17	Test 02 maximum vertical and horizontal components of soil displacement versus depth below scour base	178
4.18	Top : Photograph of model scour created in Test 03; Bottom : Plan view drawing illustrating scour surface features	182
4.19	Top : Plan view photograph of model scour created in Test 04; Bottom : Plan view drawing illustrating scour surface features . . .	186
4.20	Top : Average cross - section surface profile for steady - state region of Test 04 scour; Bottom : Axial section plot of measured scour depths and berm elevations	187
4.21	Test 04 pore pressure responses during event - transducer channels 01 to 08	189
4.22	Test 04 horizontal and vertical components of the resultant force plotted against model horizontal position	191
4.23	Test 04 model iceberg orientation and resultant force vectors . . .	193
4.24	Top : Test 04 plan view drawing of surface displacement vectors; Bottom : Average axial and lateral surface displacements versus distance from the scour axis	194
4.25	Test 04 initial / displaced plot of lateral grid at $x = -19$ shown in cross - section and plan view	196
4.26	Test 04 initial / displaced plot of axial grid located at final horizontal position of model iceberg	197
4.27	Test 04 values of vertical and horizontal components of soil displacement versus depth below scour base	198
4.28	Top : Plan view photograph of model scour created in Test 05; Bottom : Plan view drawing illustrating scour surface features . . .	202
4.29	Top : Average cross - section surface profile for steady - state region of Test 05 scour; Bottom : Axial section plot of measured scour depths and berm elevations	203

4.30	Test 05 pore pressure responses during event for seven transducer channels	205
4.31	Test 05 horizontal and vertical components of the resultant force plotted against model horizontal position	207
4.32	Test 05 model iceberg orientation and resultant force vectors	209
4.33	Top : Test 05 plan view drawing of surface displacement vectors; Bottom : Average axial and lateral surface displacements versus distance from the scour axis	210
4.34	Test 05 initial / displaced plot of lateral grid at $x = + 41$ shown in cross - section and plan view	212
4.35	Test 05 initial / displaced plot of axial grid located at final horizontal position of model iceberg	213
4.36	Test 05 maximum vertical and horizontal components of soil displacement versus depth below scour base	214
4.37	Top : Photograph of model scour created in Test 06 - view in direction of travel; Bottom : Plan view drawing illustrating scour surface features	218
4.38	Top : Average cross - section surface profile for steady - state region of Test 06 scour; Bottom : Axial section plot of measured scour depths and berm elevations	219
4.39	Test 06 pore pressure responses plotted for final section at reduced rate	220
4.40	Test 06 horizontal and vertical components of the resultant force plotted against model horizontal position	222
4.41	Test 06 model iceberg orientation and resultant force vectors	224
4.42	Top : Test 06 plan view drawing of surface displacement vectors; Bottom : Average axial and lateral surface displacements versus distance from the scour axis	226
4.43	Test 06 initial / displaced plot of lateral grid at $x = + 54$ shown in cross - section and plan view	228

4.44	Test 06 initial / displaced plot of axial grid located at final horizontal position of model iceberg	229
4.45	Test 06 maximum vertical and horizontal components of soil displacement versus depth below scour base	230
4.46	Top : Plan view photograph of model scour created in Test 07; Bottom : Plan view drawing illustrating scour surface features . . .	234
4.47	Top : Average cross - section surface profile for steady - state region of Test 07 scour; Bottom : Axial section plot of measured scour depths and berm elevations	235
4.48	Test 07 pore pressure responses during event - transducer channels 01 to 08	237
4.49	Test 07 vertical component of the resultant force plotted against model horizontal position; approx. steady - state region : x = - 100 to 50	240
4.50	Top : Test 07 plan view drawing of surface displacement vectors; Bottom : Average axial and lateral surface displacements versus distance from the scour axis	241
4.51	Test 07 initial / displaced plot of lateral grid at x = - 25 shown in cross - section and plan view	243
4.52	Test 07 initial / displaced plot of axial grid located near beginning of scour	244
4.53	Test 07 maximum vertical and horizontal components of soil displacement versus depth below scour base	245
4.54	Top : Plan view photograph of model scour created in Test 08 - view in direction of travel; Bottom : Plan view drawing illustrating scour surface features	249
4.55	Top : Average cross - section surface profile for steady - state region of Test 08 scour; Bottom : Axial section plot of measured scour depths and berm elevations	250
4.56	Test 08 pore pressure responses plotted for final section at reduced rate	252

4.57	Test 08 horizontal and vertical components of the resultant force plotted against model horizontal position	254
4.58	Test 08 model iceberg orientation and resultant force vectors	256
4.59	Top : Test 08 plan view drawing of surface displacement vectors; Bottom : Average axial and lateral surface displacements versus distance from the scour axis	257
4.60	Test 08 initial / displaced plot of lateral grid at $x = - 20$ shown in cross - section and plan view	260
4.61	Test 08 initial / displaced plot of axial grid located near beginning of scour	261
4.62	Test 08 maximum vertical and horizontal components of soil displacement versus depth below scour base	262
4.63	Top : Plan view photograph of model scour created in Test 09 Bottom : Plan view drawing illustrating scour surface features	268
4.64	Top : Average cross - section surface profile for steady - state region of Test 09 scour; Bottom : Axial section plot of measured scour depths and berm elevations	269
4.65	Test 09 pore pressure responses during event - transducer channels 01 to 08	270
4.66	Test 09 horizontal and vertical components of the resultant force plotted against model horizontal position	273
4.67	Test 09 model iceberg orientation and resultant force vectors	275
4.68	Top : Test 09 plan view drawing of surface displacement vectors; Bottom : Average axial and lateral surface displacements versus distance from the scour axis	276
4.69	Test 09 initial / displaced plot of lateral grid at $x = - 40$ shown in cross - section and plan view	278
4.70	Test 09 initial / displaced plot of axial grid located at final horizontal position of model iceberg	279
4.71	Test 09 maximum vertical and horizontal components of soil displacement versus depth below scour base	280

5.1	Relationship between theoretical modelling and centrifuge physical model study of ice scouring	282
5.2	Top : Modified Cam - clay yield surface and critical state line in effective stress space; Bottom : Normal compression, unloading - reloading, and critical state lines in compression plane	300
5.3 (a)	Modified Cam - clay strain hardening behaviour on wet side of critical state : predicted stress - strain response for shear test at constant mean effective stress	304
5.3 (b)	Modified Cam - clay strain softening behaviour on dry side of critical state : predicted stress - strain response for shear test at constant mean effective stress	305
5.4	Node ordering for interface elements and definition of rigid surface geometry	307
5.5	Non - local interface friction model, for which the condition of no relative motion was approximated by stiff elastic behaviour, as shown by the dashed line	309
5.6	Two - dimensional plane strain idealization of scouring process : finite element mesh configuration and boundary conditions adopted in analysis	323
5.7	Potential soil deformation patterns during a scouring event. Top : Side elevation view; Bottom : View in direction of motion	329
6.1	Test 04 analysis mesh configuration illustrating reference elements and nodes	337
6.2	Top : Computed effective stress paths for reference elements (EL 20, 80, and 140) during event simulation; Bottom : Element deviatoric stress against strain	338
6.3	Computed excess pore pressures during event simulation plotted against deviatoric strain for reference elements (EL 20, 80, and 140)	339

6.4	Test 04 analysis contour plots of excess pore pressure (kPa) for different rigid body positions. Top : $x = 1.8$ m; Bottom : $x = 4.1$ m	342
6.4	Test 04 analysis contour plots of excess pore pressure (kPa) for different rigid body positions. Top : $x = 8.6$ m; Bottom : $x = 14.5$ m	343
6.5	Test 04 comparison of analysis results with experimental measurements for individual pore pressure transducers	345
6.6	Test 04 analysis contact normal stress versus horizontal position for reference rigid surface interface elements	349
6.7	Top : Test 04 comparison of computed and measured resultant force components; Bottom : Analysis force records for different interface friction coefficients	351
6.8	Test 04 analysis results - final rigid body position; Top : Displaced configuration of mesh (initial shown dashed); Bottom : Displace - ment vectors (maximum length $x = 14.5$ m)	353
6.9	Test 04 analysis contour plots of horizontal component of soil displacement (m) for different rigid body positions. Top : $x = 1.8$ m; Bottom : $x = 4.1$ m	355
6.9	Test 04 analysis contour plots of horizontal component of soil displacement (m) for different rigid body positions. Top : $x = 8.6$ m; Bottom : $x = 14.5$ m	356
6.10	Test 04 analysis contour plots of vertical component of soil displacement (m) for different rigid body positions. Top : $x = 1.8$ m; Bottom : $x = 4.1$ m	357
6.10	Test 04 analysis contour plots of vertical component of soil displacement (m) for different rigid body positions. Top : $x = 8.6$ m; Bottom : $x = 14.5$ m	358
6.11	Test 04 analysis contour plots displaying magnitude of plastic strain for different rigid body positions. Top : $x = 1.8$ m; Bottom : $x = 4.1$ m	360

6.11	Test 04 analysis contour plots displaying magnitude of plastic strain for different rigid body positions. Top : $x = 8.6$ m; Bottom : $x = 14.5$ m	361
6.12	Test 04 comparison of measured and computed values of the horizontal component of soil displacement plotted against depth below the scour base	363
6.13	Test 04 comparison of measured and computed values of the vertical component of soil displacement plotted against depth below the scour base	364
6.14	Test 04 comparison of computed displacement profiles before and after unloading and associated elastic rebound	365
6.15	Test 04 analysis comparison of profiles of the horizontal displacement component for different interface friction coefficients	367
6.16	Test 04 analysis comparison of profiles of the vertical displacement component for different interface friction coefficients	368
6.17	Test 05 / 09 analysis mesh configuration illustrating reference elements and nodes	370
6.18	Top : Computed effective stress paths for reference elements (EL 23, 97, and 171) during event simulation; Bottom : Element deviatoric stress against strain	373
6.19	Computed excess pore pressures during event simulation plotted against deviatoric strain for reference elements (EL 23, 97, and 171)	374
6.20	Test 05 / 09 analysis contour plots of excess pore pressure (kPa) for different rigid body positions. Top : $x = 3.0$ m; Bottom : $x = 7.1$ m	376
6.20	Test 05 / 09 analysis contour plots of excess pore pressure (kPa) for different rigid body positions. Top : $x = 9.9$ m; Bottom : $x = 12.8$ m	377
6.21	Test 05 comparison of analysis results with experimental measurements for individual pore pressure transducers	379

6.22	Top : Test 05 / 09 analysis normal stresses compared with measured peak and average values; Bottom : Transducer records for inclined surface and horizontal base	384
6.23	Top : Test 05 / 09 comparison of computed and measured resultant force components; Bottom : Analysis force records for different interface friction coefficients	386
6.24	Test 05 / 09 analysis results - final rigid body position; Top : Displaced configuration of mesh (initial shown dashed); Bottom : Displacement vectors (maximum length $x = 12.8$ m)	388
6.25	Test 05 / 09 analysis contour plots of horizontal component of soil displacement (m) for different rigid body positions. Top : $x = 3.0$ m; Bottom : $x = 7.1$ m	391
6.25	Test 05 / 09 analysis contour plots of horizontal component of soil displacement (m) for different rigid body positions. Top : $x = 9.9$ m; Bottom : $x = 12.8$ m	392
6.26	Test 05 / 09 analysis contour plots of vertical component of soil displacement (m) for different rigid body positions. Top : $x = 3.0$ m; Bottom : $x = 7.1$ m	393
6.26	Test 05 / 09 analysis contour plots of vertical component of soil displacement (m) for different rigid body positions. Top : $x = 9.9$ m; Bottom : $x = 12.8$ m	394
6.27	Test 05 / 09 analysis contour plots displaying magnitude of plastic strain for different rigid body positions. Top : $x = 3.0$ m; Bottom : $x = 7.1$ m	395
6.27	Test 05 / 09 analysis contour plots displaying magnitude of plastic strain for different rigid body positions. Top : $x = 9.9$ m; Bottom : $x = 12.8$ m	396
6.28	Test 05 / 09 comparison of measured and computed values of the horizontal component of soil displacement plotted against depth below the scour base	400

6.29	Test 05 / 09 comparison of measured and computed values of the vertical component of soil displacement plotted against depth below the scour base	401
6.30	Maximum horizontal component of soil displacement plotted against depth below the scour base - summary of results from experimental programme	417
6.31	Maximum vertical component of soil displacement plotted against depth below the scour base - summary of results from experimental programme	418
6.32	Schematic illustration of procedures involved in implementation of engineering model of ice - soil - pipeline interaction	425
6.33	Test 04 comparison of predicted and measured values following unloading. Top : Pipeline displaced configuration; Bottom : Bending strain	428

List of Tables

1.1	Ice scour dimensions for the continental shelf of the Canadian Beaufort Sea	4
1.2	Ice scour dimensions for the eastern Canadian continental margin	5
2.1	Scaling relationships for centrifuge modelling	43
2.2	Scaling relationships for model pipelines	81
4.1	Proposed test matrix	137
4.2	Test instrumentation	142
4.3	Top : Test 01 measured pore pressure transducer locations; Bottom : Maximum and minimum excess pore pressures and horizontal distance from model	151
4.4	Test 01 resultant force data tabulated for different model horizontal positions	154
4.5	Top : Test 02 measured pore pressure transducer locations; Bottom : Maximum and minimum excess pore pressures and horizontal distances from model	170
4.6	Test 02 resultant force data tabulated for different model horizontal positions	172
4.7	Top : Test 04 measured pore pressure transducer locations; Bottom : Maximum and minimum excess pore pressures and horizontal distance from model	190
4.8	Test 04 resultant force data tabulated for different model horizontal positions	192
4.9	Top : Test 05 measured pore pressure transducer locations; Bottom : Maximum and minimum excess pore pressures and horizontal distance from model	206
4.10	Test 05 resultant force data tabulated for different model horizontal positions	208

4.11	Top : Test 06 measured pore pressure transducer locations; Bottom : Maximum and minimum excess pore pressures and horizontal distance from model	221
4.12	Test 06 resultant force data tabulated for different model horizontal positions	223
4.13	Top : Test 07 measured pore pressure transducer locations; Bottom : Maximum and minimum excess pore pressures and horizontal distance from model	238
4.14	Top : Test 08 measured pore pressure transducer locations; Bottom : Maximum and minimum excess pore pressures and horizontal distance from model	253
4.15	Test 08 resultant force data tabulated for different model horizontal positions	255
4.16	Top : Test 09 measured pore pressure transducer locations; Bottom : Maximum and minimum excess pore pressures and horizontal distance from model	271
4.17	Test 09 resultant force data tabulated for different model horizontal positions	274
5.1	Values of the interface angle of friction between kaolin and other materials	320
6.1	Summary of material parameters for Speswhite kaolin and additional input conditions, as specified in numerical analyses of representative tests	335
6.2	Horizontal and vertical displacement magnitudes at scour base and limiting depths below scour base - summary of results from experimental programme	419
6.3	Model pipeline performance for different initial depths of segments below base of scour - summary of results from experimental programme	422

List of Symbols

LATIN

a	adhesion at ice / soil interface
$asym$	denotes anti - symmetric part of matrix
c	soil cohesion
c_u	undrained shear strength
c_v	coefficient of consolidation
dx	horizontal distance between model iceberg and transducer position
e	void ratio
f	yield function, delineates boundary of elastically attainable combinations of the effective stresses
g	acceleration due to gravity
g	plastic potential
h	depth of soil model
h	length of drainage path
h	measure of the overclosure of interacting surfaces
k_h	horizontal permeability coefficient
k_s	stiffness defining elastic slip at interface, permitted before frictional slip
k_v	vertical permeability coefficient
l	a characteristic length
m	mass per unit length of pipeline
m	material parameter in relation describing K_u variation with OCR
$max du$	maximum recorded pore pressure increase
$min du$	maximum recorded reduction in pore pressure
n	local normal to rigid surface, tensor quantity
p	mean normal effective stress
p_c	isotropic preconsolidation mean effective stress
p_e	equivalent consolidation pressure, at current specific volume on isotropic normal compression line

q	generalized deviatoric stress
q_i	deviatoric stress at failure or maximum shear stress
r	radial distance from centrifuge axis to point in model
r_o	radial distance from centrifuge axis to model surface
sym	denotes symmetric part of matrix
t	elapsed time
u	displacement, tensor quantity
u_i	equilibrium pore pressure at model <i>in situ</i> stress state
v	velocity of movement relative to model
v	velocity of material point, tensor quantity
w	soil moisture content
x	characteristic displacement of point
x	horizontal coordinate, position of model iceberg along scour axis
x	current spatial coordinates of material point in deformed configuration, tensor quantity
x_A	current coordinates of node on contact surface of mesh, tensor quantity
x_C	current coordinates of rigid body reference node, tensor quantity
y	lateral coordinate, measured outward from scour axis
z	vertical coordinate, with positive values measured as depths below initial model surface
A	displacement magnitude
A	area of pipeline cross - section
CSL	critical state line or locus of ultimate states in effective stress space
D	scour depth
D	diameter of vane blades
D	rate of deformation and a measure of strain rate, tensor quantity
E	Young's Modulus of pipeline material
EL	reference finite element
F	resultant scour force
G	elastic shear modulus in terms of effective stresses

H	height of vane blades
I	moment of inertia
I	unit or identity matrix
IPT	inductive pressure transducer used in contact pressure measurement
J	Jacobian of elastic deformation - ratio of material volume in current and natural configurations
K	elastic bulk modulus in terms of effective stresses
K_o	coefficient of lateral earth pressure at rest
K_{oc}	coefficient of lateral earth pressure at rest in normally consolidated state
LVDT	linearly variable differential transformer
M_p	plastic moment capacity
N	gravity and model scaling factor
N	specific volume on isotropic normal compression line associated with unit value of mean effective stress
NCL	isotropic normal compression line
OCR	overconsolidation ratio in terms of vertical effective stresses
PPT	pore pressure transducer
R	rigid body rotation at material point, tensor quantity
T	peak value of vane torque
T_v	dimensionless time factor in one - dimensional consolidation solution
TLC	tension load cell used in horizontal force measurement
URL	unloading - reloading line in compression plane
V	volume occupied by material at current point in time
V_o	natural reference volume of material
W	buoyant weight or vertical force imposed by ice feature
GREEK	
α	angle of attack of ice keel
α, β	empirically defined material constants in undrained shear strength relation
δ	pipeline deflection or displacement

δ	angle of friction at soil / rigid surface interface
δ	denotes virtual or infinitesimally small variation of physical measures
$\delta \gamma_i$	rate of slip in i - direction at contact surface
$\delta \gamma_{eq}$	equivalent rate of slip at contact surface
$\delta \epsilon_p$	increment of volumetric strain
$\delta \epsilon_q$	increment of deviatoric strain
$\delta \epsilon_1, \delta \epsilon_2, \delta \epsilon_3$	principal strain increments
ϵ	a measure of pipeline strain or relative displacement
$\bar{\epsilon}_p$	equivalent plastic strain magnitude
ϵ_{ij}^p	plastic strain tensor
η	ratio of deviatoric and mean effective stresses
κ	gradient of unloading - reloading lines
λ	gradient of normal compression lines
μ	Coulomb friction coefficient
ν	Poisson's ratio in terms of effective stresses
ρ	submerged mass density
ρ	pipeline material density
σ	a characteristic applied stress
σ	Cauchy or true stress, tensor quantity
σ_n	contact pressure stress at point on interface
σ_v	current vertical effective stress at point in soil model
σ'_{v0}	preconsolidation vertical effective stress
$\sigma_1, \sigma_2, \sigma_3$	principal effective stresses
τ	Kirchoff stress, tensor quantity
τ_{cr}	critical shear stress in Coulomb friction model
τ_{eq}	equivalent shear stress at contact surface
v	specific volume

v_u	specific volume on unloading - reloading line associated with unit value of mean effective stress
ϕ'	effective angle of friction
ϕ_{cv}	effective angle of friction at constant volume
ψ	denotes a functional relationship or dependency
ω	angular velocity of centrifuge
ω	frequency of motion
Γ	specific volume on critical state line associated with unit value of mean effective stress
Δ	denotes an incremental value
$\Delta\omega$	central difference integration of rate of spin, tensor quantity
M	critical state frictional constant
:	denotes a scalar product of two matrices

SUBSCRIPT

cs	critical state
cv	constant volume
h	horizontal
m	model
p	prototype
p	volumetric
q	deviatoric
t	beginning of time increment
t + Δt	end of time increment
v	vertical

SUPERSCRIPIT

e	elastic component
p	plastic component

Chapter 1

Introduction

1.1 Background

1.1.1 Ice Scour

Curvilinear sea bottom gouge features which are typically one half to two metres in depth, tens of metres wide, and hundreds of metres or several kilometres in length are found over vast areas of the Arctic and sub - Arctic continental margins. These features are attributable to the process of ice scouring which occurs when drifting ice masses (icebergs, sea ice pressure ridge keels and ice island fragments) impinge upon and move through seabed sediments. The principal motivation for research pertaining to this phenomenon arises from the hazard posed to marine pipelines and other prospective subsea installations in cold ocean regions. Considerable literature exists regarding ice scouring, including field, experimental, and theoretical studies (cf. the bibliography edited by Goodwin et al., 1985). The developing understanding of ice scouring and related design issues for marine pipelines was recently summarized at an international workshop (Canada Oil and Gas Lands Administration, 1990).

In North America, comprehensive field studies of ice scour have been undertaken in the potential production areas of offshore hydrocarbon reserves, which include the continental shelf regions of the Arctic Ocean and the Canadian east coast. The bulk of available information on scour form and distribution are derived from sidescan sonar records (Figure 1.1), including rates of scour generation evaluated from repetitive mapping surveys. Scour surface morphology is also defined based on high - resolution sub - bottom profile data and, less frequently, through direct visual observations during diver or manned submersible investigations (Figure 1.2).

On the Arctic continental shelves, most scour features are formed by the deep keels of sea ice pressure ridges. Average scour dimensions for the Canadian Beaufort Sea are summarized in Table 1.1 (Lewis and Blasco, 1990); however, current dimensions may deviate from referenced values as the result of ongoing revision of the existing scour database. The seabed in this region is effectively saturated with long, curvilinear scours in water depths ranging from 10 to 40 m, and recent or new features are apparent in water depths up to 72 m. The average scour is 0.5 m deep (7.1 m maximum) and 26 m wide (1375 m maximum). Scour lengths are estimated to be on the order of several hundred metres to kilometres, with a maximum recorded value of 13 km (Hnatiuk and Brown, 1977). Scouring rates as high as 8.2 events / km / year for the 22 to 25 m water depth interval, have been determined from repetitive mapping programs; although, there is considerable variation in the frequency of scour formation with changes in both geographical location and water depth on the shelf (Lewis and Blasco, 1990).

Along the eastern Canadian seaboard, ice scouring is associated with seasonal incursions of glacial ice in the form of icebergs. Survey data from the Grand Banks of

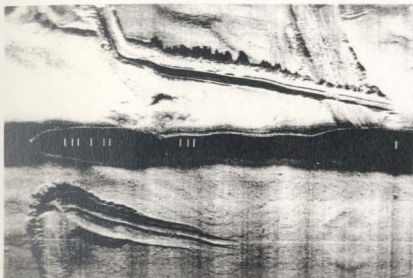


Figure 1.1 500 kHz sidescan sonar image (swath width 75 m) showing ice scour features at 15 to 25 m water depth interval in Resolute Bay (courtesy of the Atlantic Geoscience Centre)



Figure 1.2 An underwater view of a small ice island keel scouring into unconsolidated sediments (courtesy of the Geological Survey of Canada)

Table 1.1 *Ice scour dimensions for the continental shelf of the Canadian Beaufort Sea (source : Lewis and Blasco, 1990)*

Parameter	Dimension	Survey Population
Mean Scour Depth	0.5 m	10 385 events
Extreme Scour Depth	7.1 m (45 m water depth)	
Mean Scour Width	26 m	66 549 events
Extreme Scour Width	1375 m	
Scour Length	5 to 10 km	estimated
Mean Berm Width	15.3 m	100 events
Mean Berm Height	0.7 m	100 events

Newfoundland (Fader and King, 1981; Lewis and Barrie, 1981) reveal a relatively low - density population of modern iceberg scours and iceberg - created seabed pits (Mobil Oil Canada Ltd., 1985; Barrie et al., 1986) at water depths less than about 230 m (within the limit of observed iceberg drafts). The cross - cutting pattern of curvilinear furrows with parallel side berms displayed in extensively scoured regions is comparable with the observed seabed morphology in the Beaufort Sea. Relic scour formations are differentiated on the basis of discordant trends, dense occurrence, and the presence of features with greater dimensions. Table 1.2 lists characteristics for the sparse population of modern scour features on the Grand Banks in comparison with survey data for other scours on the continental shelves off Baffin Island, Labrador and Newfoundland, including relict features in deeper waters (Geonautics Ltd., 1989; Lewis and Blasco, 1990). The majority of measured scours within the water depth range of modern iceberg drafts are less than 2 m deep, and the widths of most scours range between 20 and 60 m, with rare occurrences exceeding 100 m (Lewis and Blasco, 1990). The

Table 1.2 *Ice scour dimensions for the eastern Canadian continental margin (source : Geonautics Ltd., 1989; Lewis and Blasco, 1990)*

Parameter	Grand Banks (modern features)	Canadian east coast (all ages)
Mean Scour Depth	1.3 m	1.6 m
Extreme Scour Depth	5.0 m	11.5 m
Mean Scour Width	25 m	58 m
Extreme Scour Width	100 m	330 m
Scour Density	0.3 events / km	4 events / km
Water Depth Range	down to 200 m	down to 750 m
Survey Population	407 events	21 000 events

frequency of scouring on the Grand Banks is not well known and may be expected to be highly variable, reflecting deviations in the annual flux of iceberg incursions. Maximum long term scouring rates on the northern exposed margin of the Grand Banks on the order of 1 event / 100 km² / year are predicted based on available iceberg arrival data (Lewis and Parrott, 1987; Lewis et al., 1988).

1.1.2 Marine Pipelines

Development Scenarios

Marine pipelines offer a potentially safe, reliable, and cost - effective mode of conveyance for offshore hydrocarbon reserves in cold ocean regions. Pipeline transport is not dependent on the prevailing climatic conditions and may provide a less environmentally threatening alternative to tanker transport in ice - covered waters. To

date, no major oil or gas pipeline has been installed in areas which are subject to scouring by sea ice or icebergs. At present, the Hibernia Field on the Grand Banks of Newfoundland is the only actively scoured area under development for oil production (Bruce, 1991; Chipman, 1992). Seabed soil and ice conditions in this region make it prohibitive to deliver oil and gas to market through marine pipelines, and tanker transport is an integral component of the proposed production scheme. The development will include subsea flowlines as a part of the collection system local to the Gravity Base Structure, in addition to pipelines which will export crude oil to offshore loading systems situated approximately 2 kilometres away from the structure. The future exploitation of smaller fields off the Canadian east coast may be expected to incorporate some aspects of the following development approaches : multiphase pumping and flowlines for subsea developments; seasonal, mobile production systems, and; iceberg detection, avoidance, and management programmes (c.g. Lever, 1991).

In Arctic regions, there is potential for a considerable system of offshore oil and gas transmission and gathering pipelines (K.R. Croasdale & Associates, 1994). The Panarctic Drake F - 76 project demonstrated the feasibility of production of a subsea gas well connected to onshore process facilities through a 1200 m flowline bundle, from fields off Melville Island in the Canadian Archipelago (Palmer et al., 1979; Brown, 1990). On a much larger scale, Gulf Canada Resources Limited evaluated production from the Amauligak Field in the Canadian Beaufort Sea, with continuous flow to shore via marine pipeline, over a distance of approximately 50 kilometres (Rogers, 1990). In general, the interaction of ice with the seabed is the most important design consideration for all marine pipelines planned in association with oil and gas

production in the cold ocean regions of Canada. Pipeline design issues related to ice scouring must also be addressed in regions of the Russian Arctic where offshore developments are proposed, including areas adjacent to Sakhalin Island (e.g. Truskov and Surkov, 1991; Skurihin et al., 1992) and in the Kara Sea. Most recently, a major project has been initiated to expand production of onshore gas fields on the Yamal Peninsula in northern Russia, which involves the construction of six large - diameter pipelines across Baydaratskaya Bay over a distance of approximately 70 kilometres (Palmer, 1994).

Pipeline Safety

The forces imposed directly on the seabed during formation of a typical scour feature are large enough to cause severe distress to an unprotected, conventionally - designed marine pipeline, likely accompanied by rupture and loss of containment. Simplified calculations (Palmer et al., 1990) show that loads anticipated during scouring events are one or two orders of magnitude larger than anchor forces, which are known to cause damage. It is not practicable to design a pipeline system which is able to withstand the large forces applied during direct ice contact; at least not over considerable distances at an acceptable cost. It follows that the pipeline must be protected by burial. The selection of a safe burial depth may determine the viability of pipeline transport which, in some instances, may render development of the oil or gas field uneconomical. Incremental increases in the design depth beyond limits achievable using conventional pipeline trenching methods may result in nearly exponential increases in projected costs (e.g. McKeehan, 1990).

In order to evaluate the risk of direct ice - pipeline contact associated with a particular burial depth, the following two conditions must be resolved : (1) the

probability that an ice keel will intersect the prescribed pipeline route during the time interval of interest, and; (2) for a given ice keel traversing the route, the probability that the depth of scouring will exceed the burial depth of the pipeline. The overall risk of failure due to direct contact may then be established with consideration of both intersection and depth exceedance (Comfort et al., 1990). An extensive base of information has been compiled on the distributions of scour characteristics in the Canadian offshore including scour depth, width, orientation, and spatial and temporal frequencies (e.g. Gilbert et al., 1985; King and Gillespie, 1985; Gilbert and Pedersen, 1986; Gilbert et al., 1989; Geonautics Ltd., 1989). The seabed scour data may be used in probabilistic analyses to provide a quantitative risk assessment for a prescribed pipeline route (e.g. Det norske Veritas, 1988; Murray et al., 1990). Alternatively, ice environmental data may be applied explicitly in the prediction of ice - pipeline encounter frequencies (e.g. Pilkington and Marcellus, 1981; Wadhams, 1982); however, at present, this approach is limited by deficiencies in the available ice information, including a lack of sufficient continuity in coverage or resolution of imagery or mapped data. It may be possible to use ice information to augment the seabed scour database by relating the differences in ice regimes to observed scour distributions, by correlating between actual ice features and specific scours or groups of scours, and by developing new scour rate predictions based on ice parameters (Dickins et al., 1991).

An implicit assumption of early ice scour research was that a buried pipeline would only be endangered if it was located above the base of the scouring ice keel. A pipeline may, however, also be damaged in a circumstance where the ice itself did not contact it directly. The large forces exerted on the seabed during a scouring event must

be transmitted to the soil beneath the scour, inducing high stresses and possibly causing large deformations. Experiments carried out in a laboratory scour tank facility (Poorooshasb et al., 1989; Poorooshasb, 1989; Paulin, 1992) supported evidence from investigations of relict features and small scale field observations (Woodworth - Lynas, 1990, 1992) of large sub - scour soil movements. Furthermore, in recent studies (Palmer et al., 1989, 1990; Golder Associates Ltd., 1990), it was demonstrated that the response of a pipeline subject to scouring will be predominantly dependent on the soil deformation induced in the vicinity of the pipeline. The maximum stresses that can be transmitted by the soil are limited by its strength, and, for most soil conditions, a typical marine pipeline can be expected to safely resist these stresses without incurring excessive strains (Been, 1990). A pipeline situated in a zone of large soil deformation below a scouring ice keel will be deflected as a flexible structure, unless the soil is very soft and able to flow around the pipeline (Figure 1.3). The soil subjected to failure stresses will be moved over large distances causing pipeline deflection and associated distress.

The safe burial depth of the pipeline must therefore be established not only below the maximum depth of ice intrusion, but also beneath a zone of excessive sub - scour soil deformation. The implication of the latter condition is that in order to facilitate rational pipeline design methods, a deterministic model is required to provide reliable predictions of the magnitude and extent of soil deformation during a scouring event. Once soil displacements are defined, pipeline performance can be evaluated. The development and verification of an appropriate model of ice - soil interaction is dependent upon the availability of quantitative data on the effects of scouring, applicable to well - defined events which are relevant to anticipated full scale situations.

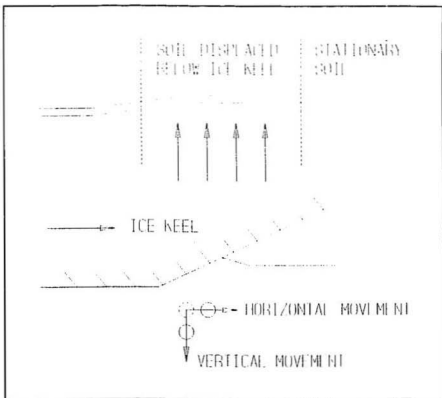


Figure 1.3 *Plan and side elevation views of pipeline movement in a zone of large soil deformation beneath a scouring ice keel*

1.2 Previous Work

The majority of research involving experimental and theoretical investigations of the effects of ice scouring has been undertaken over the last two decades. Early laboratory - based studies were carried out within scour tank facilities constructed at the Memorial University of Newfoundland (e.g. Chari, 1975, 1979 and 1980; Chari and Peters, 1981; Chari and Green, 1981; Chari et al., 1982; Green, 1983; Prasad, 1985, and; Prasad and

Chari, 1986). Small scale physical model studies were also conducted by Arctec Canada Limited (Abdelnour and Lapp, 1980; Abdelnour et al., 1981, and; Abdelnour and Graham, 1984). This work provided insight into the parameters which influence the forces applied to the seabed during a scouring event. In general, the experimental work was used to verify theoretical models for the prediction of the scour depth, for given soil conditions, of an idealized ice feature subject to specified environmental loadings.

Early theoretical representations of ice scouring included the dynamic model proposed by FENCO (1975), and the work - energy models of Chari (1979) and FENCO (1975). In the dynamic model approach, the differential equation of motion was solved numerically in a time series fashion for all applied external loads, including soil, wind, wave, pack ice, and current forces. The horizontal soil reaction was calculated using Coulomb's trial wedge solution with a plane failure surface, assuming full mobilization of the passive pressure. The vertical soil reaction was calculated either as a plastic material, based on the ultimate bearing capacity, or as an elastic material characterized by spring constants. In the work - energy model approach, energy balance considerations were used to estimate scour depths. The initial kinetic energy of the iceberg, together with the work done by current - and wind - drag forces, was equated to the work expended in ice scouring of the seabed. The work done at the seabed was used to overcome the fully mobilized passive soil resistance as given by Coulomb's earth pressure theory, for an idealized keel geometry with a vertical scouring face. Chari (1982) extended the model by incorporating the method of stress characteristics (Sokolovski, 1965) to evaluate the soil resistance. Comfort and Graham (1986) reviewed the available theoretical models of ice scouring and concluded that they were best suited

for the following applications : (1) assessing the risk of damage (through direct contact) to buried pipelines by icebergs; (2) estimating scour pressures on buried installations, and; (3) predicting scour potential in areas where field data is scarce. The models may also be employed to set physical limitations on maximum scour depths, corresponding with extreme values of the expected driving and resistive forces.

Research related to soil deformation and associated mechanisms of failure during scouring has been relatively limited. The first compelling evidence of large sub - scour soil movement was obtained from onshore field studies of relict iceberg scours exposed on the former seabed of glacial Lake Agassiz in southeastern Manitoba (Figure 1.4) (Woodworth - Lynas and Guigne, 1989, 1990; Woodworth - Lynas, 1992). Detailed mapping of the sidewalls of an excavation through a large scour approximately 50 m in width, revealed well - defined shear planes in overconsolidated clay, extending to at least 3 m below the base of the inferred scour incision surface (Figure 1.5). Sub - scour displacements as large as 3.5 m were deduced from measured offsets of remnant bedding. The shear planes plunged at an angle of about 25 degrees to the horizontal which is comparable with the angle of internal friction of the Lake Agassiz clay. This evidence suggested that the soil beneath the ice may have experienced a bearing capacity failure with the formation of a Prandtl - type mechanism, in accordance with the solution of Terzaghi (1943). Clark and Poorooshasb (1989) postulated two distinct modes of failure during a scouring event. The first mode involved the ploughing out of near - surface material and subsequent lateral movement from the path of the ice to berms on both sides of the resulting scour incision. The second mode was that of a bearing capacity failure, in which the downward movement of the soil wedge below the ice keel



Figure 1.4 Aerial photo of the study region near Lorette, Manitoba. Relict iceberg scour features appear as prominent white lines in cross-cutting patterns (courtesy of Chris Woodworth - Lynas, C - CORE)

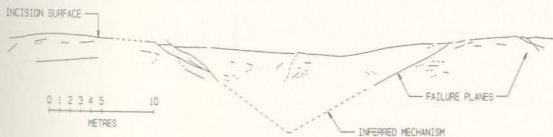


Figure 1.5 Cross-section through large relict scour showing mapped shear planes and deformed bedding beneath the incision surface (after Woodworth - Lynas, 1992)

is equivalent to the total volume of soil displaced from the scour trough less the total volume of soil comprising the adjacent berm structures. The information obtained from the study of relict scours in Manitoba prompted further field and laboratory investigations to define the nature and extent of sub - scour soil deformation.

Field programmes were conducted by C - CORE, St. John's, Newfoundland to investigate soil deformation beneath modern small scale scours formed by pan ice during spring breakup on the tidal flats of the St. Lawrence estuary near Montmagny, Quebec and at Cobequid Bay, Nova Scotia. Some of the results of these investigations were described by Poorooshab and Clark (1990) and detailed observations were presented by Woodworth - Lynas (1992). The scour features studied were typically 0.5 to 1.0 m in width, and ranged in depth from about 0.15 to 0.2 m. At the Montmagny site, the scour - affected soil was a recently - deposited, very soft, brown silt which overlies a stiffer marine clay, whereas the Cobequid Bay sediments consisted of soft to firm, highly laminated tidal silts. Excavations were made through several of the scour tracks to obtain visual records of the effects of scouring at the section, and to permit local shear strength measurements using a hand - operated vane shear apparatus. The extent of soil disturbance below the scour was estimated based on the shear strength measurements and also through mapping of distorted soil horizons. This work provided evidence of sub - scour soil movements in which the pattern of soil displacements was similar to the morphology of the scoured surface. Contouring of shear strength measurements suggested a poorly - defined zone of slightly increased strength immediately below the scour incision. At Cobequid Bay, deflected sediment layering, small scale folds, and faults were localized beneath and immediately adjacent to scour features. Sediment layers were

deflected vertically downward such that the magnitude of deflection diminished with depth to negligible values approximately 0.5 m beneath the trough of a typical feature. On both edges of the trough, sediment layers were deflected upward over regions exceeding 0.8 m in width, corresponding with heave of the scoured surface. In addition, some evidence of low angle shear plane development, similar to that observed below relict iceberg scours in Manitoba, was obtained.

Laboratory studies undertaken by C - CORE within the scour tank facilities at the Memorial University of Newfoundland included model tests conducted in both silt and sand (Porooshab et al., 1989; Porooshab, 1989; Paulin, 1992). The first set of tests investigated the scouring process in a 0.4 m thick gravity - consolidated silt unit possessing an average undrained shear strength of 4 kPa. The silt unit was overlain by a clay layer of 10 mm thickness, with an average strength of 10 kPa. The entire model seabed was saturated and submerged during testing. The model iceberg comprised a series of aluminum plates assembled to form a complex prism shape. The model was permitted to pitch and heave during scouring, and these movements were dependent upon the stiffness of springs which formed a part of the mounting system. The model was driven forward at a constant velocity of 0.06 m/s to create a scour. Tests were performed at two different scour cut depths of 40 and 70 mm. The results were fully reported by Porooshab et al., (1989). The effects of scouring were evaluated based on pore pressure measurements and through observation of layer deformation. In each test, deep - seated deformations were observed, which appeared to correspond with large transverse movements in the plane perpendicular to the direction of travel. Pore pressure measurements suggested that stress changes may be expected at depths less than about

seven times the depth of scouring. Below the shallower scour, soil displacements were recorded to a maximum depth of about 200 mm, whereas apparent remoulding of the soil, with the obliteration of pre - existing laminae, occurred to a depth equal to twice the scour depth below the deeper feature. In general, the effects of scouring observed in these experiments tended to support phenomenological data acquired from preceding field studies of relict and small scale scour features.

More recently, a series of model tests were carried out to investigate the scour process in both dry and submerged sand (Paulin, 1992), as a continuation of the experimental programme initiated by Poorooshasb (1989). In total, eight tests were conducted, of which two involved submerged conditions. The model seabed was 0.4 m deep, 3 m wide, and 5 m long, and was composed of silica sand prepared at specified relative densities which were varied between tests, from 0 to 50 percent. The model iceberg was constructed of aluminum plates, arranged in a regular polygonal shape with a horizontal base and a flat inclined front face. The width of the model was set at either 430 or 860 mm for a particular test, and the attack angle of the front face was similarly fixed at either 15 or 30 degrees to the horizontal. During testing, the model was advanced at a constant velocity of 0.06 m/s. Two different scour cut depths of 40 and 75 mm were investigated.

The results of this test series provided further indication of the boundary conditions and material states for which the effects of scouring may be expected to be significant. Soil displacements were measured to depths below the initial surface as great as 3.5 times the depth of scouring, and the horizontal component of displacement was dominant. The magnitude and extent of the sub - scour displacements increased

significantly with decreasing sand density. Soil displacements were restricted to a region immediately beneath the model keel (within approximately 5 mm) for the tests performed in sand of higher density. A change in the attack angle of the model iceberg from 30 to 15 degrees also produced a noticeable increase in the amount of disturbance beneath the scour. For sands of different densities, relatively negligible sub - scour displacement was recorded in tests where the attack angle of the model was set at 30 degrees. As scouring progressed in a test, successive strong discontinuities, inferred as rupture planes, were observed to surface both in front of and to the sides of the model iceberg. Paulin (1992) concluded that vertical forces exerted during the model scouring events were of sufficient magnitude to induce bearing capacity failure, based on comparison of calculated bearing capacity values with measured vertical loads, together with evidence of upward vertical displacement adjacent to the scour incision.

Poorooshasb and Clark (1990) reviewed the results of laboratory studies conducted by C - CORE and submitted general conclusions as follows : (1) under certain conditions, significant sub - scour deformations occur in model tests in fine and coarse materials; (2) in coarse materials, the deformations are largest in loose soils; (3) in coarse materials, the effect of reducing the attack angle is to increase the force required for scouring and to increase the amount of sub - scour deformation; (4) in coarse materials, low strength zones appear to attract deformations; (5) in medium to dense sands, the vertical total stress decreases and then increases during the approach of a model iceberg; (6) the stress levels fall off rapidly as the distance beneath a scouring iceberg increases in coarse materials; (7) in low strength fine materials, shear strains are set up by the passage of a model iceberg at up to seven times the scour depth, and; (8) in

fine materials, small surface deformations may coincide with significant sub - scour deformations.

A 1/4 scale model test facility was established by Esso Canada Resources Limited to obtain large - scale three - dimensional performance data on the behaviour of a buried pipeline subjected to soil movements induced by ice scouring (Weaver et al., 1988). The authors described the test facility and instrumentation, and discussed their effectiveness in light of the results of three initial experiments. The apparatus included an ice keel simulator which comprised a 1.0 MN reaction frame and a 3 m wide by 1 m high rigid indenter. The indenter may be advanced a distance of 2 m at an angle of 20 degrees to the horizontal, toward a 30 m long steel pipe section, buried up to 1 m in soil and anchored at both ends. During a test, the pressure distributions on the pipe and indenter were monitored using a variety of instrumentation, including devices developed specifically for this experimental study. Test results were to be used to calibrate existing analytical models of the ice - soil - pipeline interaction.

Considerable research into the effects of ice scouring and the response of buried pipelines was recently conducted by Golder Associates Ltd. in conjunction with Andrew Palmer and Associates Ltd. (Palmer et al., 1989; Been et al., 1990; Palmer et al., 1990; Golder Associates Ltd., 1990; Been, 1990; Palmer, 1990). The main objective of this research was the development of deterministic models of the interaction between the scouring ice, the soil seabed, and a pipeline buried in the seabed. To begin with, the authors suggested a useful conceptual framework in which to categorize soil deformations and their effect on a pipeline. As illustrated in Figure 1.6, the soil displacement field in the vicinity of a scouring ice feature was subdivided into three distinct regions : (1) an

upper large strain Zone 1, above the base of the keel, in which the soil is first displaced upward into a mound in front of the advancing ice, and is then moved laterally to berms on either side of the resulting scour; (2) a lower large strain Zone 2, below the base of the keel, in which the soil experiences large plastic deformation, and; (3) a small strain Zone 3, in which the soil is subjected to stresses transmitted from Zone 2 above, but in which the resultant soil displacements are small and essentially elastic.

Preliminary studies were undertaken to assess pipeline performance in each of the aforementioned zones (Palmer et al., 1990; Golder Associates Ltd., 1990; Palmer, 1990). For a pipeline situated in Zone 3, the potential for collapse under loading applied by the soil was evaluated through the application of the lower bound theorem of plasticity. A model was also developed to calculate the elastic stresses and strains in a pipeline buried within this zone. In this model, the plastic stresses in the failing scoured soil were computed, and stresses at the rupture surface were then applied to the elastic soil in Zone 3. Both of these analyses suggested that a typical marine pipeline buried within Zone 3 will be safe, and this conclusion was unaffected by moderate variations in assumed parameters. For a pipeline located in Zone 1 and contacted by the ice directly, analyses of plastic bending, denting, buckling, and tensile failure loads and stresses demonstrated that severe damage or rupture may be expected. Finally, it was indicated that in Zone 2, the safety of the pipeline would be dependent on the scour - induced soil deformations. As such, the following requirements were considered to be the most pertinent to pipeline design : (1) the assessment of the scour path and depth of scouring, and; (2) the determination of the extent of Zone 2 and the soil deformations developed in this zone.

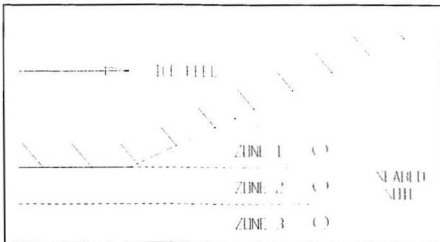


Figure 1.6 Schematic of axial section through scouring ice keel and zones of soil deformation as defined by Palmer et al. (1989)

A work - energy model and associated computer program were developed to predict the scour path and depth of scouring incrementally at small prescribed displacement intervals (Been et al., 1990; Golder Associates Ltd., 1990). With this model, it was possible to account for ice uplift, buoyant forces, ice flexural stiffness (for a ridge within an ice sheet), driving forces due to wind and current, ice - soil friction, and surcharge due to ploughed soil. User - specification of the attack angle of the ice feature was also permitted. In addition, the model allowed for consideration of scouring in a heterogeneous soil or in soils with varying strength - depth profiles. The soil resistance was evaluated through passive pressure analysis based on the method of stress characteristics of Sokolovski for a restricted class of problems in which the following conditions were assumed : (1) development of a specific rupture mechanism including the presence of experimentally observed non - deforming or dead soil wedges, and;

(2) equality of the soil friction and dilation angles. The Sokolovski analytical method was modified to include the formation of dead soil wedges within the failure zone following the procedure proposed by Hettiaratchi and Reece (1975). Simulation of an observed Beaufort Sea scour (Scour E1 documented by Shearer et al., 1986) demonstrated that reasonable agreement with the measured profile could be obtained using the model.

Been et al. (1990) compared vertical scour forces derived from their generalized passive pressure analysis with calculated bearing capacities, for a variety of seabed stratigraphies and soil strengths. In all cases, the calculations were performed for a constant scour depth and a constant ice keel attack angle at 30 degrees to the horizontal. The following trends were inferred from the results of the comparative analyses : (1) there is little potential for sub - scour disturbance in sand; (2) where clay overlies sand, there is little potential for sub - scour disturbance when the depth of scour is near the clay - sand interface; (3) in uniform clay layers, the potential for sub - scour disturbance decreases as the clay strength increases, and; (4) there is a decrease in sub - scour disturbance potential when a soft clay is underlain by a stiffer clay.

A study was carried out to predict the depth and size of Zone 2 (Figure 1.6) produced by a passive failure mechanism (Palmer et al., 1989; Golder Associates Ltd., 1990). The upper bound theorem of plasticity was used to generate velocity field solutions to the problem. A particular class of velocity fields was considered wherein regions of uniform velocity are separated by strong discontinuities in which all shear deformation and volume change is concentrated. A range of velocity fields was considered and the solutions optimized to provide an indication of the expected depth of disturbance. It was found that while it is possible to generate kinematically admissible

velocity fields in dilatant materials that exhibit sub - scour deformations, these mechanisms result in passive forces on the ice which are larger than those for velocity fields which do not exhibit sub - scour deformations. Therefore, it was tentatively concluded that sub - scour disturbance due to a passive failure mechanism is not significant. As a result of this study, the authors also indicated that strongly dilatant materials are more likely to experience deformation below the scour depth, but that such deformations are not expected to extend far. It was emphasized that velocity field solutions are not unique, and that independent data are necessary to establish that the postulated velocity fields develop during scouring events.

Palmer et al. (1990) conducted further analyses for non - dilatant soils treated as ideal perfectly - plastic materials with an associated flow rule. It was noted that this idealization may be reasonable for soil in the actively scoured zone which, as a result of repeated deformation, may have reached the critical state. The upper bound theorem of plasticity was applied to calculate the resultant scour forces. By consideration of a number of deformation modes, an interaction curve (yield locus) was generated which represented possible combinations of the non - dimensionalized vertical and horizontal components of the resultant force for a particular ice geometry. The normality rule of plasticity was applied to determine the point on the interaction curve which corresponded to horizontal motion of the ice. In this manner, simple relationships were developed from which the resultant force components may be estimated from a knowledge of the soil shear strength, and the scour width and depth.

As depicted schematically in Figure 1.7, soil deformation and failure may be attributed conceptually to two types of mechanisms (Been, 1990; Golder Associates

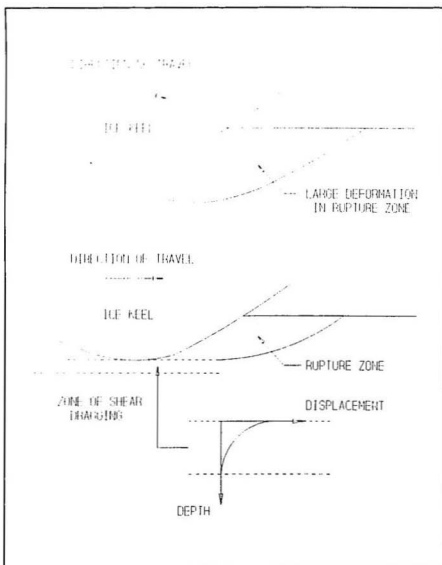


Figure 1.7 Soil deformation mechanisms during ice scouring. Top : Rupture surface due to passive or bearing capacity failure; Bottom : Shear dragging adjacent to ice keel or rupture surface (after Been, 1990)

Ltd., 1990) : (1) passive pressure or bearing capacity failure, with the development of a rupture surface in which soil undergoes large strains and displacements, and; (2) an independent shear dragging mechanism, which may account for large soil movements below the ice in Zone 2. It was recognized that soil adjacent to a rupture surface, or a rigid body sliding relative to the soil, will be dragged along in the direction of shearing. Although a detailed analysis of the dragging mechanism was not performed, the authors postulated that the depth of a zone of large dragging deformations below the ice will be unlikely to be related to the scour depth but instead will depend only on the stress - strain behaviour of the soil. Furthermore, it was proposed that, due to stress localization effects, strain hardening soils may be expected to experience a larger depth of sub - scour dragging than strain softening soils. This suggestion was noted to be consistent with available laboratory observations, where only loose sands show a significant depth of sub - scour disturbance, and softer clays display greater depths of disturbance than stiffer clays. It was also speculated that soil displacement in the direction of travel will be a function of the soil properties, the width and depth of scouring, and the magnitude of the displacement of the scouring ice relative to the soil.

A laboratory indenter testing program was undertaken by Golder Associates Ltd. (1989) in order to provide experimental data to verify analytical models, and to identify displacement patterns in soils around scours. A total of 46 tests was performed in both sand and clay soils. Sand with average densities of 1421, 1612, and 1690 kg/m³, and clay with undrained shear strengths of 10, 20, and 40 kPa were investigated. All of the tests were carried out using flat indentors inclined at either 30, 60, or 90 degrees to the horizontal, scouring at a depth of 100 mm below the original soil surface. In a given

test, an indenter width of 100, 200, or 400 mm was employed.

A summary of the results of the indenter testing program was reported by Golder Associates Ltd. (1990). Some of the conclusions presented by the authors were as follows : (1) indenter penetration into sands resulted in the development of discrete rupture surfaces and large fluctuations in loads as failure occurred on successive rupture surfaces; (2) in clays, discrete rupture surfaces also developed but these occurred less frequently in softer soils; (3) dead wedges of soil were observed in front of the indenter, but it was noted that the front face of the wedge may be close to vertical or sloping back toward the indenter rather than forward as suggested by Hettiaratchi and Reece (1975); (4) a width to depth ratio exceeding about three was required before plane strain assumptions were found to be valid; (5) analytical calculations of passive pressures based on the method of stress characteristics as modified by Hettiaratchi and Reece (1975) provided good agreement with measured forces (with allowance for spoil pile development and three dimensional effects); (6) sub - scour disturbance, attributed to the shear - dragging mechanism, was generally limited to a small zone below the indenter; (7) looser sands and softer clays exhibited greater disturbance below the indenter than was witnessed for denser sands and stiffer clays; (8) based on a limited number of observations, it was suggested that inertial effects and pore pressure generation in sands may represent important factors, and; (9) soft trench backfill materials were noted to draw the failure plane downwards below its normal level due to the development of stress concentrations at the stiff - soft material interface.

Examinations of available field data on full sized scours indicated that such data are generally not sufficiently well - defined to permit reliable evaluation of failure

mechanisms or sub - scour deformations (Gilbert, 1990; Comfort et al., 1990; Lewis and Blasco, 1990). Acoustic disturbance below ice scours has been infrequently recorded on high - resolution sub - bottom profiles of the scoured seabed in the Beaufort Sea. Observations of this phenomenon were typically limited to the Mackenzie Trough physiographic region, where disturbances are preserved in bedding planes due to high sedimentation rates and relatively low scouring rates (Comfort et al., 1990). Figure 1.8 displays two scour features for which a region of apparent disturbance may be identified, possibly related to the effects of the corresponding scouring event (O'Connor and Associates Ltd., 1980). The scour depth (D) of the larger feature was 2.3 m; however, it was estimated that about 2 m of infilling (1) may have occurred. It may also be inferred from the acoustic character change (2) that the sediments in an extensive region below and adjacent to the scour trough were affected, and a similar region of disturbance (3) may be defined for the smaller feature, shown to the right in the section. Studies of several thousand line kilometres of sub - bottom profiler data in the Canadian Beaufort Sea revealed only 38 cases where this type of disturbance is present. The analysis of this data indicated that, on average, the inferred depth of disturbance was less than about 1.5 times the scour cut depth in soft clayey sediments, and the width of disturbance was approximately equal to the width of the scour (Comfort et al., 1990).

The region of disturbance identified on sub - bottom profiles (Figure 1.9) may be attributed to sub - scour soil deformation caused by the single event in question, it may be the result of previous scouring activity or the infilling of the existing scour, or it may be an acoustic artifact (Lewis and Blasco, 1990). According to the authors, the presence of the scour incision itself alters the travel paths of normally vertical incident

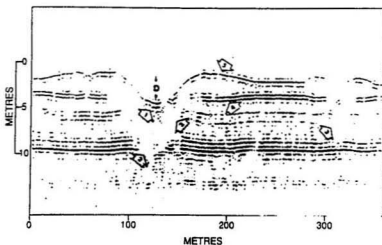


Figure 1.8 High - resolution sub - bottom profile showing cross - sections of two ice scours in stratified sediment (O'Connor and Associates Ltd., 1980)

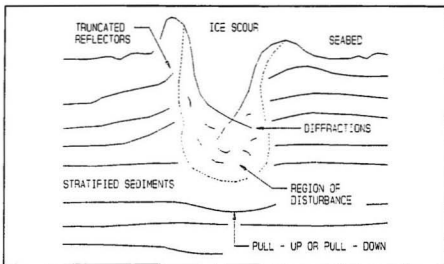


Figure 1.9 Schematic diagram of apparent sub - scour disturbance, as exhibited on sub - bottom profile records (after Lewis and Blasco, 1990)

sound waves emitted and received by the profiling instrument. This travel path distortion may result in either an artificial acoustic void beneath the scour or an apparent pull - up or pull - down of horizontal sediment layers. It may be difficult to discriminate between these acoustic artifacts and the actual effects of scouring, leading to further uncertainty in the interpretation of profile data.

1.3 Current Research

Objectives and Scope

A knowledge of scour - induced soil deformation is essential to allow for a rational approach to the design of marine pipelines in regions vulnerable to ice scouring. With the exception of work cited in the foregoing section, research conducted in this area has been relatively limited and inconclusive. Theoretical studies are unable to provide definitive solutions without independent verification of predictions of physical behaviour. Unfortunately, direct measurements of the effects of ice scouring beneath the modern seabed are generally not feasible, and high - resolution geophysical data are not conclusive in resolving the extent of sub - scour deformation. In addition, field investigations of onshore relict scours are restricted by the age of the features, and inadequate information regarding the scouring event itself. Moreover, small scale laboratory model tests cannot be expected to provide results which are directly applicable to the field situation, due to departures from similarity arising from unrealistic initial stress levels in the soil.

The deficiencies inherent in conventional experimental studies may be surmounted

by the application of centrifuge modelling, which ensures improved representation of soil behaviour through the attainment of similarity of effective stress and pore fluid pressure fields with the prototype. The present study involved the design and implementation of a programme of small scale model tests of ice scouring in a geotechnical centrifuge. The tests were undertaken to obtain insight into the mechanics of the ice - soil interaction, and to yield quantitative data on the effects of ice scouring, for well - defined events which were representative of particular situations at full scale.

The centrifuge test data provided a basis for the development and verification of deterministic models of the ice - soil interaction. The prediction of scour - induced soil displacements may not be comprehensively resolved without recourse to a numerical analysis incorporating statics, kinematics, and a complete constitutive relation. In the present study, the application of a large strain elastic - plastic finite element formulation was investigated, in order to account for the material and geometric nonlinearities which are inherent to the problem. The objectives of the study may be subdivided as follows.

(1) Develop a centrifuge model idealization of ice scouring through an assessment of the relevant field ice scouring conditions, and based on the available information from previous laboratory studies. Define the limitations of the idealization which may arise due to physical features or complexities of the event which are not reproduced, or which result from scaling relationships that cannot be satisfied simultaneously.

(2) Design a centrifuge test package to simulate the idealized scouring condition, and demonstrate the effectiveness of the proposed apparatus for use in the high - gravity environment with remote data retrieval and system control. Provide appropriate instrumentation to measure the stress and deformation fields within the soil, the

qualitative effects of scour on model pipeline segments, and the resultant forces acting on the model ice feature during a scouring event.

(3) Conduct a series of centrifuge model tests to investigate limited variations in parameters expected to influence the effects of scouring. In addition, conduct tests which model an identical prototype at two different scales, to establish the internal consistency of the modelling method.

(4) Reduce and document the results from each centrifuge test to render a unique data set on the effects of scouring for an event which corresponds directly with a notional full scale situation.

(5) Apply finite element analyses to simulate an idealized scouring condition. Detail the limitations of the proposed numerical representation. Provide preliminary verification of the numerical approach through comparison with centrifuge test results.

(6) Discuss the direct implications of the centrifuge test results, and the implications of a comparative examination of the results of both centrifuge modelling and numerical analyses, for the design of marine pipelines situated in ice scoured terrain.

(7) Provide recommendations for further physical and theoretical modelling, in support of the development of a reliable engineering model of the ice - soil - pipeline interaction.

The scope of the physical modelling study was limited to a series of nine tests performed using the beam centrifuge at the University of Cambridge Geotechnical Centrifuge Centre in Cambridge, England. The soil type in which all of the model scours were created was a reconstituted kaolin clay, and the stress history of each clay specimen was defined to establish desired stress states without detailed reference to specific field

conditions. The numerical analyses were restricted to two - dimensional plane strain representations of the problem, and were implemented through use of a commercially available general purpose finite element code.

Thesis Outline

The thesis was organized into seven chapters. Chapter 2 indicates the rationale for use of the centrifuge, and defines the physical model idealization and its limitations, with reference to available information on relevant field conditions. Chapter 3 describes the equipment and experimental procedures which were used to fulfil the model design requirements. Chapter 4 outlines the centrifuge test programme and presents detailed results for the individual tests. Chapter 5 describes the finite element formulation adopted and the implementation of the analysis, with consideration of the restrictions imposed by the numerical approach. Chapter 6 provides a comparison of the results of the analysis with the experimental data from representative centrifuge tests, and discusses the results of both physical and numerical modelling with regard to characterization of the effects of scouring, the influence of test parameters, and implications for the design of marine pipelines. Finally, Chapter 7 summarizes the main contributions of the present study and provides recommendations for further research.

Chapter 2

Physical Modelling

2.1 Introduction

Physical modelling is an important tool for the investigation of soil behaviour during an ice scouring event. Models provide an alternative means of obtaining the information necessary to design or analyze systems involving natural phenomena which cannot be rigorously described through the application of mathematical techniques. Full scale observation should offer the best approach for study of the problem; however, difficulties relating to control of conditions, instrumentation of a suitable site, and time considerations (in that occurrences of particular scour events are relatively unpredictable) restrict the practical implementation of field investigations. Small scale modelling has advantages in terms of the ease of construction of models and the controlled environment in which the test is performed. Results from widely different model conditions may be obtained with the same experimental apparatus at a saving in time, cost, and labour in relation to a full scale study.

Physical simulations of ice scouring have thus far involved small or medium - sized model tests in which the stress scale has not been altered. To address the

deficiencies inherent in conventional small scale modelling of geotechnical phenomena, the present research programme applied the method of centrifuge modelling to the study of ice scouring. The model tests were conducted to gain a better understanding of the mechanics of scour and also to obtain information on the nature, magnitude, and effect of the parameters that are present in the system. This chapter describes the physical model idealization of the ice scour problem and the relevant similarity requirements. The practical issues involved in implementation of the experiments are considered in Chapter 3. A brief discussion of physical modelling is first presented to illustrate the principles involved in the development of model design criteria and to rationalize the use of the centrifuge technique.

2.2 Physical Models and Similarity

Physical modelling is commonly used to investigate complex engineering problems. A model may be defined as a device which is related to a physical system, the prototype, in such a way that observations and measurements made on the model may be used to predict the performance of the prototype in the desired respect. The prototype may be an existing system or, in some circumstances, it may be a notional situation envisaged in a research study, representative of a particular class of event. In all cases, model design criteria or similarity requirements for the system must be satisfied to ensure that the important physical aspects of the prototype are reproduced at specified scales.

The results of model tests may be extrapolated to predict the prototype response providing that the model can be demonstrated to be relevant to the prototype situation.

A valid model and prototype must be similar systems. If the parts of the two systems have the same shape, they are said to be geometrically similar. This is a basic requirement for most model studies and it implies a point to point correspondence in terms of a linear dimension scale. The concept of similarity must also be extended to all other characteristics which influence the phenomena under consideration. For example, in geotechnical studies, similarity of material behaviour between model and prototype is essential but has often been improperly neglected in conventional laboratory investigations conducted at Earth's gravity. In general, the prototype conditions which significantly influence the behaviour in question should be equivalent at corresponding points in the model and any dissimilarities should be shown to be of minor importance. Practical constraints may require that compromises be made in the replication of prototype conditions. The recognition of these model distortions or departures from complete similarity is essential to assess the limitations of the model in the interpretation of test results.

The general principles of modelling theory are well established (e.g. Langhaar, 1951; Sharp, 1981) although, to date, these principles have not been widely exploited in the field of soil mechanics (Scott, 1988). The development of similarity requirements and scaling relationships for the model and prototype may be accomplished using different approaches. Modelling criteria may be determined directly through evaluation of the characteristic equations which govern the phenomena under consideration. However, this approach is not viable for model studies undertaken to investigate conditions which are not amenable to rigorous mathematical analysis and, in these cases, modelling criteria must be developed from partial analyses which are based on dimensional or similarity

considerations. Dimensional analysis allows information about a phenomenon to be determined from the basic premise that the phenomenon can be described by a dimensionally homogeneous equation among certain variables. Techniques for deriving a dimensionless functional equation from a specified list of variables that is both adequate and minimal are thoroughly discussed throughout the literature. Inspection of the dimensionless equation leads to the establishment of model design criteria from which suitable scale ratios for the model may be determined.

Consider an idealized scouring event in which a body of ice (assumed as rigid) cuts a scour in a uniform clay. The geometry of the ice feature and the scour may be defined by a characteristic length, taken as the scour depth D and by the interface attack angle α . The buoyant weight or vertical force W imposed by the ice feature may also influence the problem. The event is sufficiently rapid in the relatively impermeable soil such that undrained conditions exist, even at the small scale of a model. The clay may be described as an ideal cohesive material in terms of the undrained shear strength c and the submerged mass density ρ as well as the adhesion a developed at the ice - soil interface during relative motion. A strain rate effect on the strength of the cohesive soil is not introduced in the analysis. Inertia forces related to the change of momentum of the soil are also considered to be negligible for the range of velocities of interest. The simplified physical system can therefore be specified by the following functional equation :

$$F = f (c, a, \rho, g, W, D, \alpha) \quad (2.1)$$

which indicates that the resultant scour force F is related to the geometry and weight of the rigid body, and to the properties of the soil, where g is the gravitational acceleration. A partial analysis then leads to an equation in which the variables have been combined to form dimensionless parameters as follows :

$$\frac{F}{c D^2} = \psi \left\{ \frac{c}{\rho g D}, \frac{a}{c}, \frac{W}{c D^2}, \alpha \right\} \quad (2.2)$$

where ψ implies a functional relationship or dependency.

Model design criteria may now be established on the basis of Equation 2.2. The resultant force F non - dimensionalized with respect to $c D^2$ will have the same value in the model and prototype providing that each of the terms on the right hand side of the equation is equivalent in both systems. The initial two similarity requirements relate to the scaling of the soil medium and pose the greatest difficulty from a modelling standpoint. These conditions may be expressed as

$$\left[\frac{c}{\rho g D} \right]_m^{(\alpha)} = \left[\frac{c}{\rho g D} \right]_p \quad \text{and} \quad \left[\frac{a}{c} \right]_m = \left[\frac{a}{c} \right]_p$$

where the subscripts m and p refer to model and prototype respectively. A geometrically similar model of linear scale N will have a scour cut depth of D_p / N . It follows that in order to satisfy the first requirement at normal gravity levels on the laboratory floor, the low self weight stresses must be matched by small soil strengths. The undrained shear strength must be reduced in proportion to the model scale N , and a small scale model would therefore have to be constructed from a very soft wet soil. Furthermore, in accordance with the second requirement, the ratio of adhesion to soil strength (which is

known to decrease with increasing clay strength) must be the same in both model and prototype.

Experience has shown that these types of scaling relationships for soil properties are difficult or impossible to fulfil. If they are not satisfied, the model is distorted. In general, to compensate for reduced self weight stresses in laboratory geotechnical models an analogue material must be used which does not usually scale all of the relevant strength and stiffness properties concurrently. In addition the scaled - down strengths of the model make sample preparation difficult, imposing a limit on the factor by which the prototype scale can be effectively reduced in practice. There are, therefore, inherent difficulties in performing model tests at small scale in the laboratory which can be deemed representative of particular situations at a larger scale.

Further inspection of the first modelling requirement in Equations 2.3 indicates that if the prototype soil were to be used in building the model, the body forces ρg must be increased by a factor equal to the model scale N . The concept of controlling body forces gives rise to the technique of centrifuge modelling and also suggests a fundamental similarity requirement for geotechnical models.

2.2.1 Soil Behaviour and Geotechnical Models

In the study of geotechnical problems, allowance must be made for the dependency of the mechanical behaviour of soil on the overall stress state. To accomplish this in a physical model study, the state of stress of a given soil element at corresponding points in the model and prototype must be equal. This condition will not be met for model tests

performed in a one gravity environment using prototype materials, unless a full scale model is constructed. Centrifuge modelling is a technique through which the important similarity condition of equivalent effective stresses and pore fluid pressures in a small scale model and a prototype may be achieved.

Model preparation generally begins with a reconstituted soil which is then subjected to prescribed loading paths; the stress history is defined to bring the soil at points in the model into states which are representative of elements of soil at corresponding points in the prototype. The centrifuge test involves an initial stage in which the model stratum of soil is brought into equilibrium under a generalized stress in steady centrifuge flight, followed by the test proper in which that equilibrium is perturbed in a similar fashion to the prototype event. Both stress history and stress increments must be correctly reproduced if the correct stress - strain - strength response is to be obtained. The mechanical behaviour of soil alters with the changing state of the soil depending on the effective stresses and also the volumetric condition which provides a more complete indication of the current state of the soil in relation to its previous history. Schofield (1980) suggested the division of soil behaviour at limiting states into three regions in a constant volume section, as illustrated in Figure 2.1 : (1) A region of strain hardening behaviour with stable yielding at high effective stresses; (2) A region of strain softening behaviour with Mohr - Coulomb type rupture at lower effective stresses, and; (3) A region of fracture which might be governed by a condition of limiting tensile strain or of no tension at very low effective stress levels. Each part of a model may therefore be made to exhibit a different mode of behaviour depending on the imposed stress history. In this manner, models may be used to gain information on a

inhomogeneities must be recognized in the assessment of test results. The experimental data are generally interpreted in an analytical framework, which is subsequently applied to the field situation.

2.2.2 Centrifuge Modelling

Centrifuge modelling provides a direct method of obtaining the correct stress field within a small scale geotechnical model. A prototype stratum of soil is represented by a geometrically similar model of linear scale N which has been constructed of the same material. The model is rotated about the central axis of the centrifuge. The orientation of the model is such that the outward radial direction in the centrifuge corresponds with the vertical downward direction of the prototype in Earth's gravity field. The angular velocity ω at which the model is rotated is selected such that for a model at radius r the centripetal acceleration $r\omega^2$ is equal to Ng where g is the gravitational acceleration. Under this condition, depicted schematically in Figure 2.2, the gravity - induced prototype stresses will be reproduced at corresponding points in the model. In both model and prototype, the upper surface of the body is unstressed, and the pressure increases through the depth of the soil body.

Use of the centrifuge allows for the development of appropriate scaling relationships between model and prototype without the need for compensation of discrepancies related to differences in stress levels. The scaling relationships which are generally applicable to centrifuge models are well established. Lee (1985) reviewed previous analyses and presented derivations based on the governing equations (the

equations of equilibrium or motion, compatibility equations, generalized stress - strain laws, and boundary conditions) for a saturated porous medium. Table 2.1 provides a summary of common scaling factors which are relevant to centrifuge modelling.

Divergence of Radial Acceleration Field

The scaling relationships presented in Table 2.1 strictly apply in the case of a uniform acceleration field. The centrifuge acceleration field deviates slightly from this ideal condition in that it is radially directed and the accelerations, which are proportional to the radius, increase through the model. The vertical stress distributions for the model and prototype are illustrated in Figure 2.3. Schofield (1980) has shown that errors in the vertical stress due to the variation of acceleration with depth in a model can be minimized by ensuring that the model and prototype stress profiles correspond at a depth equal to two thirds of the total depth of interest in the model. The vertical stress σ_v at depth z may be computed by integration from the surface of the model at radius r_0 to the given depth, as follows :

$$\sigma_v = \int_{r_0}^{r_0+z} \rho \omega^2 r \, dr = \frac{1}{2} \rho \omega^2 z (z + 2 r_0) \quad (2.4)$$

In order to attain the appropriate model stress distribution, the linear scaling factor N must be calculated at a depth equal to one third of the model depth h such that

$$\sigma_v = \rho N g z \quad \text{and} \quad N g = \left(r_0 + \frac{h}{3} \right) \omega^2 \quad (2.5)$$

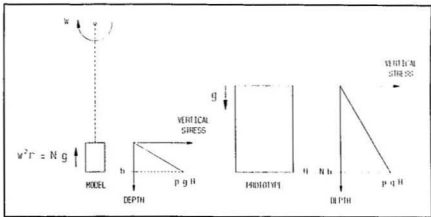


Figure 2.2 *Inertial stresses in centrifuge model correspond with gravity - induced prototype stresses*

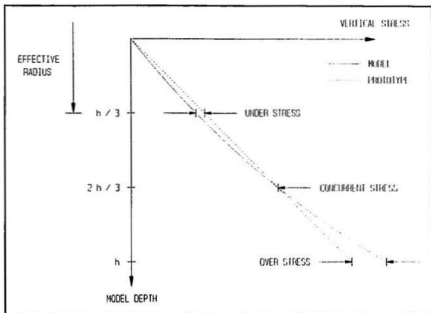


Figure 2.3 *Variation of vertical stress with depth in centrifuge model*

Table 2.1 *Scaling Relationships for Centrifuge Modelling*

Quantity	Full Scale : Model at N_g
Linear Dimension	$1 : 1 / N$
Area	$1 : 1 / N^2$
Volume	$1 : 1 / N^3$
Density	$1 : 1$
Mass	$1 : 1 / N^3$
Force	$1 : 1 / N^2$
Stress	$1 : 1$
Strain	$1 : 1$
Displacement	$1 : 1 / N$
Time (inertial events)	$1 : 1 / N$
Time (diffusion phenomena)	$1 : 1 / N^2$
Time (viscous flow)	$1 : 1$

The error in stress at a given depth expressed as a ratio of the prototype stress at that depth is then equal to $h / 6r$. In the present study, models occupied a radial distance less than one tenth of the centrifuge radius, and the maximum error in the model stress profile was only about 1.1 percent of the prototype stress.

In the centrifuge, the resultant acceleration vector does not act perpendicular to the model surface at all points in the model. The concentric acceleration contours define curved phreatic surfaces in models. The radial field also produces small lateral components of acceleration which increase with distance away from the centre of the model. At the extremities of a 500 mm diameter central portion of the model, the inclination of acceleration field was about 3.5 degrees relative to the prototype vertical direction. Although the radial divergence of the acceleration field had only limited influence on model behaviour, it was an important consideration in the design of the system used to regulate water levels within the centrifuge test package.

The effect of Earth's gravity, acting perpendicular to the centrifuge acceleration field was reduced by mounting the model on a wedge with slope 1 : N. This provision ensured that the vertical axis of the model coincided with the direction of the resultant acceleration under test conditions.

A different source of error relates to movements of a part of the model in the plane perpendicular to the axis of rotation of the centrifuge. This part of the model will experience an additional Coriolis acceleration equal to $2 \omega v$ where v is the velocity of movement relative to the model. The error caused by the Coriolis acceleration is given by $2v / \omega r$ when expressed as a ratio with respect to the centripetal acceleration of the model (Schofield, 1980). For events involving relatively slow movements such as in

scepage problems, the error is small. At higher velocities, the errors increase and movements in the model follow unrepresentative curved trajectories; although, at very high velocities (above an upper limit exceeding approximately twice the velocity of the centrifuge model) Coriolis effects again become negligible (Pokrovsky and Fyodorov, 1968). In general, the potential adverse effects of the radial acceleration field were taken into account in model design for the present study, particularly in relation to the positioning and orientation of the model scouring event and associated equipment.

Modelling of Models

Quite apart from the errors which derive from the use of an artificial gravity field, it will generally not be possible to replicate all aspects of the prototype situation in a small scale model, especially in a model of a complex event such as ice scouring. The discrepancies may be physical features which cannot be reproduced or they may arise due to scaling relationships which cannot be satisfied simultaneously. These problems need to be addressed each time a new model test is undertaken. One approach to the validation of model studies is to compare the model test results directly with prototype observations where they are available. In the absence of suitable field data, a useful alternative approach is the modelling of models (e.g. Ovesen, 1985) wherein an identical prototype event is modelled at different scales. The correspondence of the test results from different sized models provides a check on the consistency of the centrifuge model testing scheme and validates the scaling relations, at least within the range of model scales investigated.

2.3 Field Conditions for Ice Scouring

Figure 2.4 shows a schematic section through a scouring ice feature and indicates several factors which may affect the ice / soil / pipeline interaction. It is clear that the scour processes and effects, including soil deformations, will depend strongly on the soil type and stress state. In addition, a variety of ice scour event scenarios can be envisaged depending on the environmental driving forces which are acting and the characteristics of the ice feature. As it is generally not possible to observe the creation of full - sized ice scours directly, many uncertainties still exist concerning the physical conditions which are appropriate in describing the problem. Knowledge of the possible field ice scouring conditions that may arise is essential to the development of a relevant idealization, and it is also required in order to assess the limitations of the model.

The ice scour processes may be expected to differ for the continental shelf regions of the Arctic Ocean and the Canadian east coast where the usual offending features are respectively sea ice pressure ridges and icebergs of glacial origin. The prevalent field ice conditions for each region are therefore addressed separately in the following sections.

2.3.1 Arctic Sea Ice Scouring Regime

Ice Geometry and Structural Integrity

The seasonal variation and morphology of the sea ice canopy overlying the continental shelves of the Arctic Ocean and, in particular, the southern Beaufort Sea have been described in several publications (e.g. Kovacs and Mellor, 1974; Wadhams, 1975; Lewis

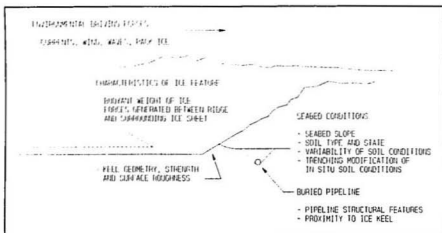


Figure 2.4 *Elements of the ice scour problem*

and Blasco, 1990). In general, scouring activity in this region may be attributed to either sea ice pressure ridge features or to tabular icebergs (ice island fragments) which originate from the northern coast of Ellesmere Island, Canada. The latter may represent the most probable generator of scours in extreme water depths greater than 55 m (Dickins et al., 1991); however, predicted return periods for ice island entry into the water depth range from 20 to 70 m in the Beaufort sea are on the order of one to two thousand years (De Paoli et al., 1982).

Sea ice pressure ridges form as an accumulation of angular ice blocks resulting from the interaction and failure of abutting ice floes. For large ridges to develop, appreciable differences need to exist between the thicknesses of the ice sheets and the relative motion must be primarily compressive. Extreme free - floating ridges may extend up to 13 m above sea level (Kovacs et al., 1973) although ridge heights in excess of 6 to 8 m are infrequent. Data on keel measurements is less well documented, however,

the subsurface portion of the ridge is typically much more extensive than its sail portion above water. The deepest ice keel in the Arctic Ocean reported to date projected some 47 m beneath the water surface (Lyons, 1967).

The ice strength and structural integrity of a pressure ridge increases with time as brine is expelled from the ice crystal structure and the ridge consolidates. Sea - ice deformation structures which survive beyond one summer melt season are referred to as multi - year features. During the melt season, the angular ice blocks incorporated in the ridge are gradually rounded through ablation, the inter - block voids are filled with fresh water from melting snow and ice, and the overall relief of the ridge is smoothed. The ice blocks are subsequently bonded together through freezing of the interstitial water. Visual observation of exposed fracture faces and drilling carried out in conjunction with field investigations established that multi - year ridges comprise an essentially solid mass of low salinity ice with a complete absence of open cavities (Kovacs et al., 1973; Kovacs and Gow, 1976; Hnatiuk et al., 1978).

Scouring forces will generally not be limited by the overall structural adequacy of the ice keel. For solidly refrozen multi - year sea ice, the expected stresses in the ice during a scouring event are much smaller than the available confined compressive strength of the material, and are low by comparison with those measured in ice - structure interactions on the same scale (e.g. Sanderson, 1983). Kovacs and Mellor (1974) indicated that a first - year ridge with a well - bonded keel block structure can also withstand the scouring forces associated with a typical event without crumbling or mobilizing internal friction. Fracture of the ice may however occur initially when the keel may have sharp edges or in the case of an unconsolidated first - year

ridge (Palmer et al., 1989). Fragments of the ice can break loose and modify the keel geometry, since the outer surface of the ice is at a temperature near to its melting point and is relatively weak. Field investigations have indicated that free - floating first - year ridges are often poorly consolidated within the bottom half of their keel structure (Edwards et al., 1978; McGonigal and Wright, 1982; Lowrings and Banke, 1983). Dickins et al. (1991) suggested that such ridges are unlikely to generate deep scours, and inferred that most scours greater than 0.5 m deep located in water depths exceeding 20 m (within the transitional ice zone) were created by multi - year features. First - year ridges which are grounded and formed *in situ* are relatively stronger and more consolidated than free - floating ridges formed from the current year's ice. According to the authors (ibid.), deep scours found inside of the 20 m isobath (within the landfast ice zone) are thought to be primarily related to these ridge systems.

Studies of first - year ridge geometry indicated an average sail height to keel depth ratio of approximately 1 to 4.5 and an average keel slope of about 33 degrees (Kovacs, 1972; Kovacs and Mellor, 1974). The highly irregular block structure of the V - shaped keel of a typical first - year ridge is gradually smoothed over one or more melt seasons. An average ratio of about 1 to 3.3 between the sail height and keel depth was determined through field investigations in which several multi - year ridge cross - sections were measured (e.g. Kovacs and Mellor, 1971; Kovacs et al., 1975; Kovacs and Gow, 1976; Dickins and Wetzell, 1981; Voelker et al., 1981). The keel geometry was commonly observed to be gently convex or bowl - shaped in cross - section. Figure 2.5 shows an example of the surveyed cross - section of a multi - year pressure ridge, and also displays a geometric model proposed by

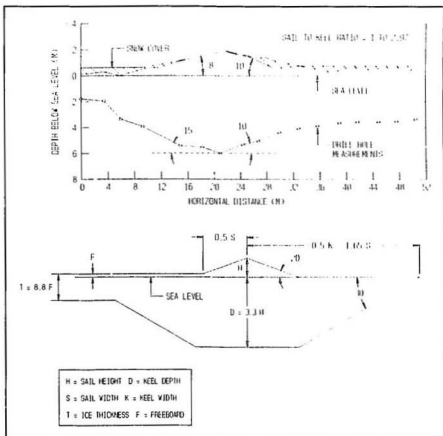


Figure 2.5 Top : Multi - year pressure ridge cross - section; Bottom : Geometric model of multi - year pressure ridge (Kovacs, 1975; Wright et al., 1979)

Kovacs (1975). In development of this idealized shape, a flat - bottomed keel was assumed in order to simplify the representation of low keel face angles suggested by available field evidence. Keel shapes with low attack angles are also found to be relevant based on considerations of the integrity of the ice during a scouring event, as described in Section 2.3.2.

Driving Forces and Ice Motion

To initiate a scouring event, the ice feature must be driven by forces which may derive from a combination of current, wind, and ice interactions. First - year sea ice can transmit the forces required for scouring to either isolated features or wide pressure ridges (Kovacs and Mellor, 1974). The forces may be generated through currents, by wind shear acting over areas of adjacent sea ice, or as a result of loading from pack ice. Relationships developed between seabed scouring and the ice environment in the Beaufort Sea (Dickins et al., 1991) indicated that most scours greater than 0.5 m deep found within the transitional ice zone were created by multi - year floes / fragments moving in constrained pack ice conditions during winter months. A strong correlation was also established between observed deep scours and ice motion during storm episodes.

The mean long - term winter ice drift velocities in the transitional zone are on the order of 0.03 m/s with a reported maximum movement of 50 km in one day (Kovacs and Mellor, 1974). Dickins et al. (1991) observed that winter ice motion in this zone is highly variable, and that short duration velocity increases are generally associated with periods of low ice concentration. Mean monthly wind speeds in the southern Beaufort Sea typically range from 3.6 to 5.6 m/s. Storms with gust winds greater than 20 m/s are common, whereas events involving 35 m/s wind speeds have a return period of 25 years (Boyd, 1965). The velocity of the ice canopy rarely exceeds about 2 percent of the prevailing wind speed due to inertial effects and stresses developed within the ice, as well as the influence of drag near to the edge of the fast ice zone (Kovacs, 1972). Storms accelerate the ice motion, imparting greater kinetic energy to the pack which may be subsequently dissipated through grounding and scouring of the seabed sediments.

The characteristics of the ice feature are important in determining its complete motion during a scouring event. The motion of a sea ice pressure ridge is constrained by the forces developed between the ridge and the ice sheet in which it is enveloped. Wave - induced movements of the scouring feature are not expected to be significant due to the damping effect provided by surrounding pack ice. Non - horizontal ice movements may, however, originate as a result of soil uplift forces during scouring. As the pressure ridge is driven into shallower water, it is lifted by the vertical soil reaction such that scouring occurs at a uniform depth relative to the seabed, rather than relative to the water surface (Palmer et al., 1990). Field data were collected which show rise up of the base of the scour corresponding with reduction in the bathymetric profile, with distance along the track of long scours (Wahlgren, 1979; Shearer et al., 1986). These data may reflect processes involving either vertical uplift or rotation of the scouring ice feature or abrasion of the keel during the event. Vertical movements during scouring were also documented through field observations of ridge fragments which show evidence of uplift due to grounding and scouring (e.g. Kovacs and Mellor, 1974; Kovacs and Gow, 1976).

Uplift during scouring is dependent on the forces developed at the ice / soil interface as well as the forces generated between the ridge and the surrounding ice sheet. Golder Associates Ltd. (1990) examined a range of possible interaction conditions which may arise due to vertical movement during a scouring event. These conditions included hydrostatic uplift of the ice sheet, elastic deflections of the ice sheet, and failure of the ice sheet assuming different failure mechanisms. The failure mechanisms investigated by the authors included circumferential and radial cracking (Nevel, 1968), shear or plug failure, and failure involving tearing of the complete ridge from the ice sheet (Abdelnour, 1988).

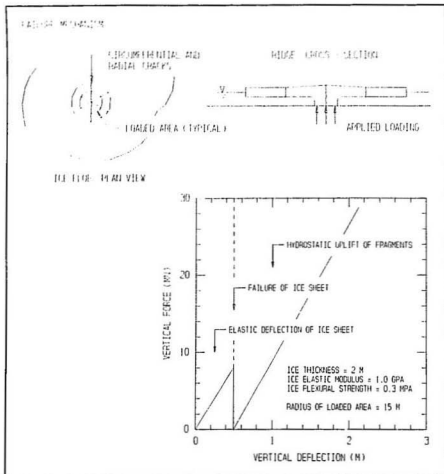


Figure 2.6 Vertical force - deflection relationship for assumed failure mechanism and typical ice conditions (Golder Associates Ltd., 1990)

Figure 2.6 shows the predicted vertical force - deflection relationship for typical conditions in which the ice sheet was assumed to fail by circumferential and radial cracking. The preliminary analyses suggested that, initially, the ice sheet may be expected to undergo elastic deformations rather than being lifted as a complete mass, and

that failure will result with continued vertical movement. The deflections necessary for ice sheet failure (on the order of one metre for a typical case) were found to be less than the uplift movements which have been deduced from field observations. The scouring process may still continue beyond ice failure, as horizontal forces may be transferred across the failure surfaces to the ice fragments which remain in contact with the seabed. Furthermore, the magnitude of the hydrostatic stiffness of the failed ice fragments may not be dissimilar to the elastic stiffness of the intact ice sheet. As such, the vertical forces applied to the seabed are not expected to be significantly limited by ice failure during uplift.

2.3.2 Eastern Canadian Iceberg Scouring Regime

Ice Geometry and Structural Integrity

The large icebergs which scour the seabed of the continental shelves of Baffin Island, Labrador, and Newfoundland originate predominantly from the tidewater glaciers in and around the periphery of Melville Bay in West Greenland (Murray, 1969). The system of cold oceanic currents in Baffin Bay, Davis Strait, and the Labrador Sea is the driving force responsible for the transport of icebergs southward along the eastern Canadian margin. In an average year, about 3000 icebergs travel beyond Hudson Strait, 1000 pass the Strait of Belle Isle, and 400 survive to drift south of 48° N latitude onto the Grand Banks of Newfoundland (Dinsmore, 1972; Ebbesmeyer et al., 1980). The annual flux is inconsistent and may deviate by a factor of 3 or 4 times the average, depending on the upstream population and rate of production of icebergs, as well as on storm events and

changes in oceanic transport conditions (Gustajtis, 1979).

The size and geometry of icebergs also vary widely, depending on the details of their origin and the degree of their deterioration during transport. Icebergs are in isostatic equilibrium in surrounding seawater with approximately 87 percent of their mass below the water surface; however, the height to draft ratio of individual features ranges considerably as a result of the diversity of existing geometries. Iceberg drafts have been estimated from above - water dimensions, inferred from the water depth around grounded features, and directly measured using dragline, diver, radar, and acoustic profiling techniques. The quantity of direct measurements of the subsurface portion of icebergs available within the public domain is limited (Brooks, 1982; Hotzel and Miller, 1983). Iceberg shape also changes slowly due to melting and other degradation phenomena, and associated mechanical calving of large ice fragments. These processes result in instability and capsizing, and may produce features with draft dimensions that exceed the depth of the parent iceberg (Grant, 1973; Bass and Peters, 1984).

The results of the Dynamics of Iceberg Grounding and Scouring (DIGS) field programme (Hodgson et al., 1988) during which several iceberg grounding events were monitored on the Labrador continental shelf, provided insight into conditions at the keel / seabed interface. Inferences were made pertaining to ice morphology and keel modification during scouring events based on visual observations of the iceberg - deformed seabed sediments from manned submersibles (Woodworth - Lynas et al., 1991; Woodworth - Lynas, 1992). The investigations confirmed that there may be considerable attrition of the ice during grounding and scouring events, and that in some instances seabed material may be mechanically incorporated into the ice keel.

Characteristically flat - bottomed scour troughs implied that the initially irregular ice geometry was altered to form a planar surface in the region of seabed contact. This is exemplified in Figure 2.7, which shows the debris - laden, flat section of an overturned iceberg, interpreted to be the former keel surface. Further evidence was provided through observation of the underwater calving of an iceberg which generated sediment - covered ice fragments from the edge of the grounded keel. The reconnaissance of recently formed scours also revealed pieces of ice that had spalled from the keel as shown in Figure 2.7, and melt - out depressions where ice had previously been embedded below the scour surface. In the interpretation of these direct field observations, it was proposed that ice failure occurs during scouring so as to produce a more efficient shape which offers less resistance to the advancement of the ice (Clark et al., 1989). The relative uniformity in the shape and dimensions of individual scours along their track indicated that modification of the keel occurs rapidly, likely as the result of shear fracture of the ice during the imposed dynamic loading of the initial grounding event. The infrequent occurrence of small melt - out voids in scour features, which implied the breakout of minor ice volumes, suggested that further modest changes in the ice geometry may also result from continued abrasion or fracture during scouring.

Driving Forces and Ice Motion

An iceberg moves under the combined effects of currents and wind, as well as the forces developed due to gravity, Coriolis acceleration, ocean surface slope (pressure gradient), waves and swell (Sodhi and El - Tahan, 1980). In circumstances where pack ice is present, iceberg motion may also be influenced through loads transmitted by the

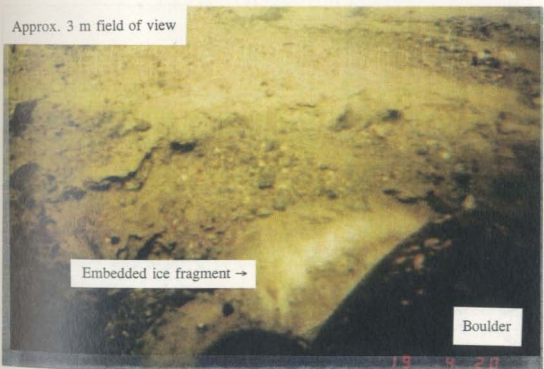
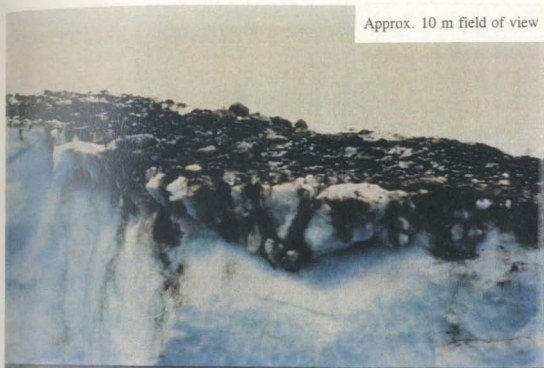


Figure 2.7 Top : Sediment - covered flat (keel) surface of an overturned iceberg;
Bottom : Ice fragment embedded in iceberg - deformed seabed sediments (Photographs
courtesy of Chris Woodworth - Lynas, C - CORE)

surrounding ice sheet (Gustajtis, 1979; Clark, 1991). Almost all of the forces which contribute to drift act on the iceberg through transfer functions of its size and geometry. Currents are the predominant driving force in most cases (Dempster and Bruneau, 1973); wind - induced forces are generally less significant, except during storm events or for movement under constrained pack ice conditions. Average drift speeds for icebergs on the eastern Canadian continental margin typically range from 0.1 to 0.3 m/s, with maximum speeds approaching 1.2 m/s (e.g. Berenger and Wright, 1980; Ball et al., 1981; El - Tahan and El - Tahan, 1983). The velocities of actively scouring icebergs are effectively indistinguishable from those of icebergs which are freely - floating (Woodworth - Lynas et al., 1985).

Icebergs, like ships, have six possible rigid body modes of motion in the general case (Bailey, 1994) and are susceptible to rotational movements under the influence of environmental forces. Contact with the seabed may be initiated in one of three ways (Woodworth - Lynas, 1992) : (1) by drifting into progressively shallower water; (2) by weak rotational capsizing, caused by ablation and minor calving, to a deeper - draft orientation (e.g. Bass and Peters, 1984; Hodgson et al., 1988), or; (3) by catastrophic splitting that causes high energy rotation of one or both fragments to a deeper - draft orientation (Hodgson et al., 1988; Lever et al., 1989). The seabed feature created by the interaction is normally a curvilinear iceberg scour, provided that motion continues in the forward direction, or less commonly a discrete pit, if the iceberg remains stationary following the initial seabed contact (Barrie et al., 1986).

Introduction of the seabed force creates an imbalance at the inception of the scouring event, and rotational movements are induced about the vertical and horizontal

axes of the iceberg. An equilibrium orientation is re-established when the restoring moment due to the shift of the buoyancy force counterbalances the moment set up by the seabed reaction (Lever et al., 1989). Based on observations made during the DIGS field experiment (Hodgson et al., 1988), it was inferred that the iceberg may undergo initial rotation about a vertical axis such that subsequent rolling motions occur about the weakest horizontal axis. These rotational movements also have the effect of minimizing the scouring force developed at the ice / soil interface. Once these conditions are established, further rotations about a vertical axis cease. Examinations of seabed microtopography resulting from irregularities in the ice keel contact surface, indicated that ridges and grooves formed within the scour trough were characteristically parallel to the axis of the scour, reflecting the rotational stability of the scouring iceberg about a vertical axis (Woodworth - Lynas et al., 1991).

A study of iceberg scours that occurred both up - slope and down - slope (Woodworth - Lynas et al., 1986) demonstrated that scour morphology remains relatively constant for changes in seabed relief as large as 15 m. As the iceberg scours into reduced water depths, it is lifted such that the buoyant weight of the ice continues to balance the vertical component of the soil reaction force (Palmer, 1990). Rigid body uplift movements of this kind explain the relative uniformity of scour depth and breadth typically observed over long distances and large ranges in bathymetry. The iceberg may also accommodate the changing seabed force through rotational movements (pitch adjustments) about a horizontal axis during scouring, as suggested by Woodworth - Lynas et al. (1985). The response of the iceberg to shoaling or increasing water depths is clearly a function of both its vertical and rotational hydrostatic stiffness. Additional

vertical movements may occur due to factors other than the seabed uplift force, such as wave loading of the iceberg. Passive failure of the soil resulting from wave forces acting on a grounded iceberg, represents a possible mechanism for the creation of pits having dimensions exceeding those normally associated with the initial impact of the seabed (Clark and Landva, 1988). Extended linear groupings of pits, referred to as crater chains (Bass and Woodworth - Lynas, 1986), may be generated through heave resonance of the iceberg in response to ocean swell. Seabed features of this type are rare, reflecting the improbability of resonant iceberg oscillation during scouring (Woodworth - Lynas et al., 1991). Furthermore, contact with the seabed serves as an extremely effective damping mechanism against wave - induced iceberg motion.

2.4 Centrifuge Model Idealization

2.4.1 Materials Selection

Variability of Seabed Environments

The surficial sediments on the continental shelf of the southern Beaufort Sea are characterized by extreme variability and patchiness over short lateral distances, and in water depths of 15 to 40 m the entire seafloor is re - worked by modern ice scouring activity (Barnes et al., 1980; 1982). The correlation of shallow seismic profiling and borehole data, limited radiocarbon dating, and paleo - environmental information led to the development of a geological model which describes the stratigraphy of the Beaufort shelf (O'Connor and Associates Ltd., 1980; 1982). The shelf is blanketed with a

normally thin veneer of recent marine clays or silty clays deposited following the last sea level rise (Unit A), which grades downwards into interbedded sands, silts, and clays of a complex sequence (Unit B) that was deposited from a transgressing sea. Both Units A and B overlie older, rapidly deposited sediments of glacial fluvial - deltaic origin (Unit C), which may vary regionally from sands to clay, reflecting changes in the depositional environment. The upper boundary of Unit C is an unconformity surface representing a significant period of subaerial exposure, which provided conditions for the growth of permafrost. The distribution of relic permafrost is closely related to the surficial geology and is primarily confined to Unit C, although ice content is infrequently observed within the overlying units. Specific features identified on the continental shelf (massive ice, shallow gas, relic thermokarst depressions) have indicated that the submarine environment may be as complex as the adjacent permafrost - affected land (O'Connor and Associates Ltd., 1980).

On the eastern Canadian continental shelves, the geological setting is generally less complex and associated soil conditions are less variable, in comparison with conditions encountered along the Beaufort shelf. Physiographic features common to both the Labrador Shelf and the Grand Banks of Newfoundland include an inner shelf of rough, resistant crystalline rock with shallow Quaternary sediment cover; a central region of longitudinal depressions, partly infilled by fine grained sediments, and; an outer shelf of large shallow bank areas separated by transverse saddles (topographic depressions), underlain by Cretaceous to Tertiary sedimentary rocks, mantled by re - worked till and glacio - marine deposits (Brown, 1986). The surficial Quaternary sedimentary cover of the Labrador Shelf may be divided into several units, including pro - and post - glacial

sand, silt and clay formations which overlie the lower sequences of glacial till comprising the Labrador Shelf Drift Formation (Josenhans, 1983; Josenhans et al., 1986).

The surficial and shallow bedrock geology of the Grand Banks of Newfoundland have been systematically mapped and described by the Geological Survey of Canada (e.g. Fader and King, 1981; Fader and Miller, 1986). The advance and recession of Pleistocene continental ice sheets served to erode existing sediments and bedrock, and deposited a relatively thin sequence of glacio - marine sediments and till over the region. Subaerial exposure during a late Pleistocene - Holocene low sea level stand resulted in desiccation of the near - surface sediments producing a relatively hard crust several metres in thickness (Segall et al., 1985). The subsequent marine transgression eroded and re - deposited the sediment cover. The recent oceanographic regime further re - works the shallow water sediments and transports icebergs which scour the seabed (Fader and Miller, 1986). Thompson and Long (1989) described the geotechnical conditions in the vicinity of the Hibernia oil field, situated in the northeastern region of the Grand Banks. At all sites investigated, very dense granular soils (typically fine to medium grain sand) were dominant from the seabed to depths of 50 to 60 m, and hard cohesive soils alternating with layers of sand and silty sand were observed at greater depths.

Reconstituted Model Soil

As may be inferred from the preceding descriptions, a buried pipeline traversing ice scoured terrain in the Arctic or eastern Canadian offshore may be expected to encounter a wide variety of soil types and conditions. To understand the fundamental soil behaviour during an ice scouring event, uncertainty regarding the nature and structure of any

anisotropic and heterogeneous field soil deposit must be removed. In order to provide data for the development of theoretical models, it was therefore desirable to examine relevant prototype behaviour using a range of known laboratory materials. As a starting point, the present study considered a class of soil event in which a soil of a particular type and mineralogy was investigated. Provided that the modelling capability could be demonstrated in this case, the approach could then be extended to consider other soil conditions. The use of reconstituted soils in centrifuge models was described in Section 2.2.1.

The soil type in which the model scouring was conducted was Speswhite kaolin clay. An extensive base of material properties data exists for this soil type, as the outcome of research conducted by the Cambridge University Soil Mechanics Group (e.g. Airey, 1984; Al - Tabbaa, 1988). Typical values for some of these properties may be summarized, as follows (Clegg, 1981) :

Liquid Limit	= 69 %
Plastic Limit	= 38 %
Plasticity Index	= 31 %
Specific Gravity	= 2.61
ϕ' degrees	= 23.0
c_u / σ'_{v0}	= 0.22 (normally consolidated)
K_u	= 0.69 (normally consolidated)
λ	= 0.25
κ	= 0.05
Γ	= 3.44
M	= 0.90

where ϕ' is the effective angle of friction, $c_u / \sigma'_{v,0}$ is the normalized undrained shear strength, K_0 is the coefficient of lateral earth pressure at rest, and λ , κ , Γ , and M are parameters of the Cam clay model (see for example Wood, 1990). Values of the slopes λ and κ of the normal compression and unloading - reloading lines were acquired from accumulated experience at Cambridge University with oedometer and triaxial tests. The slope M of the critical state line in the effective stress plane and the parameter Γ describing the position of the critical state line in the compression plane were obtained from undrained triaxial tests with pore pressure measurement. Further details concerning the material properties of Speswhite kaolin clay are presented in Chapter 5.

The techniques employed in the preparation of clay specimens are outlined in Chapter 3. The laboratory pre-consolidation stress level was altered in particular tests to examine the influence of soil state on the effects of ice scouring. The stress history of each clay specimen was selected to establish desired stress states in the specimen without detailed reference to a specific prototype. To ensure that the results which were obtained would be relevant in practice, general reference was made to the geotechnical properties of Beaufort Sea clays which form a part of the surficial Unit A sequence, described briefly in the following.

Comparison with Beaufort Sea Clays

The recent marine sediments on the Beaufort shelf commonly consist of soft to very soft silty clays of low to medium plasticity. The measured thickness of the surficial Unit A clays is generally less than 6 m, but may increase to 15 or 20 m where large topographic depressions are infilled (Meagher, 1978). As a result of their shallow extent and soft

consistency, these materials are difficult to sample and therefore only limited data are available on their geotechnical properties. Been et al. (1986) provided a summary of test results for seabed clays on the Akpak Plateau and Tingmiark Plain regions of the Beaufort shelf. The data presented by the authors indicated consistent trends despite widely spaced site locations. The most notable feature reported was high liquidity indices, which ranged from 2 to 3 at the seabed, to values in excess of 1 with depth. High water contents and liquidity indices were reflected in the associated undrained shear strength profiles. The strength data were scattered but showed a linearly increasing trend at a rate of about 6 kPa/m with depth, and a projected zero strength value at the seabed surface. Results were presented for a single consolidated undrained triaxial test performed on a relatively undisturbed surficial clay sample. The observed stress - strain response was described as elastic - plastic, with no evidence of strain softening. The effective stress path indicated modestly dilatant behaviour, which appears to be a common feature of Beaufort Sea clays (Crooks et al., 1986). Studies were also undertaken to define the compressibility and stress history characteristics of the recent marine sediments (Hivon, 1983; Christian, 1985; Christian and Morgenstern, 1986). The clays were shown to be apparently overconsolidated within upper 6 to 10 m of burial. High values of the overconsolidation ratio at the seabed surface may be attributed in part to the existence of a finite effective cohesion at zero effective stress (Christian and Morgenstern, 1986).

In each centrifuge test, the mechanical behaviour of a full scale prototype stratum of saturated clay, 18 m in depth at Earth's gravity, was studied at 1/100 scale in a model specimen of equivalent soil brought into equilibrium at 100 gravities in - flight. The

preparation of models in the laboratory permitted control of the stress history, so that it was possible to obtain a desired range of strength and stiffness. At equilibrium conditions on the centrifuge, the near surface clay of each specimen was in an overconsolidated state and exhibited undrained shear strengths in the range of 10 to 20 kPa. For comparison, Figure 2.8 shows undrained shear strength plotted against prototype depth for the baseline centrifuge model conditions investigated in the present study, together with the strength profile suggested by Been et al. (1986) for surficial Beaufort Sea clays. A comparison of the associated profile of overconsolidation ratio with results reported by Hivon (1983) for the Kringalik Plateau region of the Beaufort shelf is also presented in Figure 2.8. These plots demonstrate that a comparable range of soil behaviour existed for the proposed model specimens and relevant field conditions.

Another factor which may be expected to influence the behaviour of field soil deposits is the re - working of surficial sediments due to ice scouring. An interval of about 4 to 5 m over which the original bedding of seafloor sediments has been destroyed by active scouring, is a common feature observed on nearly all of the high resolution seismic records collected for the Beaufort shelf (O'Connor and Associates Ltd., 1980). A process of repeated deformation and subsequent re - equilibration with diffusion of water between scouring events, may bring the soil to a critical state (Palmer et al., 1990). This implies that soil in the active scour zone may undergo continued shear deformation without any tendency to dilate or develop changes in pore pressure. The depositional environment on the Beaufort shelf in addition to the existence of a re - worked zone, may commonly produce surficial sediments with layers which exhibit markedly different soil behaviour. Horizontally bedded sediments were not investigated

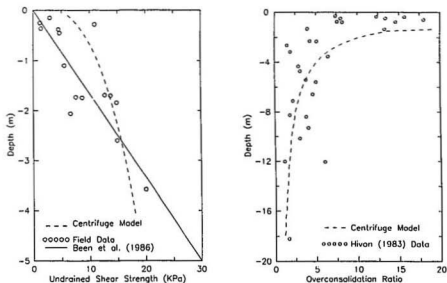


Figure 2.8 Comparison between baseline centrifuge model conditions and field data for Beaufort Sea clays. Left : Undrained shear strength profile; Right : Overconsolidation Ratio

in the research reported here; however, layered deposits represent a relevant field soil condition for further study.

2.4.2 Model Scouring Event

The description of field conditions provided in Section 2.3 suggests that ice scouring is a complex phenomenon which involves the interaction of an ice feature (subject to environmental driving forces which may include wind, wave, current, and pack ice loading) and the seabed soil. The ice feature may be independent or it may reside within a relatively continuous ice sheet. It may experience uplift or rotational movements and these movements

may be resisted by its buoyant weight or through forces generated between the feature and a surrounding ice sheet. The ice keel may also be irregular in shape and its geometry may be altered through abrasion and fracture. In addition, the seabed may exhibit a significant slope or unusual surface morphology. Finally, as indicated in the preceding section, the scouring event may involve a considerable range of soil types and conditions.

Despite the inherent complexity of ice scouring, the field evidence also indicates that most scour features are curvilinear in nature and exceptionally uniform in cross - section over long distances. For modelling purposes, it can be reasonably assumed that the forces which are driving the ice feature in these instances are large enough to ensure its continued motion. Horizontal movement of the ice at an effectively constant velocity may represent the most relevant scouring condition in practice, and this steady - state case also forms a rational starting point for quantitative analysis (Palmer et al., 1989).

Experimental studies of ice scouring, as referenced in Chapter 1, commonly involved constant velocity displacement - controlled simulations. Most studies also considered single degree of freedom representations in which the model ice feature was constrained to translate horizontally at a fixed scour depth. In the general case, the ice feature may undergo vertical and rotational movements through its interaction with the seabed. Vertical ice movements are directly related to the vertical forces applied to the seabed. The effects of the scour process may therefore be expected to vary depending upon the restrictions imposed on the movements of the scouring ice. Physical modelling which allows for uplift of the model ice feature during the event and which considers a range of plausible vertical stiffness conditions may permit a rational assessment of the

importance of vertical movements on scour effects.

Appropriate modelling of the ice feature geometry and structural integrity is also hindered by uncertainties concerning full scale geometry and properties. A logical starting point is the idealization of the ice keel as a rigid body which has sufficient strength to withstand the forces developed during scouring. The shape of the rigid keel may be chosen to reflect the equilibrium geometry of the ice developed during steady - state scouring. The field evidence given in Section 2.3 provides a basis for the development of an appropriate idealization. Keel shapes with low attack angles which form a planar surface in the region of soil contact appear to be relevant based on the available data, the geometry of scour features, and inferences pertaining to keel modification during the initial stages of the event.

The prototype scouring event investigated in the present study involved the horizontal movement of an ice feature through a homogeneous, level seabed at a constant velocity. At model scale, the ice feature was represented by a rigid body which was free to lift or rotate to achieve a steady - state position. These movements were determined by its buoyant weight in free surface water, and by forces developed through interaction with the soil (hence, the term model iceberg is used). The basic geometrical characteristics of the model iceberg were represented by specifying the attack angle of a planar leading face, and the length, width, and depth of the portion of the model which was in contact with the soil. The model iceberg configuration and associated parameters are depicted schematically in Figure 2.9. These parameters may be varied over ranges presumed to be relevant to the field situation, to examine their influence on the effects of scouring. For the series of tests reported here, the soil initial stress state, and the

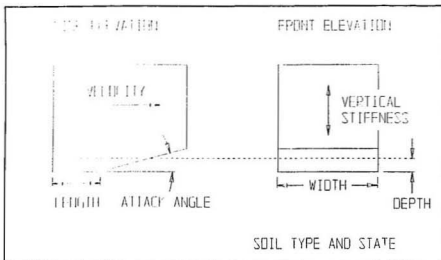


Figure 2.9 Model iceberg geometry and parameters of the scour problem

attack angle, width, and vertical stiffness of the model iceberg were investigated as test variables. The following sections address particular issues related to the specification of relevant model conditions for ice scouring.

Three Dimensional Representation

The ice scouring process may be modelled as either a two dimensional plane strain problem or as a three dimensional problem. To simulate plane strain conditions in centrifuge tests, the two important boundary conditions of zero out - of - plane normal strain and zero in - plane shear stress must be fulfilled. In practice, a long narrow rectangular container is commonly employed, and side friction effects are minimized by suitable choice of materials and lubricants. In this type of arrangement, a half model iceberg would travel adjacent to a transparent side wall of the container which would

coincide with the vertical plane through the scour axis. An advantage of this representation is that subsurface soil deformation along this plane of symmetry may be observed and recorded during the event.

A plane strain physical model may provide an inadequate description of the effects of ice scouring. Experiments conducted in both coarse and fine grained soils (e.g. Poorooshasb et al., 1989; Poorooshasb, 1989; Paulin, 1992) supported field observations (Woodworth - Lynas et al., 1990) which implied that large transverse soil movements occur in the plane perpendicular to the direction of travel. The implementation of a two dimensional representation may therefore impose stress and displacement constraints on the model which do not exist in the prototype. To ensure test results which were consistent with real behaviour, three dimensional models were used in the present study, accepting the limitation that subsurface soil deformation could only be investigated after the completion of the scouring event.

Model Vertical Stiffness

The prototype ice feature was represented by a geometrically similar rigid body which was partially immersed in free surface water. For hydrostatic conditions, fluid pressures were identical in the model and prototype, and other quantities scaled in accordance with the relationships presented in Table 2.1. Since soil behaviour is exclusively dependent upon changes in effective stress (Terzaghi, 1936), an identical soil response was expected during scouring regardless of the depth of free water, provided that the soil was fully saturated at all points. The fluid conditions were, however, important, in conjunction with the geometry of the submerged portion of the model iceberg, in determining its

overall movement and stability during a scouring event.

The available field evidence pertaining to scouring ice motion is outlined in Section 2.3. Specific pressure ridge interaction conditions which involve ice sheet failure during uplift, as illustrated in Figure 2.6, were not modelled in the present study. Initial rotational movements (pitch adjustments) and rigid body uplift prior to steady - state scouring, were permitted as expected conditions for an independent ice feature. Furthermore, due to model symmetry about the scour axis and the imposed constant direction of travel, there was no tendency for rotation about a vertical axis or lateral translation. To ensure uplift movements which were representative of relevant field behaviour, it was required to model the prototype vertical stiffness conditions. In practice, this implied specification of the maximum practicable waterplane dimensions for the model, to achieve stiffness values which were plausible for a full - sized iceberg or pressure ridge. While it was desirable to investigate a range of conditions, only limited variation was possible in this test series. The model iceberg buoyancy characteristics for individual tests are detailed in Chapter 4.

Interface Conditions

The relative displacement or slip between the ice feature and the soil affects the soil response and depends upon the type of contact surface and the intensities of normal and shear stress developed at the interface. The limited field evidence suggests that the ice - soil interface is approximately planar and that contact surface roughness conditions may vary as the result of ice - entrained seabed material. Dead zones of soil with small or negligible movement relative to the interface may also be expected to form within the

rupture surface in front of the ice keel. This type of soil behaviour has been observed in soil cutting and indenter experiments (e.g. Hettiaratchi and Reece, 1975; Golder Associates Ltd., 1990), and serves to alter the effective interface geometry and properties. In addition, observations of trenching ploughs in soft clays indicated that most of the relative motion between the plough and the clay occurs within a boundary layer adjacent to the plough contact surface (Palmer et al., 1979).

In general, limited information was available to define full - scale interface conditions and it was not feasible to model such conditions directly in the tests reported here. Instead, a reasonably well - defined contact surface was used, with surface roughness attributes expected to fall within the range of conceivable field conditions. Further investigation is required to assess the influence of changes in interface properties on the effects of ice scouring. This may be accomplished through parametric studies based on theoretical models which have been validated against experimental results for known interface conditions.

Scaling of Time Dependent Processes

A velocity of approximately 0.1 m/s was selected for the notional prototype event to be modelled in each test. For icebergs on the Canadian east coast, average drift velocities are typically about 0.2 m/s, whereas mean long term winter ice drift velocities in the transitional zone of the Beaufort Sea are on the order of 0.03 m/s. In the latter case, however, scouring activity has also been strongly correlated with storm episodes which serve to accelerate the ice motion. Palmer et al. (1989) suggested that field scouring deformations in clay and fine silt are always undrained, and that in sands and coarser

silts, velocities greater than about 1 m/s are required for undrained deformations to occur. The authors based these conclusions on the observed behaviour of seabed ploughs.

It was required to select the rate at which the model iceberg was advanced such that the prototype event was scaled correctly. Unfortunately, there exist different categories of time - dependent phenomena for geotechnical models, for which different scaling relationships are applicable. The time scale for an event in which pore pressure dissipation is to be modelled may be derived from the theory of one - dimensional consolidation (e.g. Taylor, 1948). The solution of the basic differential equation for a one - dimensionally consolidating soil layer is commonly specified in terms of a relationship between a dimensionless degree of consolidation and a dimensionless time factor. To ensure similarity, the time factor T_v must therefore be equivalent for both the model and prototype systems. This condition may be expressed as

$$T_v = \left[\frac{c_v t}{h^2} \right]_m = \left[\frac{c_v t}{h^2} \right]_p \quad (2.6)$$

where the subscripts m and p refer to model and prototype respectively, c_v is the coefficient of consolidation, and h is the length of a drainage path. In a model with the same soil and pore fluid as the prototype, c_v is the same for both systems, and if the linear dimensions are scaled by the factor 1/N from the prototype, the length of a drainage path is also reduced in accordance with the change in linear scale. Hence, from Equation 2.6, the times for consolidation in the model and prototype are related by

$$t_m = \left\{ \frac{1}{N^2} \right\} t_p \quad (2.7)$$

such that consolidation proceeds much more rapidly in the model than in the prototype. For the scale factor $N = 100$, this relation indicates that one hour of model time represents greater than one year of prototype consolidation time.

For dynamic events, a different time scale factor is derived from consideration of the equations of motion. The accelerations in the model and prototype are related by the scale factor N , and the following expressions may be written to describe the motion :

$$\frac{d^2 x_p}{d t_p^2} = A \omega^2 \sin (\omega t_p) \quad \text{and} \quad \frac{d^2 x_m}{d t_m^2} = N A \omega^2 \sin (N \omega t_m) \quad \dots (2.8)$$

where A is the displacement magnitude and ω is the frequency of the motion. This leads to relationships for displacements in the two systems given by

$$x_p = A \sin (\omega t_p) \quad \text{and} \quad x_m = \frac{A}{N} \sin (N \omega t_m) \quad (2.9)$$

which implies that model and prototype times are related by

$$t_m = \left\{ \frac{1}{N} \right\} t_p \quad (2.10)$$

Since any motion may be represented as a Fourier series which is a summation of sine functions, the time scaling relationship given by Equation 2.10 is generally applicable to any displacement or loading. However, this result conflicts with the time scaling requirement for consolidation in Equation 2.7, and inconsistencies arise when both drainage and inertial effects need to be considered. In some instances, particularly where the dynamic behaviour of sand models is to be investigated (c.g. Dean and Schofield, 1983), this conflict between time scaling factors may be surmounted by using a pore fluid with a similar density to the prototype fluid but a much higher viscosity. The

effect of scaling up the viscosity of the pore fluid is to increase the model consolidation time so that it is compatible with the inertial time.

For a rapid event and impermeable soil, the inertial scaling factor is the only one of relevance. Model scouring in the present study was regarded as an approximation to this case, with negligible pore pressure dissipation during the event. Model time was determined in accordance with the scaling relationship given by Equation 2.10 and, therefore, the specified rate of scouring for the model was identical to the prototype velocity (i.e. approximately 0.1 m/s). This implied that model pore pressure dissipation transpired more rapidly relative to other time dependent events and that, at corresponding points in the model, pore pressure build - up was smaller than in the prototype. Model time scaling based on Equation 2.7 would entail scouring rates which were N times greater than prototype velocities. For the scale factor $N = 100$, this would necessitate a model speed on the order of 10 m/s, which was an impracticable requirement in consideration of the available equipment and instrumentation.

The extent of drainage during the model event may be assessed through the inspection of isochrones which display the variation of excess pore pressure with position at specified times. Consolidation, with dissipation to a drain at the surface, begins near the surface and progresses downward through the soil. The gradient of an isochrone, and therefore the seepage velocity, increases with proximity to the surface. In the present study, the total length of advance of the model was less than 500 mm which implied an event duration of about 5 seconds at a model speed of 0.1 m/s. Hence, for Speswhite kaolin clay, having a coefficient of consolidation in swelling of about $1.0 \text{ mm}^2 \text{ s}^{-1}$, the

maximum isochrone depth L developed during the event may be approximated as follows :

$$L = \sqrt{12 c_v t} = \sqrt{12 \times 1.0 \times 5} \approx 7.8 \text{ mm} \quad (2.11)$$

using the expression derived from the method of parabolic isochrones for an initially uniform excess pore pressure (Schofield and Wroth, 1968). This result provides an indication of the rate at which the effects of consolidation progressed into the soil from the drainage boundary of the model. It may be expected that excess pore pressure dissipation during the event was confined to the surficial region above the calculated depth of isochrone penetration.

Strain Rate Effects

Another scaling effect for time dependent processes may arise due to the rate of deformation (Craig, 1982). The mechanical properties of clay are strain rate dependent. Typically, a ten - fold increase in strain rate may lead to an increase in the apparent undrained shear strength on the order of 5 percent. The model event should therefore ideally be conducted at the same strain rate as the prototype event, to ensure that the same soil behaviour is observed in both systems. This requires that the model event be undertaken over the same time scale as that of the prototype. For model times in the tests reported here, altered according to inertial similarity (Equation 2.10), the strength mobilized may be expected to increase by a factor consistent with a strain rate increase of $N = 100$, with strains being equal at all homologous points in model and prototype as discussed by Bolton et al. (1973). The implementation of the time scaling relationship

for diffusion phenomena given by Equation 2.7, would have produced substantially higher rates of strain and associated effects in the model.

For the particular clay and rate of deformation investigated in this study, the possible scaling effect introduced by differences of strain rate was not expected to be highly significant. For example, from the results of cone penetration tests conducted in Speswhite kaolin clay, it was observed that the measured point resistance was not significantly influenced by the penetration rate, for rates as high as 20 mm/s (Cheah, 1981; Almeida and Parry, 1983). The magnitude of the rate effect may not be measurable for the tests reported here, as it is comparable to acceleration, curvature, and Coriolis errors, each of which contributed to limiting the accuracy of the centrifuge model tests.

2.4.3 Model Pipeline Scaling

A typical marine pipeline has an outside diameter of 610 mm (24 inches) and a wall thickness of 15.9 mm (0.625 inches) (e.g. Golder Associates Ltd., 1990); although, in the extreme, a buried pipeline as large as 1422 mm (56 inches) with a wall thickness of 19.1 mm (0.750 inch) was installed offshore in the Gulf of Mexico (Andrier, 1981). Flowlines and transmission pipelines for oil and gas are constructed from carbon steel alloyed with manganese and conforming to the API 5L Specification. The API Specification details the properties of the steel; pipeline steel grade is identified by the yield strength as X42 to X80, where the numbers indicate the yield strength in units of ksi. Over the period of the last three decades, the strength of commonly used line pipe

has increased from 290 to 448 MPa (corresponding to API X65 grade steel) (Cold Ocean Design Associates Ltd., 1994).

The main objective of the tests reported here was to understand soil behaviour during ice scouring by investigation of the stress and deformation fields developed for well - defined soil conditions. Model pipelines were also included in the test representation to provide limited direct evidence of the effects of scouring on buried pipelines. Prior to the test, the model pipelines were set into trenches excavated within the specimen and the trenches were backfilled with the clay that had been removed. The maximum pre - consolidation stress was reapplied to the clay specimen following installation, in order to dissipate excess pore pressures and minimize the effect of disturbances associated with the trenching activities. The resultant remoulded state of the infilled material was representative of field soil conditions produced by ploughing and backfilling operations. The model pipeline installation procedures are detailed in Chapter 3.

The deformation of a buried pipeline may be influenced by several factors, and it was not practicable to reproduce all aspects of the full - scale situation in the model. Only finite pipeline lengths were modelled, as constrained by the dimensions of the tub in which the clay specimen was contained. As a result, the ends of the model pipeline segments assumed an unknown degree of fixity in the surrounding soil during a test. Moreover, other prototype features such as operating internal pressures and temperatures, and concrete weight - coating of the pipeline were not modelled in these tests.

Some of the scaling relationships applicable to model pipelines may be developed from consideration of soil loading - induced deformation through bending effects or axial

compression under shear. Other possible mechanisms of deformation and failure, such as twisting, buckling, or indentation, are neglected in the subsequent derivation. To specify the simplified physical system for an ideal elastic - plastic material, a functional equation describing the pipeline deflection δ may be written as follows :

$$\delta = f (EI, M_p, EA, m, \sigma, l, \rho) \quad (2.12)$$

in which the symbols used are defined such that : E = Young's modulus; I = moment of inertia; M_p = plastic moment capacity; A = cross - sectional area; m = mass per unit length; σ = a characteristic applied stress; l = a characteristic length, and; ρ = material density. The application of partial analysis to this system then yields the following equation expressed in terms of non - dimensional groups :

$$\epsilon = \psi \left\{ \frac{EI}{\sigma l^4}, \frac{M_p}{\sigma l^3}, \frac{EA}{\sigma l^2}, \frac{m}{\rho l^2} \right\} \quad (2.13)$$

where ϵ refers to a relative displacement or strain and ψ indicates a functional relationship or dependency. Model design criteria which satisfy the requirements of Equation 2.13 are presented in Table 2.2 for a geometrically similar model pipeline subjected to the same applied stresses as the prototype. The implication of the relationships specified in this table is that in order to ensure similarity between model and prototype effects, the pipeline material used in both systems must have the same stiffness characteristics and yield stress. In particular circumstances where only the elastic behaviour is of interest, a different material with a reduced elastic modulus may be employed in the model, provided that wall thickness is increased such that the first term

Table 2.2 *Scaling Relationships for Model Pipelines*

Quantity	Full Scale : Model at N_g
Diameter and Wall Thickness	1 : 1 / N
Elastic Bending Stiffness, $E I$	1 : 1 / N^4
Plastic Moment Capacity, M_p	1 : 1 / N^3
Axial Compressive Stiffness, $E A$	1 : 1 / N^2
Mass / Length, m	1 : 1 / N^2

on the right hand side of Equation 2.13 is equivalent in both model and prototype systems.

In the present study, model pipelines were used to provide an indication of the plastic deformation which may be experienced by typical prototype pipelines situated at different depths below a scouring ice keel. In order to accurately model the plastic response, it was therefore required to use model pipelines which were comprised of the same material as the prototype, with external diameter and wall thickness dimensions reduced in proportion to the length scaling factor for the centrifuge model. The selection of material properties and sectional dimensions was limited by the availability of appropriate steel tubular sections. Details of model pipeline characteristics are provided

in Chapter 3. In general, two model pipeline segments were used in each test, and placed at different depths within the clay specimen. These were 800 mm length segments of stainless steel tubing having an outside diameter of 6.35 mm and a wall thickness of 0.25 mm. The maximum yield stress of the tubes was about 380 MPa. The corresponding prototype system therefore involved a pipeline with a thickness to diameter ratio greater than the range of values which may be used in common field situations. Furthermore, the material yield stress was somewhat less than that required for pipeline steels currently employed in practice. These inadequacies of the representation must be taken into consideration in the evaluation of model test results.

The specified material and boundary conditions which defined the model scouring events investigated in individual tests, selected in accordance with the discussion of Section 2.4, are presented in Chapter 4.

Chapter 3

Experimental Devices and Procedures

3.1 Introduction

The concepts discussed in the preceding chapter were applied in the development of a programme of small scale model tests of ice scouring. The objective of the model tests was to collect accurate data for well - defined physical events. Testing within the centrifuge environment imposed practical restrictions on the methods used to achieve this objective. The size of the model was limited by the physical dimensions and payload capacity of the centrifuge. The elevated acceleration field and the remote communication requirements also constrained the design and selection of the systems used for test control and data retrieval. To accommodate these constraints, whenever applicable, proven modelling techniques and apparatus developed in conjunction with past research at the Cambridge University centrifuge facility were employed in the present study.

The test apparatus and experimental methods used to investigate the problem of ice scouring are described in this chapter including : the laboratory preparation of clay specimens prior to centrifuge testing; the equipment and instrumentation used in the simulation and monitoring of an idealized scouring event in - flight on the centrifuge,

and; the post - test site investigation procedures used to further evaluate the effects of the model scouring event. Modifications were made to improve the experimental set - up and methods on the basis of knowledge gained as the study progressed. Therefore, a general outline is presented here, and variations in individual tests are described with the corresponding test results in Chapter 4.

3.2 Preparation of Clay Specimens

The techniques and apparatus used in the laboratory preparation of clay specimens are considered in this section. The installation of pressure transducers and other inclusions within the specimen which were used to obtain internal measurements of the material responses are also described.

3.2.1 Laboratory Consolidation

The clay was consolidated in the laboratory to ensure the establishment of appropriate stress states at consolidation equilibrium conditions under self - weight stresses in the centrifuge. For the tests performed in the present study, this involved the application of a total stress to the clay and dissipation of the resulting excess pore water pressures in order to establish a uniform vertical effective stress over the depth of the specimen. The portion of the soil body with in situ effective stresses below this maximum stress was then overconsolidated. The level of pre - consolidation was selected to obtain a desired profile of the overconsolidation ratio and was altered in particular tests to examine the influence of soil conditions on the effects of ice scouring.

A single specimen of clay was prepared for each of the centrifuge tests performed. The stress history of the material was initiated in the laboratory where it was reconstituted from a slurry. Speswhite kaolin clay, supplied commercially in dry powder form, was combined with deionized water to produce the slurry. The slurry was mixed in batches which comprised 50 kg of kaolin powder and 60 litres of water to yield nominal moisture content values of 120 percent (about twice the liquid limit of the clay). Three batches were prepared for each test to allow for sufficient slurry to produce a consolidated specimen thickness of 180 mm. The mixing of each batch was carried out under a partial vacuum of approximately 0.5 atmospheres for a minimum time period of two hours. This procedure resulted in a homogeneous slurry of smooth consistency and ensured a high degree of saturation in the subsequently consolidated clay specimen.

A steel, cylindrical tub, 850 mm in diameter and 400 mm deep, served to contain the clay specimen both during laboratory preparations and in - flight on the centrifuge. Of the containers available at the Cambridge facility, this design afforded the maximum surface area in which to conduct the model scouring event.

The container approximated the boundary conditions required for one - dimensional consolidation. The walls of the tub provided a condition of high lateral stiffness and were coated with a water - resistant grease to reduce friction. Allowances were made for two - way drainage at the bottom and top of the clay specimen. A steel plate with channels cut in its surface was positioned on a rubber mat which rested on the base of the tub. The plate served as part of the drainage system for the tub and also facilitated post - test extrusion of the specimen. A porous sintered plastic sheet was set on top of the plate to permit vertical drainage from the clay to a bottom drainage outlet

in the tub situated at the level of the plate. Prior to placement of slurry within the tub, the base drainage layers were saturated with deionized water and moist filter paper was laid on top of the porous sheet. The slurry was then placed in the tub, with precautions taken to ensure that air was not trapped within the soil mass or the underlying drainage layers. Finally, the slurry surface was covered with filter paper and a second sheet of porous plastic to permit drainage at the top of the specimen.

A large hydraulic press or consolidometer, shown in Figure 3.1, was used to apply the required constant total stress to the clay. The tub containing the slurry was assembled into the consolidometer and the rigid piston was brought to bear on the upper sheet of porous plastic. During consolidation, drainage was allowed through the outlet at the base of the tub to an external reservoir, and water was also expelled around the edges of the piston at the upper surface. The stress was applied in a series of increments. The slurry was initially left to consolidate under the ram and piston self weight (about 5 KPa) for a period of one to two days. Each successive increment imposed was then about two times as large as the preceding increment until the maximum consolidation stress was attained. The entire procedure was generally completed in three to four weeks with roughly three days allowed for each increment. The degree of consolidation was monitored by measurement of the vertical settlement of the consolidometer piston and also by pore pressure transducers installed within the specimen.

3.2.2 Pore Pressure Transducers and Installation

Pore water pressures were measured throughout the various stages of laboratory

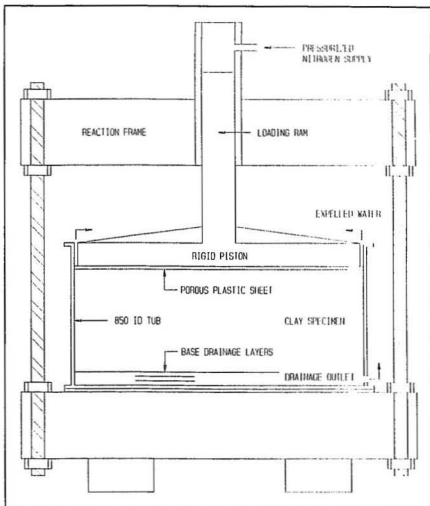


Figure 3.1 *Sectional view of laboratory consolidometer*

preparations and centrifuge testing, both as a monitor on the extent of consolidation and as a means of defining the soil response during the scouring event. These measurements were made using miniature differential pore pressure transducers with an operating

pressure range of 350 KPa (type PDCR 81 manufactured by Druck Ltd.) shown in Figure 3.2. The advantage of these devices for use in the present study derived from their small size (6.4 mm diameter, 11.4 mm length) and their rapid response time, which is on the order of 0.1 seconds in saturated kaolin clay (Mair, 1979). The active face of the transducer consists of a crystal silicon diaphragm with a strain gauge bridge diffused into its surface. The diaphragm is shielded by a porous (ceramic) stone which resists the effective stress of the soil particles to isolate water pressure for measurement. To ensure a high degree of saturation of the transducer, the porous stone was de-aired by boiling in water for a period of about 15 minutes. In addition, the transducer was immersed in water during attachment of the stone immediately prior to placement in the specimen.

A total of eight pore pressure transducers was installed. The installation procedure was carried out before application of the final stress increment during laboratory consolidation. The bottom drainage outlet was closed, excess water was removed from the surface of the specimen, and the consolidation pressure was released. The pore pressure transducers were placed at particular depths in the specimen through ports situated at four equidistant points around the tub wall. An extension piece was first secured to the port to provide alignment for the insertion of a 7 mm diameter greased thin-walled tube. The tube was driven horizontally into the clay specimen to a position which was about 5 mm short of the proposed transducer location. The clay within the tube was augered out and the tube was withdrawn leaving a clear passageway to allow for placement of the transducer. The de-aired transducer was then set on a guide and pushed into position within the clay at the end of the passage. To backfill the void left in the specimen, clay slurry was injected using a pump with a long hypodermic tube.

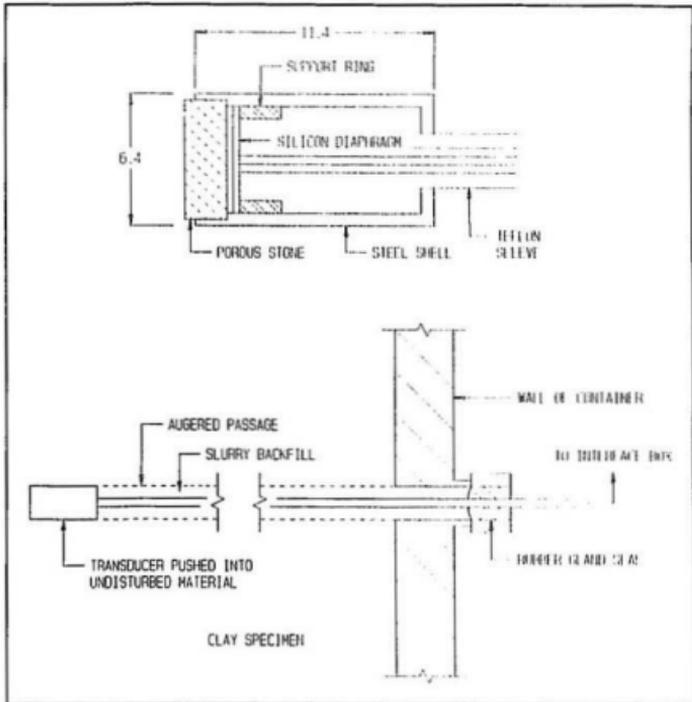


Figure 3.2 Top : Schematic section of pore pressure transducer; Bottom : Diagram of transducer insertion into clay specimen

Finally, the entry port was plugged with a rubber gland seal fitted around the transducer lead at the side wall of the container (Figure 3.2). The gland seal allowed for venting through the lead to provide the reference (atmospheric) pressure for the transducer.

The installation procedure generally permitted positioning to within ± 5 mm of the proposed transducer location. However, encroachment of the soft sidewalls of the

placement shaft and separation of the instrument from the guide could result in substantially larger inaccuracies. The procedure was repeated for the remaining transducers and was generally completed in less than three hours. The pressure on the specimen was then restored to its former level and drainage at the base outlet was reinstated.

3.2.3 Visual Techniques for Soil Deformation Measurement

The methods employed to measure sub - surface soil displacements involved the placement of grids of easily deformable materials at sections both parallel - and perpendicular - to the scour axis. Grids which comprised horizontal and vertical members placed at 10 mm intervals were used; a more detailed mesh sizing was considered impractical in light of the procedures required to construct and install the members. The horizontal members consisted of segments of very fine solder attached to strands of coloured, dry spaghetti of nominal 2 mm diameter. The spaghetti strands were retained at the appropriate spacing (accurate to within ± 0.5 mm) by similar vertical pieces fixed at 100 mm intervals, which facilitated the installation of all members as a single unit. After placement within the sample, the spaghetti became pliable due to the presence of water but retained its initial configuration.

Lead powder trails were injected into the specimen to form the vertical members of a grid. Both the lead trails and the solder segments were amenable to detection using radiographic techniques. The deformed pattern of each grid could also be determined by

direct excavation of the grid members. The post - test investigation procedures are detailed in Section 3.6.

To minimize disturbance of the clay specimen, model pipeline segments were installed concurrently with the grids used to monitor soil displacements. The model pipelines were lengths of commercially available stainless steel tubular sections (material designation T304, seamless). The tubes have an outside diameter of 6.35 mm and a wall thickness of 0.25 mm with tolerances of ± 0.10 and ± 0.04 mm respectively on these dimensions. The maximum yield strength of the tubing material is approximately 380 MPa. In general, two 800 mm length segments were installed within the clay specimen at sections perpendicular to the scour axis, each at different depths.

For practical reasons related to the initial test objectives and the availability of supplies at the time of testing, a different type of tubing was used to represent the pipeline segments in the first centrifuge test of the series. The sections used in this test are extruded from an aluminum alloy (material designation 6063 - TF) with a minimum 0.2 percent proof stress of 160 MPa. The tubes have an outside diameter of 6.0 mm and a wall thickness of 0.7 mm. Both dimensions have a tolerance of ± 0.1 mm. A total of five 650 mm length segments were placed in the Test 1 specimen.

Installation of Grids and Model Pipelines

The installation of soil deformation grids and model pipeline segments was carried out subsequent to the establishment of equilibrium conditions under the maximum pre - consolidation stress increment. To allow access to the clay surface, the specimen was unloaded and removed in its tub from the consolidometer. The pressure was reduced

in steps during unloading to avoid the onset of cavitation caused by high pore water pressure suction. The confining piston, porous plastic sheet, and filter paper were next removed. The exposed top of the clay specimen was then scraped to remove a small amount of excess material, to yield a smooth level surface at the final elevation. An allowance was made in determination of the required elevation for the elastic rebound of sample as measured during unloading.

Trenches were excavated within the clay specimen to permit the placement of grids and model pipelines at particular depths below the initial surface level. Markings were first lightly etched into the clay surface to give an accurate plan of trench locations relative to the proposed scour axis. To provide a guide for the tool used to cut the trenches, two steel bars were spanned across the top of the tub, supported at either end by the upper flange of the container. The positions of the bars were adjusted to ensure correct alignment of the tool during the cutting process, and the bars were then clamped in place. The cutting tool comprised a flat plate with a narrow protruding section of width equal to the required 12.5 mm trench width and length somewhat greater than the maximum proposed trench depth of 75 mm. To create a trench, the rounded tip of the narrow section of the tool was pushed into the clay to a fixed depth and the tool was drawn across the specimen while maintaining contact with the guide bars. The extruded clay was intermittently removed from the face of tool and stored in plastic wrap for later usage in backfilling operations. A section of angle bolted to the tool rested on the guide bars during the cutting process. The height of the angle was adjusted to set the depth of the cut. To reduce associated disturbance of the clay specimen, the trenches were excavated gradually in 5 mm cutting depth increments.

After the completion of excavation, the prepared grid was lowered into the trench, aligned at the required depth, and then gently pressed into the trench side wall to fix its position and prevent damage during backfilling. At axial sections, the grid was placed against the trench wall coincident with the scour axis whereas, at cross - sections, it was placed at the front wall relative to the direction of scouring. The trench was then backfilled by hand using a small spatula with an angled blade. The clay that had been removed during excavation was returned to the trench in a highly remoulded state as a result of handling and placement procedures. To install the model pipeline at a cross - section, the trench was first backfilled to a depth slightly higher than the desired elevation of the model pipeline invert. The trench cutting tool was then used to remove the excess material to provide a level base onto which the tubing segment was placed. The backfilling process was then resumed to completion. The installation procedures were carried out over a two day period during which efforts were made to prevent exposure of the clay surface in order to limit the ingress of air into the specimen. The positions for insertion of lead powder trails were then marked out, the specimen was covered with a layer of plastic wrap, and the piston self weight was reapplied overnight to ensure an even surface.

Lead Powder Trail Insertion

Lead powder trails were formed by injecting a lead suspension into the specimen to create a lead - coated shaft. Figure 3.3 illustrates the preparation and insertion procedures. The lead suspension was hand mixed from lead powder (less than 100 mesh size) and water soluble machine cutting oil. A sufficient quantity of lead powder was

added to ensure an even deposition on the wall of the shaft after diffusion of the oil into the surrounding clay.

The mixture was first drawn into a piston cylinder to allow for discharge to the hypodermic tubing used for injection. The length of the tubing was selected to provide a depth of insertion of 80 mm for the vertical trails forming part of the soil deformation grids. The tubing consists of a narrow section probe (1.6 mm outer diameter, 0.5 mm wall) to be inserted within the clay, brazed to a larger section barrel. The end of the barrel is threaded to permit attachment to a port on the cylinder. To fill the probe and barrel, the piston was slowly advanced to force the lead suspension from the cylinder into the tubing, with care taken to expel entrapped air pockets.

Special apparatus was used to locate and guide the probe during insertion of the lead trail. The location of a line of lead trails was fixed at a section by a rail placed across the top of the tub, supported and clamped to the upper flange of the container. A square bar template with tight clearance holes to guide the probe was moveable along the rail. The position of the template was adjusted until the guide hole was directly above the proposed site, and the bar was then clamped to the rail to set the location of a particular lead trail. A vertical guide was attached to the template. A channel is machined into a bottom plate on the guide to align the barrel of the tube. A removable assembly could also be fitted onto the top portion of the guide to fix the position of a piston rod in line with the channel, directly above the hole in the template.

To begin the insertion procedure, the charged hypodermic tube was held parallel to the vertical guide and placed through the hole in the template. The probe was then pushed slowly into the clay while the barrel was maintained within the channel along the

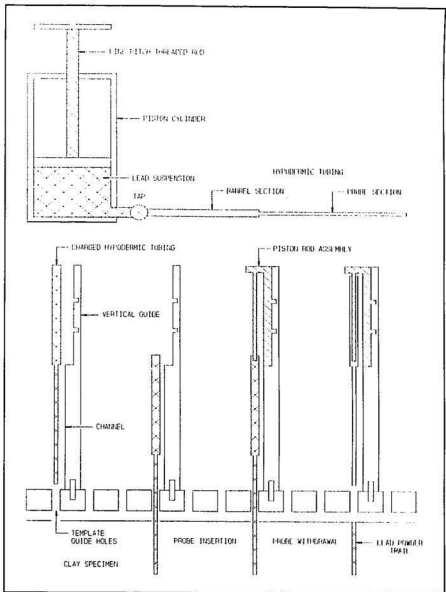


Figure 3.3 Top : Recharging hypodermic tubing with lead suspension; Bottom : Outline sketch of stages in lead powder trail insertion (after Phillips, 1990)

guide. The piston rod assembly was then attached to the guide such that the tip of the rod fitted within the top of the tubing barrel. Finally, the tube was gradually removed from the specimen; the barrel portion was withdrawn over the piston rod which prompted the expulsion of the lead suspension from the tube into the shaft left by the probe. The procedure was completed when the tip of the probe was above the clay surface. The piston rod assembly and the tube were then removed from the guide. To place additional lead trails, the tube was recharged with lead suspension, the template position was reset, and the process was repeated.

A total of 74 lead trails, comprising the vertical members of four separate grids, were generally installed in the specimen. The quantity was limited as it was recognized that the open shafts of the trails may act as drainage paths within the specimen. The insertion procedures were completed in a single working day after which the tub was returned to the consolidometer. The maximum pre - consolidation stress level was reapplied to the clay specimen to dissipate excess pore pressures and reduce the effect of disturbances caused by the installation of grids and model pipelines.

Surface Markers and Final Specimen Preparation

The remaining tasks involved in preparation of the clay specimen were carried out one day before the scheduled centrifuge test. Drainage access to water was disallowed, the specimen was unloaded, and the tub was removed from the consolidometer. The clay surface was then uncovered to enable cutting of an initial bay for the model iceberg, and to permit the placement of surface markers.

To set the initial depth of the model iceberg at a level below the expected equilibrium scour depth, a bay was cut within the specimen in which the model was to be situated prior to the scouring event. To construct the bay, the clay surface was incrementally scraped and levelled to a depth of 23 mm within a region which extended 200 mm forward from the tub wall and 280 mm in width perpendicular to the scour axis. A relatively stiff and light 3 mm thick plastic plate was placed within the bay to support the model iceberg with negligible settlement from an initial 20 mm depth. The support plate was pegged into the clay surface near to the tub wall to prevent its movement.

Surface markers were placed at prescribed locations on the specimen; plan view photographs of the specimen taken both before and after the test then allowed for the evaluation of the movements of the surface markers using a film measurement machine as described in Section 3.6. The markers were 2 mm diameter spherical lead - shot, selected to aid in definition of the model boundaries during radiographic examination. Measurements based on these markers were expected to underestimate surface soil displacement magnitudes.

To install the lead spheres, a clear plastic template of 6 mm thickness with an array of tapered guide holes spaced at regular intervals was used. The template was positioned on the clay surface and the lead spheres were inserted into the guide holes. A specially fabricated tool was then used to indent each sphere into the surface of the specimen to a distance of slightly less than one sphere diameter. A rectangular pattern of markers (240 mm width, 500 mm length) were installed at 20 mm spacings centred on the proposed scour axis. The spacing interval was selected to allow for post - test identification of the bulk of the markers after large soil movements, and to ensure a

negligible influence on model behaviour. Four reference markers were also placed at far - field positions which were unlikely to be affected by the scouring event.

Preparation of the clay specimen was completed with the installation of the lead sphere markers. The general layout of pore pressure transducers, soil deformation grids, model pipeline segments, and surface markers is shown in elevation and plan view in Figure 3.4. Individual test variations in the arrangement are detailed in Chapter 4.

The surface of the specimen was photographed to provide a record of the pre - test pattern of the lead shot markers. The camera used was a Hasselblad Model 500 EL/M loaded with a high quality 70 mm Aerographic film (Kodak 2645, Estar base). The camera mounting position was fixed and measured relative to the clay surface so that the same location could be established for the corresponding post - test photographs. The clay surface was then covered with plastic wrap. At this stage, the tub containing the prepared clay specimen was ready for assembly with external equipment and instrumentation to form the complete centrifuge test package.

3.3 Equipment and Instrumentation

The foregoing described construction of the soil model with a prescribed stress history, and the accommodations made for the measurement of internal soil effects. In addition to the stress history and current stress state, the soil behaviour is also dictated by the stress path followed during the test. The test package equipment and instrumentation were designed to address this model requirement through appropriate simulation of the prototype perturbation. In addition, the test apparatus allowed for monitoring of the

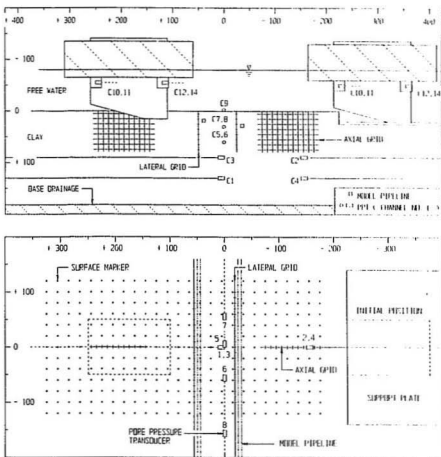


Figure 3.4 Layout of pore pressure transducers, deformation markers, and model pipeline segments, shown in elevation and plan view

imposed conditions and external model responses, to ensure a well - defined event.

The various components of the package were mounted on a 9.5 mm thick steel cover plate to form an integral unit which could then be bolted to the upper flange of the tub containing the prepared clay specimen. An opening was provided in the centre of the

cover plate to permit access to the clay surface and to allow observation during the event. Steel box sections were welded to the cover plate to enhance stiffness and prevent excessive deflections in the high gravity environment. The external equipment was firmly secured to the cover plate to preclude disturbance of the soil and to allow for mechanical handling of the complete package.

3.3.1 Drive System

Simulation of the ice scour perturbation entailed both the model iceberg (described in Section 3.3.2) and the drive system used to actuate the model. Power to drive the model was derived from a variable speed D.C. permanent magnet electric motor (type PM 2MB manufactured by Parvalux Ltd.). The electric motor met output torque requirements based on estimated loads and satisfied power requirements for the proposed model speed of 0.1 m/s. A thyristor controller was used with the device to facilitate remote operation and speed regulation from the centrifuge control room. The appropriate fixed controller setting for the constant velocity scouring event was established through laboratory calibration prior to centrifuge implementation.

The electric motor provided a relatively simple and reliable method of actuation and its size and construction were suitable for incorporation into the centrifuge package. The motor was supported by an external housing constructed of welded steel plates, bolted to the package cover plate. To ensure serviceability in the centrifuge environment, the device was aligned with the axis of the rotor parallel to the direction of centripetal acceleration. The increased rotor weight was transmitted from the main output shaft to

thrust bearings at the base plate of the housing. The loads imposed on the device were also carried through bearings at each end of the double - ended shaft on the gearbox.

Figure 3.5 shows a drawing of a vertical section through the package along the scour axis. To advance the model iceberg, the electric motor rotated a 1.5 mm diameter galvanized steel cable around a 20 mm diameter capstan fixed to one end of the drive shaft. A box section welded to the bottom of the motor housing extended downward through the package cover plate. The flexible cable was guided around a pulley attached at the base of the box section and was connected to the front of the model iceberg, initially located at the other extremity of the centrifuge container. In this manner, the model was driven by application of a horizontal pulling force at a prescribed elevation above the clay specimen.

The drive system did not restrict the behaviour of the model iceberg. The model was permitted to undergo motion with six degrees of freedom. In practice, due to symmetry of the model geometry and the applied driving force, movements were limited to the imposed horizontal translation (surge), as well as vertical translation (heave) and rotation about a transverse axis (pitch). Heave and pitch motions were developed through interaction with the soil and were dependent upon the vertical and rotational hydrostatic stiffness of the model. Other types of movement could arise as a result of unanticipated load eccentricity or specimen inhomogeneity. The direction of travel was specified parallel to the axis of rotation of the centrifuge (upward movement as viewed external to the package) in order to minimize errors due to the radial acceleration field and Coriolis effects.

The forward motion of the model iceberg was terminated automatically to end the

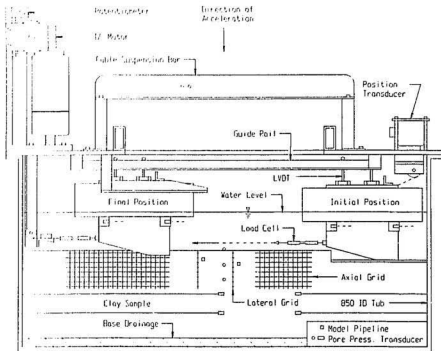


Figure 3.5 Sectional view of centrifuge test package

scouring event. For this purpose, two micro - switches were connected in series with the electrical supply to the motor. The switches were supported by a plate positioned in front of the pulley, and the pulling cable was directed between the switches through a groove in the plate. A small aluminum cone was fixed to the cable at a set position in front of the model iceberg. The cone contacted and activated the switches to stop the motor when the model had travelled a predetermined distance.

The horizontal position of the model iceberg was monitored using a position transducer (type PT 101 manufactured by Celesco Transducer Products Inc.) linked

directly to the model. The transducer casing was inverted and mounted on brass supports which were bolted to the package cover plate above the initial location of the model. This orientation permitted extension of the transducer measuring cable vertically downward from the device through a hole in the cover plate. The cable was guided around a pulley mounted on the underside of the plate, and then fastened to the back end of the top plate on the model. The position transducer employed a linear potentiometer which provided a continuous record of the horizontal position of the model to within an error of ± 0.5 mm. The extension of the transducer measuring cable associated with catenary at the test acceleration level was estimated to introduce additional deviation of the same order of magnitude.

An indirect measurement of the model position was also obtained by means of a rotary potentiometer connected to one end of the motor drive shaft. This latter measurement included the effect of a slight pre - tensioning of the pulling cable prior to the inception of model movement.

3.3.2 Model Iceberg

The model iceberg was constructed of aluminum, to represent a rigid keel of prescribed geometry, and balsa wood, to provide buoyancy and establish the vertical stiffness of the model in free surface water. Aluminum plates (6.3 and 12.5 mm thicknesses) were welded to form the keel geometry displayed in Figure 2.9. The model was fabricated oversized and machined to the required final external dimensions. Balsa wood segments were coated with water resistant varnish and bonded to the periphery of the upper portion

of the aluminum shell using a high strength adhesive. The wood segments served to extend the plan area of the model at the waterplane, and thereby to increase the vertical stiffness of the model to a specified value. The baseline model configuration, shown in Figure 3.6, included a keel width of 100 mm, a horizontal base length of 50 mm, and an attack angle of 15 degrees. The waterplane area of the model was 250 by 250 mm² which corresponded with a vertical stiffness of 61 N/mm.

The model iceberg design was varied to accommodate changes in parameters proposed for specific tests in the series. The parameters and corresponding model geometries for each test are given in Chapter 4. Some of the individual model configurations are exhibited in Figures 3.7 and 3.8 to illustrate particular construction features and other physical characteristics. The initial configuration, shown in Figure 3.7, possessed an irregular waterplane geometry with augmented bow area dimensions. The tendency to overturn during the scouring event was reduced by concentration of the model mass at the stern and placement of the balsa wood float at the front plate. The model was modified in subsequent tests to increase vertical stiffness through provision of the maximum practicable waterplane dimensions.

In general, changes to the keel shape produced changes in the buoyancy characteristics of the model. To isolate the effect of the test variable, it was therefore necessary to make further adjustments to the model configuration to maintain the same magnitude and point of action of the buoyant weight. This was achieved through re-design of the aluminum shell of the model, by the addition of ballast within the model, and by the attachment of balsa wood pieces to the exterior of the model. Adjustments were also required to ensure a consistent point of application of the horizontal force in

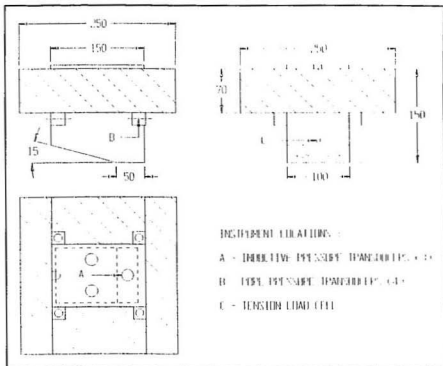


Figure 3.6 *Baseline model iceberg configuration and instrumentation*

successive tests. Furthermore, it was necessary to account for the weight distribution of the instrumentation attached to the model, in tests where devices were added or in which the model scale was altered.

Model Iceberg Instrumentation

Each model iceberg was instrumented to yield data which facilitated determination of the resultant scour forces, the pressures acting on the rigid keel, as well as the changes in depth and attitude of the model throughout the event.

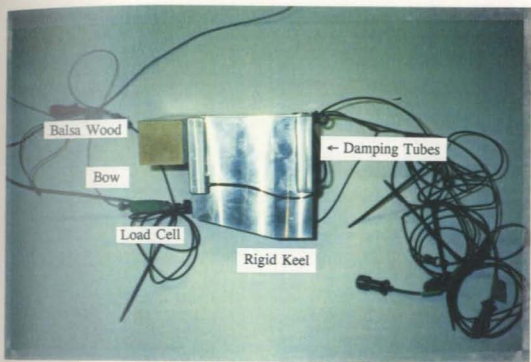


Figure 3.7 Side elevation view of model iceberg used in Tests 01 and 02

The drive system pulling cable was linked to the model by a tension load cell which measured the horizontal force developed when the model was advanced. The load cell was fabricated from an aluminum alloy (material designation HE15W). The total length of the device was 63 mm including end segments drilled with mounting holes. A central web, which was 13 mm in length and 8 by 2 mm² in section, functioned as the sensing element. Four semiconductor strain gauges were bonded to the web (two per side oriented with two opposite gauges in the axial direction and two opposite gauges in the transverse direction) and the arrangement was configured to form a Wheatstone bridge circuit. The load cell was required to operate while submerged in water at pressures as large as 100 KPa for a continuous period of up to 10 hours. The device was therefore

waterproofed by coating the circuit and lead wires with a commercially available silicone rubber sealant suited to this application.

One end segment of the tension load cell was coupled to the model. An aluminum connecting piece machined as a shackle was attached to the centre of the model iceberg at a fixed elevation. The load cell was permitted to rotate freely in a vertical plane about the pin of the shackle but allowed only limited lateral movement. The pulling cable was looped through the mounting hole at the opposite end of the device and secured with a crimped anchoring pin.

Contact pressures acting on the horizontal bottom and inclined leading face of the model iceberg were measured to provide information on interface stress conditions during the scouring event. Interface measurements are affected by the stiffness of the sensing element in relation to that of the surrounding boundary material, as well as by arching in the soil medium. Similarly, measurements derived from a relatively stiff pore pressure transducer implanted within the soil (Section 3.3.2) are prone to influence by stress concentration and arching effects (Kutter et al., 1988).

The soil - and water - induced interface pressures were estimated through use of inductive pressure transducers (type P11 manufactured by Hottinger Baldwin Measurements Inc.) with a nominal pressure range of 500 KPa. This type of device is suitable for measurements involving short pressure peaks as well as quasi - static or dynamic conditions with rapid fluctuations. The pressure medium acts directly on a 19 mm flat steel diaphragm. The deflection of the diaphragm is directly proportional to the differential pressure relative to the ambient value and is sensed accurately by an internal displacement transducer. The transducer response is converted into an analogue

electrical signal by means of an inductive half bridge energized via an external measuring converter unit (type MC 2A).

A total of three inductive pressure transducers (length 72 mm) could be accommodated within the model iceberg. A top plate or lid on the model was removed to permit installation of the pressure transducers and sealed to provide splash - proof containment. One transducer was located at the centre of the horizontal base plate. The two remaining devices were positioned at a height of 10 mm, and midway between the centre and each edge on the inclined leading face of the model, as shown in Figure 3.6. The transducers were fitted directly into threaded holes machined in the aluminum plates and flush - mounted with the exterior of the model. A narrow cavity between the diaphragm and the edge of the threaded hole was closed with a metal body - filler to render a smooth outer surface. Sealing between the mounting plane and the device was effected by means of a gasket at the shoulder of the device, adjacent to the thread. The electrical cables were secured within the model and fed out through an opening at the front of the top plate to permit connection to the measuring converter units.

The model iceberg was unconstrained and it was necessary to monitor its vertical position and orientation to define the scouring event, and to permit evaluation of the resultant vertical force acting between the model and the soil. Four pore pressure transducers (described in Section 3.2.2) were installed at a fixed distance below the free water surface, at each of the four corners of the model. The transducers furnished direct measurements of water pressures which served as an indirect monitor on the variation of model elevation (scour depth) during the event. The response time of these devices in pure water is on the order of 1 millisecond (Kutter et al., 1988). Wind - induced ripples

or local water level changes provoked by model movement represented a potential source of measurement error. To minimize the effect of these disturbances, the pore pressure transducers were mounted within tubes attached to the side of the model, as shown in Figure 3.7. The tubes were machined with a 13 mm diameter shaft open to the atmosphere and a 3 mm bottom aperture to permit water entry. The transducer was push - fitted into a mounting hole located 10 mm above the base of the tube, such that the active face of the device (with porous filter stone removed) was situated at the shaft centreline.

To reduce uncertainty associated with the assessment of the model vertical position, redundant measurements were undertaken in particular tests using other instrumentation. Initially, two linear position sensors (potentiometers) with 10 mm electrical stroke and small physical dimensions and mass were mounted on the top plate of the model iceberg, as shown in Figure 3.8. To record model movements during the event, the spring loaded plunger of each device was placed in contact with a guide rail at fixed elevation. This measurement system proved unreliable due to self - weight compression of the sensors in the centrifuge environment coupled with their limited measuring range. To address these deficiencies, the arrangement was modified in the subsequent test. In this instance, two ± 15 mm stroke linear variable differential transformers (LVDT; type DC 15 manufactured by Sangamo Ltd.) were placed within the model and clamped in position at the top plate (Figure 3.8). The displacement transducers were oriented such that the spindle of each device protruded vertically outward from the upper surface of the model. The top of each spindle was fitted with a low - friction pad which rested on a level rail spanning across the opening in the package

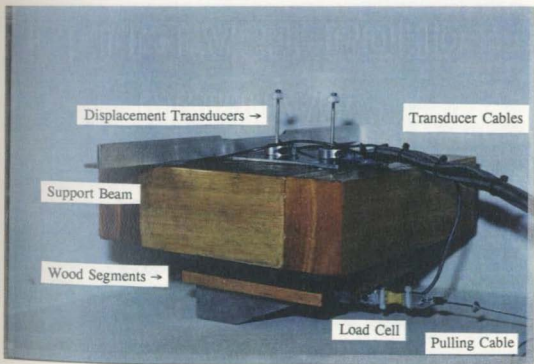
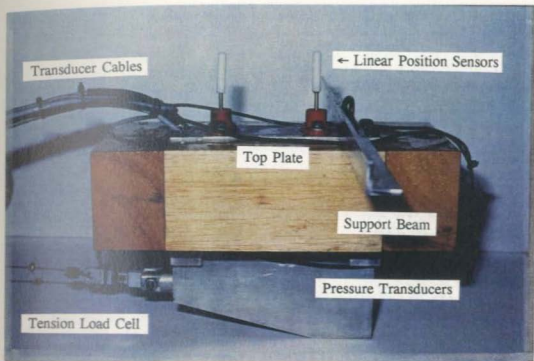


Figure 3.8 Instrumented model icebergs used in Tests 07 and 08

cover plate. Contact with the rail during the event was ensured by the enhanced self weight of the spindle at the test acceleration level.

Transducers in the test package were interfaced to the data acquisition system through junction boxes mounted on the cover plate, as described in Section 3.4. For the model iceberg instrumentation, this necessitated the connection of devices in motion with the model to conditioning units fixed to the test package. The electrical leads from the model instrumentation were routed to the upper surface of the model and tied together to form a single bundle. The bundle was attached in a flexible manner to a bar suspended above the package cover plate. As the model iceberg traversed the soil specimen, the lead lengths provided were sufficient to permit advancement with the model while pivoting about the point of attachment. This arrangement reduced the likelihood of possible obstruction of the scouring event arising from instrumentation connections.

Provisions for Model Support

In the initial tests performed, the soil deformation pattern at the final location of the model iceberg was altered by the effects of a bearing capacity failure below the model. The failure was initiated as the system of forces acting on the model changed in conjunction with the termination of movement. In order to reduce the influence of this additional perturbation, equipment modifications were implemented to provide support for the model at the end of its travel.

The support apparatus included two 25 mm sections of aluminum angle suspended at a specified distance from the underside of the package cover plate, each at opposite sides of the final model location. An outline drawing of the arrangement is presented in

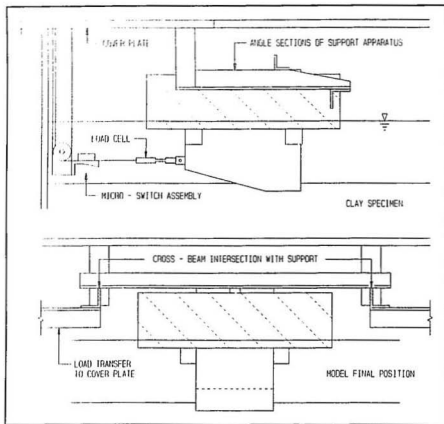


Figure 3.9 *Support apparatus for model shown in side and back elevation views*

Figure 3.9. The model was supported when a cross - beam bolted to its top plate came into contact with the upper surface of the angle sections. The beam was cantilevered over a distance of 75 mm from each side of the model and intersected with support sections at a distance of 25 mm from each end. The elevation of the top of the supports was adjusted to a level approximately 3 mm below that associated with contact for the estimated scour depth, and the ends of the sections were tapered from this height. The

clearance provided, relative to the level at which contact was expected, ensured that the scouring event was not influenced by the apparatus. This implied that a limited amount of vertical movement was tolerated.

3.3.3 Regulation of Water Levels

A system was required to control and monitor water levels within the test package. The preservation of design water levels and drainage conditions was essential to ensure appropriate pore water pressures and effective stresses in the clay specimen. The buoyancy characteristics of the model iceberg and, therefore, the representation of the prototype perturbation were also dependent on the depth of free water above the clay surface.

To maintain specified water levels during a test, water was supplied to the package at a steady rate and the excess flow was vented to a standpipe external to the centrifuge container. The water depth was regulated by the fixed height of the overflow on the standpipe. The control position could be easily adjusted between tests to allow for changes in conditions. The system accounted for potential losses due to evaporation during the test, leakage or unexpected spillages. To impose hydrostatic water pressures at the bottom and top of the clay specimen, the standpipe was linked to the centrifuge container at the base drainage outlet and also at two diametrically opposite locations immediately above the clay surface. Connections to the tub were made using compression fittings and semirigid nylon tubing.

The centrifuge tests were carried out with the surface of the clay submerged and

the proposed free water depth at the centre of the container was 80 mm (baseline condition). The control position in the standpipe and the resultant water depths across the clay specimen were calculated with allowance for the curvature of the water surface caused by the radial divergence of the acceleration field, and with consideration of the effects of Earth's gravity. At a distance of 125 mm from the scour axis (the edge of the model iceberg at waterline) the depth of free water was estimated to be 2.0 mm above the centreline value. The water depth along the scour axis increased very slightly in the direction of travel of the model, with a maximum deviation of 0.3 mm at the tub wall. The water level was monitored throughout the duration of the test using two pore pressure transducers (described in Section 3.3.2). One transducer was installed directly on the clay surface at a fixed position removed from the test area and the other device was situated at the base of the standpipe. Two pressure transducers were employed to provide a check on each other, and to assist in locating the source of possible leakages or obstructions in water supply to the package during testing.

3.3.4 Auxiliary Test Apparatus

Figure 3.10 shows a plan view schematic of the test package. Additional package equipment and instrumentation needed to observe and measure conditions during the centrifuge test included a surface settlement monitor, video camera, and vane shear test device.

A displacement transducer of the LVDT type described in Section 3.3.2 was employed to monitor settlement of the clay surface, as one means of evaluating the

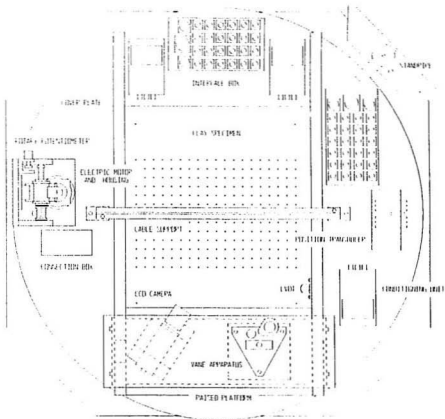


Figure 3.10 Plan view illustration of test package equipment and instrumentation

progress of in - flight consolidation. The LVDT body was clamped to the package cover plate and the base of the spindle was fitted with a perspex pad which rested on the specimen surface.

A charge coupled device (CCD) television camera with wide angle lens was installed on the test package to permit close - up visual monitoring of the scouring event. A camera mounting supported and aligned the device to provide a view of the model at

its initial position and over a portion of the scour length, including limited observation of the soil specimen through the layer of surface water. The view from the package camera supplemented an overall view of the package derived from a similar device stationed near to the central axis of the centrifuge (Section 3.4).

Vane Shear Test Device

A vane shear test device (Davies, 1981; Almeida, 1984) was added to the package to allow for the estimation of clay undrained shear strengths based on site investigation performed during centrifuge flight. The device, shown in Figure 3.11, comprises a compact set of apparatus designed to operate at an acceleration level of at least 100 gravities. The vane (12) is 18 mm in diameter by 14 mm deep with blades machined from stainless steel, and is fitted to a 6.3 mm diameter aluminum shaft (10). Connection to the shaft is through a slip coupling (11) which ensures that the vane is rotated only after approximately 10 degrees of initial shaft movement. This arrangement permits estimation of the shaft resistance, independent from the torque mobilized by the vane blades alone. A thin - walled 10 mm length of the shaft (9) serves as the sensing element for a load cell with bonded strain gauges configured to measure the applied torque.

The top of the shaft is attached to a plate (6) which can be moved vertically to advance the vane to the test location within the soil specimen. The plate is raised or lowered by an electric motor (3) acting through a simple gearing mechanism and screw drive (2). A linear potentiometer (1) is used to monitor the vertical position of the plate, and hence the penetration of the vane. The vane can be advanced over a maximum vertical distance of 200 mm. A second motor (5), coupled to the shaft through a bearing,

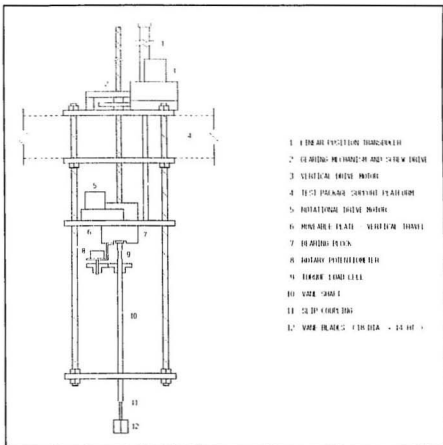


Figure 3.11 Components of the vane shear test device (after Almeida, 1984)

is used to rotate the shaft and vane to conduct the test. The rotational movement is monitored by a rotary potentiometer (8) linked to the shaft through two nylon gears.

The vane shear test device was attached to a raised platform supported by two columns bearing on the package cover plate and stiffening members. The platform could be detached from the cover plate to facilitate assembly of the apparatus. Steel box

sections were welded to the cover plate to enhance stiffness locally, to support the additional loading. The device extended downward through an opening in the cover plate such that the vane was situated immediately above the surface of the specimen at its initial position.

3.4 Cambridge Geotechnical Centrifuge

A detailed description of the Cambridge geotechnical beam centrifuge facilities and operations was provided by Schofield (1980). The main features applicable to the present study are reviewed briefly in this section.

Figure 3.12 shows a simplified schematic of the 10 m diameter rotor arm of the beam centrifuge. The centrifuge was constructed with complete symmetry such that a model may be carried at either end of the rotor with a suitable counterweight at the other. Alternatively, two models could be tested simultaneously, although this is not common practice. The machine operates with swinging platforms which have surfaces at 4.125 m radius so that the model is at a working radius of 4 m. At the peak rotational speed of 186 rpm, the acceleration in the model at 4 m radius is 155 g. The maximum acceleration level normally authorized for geotechnical testing is 125 g, and a package with mass not exceeding 900 kg can be accommodated. Therefore, in its current operations, the Cambridge centrifuge possesses 112.5 g - tonnes capacity at 4 m radius. The highest acceleration imposed during the present experimental programme was 125 g, and the mass of the ice scour package was approximately 500 kg.

The test package is mounted on a platform which is suspended on two swing arms

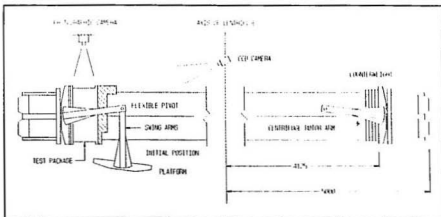


Figure 3.12 *Idealized sectional drawing of the Cambridge Geotechnical Centrifuge*

from pivot supports on the rotor. These pivots are free to move in a radial direction against the restraint of torsion bars to allow for seating of the platform on a fixed vertical face plate as the applied force reaches a predetermined value. When the centrifuge is stationary, the surface of the swinging platform is inclined at a small angle to the horizontal. As the centrifuge speed is increased, the platform rotates upward into the vertical plane at an acceleration level of about 8 g, where end - stops prevent additional rotation. With further increases in speed, the flexible pivot system permits the platform to move radially outward until it bears against the strong face plate of the rotor at about 20 g. Additional force imposed at higher accelerations is no longer transferred to the swing arms and pivot supports which, therefore, carry a substantially reduced portion of the applied loading.

The behaviour of the model is dependent on its orientation with respect to the resultant of the centrifuge acceleration field and Earth's gravity, acting perpendicularly

to the radial field. The design of swing arrangement for the Cambridge centrifuge is such that the resultant acceleration acts in a plane which is inclined at a minimum angle of about 83 degrees, both at rest and during a part of the swing - up process. Following this transition stage, the inclination increases to about $N : 1$ to the platform surface, where N is the prevailing centripetal acceleration. In the present study, the effect of the resultant inclination was reduced by placing a wedge of prescribed gradient between the test package and the platform surface. This provision was only effective at the test acceleration level.

The facilities available for visual monitoring of the model under test include both video and photographic systems. A CCD camera is fixed adjacent to the central axis of the centrifuge and directed radially outward along the rotor arm. The camera provided a continuous overhead view of the upper surface of the test package, which appeared at rest in the moving reference frame. The signals from this device were acquired remotely by television monitors and a video cassette recorder in the centrifuge control room. Photography of the moving model in flight may be achieved using an externally mounted camera and high intensity low duration light flash synchronized to the centrifuge rotor. This latter system could not be exploited to record model behaviour in the present series of tests due to the type of containment selected for the soil specimen.

Centrifuge Services and Data Acquisition

The centrifuge slip ring assembly permits communication with the external environment as required for test control and data acquisition. Above the upper bearing of the rotor, an extension of the shaft carries the slip ring stack, comprising two separate chambers

for electrical power/control rings and low - noise signal rings respectively. The centrifuge is also equipped with eight hydraulic or pneumatic slip rings which enable fluid to flow through the central axis of the machine, to supply water or compressed air to the model during a test. Water from the slip rings was piped into the ice scour test package through a standpipe as described in Section 3.3.3.

Electrical power is fed through high capacity slip rings to supply equipment and instrumentation. Three - phase 415 V AC, single phase 240 V AC, and 3 to 18 V DC power are readily available on the rotor arm. The excitation voltage required to energise package instrumentation is produced by direct current supplies located on the rotor near to the central axis. The AC power for the various onboard devices is activated remotely through solid state relays.

The centrifuge was constructed with 40 pairs of signal slip rings of which 10 are dedicated to signals reporting on the state of the machine. With a system to multiplex input signals, the overall data acquisition system currently allows for a maximum of 57 sets of signals to be recovered from a given experiment. The ice scour test package engaged a total of 28 data channels, including channels used to monitor instrumentation power supplies. The data acquisition system arrangement is illustrated in Figure 3.13.

The electrical leads from all of the test instrumentation were connected to two interface boxes mounted on the package cover plate, as depicted in Figure 3.10. Each box can accommodate up to 24 transducers. The interface boxes contain the necessary circuitry to deliver appropriate excitation voltage to the individual transducers and to condition their outputs to yield low impedance high - level analogue signals for transmission through slip rings to the data acquisition system. The signal conditioning

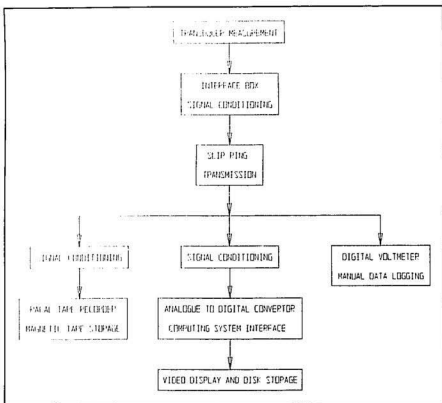


Figure 3.13 Schematic representation of data acquisition system (after Phillips, 1992)

provided includes selectable decade gain amplification and low - pass analogue filtering. This arrangement also permitted pre - test verification and calibration of instrumentation through the same electrical configuration as employed during the centrifuge test.

The multi - channel system includes further signal conditioning and an analogue to digital convertor controlled by a microprocessor (386 PC). The front - end signal conditioning consists of binary gain amplifiers which are adjusted to optimize the range

of analogue input. To acquire and manipulate digital data, the computing system is used together with commercially available Burr - Brown hardware and Labtech Notebook software. The data recorded using the acquisition software in this manner were suitable for input to other processing and analysis packages.

The signals retrieved from the centrifuge were also recorded in analogue format on magnetic tape using two Racal 14 - track tape recorders. This system functioned as a back - up to the main data logging system to prevent loss of essential test data due to inadequate logging rates or in the event of failure of the main system. The analogue information recorded on magnetic tape could be subsequently converted to digital format as required, using the computer code FLY14 (Dean and Edgcombe, 1988). Manual data logging using a digital voltmeter was also carried out throughout the duration of a test to verify instrumentation responses independent of the main logging system.

3.5 Centrifuge Test Procedures

This section describes some of the details of centrifuge test implementation following model preparations as outlined in the initial portion of the chapter. The experimental programme was planned in accordance with the Code of Practice for Safe Operation of the Cambridge Geotechnical Beam Centrifuge (Schofield, 1980). Structural analysis and centrifuge balance calculations were performed for each test to demonstrate the safety of the apparatus and proposed activities. Centrifuge proof tests were also undertaken to verify the structural integrity of the test package and to evaluate system performance at an acceleration level in excess of the normal working condition.

Package Assembly and Loading

The clay specimen was removed from the laboratory consolidometer and final model preparations were completed one day prior to the first day of scheduled centrifuge acquisition. The external equipment and instrumentation were mounted on the package cover plate and the resulting assembly was bolted onto the centrifuge container. The standpipe was attached mechanically and hydraulically to the package, and the overflow height was adjusted to test specifications. The instrumentation was connected to the interface boxes and transducer responses were verified through the data acquisition system. Electrical leads were secured at several points on the package to minimize potential distress during centrifuge flight.

The model iceberg, instrumented and sealed as described in Section 3.3.2, was placed on the plastic support plate, with care to avoid disturbance of the clay. The model and drive system were connected by the pulling cable, and the position transducer measuring cable was attached to the back end of the top plate on the model. The transducer cable provided a small reaction force to the initial pulling cable tension, and this arrangement served to stabilize the model prior to conduct of the centrifuge test. To set the position of the model in the initial tests, a frame was fitted to the model and clamped to the package cover plate during limited pre - tensioning of the pulling cable. It was subsequently found adequate to establish the location of the model manually without use of a guide frame. The final adjustments to model position were made immediately prior to commencement of the centrifuge test.

The assembled package was weighed, and its mass checked against the balance calculations manifest prepared for the test. The package was then rested on an aluminum

wedge of slope 1 : 100 and both were bolted to the swing - platform, ready for loading on the centrifuge. The swing - platform and package were transported into the centrifuge chamber by overhead crane, and the platform was mounted at pivot supports on the rotor arm. Figure 3.14 shows the completed test package loaded on the centrifuge. Hydraulic and electrical service, control, and instrumentation lines were connected to the package and final checks were performed on all systems. At this stage, assembly and loading activities were completed, and the package was ready for centrifuge testing on the following day.

Test Procedures

Immediately prior to deployment of the centrifuge test, plastic wrap was removed from the surface of the clay, the base drainage outlet was opened, and a fixed mass of free surface water was added to the test package. This initial mass and subsequent changes to the quantity of water within the package were calculated to meet centrifuge balance requirements, and to prevent overtopping of the model iceberg due to inclination of the water surface at low acceleration levels. The main data logging system was also initiated before application of centrifuge acceleration to the package. The sampling rate was set at 0.2 Hz during the transition to the test acceleration level.

To begin the test, the centrifuge motor was started and the speed of the machine was gradually increased. Following swing - up of the platform, water supply to the package was introduced at the minimum steady rate. The centrifuge nominal acceleration level was increased in stages to 15, 20, 30, 50, 75, then 100 gravities. The water level was closely monitored, and control by the standpipe overflow established at each stage.

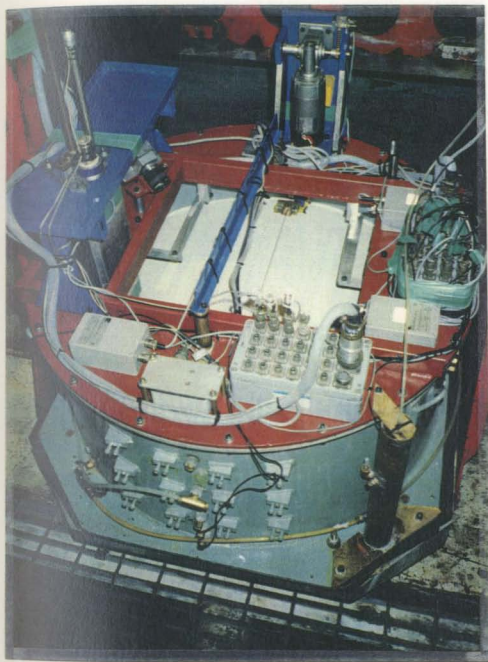


Figure 3.14 *Pre - test view of completed package mounted on centrifuge*

The water supply rate was adjusted as needed to maintain appropriate conditions. The time period required for each stage was about ten minutes and the test acceleration level was achieved following approximately one hour of centrifuge flight. The presence of free water and increased self weight during this transition phase reduced pore suctions within the soil specimen and, thereby, altered the magnitude and time required for the dissipation of excess pore pressures during the ensuing consolidation phase.

Upon reaching the test acceleration level, the clay specimen was permitted to consolidate to establish equilibrium conditions under the imposed stress regime. The sampling rate for the main data logging system was reset to 0.02 Hz during the consolidation phase. To monitor the progress of consolidation, the system provided graphical output on the control room display monitor of pore water pressure readings for transducers implanted within the soil. Manual readings were also acquired every 15 minutes and data from the surface settlement transducer were plotted. Based on this information, the degree of consolidation was assessed using the root - time method of Taylor (1948). Depending on the stress history of the clay specimen under test, greater than 95 percent of primary consolidation was completed within 4 to 6 hours of centrifuge flight time. At this stage, transducers in the clay were registering no significant excess pore pressures above their expected equilibrium values, and preparations were made to begin site investigation using the vane shear test device.

In - flight vane shear tests were undertaken at three horizons within the clay specimen. The vane was driven vertically downward from an initial position above the clay to nominal test depths of 30, 60, and 90 mm below surface. The rate of vertical penetration of the vane was 5 mm / minute. At each test site, following a brief delay of

less than one minute, the vane was rotated at a rate of approximately 75 degrees / minute over an angular distance of about 90 degrees. The rotation was then reversed to return the vane to its initial orientation, and vertical movement was reinstated to advance the vane to the next test location. The main data logging system was set up to record at a sampling rate of 10 Hz during vertical movement of the vane and 4 Hz for each vane test, as activated through a digital trigger. Vane shear test procedures were generally concluded within a time period of about one half hour.

Preparations for conduct of the model scouring event began subsequent to vane shear testing. Final checks were made to ensure serviceability of data acquisition and control systems during the event. The video cassette recorder was set up to receive the close range image conveyed by the package camera. Data logging was started on the back - up magnetic tape recording system, and sampling rates on the main system were increased to provide detailed information during the scouring event. To initiate scouring, the drive system was activated remotely to advance the model iceberg across the clay specimen. During the event, the progress of the model was verified visually on television monitors in the centrifuge control room. The total length of pull of the model was less than 500 mm, and the duration of the event was on the order of seven seconds. To capture instrument responses to the imposed perturbation, digital sampling rates were set at 20 Hz for a time period of 50 seconds surrounding the event, after which the rate decreased to 1 Hz to ensure acquisition of reasonable quantities of data for subsequent processing. Following scouring, the package was maintained at the test acceleration level for a duration of about one half hour to allow for dissipation of excess pore pressures generated during the event.

At the end of the test, water supply to the package was terminated and the speed of the centrifuge was gradually reduced. The transition from the test acceleration level to a stationary condition was carried out in stages of relatively short duration, and typically completed within less than one half hour. Immediately following stoppage of the machine, the remaining surface water was siphoned off to reduce additional swelling of the clay specimen, and cores were taken to provide moisture content samples. Supply lines were then disconnected and the package was removed from the centrifuge rotor arm.

3.6 Site Investigation Procedures

The test package equipment and instrumentation were carefully dismantled to provide access to the clay specimen for further investigation. After the cover plate assembly had been completely removed, the scour was documented photographically with the model iceberg in place and also following withdrawal of the model from the clay surface. In addition, the pattern of surface lead shot markers was re - photographed using the Hasselblad camera at the preset mounting position (Section 3.2.3). The resulting negatives were subsequently employed in the quantitative assessment of surface displacements through film measurement.

Following photographic documentation and visual inspection of scour morphology, a series of measurements were made in order to establish a profile of the clay surface. A clear plastic template of 25 mm thickness was fixed to the upper flange of the centrifuge container to provide a level reference relative to the underlying clay surface.

Profile measurements were obtained using a displacement transducer and 3 mm diameter measuring rod which was fitted through guide holes in the template. Elevations were recorded at regular 12.5 mm intervals over the entire plan area of the specimen. Errors could arise as a result of either misalignment due to the small clearance allowed between the rod and guide hole, or penetration of the rod into the clay. Measurements were repeatable to an accuracy of at least ± 0.5 mm based on successive readings taken at similar locations. Surface profiling was generally completed on the first day after the centrifuge test.

To allow for the investigation of internal scour effects through radiography and excavation, the clay specimen had to be removed from the centrifuge container. The connectors of implanted pore pressure transducers were first detached, and the ends of the electrical leads were pulled inside the tub. Sealed plugs were then removed from the base of the tub, providing holes through which vertical steel columns were placed in contact with the steel drainage plate beneath the specimen. To extrude the clay, the tub was set onto the vertical columns and pushed downward, leaving the unconstrained specimen supported on the steel plate. Soil disturbance resulting from the extrusion process was limited to the material which had been adjacent to the side wall of the container.

Radiographic Techniques

Radiographic methods for soil investigation developed at Cambridge University were detailed by James (1973 a). A radiographic examination of the clay specimen was undertaken in the present study to display the post - test deformed configuration of the

lead powder trails and solder segments which comprised reference grids (Section 3.2.3). The grid materials were sufficiently deformable and adequately spaced to ensure that the behaviour of the surrounding soil was not excessively modified by their presence, and grid displacements were representative of the movements of the corresponding soil elements. The radiographic examination also served to define the positions of pore pressure transducers and model pipelines emplaced within the specimen.

The apparatus used in the examination included an industrial type Müller MG 150 X - ray unit with a maximum source rating of 8 mA at 150 KV for a focal point size of 1.5 mm. For the investigation of clay specimens in the present study, radiographs of acceptable quality to convey the required geometrical information were obtained with a source current intensity of 4 mA at 150 KV using a fine focus setting. Continuous exposure durations of between 10 and 15 minutes were typically employed with Kodak Industrex D film. To improve definition of the radiographic image and the accuracy of subsequent measurements, the source to film distance was increased to 1.5 m, and the object to film distance was minimized. The harmful effects of scattered radiation on the quality of the image were reduced by masking the specimen locally with lead sheet, and by the use of lead foil intensifying screens placed within the film cassette. The equipment available at the Cambridge centrifuge facility allowed for manual development of X - ray films in a temperature controlled processing tank immediately following exposure. The film exposure conditions could therefore be optimized through trial variations and subsequent evaluation of the effects on the processed radiograph.

To begin the investigation, the extruded clay specimen was transferred from the steel plate to a less dense wooden support to provide suitable conditions for plan view

radiographs. These radiographs were required to determine horizontal displacements of grids placed at cross - sections perpendicular to the scour, and also to display grid and instrumentation locations to aid in subsequent dissection of the specimen. Plan view information was generally compiled from three separate radiographs centred on the cross - sectional grid positions. The accurate assessment of plan view images was limited by the object to film distance which could not be reduced below the combined thickness of the specimen and support plate.

The clay specimen was dissected to permit elevation view radiographs displaying both axial and cross - sectional grids. A sharp - edged aluminum plate coated with water resistant grease was used to cut the clay along planes which were parallel and perpendicular to the axis of the scour. Each grid was examined successively after the removal of waste clay in regions remote from the area of interest. Following the attainment of a satisfactory radiograph at the section in question, the grid members, pore pressure transducers, and model pipelines were carefully excavated to provide further documentation of internal displacement patterns and instrument locations. Finally, the exposed model pipelines were withdrawn from the specimen and visually inspected and measured to determine any permanent deformations resulting from the scouring event. The investigation of the specimen through radiography and excavation was typically completed within a time period of about one week.

Film Measurement

Surface displacements at discrete points represented by the movements of lead shot markers between pre - and post - test photographs of the clay specimen were determined

through film measurement. The out of plane vertical displacements of the surface markers were not accounted for in this assessment. Furthermore, markers positioned within the scour incision were generally displaced below the clay surface during the event and could not be visually identified to allow for measurements based on photographic evidence.

A film measurement machine was used to determine the locations of the circular images of surface markers, approximately 0.2 mm in diameter, recorded on 55 mm by 55 mm film negatives. The device was originally designed by James (1973 b) and was recently upgraded with the replacement of control, drive, and measurement systems. The modifications were implemented by Phillips (1991); the author provided a detailed description of the refurbished apparatus and also outlined operational procedures.

The film measurement machine consists of a film carriage, a two axis stepping motor drive system, a viewing system, a moire fringe coordinate measuring system, and a computer control system. The film negative is mounted on an optically level plate glass surface and illuminated from above by a cold projector light source. An overall view of the image is projected through a zoom lens and half silvered mirror onto an observation screen. The viewing system also includes a closed - circuit television camera which is used to exhibit a detailed portion of the image on a television monitor. To execute a measurement, the operator aligns the marker image with a set of cross - hairs which are superimposed on the video display. Successive images are positioned in this manner and their coordinates recorded.

The accuracy of measured displacements was dependent on various factors including camera movement between pre - and post - test photographs, camera lens and

film distortion, and the resolution of the film measurement apparatus. For the size and quality of the photographic images used in the present study, surface displacements were assessed to within approximately 0.1 mm.

Chapter 4

Experimental Results

4.1 Introduction

This chapter details the experimental results for the centrifuge tests conducted as a part of the present study. An outline of the test programme and the rationale for the selection of investigated test variables are first presented. The individual tests are then described including proposed input conditions, design modifications to test set - up or procedures, peculiarities arising from system malfunctions, and test results which characterize the effects of the scouring event.

The reduction of the measured output provided a unique data set for each test which included the following information in the general case : (1) model iceberg configuration and test set - up; (2) estimated profiles of soil strength; (3) qualitative surface morphology and measured surface profile; (4) temporal and spatial records of pore water pressures and resultant scour forces; (5) surface soil movements; (6) sub - surface soil displacements, and; (7) post - event plastic deformations of model pipeline segments. The results are documented here for well - defined model scouring events which are related to relevant prototype conditions through scaling relationships, as

presented in Chapter 2. The complete processed data records for each test are also archived on computer diskette, in suitable format for use with standard analysis packages.

4.2 Experimental Programme

The present study was limited to a total of nine centrifuge model tests, in addition to proof tests undertaken to evaluate system performance in the high gravity environment. The tests were normally carried out with 1/100 scale models at a centrifuge acceleration level of 100 gravities. Due to the limitation on the number of tests, it was not possible to conduct a comprehensive parametric study. In general, the effects of modest variations in the soil initial stress conditions, and the model iceberg attack angle, width, and vertical stiffness were examined in the experimental programme. For each of the tests performed, the material type investigated was Speswhite kaolin clay. The specified rate of advance of the model iceberg was also fixed at 0.07 m/s, throughout the test series. In addition, the horizontal bottom face of the model iceberg was normally set at a constant length of 50 mm or 5 m at prototype scale, for each configuration investigated.

Table 4.1 summarizes the proposed test conditions, in terms of the clay laboratory pre - consolidation stress σ'_{v_0} and the model iceberg attack angle, width and vertical stiffness. The model iceberg was partially buoyant and free to lift or rotate during the event to attain a steady state level. Due to the lack of restriction on movements of the model iceberg, it was not possible to accurately establish the magnitude of the scour cut depth prior to a test. In addition to changes in depth experienced by the model iceberg, initial pitch adjustments also produced small changes in the effective attack angle during

Table 4.1 *Proposed Test Matrix*

Test Number	σ'_{vo} (KPa)	Attack Angle (deg.)	Width (mm)	Vertical Stiffness (N / mm)	Test Variable
1	140	15	100	26	soil state
2	110	15	100	26	baseline
3	110	15	100	26	scour depth

4	110	15	100	61	soil state
5	140	15	100	61	baseline
6	200	15	100	61	soil state
7	140	15	50	31	model width
8	140	25	100	61	attack angle
9	140	15	80	49	125 g test

the scouring event. Therefore, while the increased freedom of motion of the model provided improved representation of field conditions, it also reduced control over input test parameters. Furthermore, in some tests, technical difficulties related to equipment and instrumentation altered the experimental inputs from the values specified in Table 4.1, and

this must be accounted for in the interpretation of the test results. Details of the conditions of individual tests are provided in the sections which follow.

The initial three tests of the series were performed during a time period scheduled for system design and verification. Therefore, equipment development and changes to the test set - up and site investigation procedures were more notable in these tests. Tests 01 and 02 served to demonstrate use of the proposed apparatus in the centrifuge with remote data retrieval and system control. These tests provided information on scour effects for a given set of boundary conditions and two different soil stress histories. Test 03 was intended to permit an assessment of the influence of scour cut depth on the effects of scour, through a change in the buoyancy characteristics of the model iceberg in relation to Test 02. In this case, the test design proved ineffective as the drive system capabilities were exceeded, resulting in malfunction.

The prototype vertical stiffness represented by the model icebergs used in Tests 01 to 03 was 2.6 MN/m. This corresponded with the lifting of a slab - sided free - floating ice mass with a waterplane area of approximately 265 m². This is below the range of vertical stiffness values normally associated with a full - sized iceberg or pressure ridge. Therefore, the uplift behaviour observed in these tests was exaggerated in relation to the corresponding behaviour of a typical full scale ice feature. In the remaining tests, to address the concern of unrealistic vertical stiffness, the model iceberg configuration was modified to provide the maximum practicable waterplane dimensions, while still allowing for a reasonable length of travel across the centrifuge tub. The prototype vertical stiffness in this case was 6.1 MN/m, representing a waterplane region of 622 m². This configuration allowed for the establishment of steady - state scouring

conditions, with only limited vertical movement to achieve relevant scour depths.

In the latter portion of the test programme, a small range of soil conditions was examined, as well as a different model iceberg width and attack angle. Previous investigations have suggested an influence of these variables on the effects of scouring (see Chapter 1). Test 05 served as a baseline test for this series of experiments. The prototype for this test comprised the following attributes (with corresponding test programme variations denoted in brackets) :

Material Type	Speswhite kaolin clay
Pre - Consolidation Stress (kPa)	140 (varied to 110 and 200)
Velocity (m/s)	0.07
Length of Travel (m)	45 (typical)
Attack Angle (degrees)	15 (varied to 25)
Scour Depth (m) (steady - state value)	1.2 (ranged from 0.4 to 2.2)
Scour Width (m)	10 (varied to 5)
Keel Horizontal Base Length (m)	5 (constant for all tests)
Vertical Stiffness (MN/m)	6.1 (varied to 2.6)

Tests 04 and 06 were designed to investigate the influence of changes in the initial stress state of the soil, and involved the application of different laboratory pre - consolidation stresses to the clay specimen. The imposed changes in initial stress conditions were relatively modest, as constrained by the requirement to avoid the development of scour forces which exceeded the capabilities of the drive system. In Test 07, the model iceberg width was reduced to half of the baseline value. Scour widths in excess of 10 m at prototype scale were deemed untenable due to the dimensions of the tub in which the clay specimen was contained and the maximum allowable g - level for the centrifuge. Test 08

was designed to allow for the assessment of the effects of a change in the attack angle. Practical considerations also limited the magnitude of this change, since it was necessary to re - design the model iceberg in order to retain the same buoyancy characteristics as the baseline configuration. In Test 09, the technique of modelling of models was employed in which the identical prototype at Earth's gravity modelled in Test 05, was modelled at 1/125 scale and at an acceleration level of 125 gravities. This test was conducted to establish the internal consistency of the method, and thereby to provide greater confidence in extrapolation of the results to full scale conditions. In general, each test involved a unique event which represented a full scale scouring situation and for which accurate data on the effects of scouring were collected.

4.3 Centrifuge Test Results

Appendix A contains detailed plots and drawings which clarify the descriptions of test conditions and results given in the following sections. The appendix information is presented in sections which correspond with the individual tests in the series, as is the material presented below. Each section of the appendix is subdivided into data groups which are identified alphabetically as follows : (A) test parameters and set - up; (B) soil strength measurements; (C) instrument data plots for consolidation and scour event phases; (D) surface profile data; (E) spatial plots of pore pressure data, and; (F) site investigation drawings based on radiographic images. The test results are presented at model scale unless otherwise denoted; prototype values may be derived in accordance with the scaling relationships given in Table 2.1. Locations in the model are described

with reference to a right - handed coordinate system with origin at the centre of the clay specimen : the x - axis is directed along the axis of the scour and defines the horizontal position of the model iceberg, with positive values in the direction of travel; the y - axis is directed laterally outward from the scour axis, and; the z - axis acts vertically with positive values measured as depths below the initial clay surface, established following consolidation settlement.

A summary of the instrumentation used in this test series is given in Table 4.2. The data acquired during the scouring event are presented in relation to the event time and the horizontal position of the model iceberg. The event time was measured with respect to the start of motion in the test. The location of the inflection line at the base of the inclined face of the model iceberg served as the reference datum for measurements of its horizontal movement, relative to the origin at the centre of the clay specimen.

4.3.1 Scour Test 01

Model Input Conditions

The model iceberg configuration and input parameters for Test 01 are given in Figure 1A.1 in the corresponding section of Appendix A. In this test, the clay was consolidated in the laboratory under a uniform vertical effective stress of 140 kPa. The model iceberg width was 100 mm or 10 m at prototype scale, and the attack angle was set at 15 degrees to the horizontal. The model iceberg used in this test, shown in Figure 3.7, possessed a vertical hydrostatic stiffness of about 26 N/mm. This model configuration included an irregular waterplane geometry, such that initial rotational

Table 4.2 Test Instrumentation

<i>Channel</i>	<i>Device (measured or derived quantity)</i>
PPT 01	pore pressure transducer (soil pore water pressure)
PPT 02	pore pressure transducer (soil pore water pressure)
PPT 03	pore pressure transducer (soil pore water pressure)
PPT 04	pore pressure transducer (soil pore water pressure)
PPT 05	pore pressure transducer (soil pore water pressure)
PPT 06	pore pressure transducer (soil pore water pressure)
PPT 07	pore pressure transducer (soil pore water pressure)
PPT 08	pore pressure transducer (soil pore water pressure)
PPT 09	pore pressure transducer (surface water level)
PPT 10	pore pressure transducer (model vertical position)
PPT 11	pore pressure transducer (model vertical position)
PPT 12	pore pressure transducer (model vertical position)
PPT 13	pore pressure transducer (standpipe water level)
PPT 14	pore pressure transducer (model vertical position)
LVDT 15	displacement transducer (clay surface settlement)
ROTARY POT. 16	rotary potentiometer (model horizontal movement)
POSITION TRANS. 17	position transducer (model horizontal movement)
IPT 18	inductive pressure transducer (contact pressure)
IPT 19	inductive pressure transducer (contact pressure)
IPT 20	inductive pressure transducer (contact pressure)
TLC 21	tension load cell (model horizontal force)
V. DISPL. 25	displacement transducer (vane vertical displacement)
V. ROT. 26	rotary potentiometer (vane rotational movement)
V. TORQUE 27	torque load cell (torque mobilized by vane blades)

movements were discouraged during the event. The nominal depth of free surface water at the location of the model iceberg was 100 mm in this test.

The arrangement of instrumentation, deformation markers, and model pipeline segments for Test 01 is shown in elevation and plan view in Figure 1A.2. The test layout was dissimilar to the baseline arrangement depicted in Figure 3.3, due to the development of procedures as the study progressed. As described in Section 3.2.3, a different type of tubing section and material were used to represent pipeline segments in the first centrifuge test. Based on consideration of elastic material behaviour, prototype steel pipelines with an outside diameter of 762 mm and a wall thickness of 25 mm were modelled. The post - yield response was strictly representative of the plastic behaviour of a prototype pipeline comprised of the same aluminum alloy as the model pipeline segments. In total, five segments were placed at different depths within the specimen. Soil deformation grids installed in conjunction with the segments, consisted of strands of coloured, dry spaghetti. In this test, lead powder trails were injected at 45 degrees to the specimen surface to form two separate grid patterns, as illustrated in Figure 1A.2. A single horizontal solder member was also placed at a specified cross - section, to establish the utility of this grid material for use in post - test investigations.

Experimental determinations of the undrained shear strength provided an indirect means of evaluating the extent to which the preferred stress history was achieved in each test, through comparison with theoretical predictions of strength values for the prescribed stress states. For undrained conditions, there is a unique relationship between the critical state strength and the moisture content for a saturated soil, independent of changes in the

total normal stress. The undrained shear strength c_u is commonly expressed as half of the deviatoric stress q_f at failure or the maximum shear stress, such that

$$c_u = \frac{1}{2} q_f = \frac{1}{2} M \exp \left\{ \left[\Gamma - (1 + G_s w) \right] / \lambda \right\} \quad (4.1)$$

where w is the moisture content, and typical corresponding material properties for Speswhite kaolin clay are listed in Section 2.4.1.

The undrained shear strength may also be related to the overconsolidation ratio OCR and the current vertical effective stress σ_v using an expression of the form

$$c_u = \sigma_v \alpha \text{OCR}^\beta \quad (4.2)$$

in which α and β are empirically defined constants. Springman (1993) summarized kaolin strength data from vane shear and single element test results presented by various researchers (Almeida and Parry, 1983b; Nunez, 1989; Springman, 1989; Hamilton et al., 1991). The use of $\alpha = 0.22$ and $\beta = 0.7$ in Equation 4.2 for vane shear strengths provided a reasonable representation of the available data for OCR in the range of 1 to 20, with some scatter attributable to different testing protocols.

In accordance with the precepts of Modified Cam Clay theory (Roscoe and Burland, 1968), it can be shown (e.g. Phillips, 1982) that the undrained shear strength is given by the cumbersome expression :

$$c_u = \frac{M(1+2K_o)\sigma_v}{6} \left\{ \frac{\text{OCR}}{2M^2} \left[\left[\frac{1+2K_{nc}}{1+2K_o} \right] \left[\frac{9(1-K_{nc})^2}{(1+2K_{nc})^2} + M^2 \right] \right] \right\}^{\frac{(\lambda-\epsilon)}{\lambda}} \quad \dots (4.3)$$

A knowledge of the variation of the coefficient of lateral earth pressure at rest K_0 with the overconsolidation ratio is required in order to evaluate the preceding equation. The following relationships were suggested by Wroth (1975) for different ranges of OCR :

$$K_0 = \text{OCR } K_{nc} - \frac{\nu}{\nu - 1} (\text{OCR} - 1) \quad \text{for } 1 \leq \text{OCR} \leq 5$$

$$3m \left[\frac{1 - K_{nc}}{1 + 2 K_{nc}} - \frac{1 - K_0}{1 + 2 K_0} \right] = \ln \left[\text{OCR} \frac{1 + 2 K_{nc}}{1 + 2 K_0} \right] \quad \text{for } \text{OCR} > 5$$

. . . (4.4)

where the effective stress Poisson's ratio ν and the parameter m are specified as 0.33 and 1.81 respectively for kaolin, and K_{nc} is the coefficient of lateral earth pressure at rest for normal consolidation (Section 2.4.1). The latter equation for high OCR values may be solved for K_0 through a process of iteration.

Figure 1B.1 shows the estimated variation of undrained shear strength with depth for the Test 01 specimen. Equation 4.1 was used to compute c_u values based on moisture contents measured from cores extruded after the completion of the centrifuge test. The results are compared with predicted empirical and theoretical profiles of the undrained shear strength determined in accordance with Equations 4.2 and 4.3. Equation 4.1 is sensitive to changes in the moisture content, and small measurement inaccuracies could lead to large errors in the estimated undrained shear strength. Furthermore, post - test determinations of c_u may be expected to be lower than theoretical predictions, since negative pore pressures are set - up with the stoppage of the centrifuge and excess water is drawn into the specimen. As the clay is relatively permeable, high pore water tensions

may also lead to air entry or cavitation. In - flight site investigation techniques were therefore required to ensure an accurate assessment of the soil conditions which were relevant during the event.

Test Results

The consolidation records for Test 01 are presented in Figure 1C.1 as plots of pore pressure against time, and clay surface settlement versus the square root of time. The pore pressure transducers (PPT Channels 1 to 8) within the clay specimen were registering no significant excess pore pressure above their equilibrium values at the completion of the consolidation phase. The apparent initial clay surface settlement was 1.7 mm. Using Taylor's root - time construction, it was estimated that greater than 95 percent of primary consolidation was completed after about 4 hours of centrifuge time. The model iceberg rested directly on the clay surface in this test and therefore underwent considerable additional settlement. In subsequent tests, a support plate was placed beneath the model in order to distribute the applied loading to ensure negligible relative movements during consolidation.

The instrument outputs during the scouring event are plotted against the event time and horizontal position in Figure 1C.2. The Test 01 event was completed in less than 7 seconds and the model iceberg travelled a total distance of 460 mm. The horizontal displacement history was derived from the displacement transducer response during the event. The average scouring rate, determined as the slope of the displacement - time curve, was 70.1 mm/s. An indirect measurement of horizontal movement was also provided by the rotary potentiometer. This record included the effect

of a slight pre - tensioning of the pulling cable prior to the start of motion in the test. The apparent duration associated with initial acceleration of the model iceberg was negligible in relation to the time period required to establish steady - state conditions.

Figure 4.1 displays a plan view photograph and related drawing of the Test 01 scour, to illustrate the surface morphology. An average cross - section surface profile is presented in Figure 4.2 along with an axial plot depicting scour depths and berm elevations at different horizontal positions. Surface profile data are detailed in Figure 1D.1 as cross - sectional plots at 50 mm intervals of horizontal position. Settlement of the unsupported model iceberg prior to the scouring event was evident from the local depression (approximately 11.5 mm depth) formed at the initial model position. The model iceberg underwent a period of rapid uprise to an apparent steady - state scour depth. The initial portion of the scour feature was characterized by an undulating surface, although the scour incision was relatively uniform in appearance after an equilibrium vertical position had been established. The mean scour depth for the apparent steady - state region was 3.8 mm or 0.38 m at prototype scale. Berm elevations averaged 2.3 mm, primarily reflecting heave of the soil immediately adjacent to the scour.

The amount of remoulded or loose berm material observed along the sides of the scour was negligible in this test. Surface displacement markers within the scour were dragged forward over a limited horizontal distance, and pushed vertically downward below the base of the incision. The model pipeline segment situated nearest to the surface (crown at 5 mm depth) was partially exposed within the scour trough. A linear depression and soil surface fractures formed in the vicinity of this pipeline, indicating movement had occurred over a substantial portion of its length. A small mound of spoil

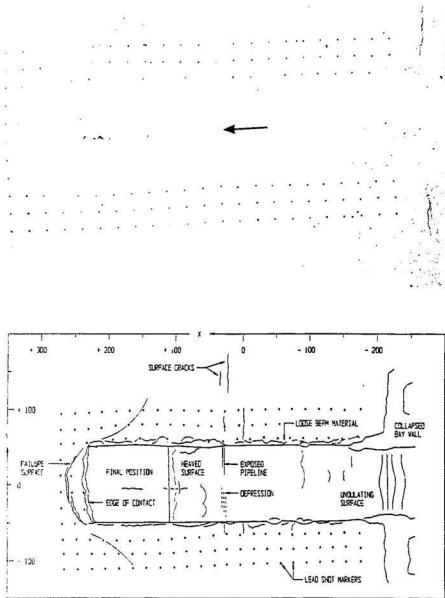


Figure 4.1 Top : Photograph of the model scour created in Test 01; Bottom : Plan view illustration of scour surface features (scales shown in mm)

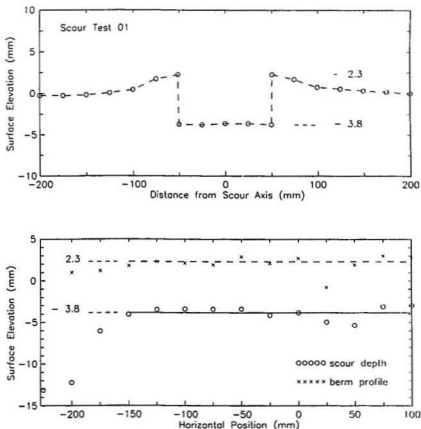


Figure 4.2 Top : Average cross - section surface profile for Test 01 scour; Bottom : Scour depth and berm elevation measurements plotted versus horizontal position

material was evident in front of the final resting position of the model iceberg. The soil in front of the model was also displaced upward and forward relative to the surrounding material, resulting in the formation of a semi - circular shaped (in plan view) rupture surface. Surface heave within the scour incision immediately behind the model iceberg

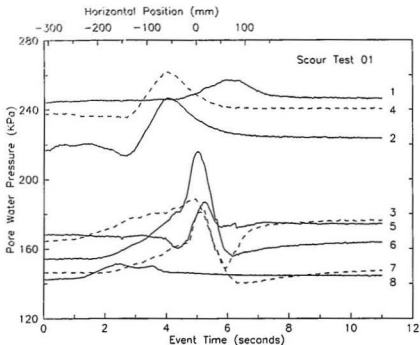


Figure 4.3 Test 01 pore pressure responses during event - transducer channels 01 to 08

was indicative of a soil bearing failure beneath the model, following the completion of horizontal movement in the event.

Figure 4.3 shows a summary of the pore water pressure responses during the scouring event. Pore pressure changes were recorded by eight transducers within a zone which extended to an approximate distance of 150 mm laterally outward near to the clay surface, and 145 mm vertically with depth below the scour. The measured locations of the transducers are given in Table 4.3 along with the corresponding peak and minimum values of the pore pressure developed during the event. The symbols used in this table

Table 4.3 Top : Test 01 measured pore pressure transducer locations; Bottom : Maximum and minimum excess pore pressures and horizontal distance from model

PPT No.	x (mm)	y (mm)	z (mm)	w (mm) ¹
1	6	3	145	100.0
2	- 138	- 7	115	99.9
3	5	- 7	64	100.0
4	- 128	3	138	99.9
5	4	- 5	68	100.0
6	- 3	- 37	54	100.2
7	- 1	47	46	100.3
8	- 143	150	42	102.8
9	0	405	- 3	121.1

¹w = free water depth at position

PPT No.	u_i (KPa)	max. du (KPa)	dx (mm)	min. du (KPa)	dx (mm)
1	244	13	+ 50	-	-
2	217	30	+ 60	- 3	- 28
3	164	24	- 21	- 16	+ 49
4	237	24	+ 50	- 2	- 43
5	168	19	+ 3	- 8	- 60
6	154	61	- 6	-	-
7	146	35	- 3	- 6	+ 91
8	142	9	- 39	-	-

are defined as follows : u_i = the equilibrium pore pressure under the imposed stress conditions at the test acceleration level; $\max du$ = the maximum increase in pore pressure; $\min du$ = the maximum reduction in pore pressure, and; dx = the horizontal distance between the model iceberg and the transducer which recorded the maximum or minimum pore pressure value.

Pore pressure changes within the clay specimen are detailed in Figure 1E.1 which displays the spatial distribution of recorded values at 50 mm intervals of model horizontal movement. The effects of the scouring event at shallow depths were first observed at a prototype horizontal distance of about 20 m in front of the current model position. The maximum increase in pore pressure measured within the apparent steady - state region of scouring was 61 kPa for a transducer (PPT 06) located 5.4 m below the initial clay surface, and 3.7 m laterally outward from the scour axis (at prototype scale). This peak value was recorded when the model iceberg (inflection line) was at a horizontal distance of 0.6 m ($dx = - 6$ mm) from the transducer position. A maximum pore suction of 16 kPa was measured at a prototype depth of 6.4 m, near to the axis of the scour (PPT 03). This reduction of pore pressure occurred immediately following the passage of the model iceberg over the transducer position ($dx = + 49$ mm).

The resultant forces acting at the model iceberg - soil interface during the event are plotted versus the horizontal position of the model in Figure 4.4. The vertical force component was evaluated indirectly from data on the current vertical position and orientation of the model iceberg in free surface water, together with detailed information on the mass and geometry of individual components comprising the model. A summary of the computational procedure is presented in Appendix B. The Test 01 force data are

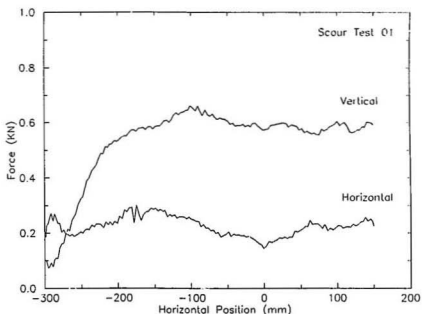


Figure 4.4 Test 01 horizontal and vertical components of the resultant force plotted against model horizontal position

also listed in Table 4.4 at 50 mm intervals of model horizontal movement. In addition, the same information is displayed graphically in Figure 4.5 which illustrates the model iceberg orientation and the system of forces acting on the model at different horizontal positions. The vector angle specified in Table 4.4 refers to the angle of the resultant force measured with respect to the horizontal. The inclination of the resultant force vector measured relative to the scouring face of the model iceberg, may be calculated by the addition of the vector angle to the effective attack angle of the model.

In this test, the vertical component of the resultant force was almost three times as large as the measured horizontal component. The average magnitudes of the vertical

Table 4.4 Test 01 resultant force data tabulated for different model horizontal positions

Horiz. Pos. (mm)	Horiz. Force (N)	Vert. Force (N)	Total Force (N)	Vector Angle (deg)	Attack Angle (deg)
- 300	185.1	102.3	211.5	28.9	21.3
- 250	203.8	320.6	379.9	57.6	22.1
- 200	233.3	531.8	580.7	66.3	20.8
- 150	288.1	584.2	651.4	63.8	17.8
- 100	249.7	660.8	706.4	69.3	16.7
- 50	203.3	604.8	638.1	71.4	14.9
0	143.7	373.2	590.9	75.9	14.6
+ 50	208.6	573.9	610.6	70.0	15.3
+ 100	225.4	603.4	644.1	69.5	17.3
+ 150	223.6	590.9	631.8	69.3	18.1
Average ¹	214.3	600.0	637.9	70.4	15.7

¹ Average values for approx. steady state region : $x = - 150$ to 100 .

and horizontal components for the apparent steady - state region of scouring were 6.0 and 2.1 MN at the corresponding prototype scale. The force record did not show evidence of significant fluctuations in loading. Some initial irregularity in the measured response may be attributed to uplift of the model iceberg and associated re - orientation (pitch adjustment). As indicated in Table 4.4, the model iceberg experienced angular rotation at the beginning of the event such that the attack angle decreased from effective values in excess of 20 degrees to the proposed test value of 15 degrees. The inclination of the resultant force vector increased during the event and, in the apparent steady - state region, the vector angle was approximately perpendicular to the scouring face of the model iceberg. The position of the force vector, calculated as the distance from the model

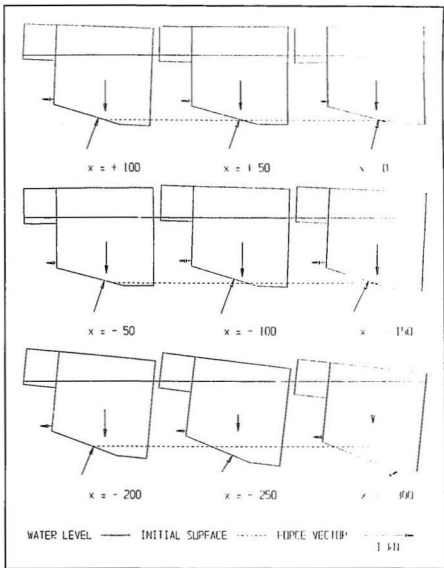


Figure 4.5 Test 01 model iceberg orientation and resultant force vectors

iceberg inflection line measured along the inclined face of the model, also increased at the start of the event toward a relatively consistent value for steady conditions. The force vector acted at an average distance of 32 mm or 3.2 m at prototype scale from the model inflection line. The pressure cells mounted directly on the model iceberg provided limited information on the distribution of stresses acting on the model (see Figure 1C.2). The data record from the bottom - mounted transducer suggested that a small portion of the resultant scour force acted on the horizontal base of the model; however, the transducer response was characterized by considerable fluctuation and the pressure measurements were subject to inaccuracies as the result of stress concentration and arching effects.

Surface soil displacements were evaluated based on film measurements of the movements of lead shot markers. A plan view drawing of surface displacement vectors at positions external to the Test 01 scour incision is presented in Figure 4.6. The average magnitudes of the axial (horizontal) and lateral components of displacement for the apparent steady - state region are also shown in this figure. At a distance of about 1 m from the edge of the scour, the average horizontal and lateral displacements were 0.56 and 0.28 m respectively at prototype scale. The surface displacements decreased gradually with distance from the scour axis to approximate values of 0.29 and 0.19 m respectively at lateral positions approximately 5 m from the edge of the scour (i.e. 100 mm from the scour axis at model scale). The displacements shown for locations within the scour incision were estimated from plan view radiographs. The internal markers were displaced vertically downward below the scour, and were also moved horizontally forward over an average distance of about 2.3 m at prototype scale. The lateral movements of surface markers within the scour were relatively small in this test,

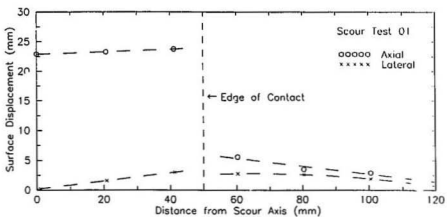
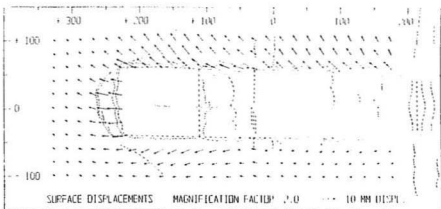


Figure 4.6 Top : Plan view drawing showing surface displacement vectors; Bottom : Average axial and lateral surface displacements versus distance from the scour axis

coinciding with infrequent observations of berm material along the edges of the scour.

The sub - surface displacements generated during the Test 01 scouring event were displayed via radiographic investigation of lead powder trails, and also through manual measurements of the grids comprising strands of coloured spaghetti. Figure 1F.1 shows a trace (digitized drawing) compiled from plan view radiographs of the clay specimen,

including pore pressure transducers, model pipeline segments, and the soil deformation grids formed from lead powder trails. The trace of a cross - sectional radiograph is shown in Figure 1F.2, including instrumentation locations and the displaced configuration of the lateral grid of lead powder trails. Figure 1F.3 shows drawings of the post - event geometry of the initial three lateral grids constructed of spaghetti strands, based on evidence obtained from manual measurements. The trace of an axial section radiograph, presented in Figure 1F.4, shows the displaced configuration of the grid of lead powder trails located at the final position of the model iceberg in the vertical plane through the scour axis.

To allow for quantification of the resultant (plastic) sub - surface soil displacements, the displaced configuration of each grid, as acquired from radiographic and manual investigations, was compared with its apparent initial geometry. The initial grid geometry was assumed to correspond with the design condition and aligned to conform with the undeformed far - field portion of the grid affected by scouring, since pre - event radiographic investigations of the clay specimen were deemed impracticable. The results are given in Figure 1F.5 as both initial / displaced plots and displacement vector plots for the various grids implanted in the specimen. Figure 4.7 shows the initial and displaced configuration of the lateral grid of lead powder trails in cross - sectional and plan view. The observed displacements in this case were in general agreement with results as presented in Figure 1F.5; however, a more detailed assessment was obtained from the radiographic investigation. Lateral soil movements were small or negligible in this test (below the accuracy limitations of the manual techniques); although, shallow lateral movements may be inferred from surface profile measurements of heave adjacent

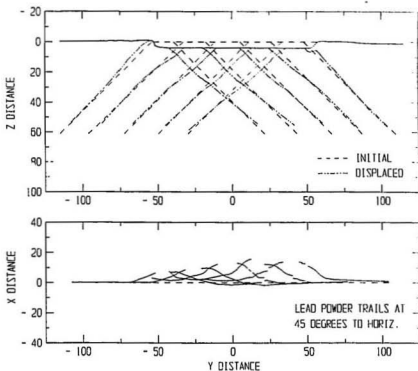


Figure 4.7 Test 01 initial / displaced plot of lateral grid shown in cross - section and plan view (scales in mm)

to the scour. The vertical component of displacement was relatively uniform across the scour width and gradually attenuated with depth below the scour. The horizontal component of displacement, in the direction of travel of the model iceberg, was larger in magnitude and decreased more abruptly with depth. Figure 4.8 shows the initial / displaced and displacement vector plots for the axial grid of lead powder trails located below the final position of the model iceberg. At this location, the displacements induced by scouring were obscured by the effects of a bearing capacity failure beneath

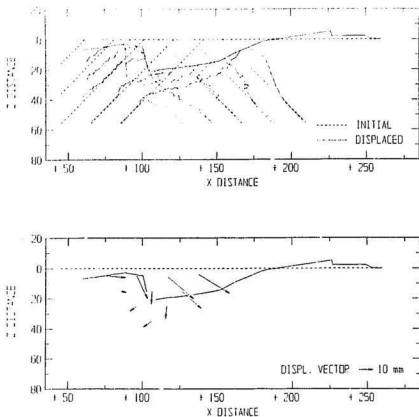


Figure 4.8 Test 01 axial grid at final position of model iceberg. Top : Initial / displaced plot; Bottom : Displacement vector plot (scales in mm)

the model. The displaced configuration of the grid therefore provided only limited information on the extent of the rupture surface which was observed in front of the final model position.

The Test 01 measurements of soil displacement are summarized in Figure 4.9 which shows a profile of the maximum values of the vertical and horizontal components.

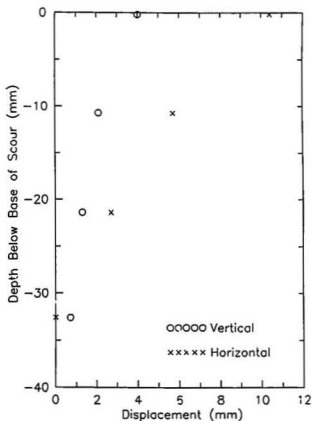


Figure 4.9 Test 01 maximum vertical and horizontal components of soil displacement versus depth below scour base

The displacement values displayed in this plot were evaluated as the average of results from soil deformation grids situated within the apparent steady - state region of scouring. The maximum values of vertical and horizontal displacement immediately below the base of the scour (interpolated at a depth below base = 0.1 m) were 0.39 and 1.00 m respectively at prototype scale. The maximum depth below the base of the scour at which

displacements were measured, was estimated for a lower bound displacement magnitude of 0.2 m, to ensure a consistent basis for comparison with the results of other tests. In this test, the limiting depths for vertical and horizontal components of displacement were 1.1 and 2.5 m respectively at prototype scale. The measured vertical and horizontal displacements extended to normalized values of 2.6 and 6.3 scour depths beneath the scour base. The measured horizontal displacements may be expected to overestimate actual soil movements to some extent, as a result of the limiting accuracy of the manual measurement techniques employed in this test, and the difficulty of obtaining undistorted plan view radiographic images.

Model pipeline segments were excavated and inspected in order to determine any permanent distress caused by the scouring event. The pipeline segments situated at prototype depths of 4.5, 3.2, 2.1, and 1.1 m below the base of the scour did not experience measurable plastic deformations. The shallowest segment, at a prototype depth approximately 0.1 m below the scour base, underwent plastic bending as a result of the scouring event. The pipeline segment was deformed predominantly in the vertical direction, with a maximum deflection measured at the location of the pipe centre - line (scour axis) of 1.1 mm or 0.11 m at prototype scale.

4.3.2 Scour Test 02

Model Input Conditions

The input conditions for Test 02 are summarized in Figure 2A.1 in the corresponding section of Appendix A. The model iceberg configuration and parameters investigated in

the first test were also examined in Test 02, with the exception of the initial stress state of the clay specimen. In this test, the clay was consolidated in the laboratory under a reduced vertical effective stress of 110 kPa. The width of the model iceberg was 100 mm or 10 m at prototype scale, the attack angle was set at 15 degrees, and the model vertical stiffness was retained at 26 N/mm. The nominal depth of free surface water at the location of the model iceberg was also preserved as 100 mm in this test.

The Test 02 layout of instrumentation, deformation markers, and model pipeline segments is shown in elevation and plan view in Figure 2A.2. The arrangement was modified from conditions in the first test to better facilitate site investigation of the clay specimen and to enhance the information acquired from the event. The model pipeline segments employed in this and subsequent tests were stainless steel tubes, described in Section 3.2.3, which represented 80 m length prototype segments comprised of an identical material with an outside diameter of 635 mm and a wall thickness of 25 mm. A total of two model pipeline segments were placed at different depths within the specimen. Soil deformation grids were installed concurrently with the pipeline segments. To form the members of each grid, continuous lengths of very fine solder, which could be detected using radiography, were attached to strands of coloured, dry spaghetti. Lead powder trails were also injected into the specimen to create separate grids. Dissimilar to conditions in the first test, the axial grid of lead powder trails was placed at a horizontal position near to the initial location of the model iceberg. In addition, the model iceberg rested upon a support plate in this test, to minimize its initial settlement.

Experimental determinations of the undrained shear strength were limited to values derived from post - test moisture content measurements. In Figure 2B.1, the

results are compared with strength profiles based on Equations 4.2 and 4.3. Estimated c_u values within the near - surface scoured portion of the clay specimen varied from about 8.4 kPa at a depth of 10 mm or 1.0 m at prototype scale, to approximately 10.5 kPa at a prototype depth of 2.0 m. In this test, the specimen was overconsolidated to a depth of 16.0 m at prototype scale and normally consolidated below this depth, in contrast with the stiffer Test 01 clay, which was overconsolidated throughout its entire stratum. The estimated difference in undrained shear strengths between the two specimens ranged from about 1.3 kPa at a prototype depth of 1.0 m to approximately 3.8 kPa at a depth of 18.0 m, near to the base of the specimen.

Test Results

Test 02 was interrupted by a power outage after 5.5 hours of centrifuge time and near to completion of the consolidation phase. The test was restarted following a delay of approximately 0.5 hours during which the centrifuge came to rest. The consolidation records for the period subsequent to this delay are given in Figure 2C.1 as plots of pore pressure against time, and clay surface settlement versus the square root of time. An additional duration of about 3.4 hours was required to re - establish equilibrium conditions in the clay specimen. The apparent initial clay surface settlement was 2.0 mm during the first stage of consolidation; 1.5 mm of surface movement was recorded following swelling / rebound of the clay specimen associated with the test delay.

Figure 2C.2 provides a summary of the test instrumentation outputs plotted against time and horizontal position during the scouring event. The time to completion of the event was 7.1 seconds and the model iceberg travelled a total horizontal distance

of 450 mm. The average scouring rate was 66.0 mm/s, as determined from the position transducer response. The horizontal displacement history was also verified through indirect measurements of the rotary potentiometer.

A plan view photograph and corresponding drawing of the model scour created in Test 02 are presented in Figure 4.10. An average cross - section surface profile for the apparent steady - state region and an axial plot of scour depths and berm elevations are given in Figure 4.11. Surface profile data are also shown in Figure 2D.1, as cross - sectional plots at 50 mm intervals of horizontal position along the scour path. The scouring event involved an initial period of relatively gradual uplift to an apparent equilibrium scour depth of 12.0 mm or 1.2 m at prototype scale. The scour depth reduced immediately to a new equilibrium level at a specific cross - section ($x \approx - 25$ mm) coincident with the horizontal position of the first model pipeline segment (crown at depth 14 mm). At sections beyond this change in model vertical position, the average scour depth was 4.8 mm. The corresponding average berm elevation was 1.9 mm, including both heave and remoulded material deposited at the sides of the scour during the event. A localized linear depression was evident in the vicinity of the shallowest model pipeline segment (crown at depth 5 mm), indicating that movement had occurred over a substantial portion of its length. The model iceberg experienced some rotational movement about its horizontal axis during approximately the final 75 mm of its travel. The inception of this non - steady motion corresponded with the horizontal position of the shallowest pipeline segment, situated directly beneath the scour base.

The reduction in scour depth to a new equilibrium level was accompanied by the

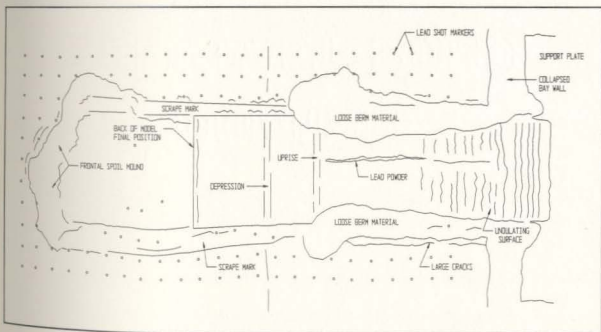
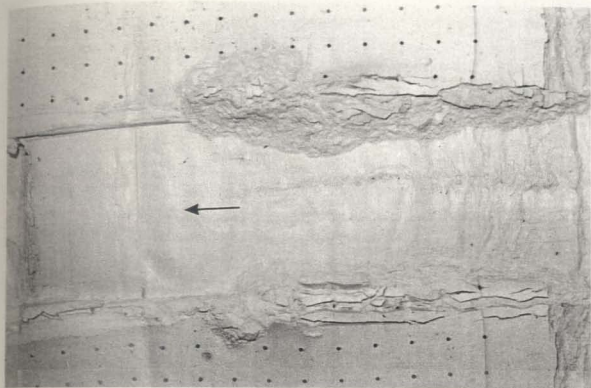


Figure 4.10 Top : Plan view photograph of model scour created in Test 02; Bottom : Plan view drawing illustrating scour surface features

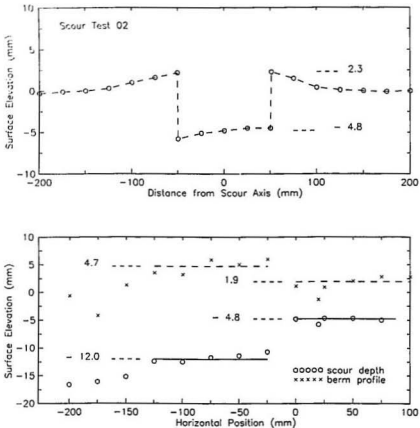


Figure 4.11 Top : Average cross - section surface profile for steady - state region of Test 02 scour; Bottom : Axial section plot of measured scour depths and berm elevations

deposition of sizable mounds of berm material which had built - up as surcharge at the front and sides of the advancing model iceberg. The initial portion of the scour feature was characterized by an undulating incision surface, collapse or caving of the scour sidewalls, and extensive heave of surface material indicative of significant lateral movements adjacent to the scour. In contrast, at horizontal positions beyond the reduction

in scour depth, the scour incision was relatively uniform in appearance, and scrape markings were evident along the sides of the scour, with negligible berm deposition. The scrape markings were formed as material carried with a stabilized frontal soil mass or adhering directly to the sides of the model iceberg, abraded the surface of the specimen as the model was advanced. A large mound of remoulded or spoil material and considerable surface heave were observed to the front and sides of the final position of the model iceberg.

The Test 02 pore water pressure responses for eight transducers situated throughout the clay specimen are shown in Figure 4.12. The measured locations of the transducers are listed in Table 4.5, together with the corresponding equilibrium pore pressure values, and the peak and minimum pore pressure changes generated during the scouring event. Figure 2E.1 shows the spatial distribution of the excess pore pressures at 50 mm intervals of model horizontal movement. The effects of the scouring event were initially recorded at a prototype horizontal distance approximately 25 m from the current position of the model iceberg. The maximum increase in pore pressure measured within the apparent steady - state region of scouring was 47 kPa for a transducer (PPT 06) located 6.3 m below the initial clay surface, and 4.2 m laterally outward from the scour axis (at prototype scale). The peak response was recorded when the model was at a horizontal distance of 2.4 m ($dx = - 24$ mm) from the transducer position. The maximum recorded pore suction was 18 kPa, for a transducer (PPT 07) situated at a prototype depth of 1.8 m and adjacent to one edge of the scour incision. The reduction of pore pressure occurred after the model iceberg had travelled a horizontal distance of 7.0 m beyond the transducer position ($dx = + 70$ mm).

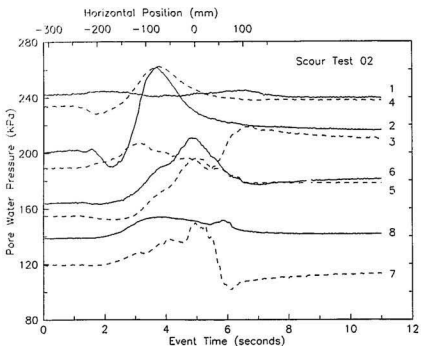


Figure 4.12 Test 02 pore pressure responses during event - transducer channels 01 to 08

Figure 4.13 shows the resultant forces acting at the model iceberg - soil interface during the event plotted against the horizontal position of the model. A listing of the force data is also given in Table 4.6 at 50 mm intervals of model horizontal position. In addition, Figure 4.14 provides an illustration of the model iceberg orientation and the system of forces acting on the model at different positions along the scour path. In this test, a large amount of surcharge was developed in front of the model during the event. The vertical component of the resultant force was generally less than two times as large as the measured horizontal component. The horizontal force component decreased over

Table 4.5 Top : Test 02 measured pore pressure transducer locations; Bottom : Maximum and minimum excess pore pressures and horizontal distances from model

PPT No.	x (mm)	y (mm)	z (mm)	w (mm) ¹
1	- 10	8	142	100.0
2	- 133	3	100	99.9
3	- 4	- 17	90	100.1
4	- 133	8	136	99.9
5	- 2	6	59	100.0
6	- 5	- 42	63	100.2
7	- 4	55	18	100.3
8	0	- 139	35	102.5
9	0	405	- 3	121.1

¹ w = free water depth at position

PPT No.	u_1 (kPa)	max. du (kPa)	dx (mm)	min. du (kPa)	dx (mm)
1	242	3	+ 100	- 3	-
2	200	61	+ 19	- 11	- 73
3	189	30	+ 111	- 1	+ 18
4	234	29	+ 21	- 6	- 107
5	155	41	- 13	- 3	- 203
6	164	47	- 24	- 1	- 226
7	119	31	- 16	- 18	+ 70
8	139	16	- 106	-	-

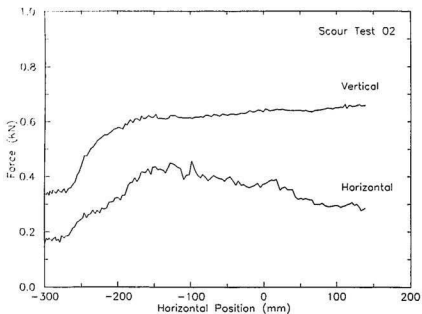


Figure 4.13 Test 02 horizontal and vertical components of the resultant force plotted against model horizontal position

the final portion of the event, corresponding with the reduction in scour depth and the extensive deposition of berm material. The average magnitudes of the vertical and horizontal components for the region beyond the reduction in scour depth were 6.4 and 3.3 MN respectively at prototype scale. The effective attack angle of the model iceberg increased at the beginning of the event to values in excess of 20 degrees, and then diminished to values corresponding with the initial model orientation over the apparent steady - state region of scouring. The inclination of the resultant force vector remained nearly constant throughout the event at an angle approximately 10 degrees from the perpendicular to the scouring face, suggesting some mobilization of friction / adhesion

Table 4.6 Test 02 resultant force data tabulated for different model horizontal positions

Horiz. Pos. (mm)	Horiz. Force (N)	Vert. Force (N)	Total Force (N)	Vector Angle (deg)	Attack Angle (deg)
- 300	158.0	338.3	373.4	65.0	15.8
- 250	245.1	436.6	500.7	60.7	17.4
- 200	323.7	579.0	663.3	60.8	19.4
- 150	433.9	615.8	753.3	54.8	20.4
- 100	457.0	613.2	764.7	53.3	18.4
- 50	394.1	623.5	737.6	57.7	16.6
0	372.6	636.3	737.4	59.7	15.8
+ 50	321.4	640.0	716.2	63.3	15.4
+ 100	295.7	650.4	705.1	65.6	15.2
+ 139	284.9	658.4	710.1	66.6	15.2
Average ¹	327.9	645.1	724.4	63.1	15.4

¹ Average values for approx. steady state region : $x = - 25$ to 139.

at the model - soil interface. The position of the force vector increased at the start of the event to a peak distance of 46 mm or 4.6 m at prototype scale from the model iceberg inflection line, and then decreased toward a steady value of 3.4 m on average, during the latter portion of the event.

The estimated interface pressures during the event are shown in Figure 2C.2 for transducers mounted at the horizontal base (IPT 18) and inclined scouring face (IPT 19 and 20) of the model iceberg. The changes in water - induced pressure due to model uprise must be accounted for in the interpretation of the measured total pressures. The pressure response at the scouring face of the model was characterized by a rapid increase

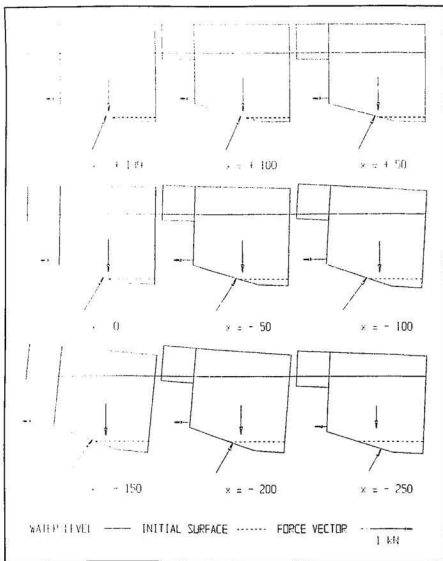


Figure 4.14 Test 02 model iceberg orientation and resultant force vectors

after initial soil contact, and an abrupt peak (maximum pressure rise \approx 140 kPa) and immediate decrease which coincided with the reduction in scour depth and associated berm deposition described previously. The interface pressure record for the transducer situated at the base of the model described a regularly fluctuating response with an initial build - up of pressure and gradual decrease toward the end of the event. The measurement of soil - induced pressure changes along the horizontal bottom surface indicated that a component of the resultant scour force acted at this location.

Figure 4.15 shows a plan view drawing of the surface displacement vectors measured at positions external to the Test 02 scour incision. A summary plot of the average values of the horizontal and lateral components of displacement for the apparent steady - state region is also presented in this figure. The average horizontal and lateral surface movements recorded at a distance of about 1 m from the edge of the scour were 0.30 and 0.32 m respectively at prototype scale. At lateral positions approximately 5 m from the scour edge (the outer limit of the surface markers) the horizontal and lateral displacements decreased to average values of 0.11 and 0.15 m respectively. The displacements of the surface markers within the scour incision were estimated from plan view radiographs. The identification of surface markers placed near to the beginning of the scour was not possible, as these markers were displaced over large horizontal distances with the surcharge in front of the model iceberg, or moved laterally as this soil was progressively cleared from the path of the advancing model. In the apparent steady - state region of scouring, the average horizontal displacement of the internal surface markers was 3.0 m at prototype scale and the corresponding lateral movements were relatively small.

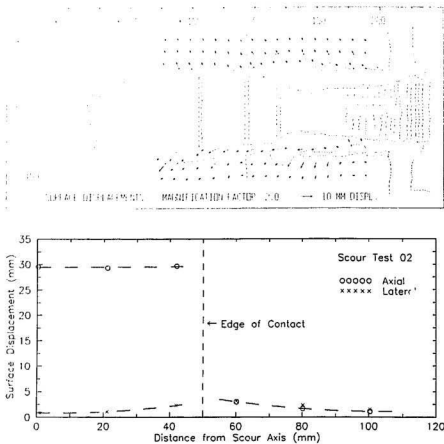


Figure 4.15 Top : Test 02 plan view drawing of surface displacement vectors; Bottom : Average axial and lateral surface displacements versus distance from the scour axis

In Test 02 and subsequent tests, information on sub - surface displacements was acquired through radiographic techniques and verified through the excavation of the soil deformation grids. Figure 2F.1 shows a trace based on plan view radiographs of the clay specimen, including the locations of pore pressure transducers and model pipeline segments, and the displaced configuration of soil deformation grids. In plan view

radiographs, the scour incision appears darker beyond the first model pipeline segment, exhibiting the distinct transition in scour depth observed at this location. The traces of cross - sectional radiographs are given in Figure 2F.2, including instrumentation locations and the lateral grids of fine solder, situated at two different horizontal positions. Figure 2F.3 presents the trace of an additional cross - sectional radiograph, depicting the lateral grid of lead powder trails. The trace of an axial section radiograph, shown in Figure 2F.4, displays the grid of lead powder trails located near to the initial position of the model iceberg in the vertical plane through the scour axis. A side elevation view of the lateral grid of lead powder trails is also evident in this axial trace.

Test O2 sub - surface displacements are illustrated in Figure 2F.5 as both initial / displaced plots and displacement vector plots for each of the soil deformation grids placed within the clay specimen. In this test, the pattern of horizontal soil displacements was atypical. Horizontal displacements in the direction of travel were observed as expected; however, grid movements in the opposite direction were also evident below a given depth. The displacements opposite to the direction of travel were most apparent in the initial region of scour depth adjustment, and diminished with the reduction in scour depth and the establishment of steady conditions.

Figure 4.16 shows the initial and displaced configuration of the lateral grid situated at the beginning of the apparent steady - state region of scouring ($x = - 25$ mm). Lateral soil displacements were small and were limited to the near - surface area adjacent to the scour edges, with some movements below the scour incision possibly attributable to deviations in the initial grid geometry. The vertical component of displacement did not vary significantly across the scour width and gradually diminished in magnitude with

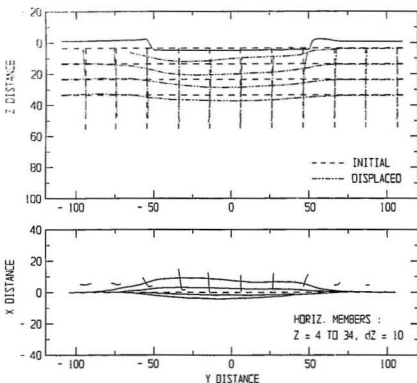


Figure 4.16 Test 02 initial / displaced plot of lateral grid at $x = -25$ shown in cross-section and plan view (scales in mm)

depth. The horizontal component of displacement decreased near to the edges of the scour, although the distortion in plan view radiographs limited the accuracy of measurements away from the scour axis. The horizontal soil movements decreased more abruptly with depth than the corresponding vertical displacements and, as described above, small negative displacements were observed below a given depth. The axial grid of lead powder trails situated within the initial region of scouring ($x \approx -200$ to -75), shown in Figure 2F.5, was placed to insufficient depth to allow for reliable interpretation

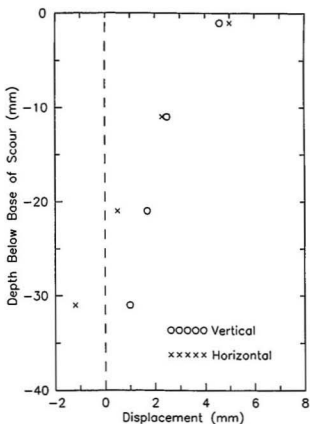


Figure 4.17 Test O2 maximum vertical and horizontal components of soil displacement versus depth below scour base

of displacements. The displaced configuration suggested that material above the extent of the grid was severely disturbed or re - worked.

Test O2 measurements of soil displacement are summarized in Figure 4.17 which displays a profile of the maximum values of vertical and horizontal movements, evaluated as the average of results from grids within the apparent steady - state region. The

maximum values of vertical and horizontal displacement immediately below the base of the scour (interpolated at a depth below base = 0.1 m) were 0.46 and 0.50 m respectively at prototype scale. The limiting prototype depths for vertical and horizontal components of displacement, estimated for a lower bound displacement magnitude of 0.2 m, were 1.7 and 1.4 m respectively. The measured vertical and horizontal displacements extended to normalized values of 3.5 and 2.7 scour depths beneath the scour base. In this test, small negative horizontal movements were also apparent at depths below the limiting value estimated for the assumed lower bound displacement.

The model pipeline segments were excavated and measured to determine any permanent distress induced by the effects of scouring. The horizontal position of the first pipeline segment was coincident with the abrupt transition in scour depth to the reduced equilibrium level. The segment was located at a depth approximately 0.2 m below the scour base in relation to the initial region preceding the reduction in scour depth. This segment exhibited a small degree of curvature predominantly in the horizontal direction; the maximum deflection recorded at the pipe centre - line (scour axis) was on the order of 0.5 mm or 0.05 m at prototype scale (model displacements were assessed to within 0.1 mm). The second model pipeline segment was located immediately below the base of the scour (0.02 m beneath the scour base at prototype scale) within the apparent steady - state region of scouring, beyond the reduction in scour depth. This segment also experienced plastic bending due to the effects of scouring. A maximum deflection of about 0.20 m at prototype scale was measured in the vertical direction at the pipe centre - line and near to one end of the deformed segment. The measured horizontal displacements were less extensive, with a maximum prototype deflection of 0.18 m

recorded at a position offset from the centre of the pipeline segment. This shallow segment also suffered a minor indentation at a position adjacent to the one edge of the scour incision, indicative of local contact with the model keel.

4.3.3 Scour Test 03

In Test 03, it was proposed to investigate the influence of the change in scour depth associated with an increase in the buoyant weight of the model iceberg. The test parameters examined were identical to the Test 02 case, with the exception of the surface water depth. The nominal depth of free water above the surface of the clay specimen was reduced to 50 mm in this test from 100 mm in the preceding tests. The model iceberg was modified to provide the same waterplane area for the revised water level, to maintain the Test 02 model vertical stiffness condition.

The test was unsuccessful, in that the initial scour depth was larger than predicted and this resulted in the development of forces which exceeded the capabilities of the drive system. The motor capacity was also less than anticipated from normal gravity trials. The model iceberg was advanced over a total horizontal distance of 135 mm in a time period of 2.8 seconds. The model descended immediately as it left contact with the initial support plate, a peak horizontal force of 0.79 kN was mobilized, and the drive motor stalled. Following a brief delay, an attempt was made to advance the model beyond its current position, with negligible movement resulting. The centrifuge acceleration level was subsequently reduced by half to 50 gravities, and the scouring event was effectively resumed to completion. A complete set of results was acquired for

the test; however, scaling changes and other irregularities must be allowed for in the interpretation of this information. As a consequence, the value of the Test 03 data is much reduced and details are not presented here.

Figure 4.18 shows a plan view photograph and related drawing of the model scour created in Test 03. The depression formed as a result of the initial scouring episode at 100 gravities, extended to a maximum depth of 51 mm or 5.1 m at prototype scale. The scour incision surface was irregular in this region, and the sidewalls of the cut collapsed or caved extensively following the passage of the model iceberg. The final segment of the scour feature, generated at the 50 gravity test acceleration level, involved an uprise to an average scour depth of 13 mm, approaching an equilibrium condition. An extensive volume of surcharge was displaced forward with the model and amassed in a semi-circular mound at the front and sides of its final resting position. The latter portion of the scour feature was also characterized by variable deposition of loose or remoulded material at the sides of the scour incision, with berm elevations ranging from 1.5 to 12.5 mm above the original surface level. Model pipeline segments situated at initial depths of 15 and 5 mm below surface were displaced vertically beneath the scour to approximate final depths of 21 and 15 mm respectively. The first pipeline segment was locally dented and experienced plastic bending with the development of a wrinkle on the compression side of the segment, and a maximum centre - line deflection of about 18 mm at model scale. The shallower second pipeline segment was also subject to indentation as the result of local contact, and assumed a severely deformed or buckled S - shape upon removal from the clay specimen, with a maximum deflection on the order of 21 mm.

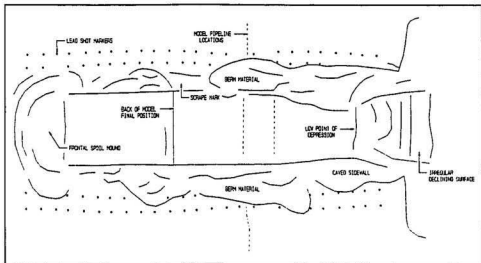


Figure 4.18 Top : Photograph of model scour created in Test 03; Bottom : Plan view drawing illustrating scour surface features

4.3.4 Scour Test 04

Model Input Conditions

The model iceberg used in Test 04 described the baseline configuration for subsequent tests. The model geometry and input parameters for this test are presented in Figure 4A.1 in the corresponding section of Appendix A. The model iceberg represented a 10 m wide prototype ice feature with a cutting face attack angle of 15 degrees. The vertical stiffness of the model was equal to 61 N/mm in free water of nominal 80 mm depth in this test. The clay laboratory pre - consolidation stress was maintained at 110 kPa; soil conditions were identical to those investigated in Tests 02 and 03.

The Test 04 arrangement of instrumentation, deformation markers, and model pipeline segments, shown in Figure 4A.2, was proposed as a standard layout, with only slight modification required in succeeding tests. The soil deformation grids were constructed using both spaghetti / solder horizontal members, and vertical members comprised of injected lead powder, as detailed in Section 3.2.3. Two separate lateral grids were installed at horizontal positions within the expected steady - state region of scouring. A total of two model pipeline segments were placed at different depths, during trenching of the lateral grids. In addition, two axial grids were installed : the first at a position near to the initial portion of the proposed scour, and the second at the final location of the model iceberg. The size of the array of surface lead shot markers was also increased in this test to facilitate improved definition of the lateral extent of surface soil movements.

The experimental methods used to evaluate undrained shear strength in this test included in-flight vane shear testing, in addition to post-test moisture content measurements. Figure 4B.1 displays estimated c_u profiles for the Test 04 clay specimen. Vane tests were to be undertaken at three horizons within the specimen; however, due to malfunction of the apparatus, test results were obtained at only one level 68 mm below surface, or 6.8 m at prototype scale. The vane test data for this level are shown in Figure 4B.2, including plots of rotation and torque against time, as well as the corresponding torque versus rotation curve. The maximum undrained shear strength was assessed from the peak torque mobilized by the vane head alone, with shaft resistance deducted. It was assumed that test conditions were effectively undrained, and that a constant shear strength was mobilized on the cylindrical surface defined by the vane blades. This led to the following relationship between the peak torque T and the undrained shear strength, expressed in terms of the vane geometry :

$$T = c_u \left\{ \pi (3H + D) D^2 / 6 \right\} \quad (4.5)$$

where D and H are, respectively, the diameter and height of the vane blades employed in the test. As illustrated in Figure 4B.1, the vane test results predicted a lower strength value in comparison with the estimates based on Equations 4.2 and 4.3. The measured vane strength was 16.1 kPa at the test level, as compared with an estimate of 18.2 kPa derived in accordance with the empirical relation given by Equation 4.2. The access of surface water to the vane head via the opening produced around the vane shaft almost

certainly resulted in some dissipation of excess pore pressures during vane rotation, and this may account for a reduction in the measured shear strength.

Test Results

Test 04 was initially stopped at the 30 gravity acceleration level, and restarted following adjustments to ensure negligible deviation from required surface water levels. Figure 4C.1 shows the consolidation records for this test, including plots of pore pressure against time and clay surface settlement versus the square root of time. In order to achieve greater than 95 percent of primary consolidation, the clay specimen was maintained at the test acceleration level for a time period of about 5.4 hours, preceding vane test implementation. The apparent initial clay surface settlement was 1.8 mm during the consolidation phase of the test. The model scouring event was carried out subsequent to the completion of vane testing. Figure 4C.2 shows the instrument outputs measured during the event plotted versus time and horizontal position. The time required to complete the event was about 5.8 seconds and the model iceberg travelled a total horizontal distance of 426 mm. The average scouring rate realized was 72.9 mm/s.

A plan view photograph and corresponding drawing illustrating the surface features of the Test 04 scour are given in Figure 4.18. An average cross - section surface profile is shown in Figure 4.19 together with a plot of scour depths and berm elevations against horizontal position along the scour axis. Surface profile data are also presented in Figure 4D.1 for cross - sections at 50 mm intervals of horizontal position. In this test, a desired scour depth and an increased length of scouring at effectively steady - state conditions, relative to preceding tests, was achieved. The average scour depth was

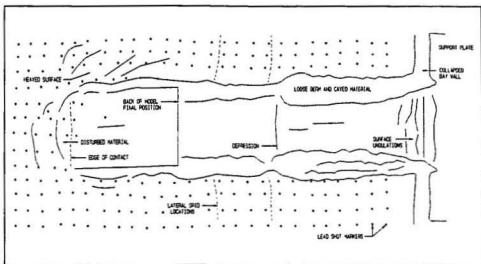
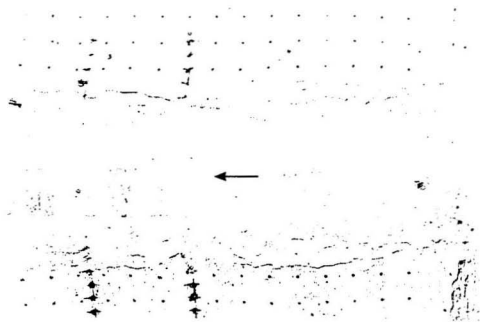


Figure 4.19 Top : Plan view photograph of model scour created in Test 04; Bottom : Plan view drawing illustrating scour surface features

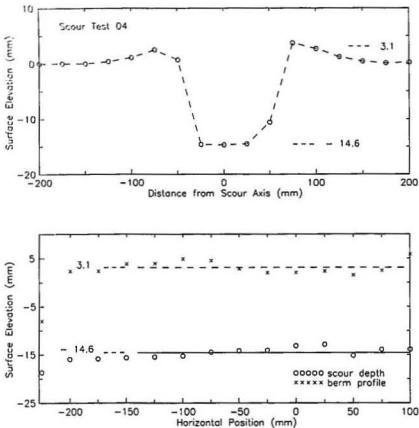


Figure 4.20 Top : Average cross - section surface profile for steady - state region of Test 04 scour; Bottom : Axial section plot of measured scour depths and berm elevations

14.6 mm or 1.46 m at prototype scale; the equilibrium value was established after a brief period of uprise from the initial model iceberg position at a nominal 20 mm depth. The corresponding berm elevations averaged 3.1 mm above the original surface level, including heave of the soil immediately adjacent to the scour in addition to loose or spoil material. Remoulded material arising from berm formation and caving of the trench

sidewalls after passage of the model iceberg was evident to a distance on the order of 20 mm from the edges of the 100 mm wide scour trough. Local surface depressions were also associated with the trench locations of model pipeline segments. Soil disturbance (surface heave) in front of the final location of the model extended to about 45 mm in a semi - circular region; however, only a limited amount of loose frontal mound material was observed.

The pore water pressure responses recorded during the scouring event are shown in plots presented in Figure 4.21. Table 4.7 lists the measured locations of the pore pressure transducers, as well as the corresponding peak and minimum excess pore pressure values measured during the event. The spatial distribution of recorded pore pressure changes is displayed in Figure 4E.1 at 50 mm intervals of model iceberg horizontal movement. The effects of scouring were first witnessed at shallow depths, at a prototype horizontal distance on the order of 25 m in front of the current model position. In the steady - state region of scouring, the maximum recorded increase in pore pressure was about 88 kPa for a transducer (PPT 03) located at a depth of 9.5 m below the initial clay surface, and 0.9 m laterally outward from the scour axis (at prototype scale). The peak value was observed when the model was at a horizontal distance of approximately 9 m ($dx = - 86$ mm) from the transducer location. A maximum pore suction of about 37 kPa was measured at the same location, immediately subsequent to the passage of the model keel ($dx = + 52$ mm).

The resultant forces acting at the model iceberg - soil interface during the event are plotted against the horizontal position of the model in Figure 4.22. Table 4.8 gives a listing of the force data at 50 mm intervals of model horizontal movement. Figure 4.23

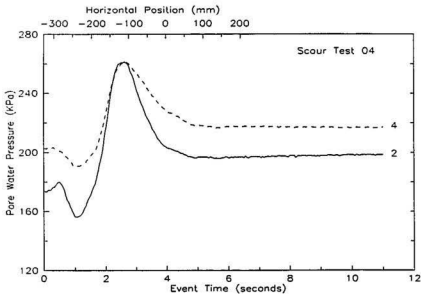
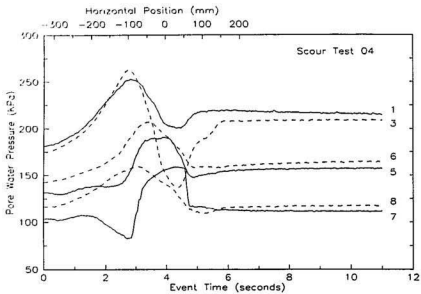


Figure 4.21 Test 04 pore pressure responses during event - transducer channels 01 to 08

Table 4.7 Top : Test 04 measured pore pressure transducer locations; Bottom : Maximum and minimum excess pore pressures and horizontal distance from model

PPT No.	x (mm)	y (mm)	z (mm)	w (mm) ¹
1	- 4	- 19	101	80.0
2	- 129	- 11	93	79.9
3	- 4	- 9	95	80.0
4	- 127	- 8	128	79.9
5	5	8	55	80.0
6	- 1	- 49	61	80.3
7	24	29	23	80.1
8	- 1	- 149	29	82.9
9	0	405	- 3	101.1

¹ w = free water depth at position

PPT No.	u_i (KPa)	max. du (KPa)	dx (mm)	min. du (KPa)	dx (mm)
1	181	72	- 78	-	-
2	173	89	+ 29	- 16	- 91
3	175	88	- 86	- 37	+ 52
4	202	59	+ 27	- 12	- 91
5	133	58	+ 1	- 3	- 258
6	144	63	- 34	-	-
7	104	55	+ 10	- 21	- 116
8	117	43	- 59	- 7	+ 120

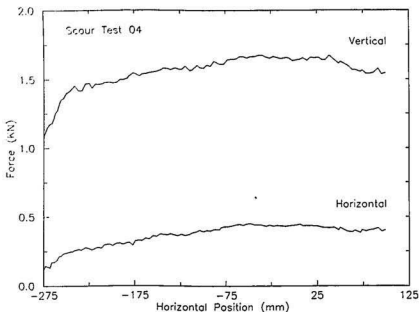


Figure 4.22 Test 04 horizontal and vertical components of the resultant force plotted against model horizontal position

displays the model iceberg orientation and the system of forces acting on the model for different horizontal positions. The vertical component of force developed in this test was nearly four times as large as the measured horizontal component. The average prototype magnitudes of the vertical and horizontal components in the steady - state region of scouring were 16.1 and 4.1 MN respectively. The effective attack angle increased initially to a value of about 16.0 degrees, and the model then retained a relatively constant orientation during scouring. The inclination of the resultant force vector was slightly above the perpendicular to the scouring face of the model, and did not change markedly over the duration of the event. The distance between the position of the force

Table 4.8 Test 04 resultant force data tabulated for different model horizontal positions

Horiz. Pos. (mm)	Horiz. Force (N)	Vert. Force (N)	Total Force (N)	Vector Angle (°)	Attack Angle (°)
- 250	237.9	1398	1418	80.3	15.6
- 200	291.6	1474	1502	78.8	15.8
- 150	356.8	1558	1598	77.1	16.2
- 100	393.0	1581	1629	76.0	16.1
- 50	451.8	1665	1725	74.8	16.1
0	439.7	1640	1698	75.0	15.8
+ 50	420.2	1628	1682	75.5	15.8
+ 100	403.1	1547	1598	75.4	16.0
Average ¹	412.0	1614	1665	75.7	16.0

¹ Average values for approx. steady state region : $x = - 150$ to 100 .

vector and the model inflection line increased to a steady value of 2.6 m on average at prototype scale, during the latter portion of the event. In this test, the inductive pressure transducers mounted on the model were damaged by the incursion of water and, therefore, no data on interface pressures were acquired.

Figure 4.24 shows a plan view drawing of surface displacement vectors at positions external to the Test 04 scour incision, as well as a plot of the average magnitudes of the horizontal and lateral components of displacement for the apparent steady - state region. The average horizontal and lateral displacements were 0.31 and 0.58 m respectively at prototype scale, at a lateral position approximately 1 m from the edge of the scour incision. The surface displacements decreased to negligible values within a distance of about one scour width from the edge of the incision (i.e. less than

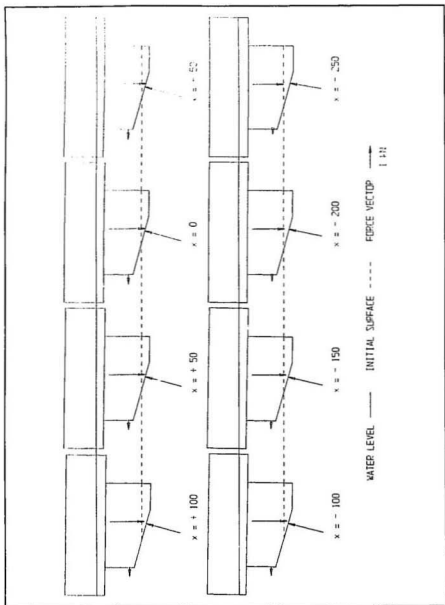


Figure 4.23 Test 04 model iceberg orientation and resultant force vectors

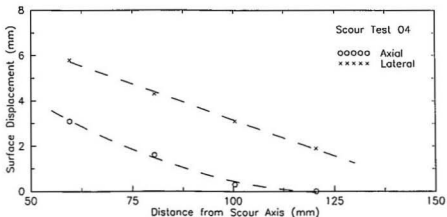
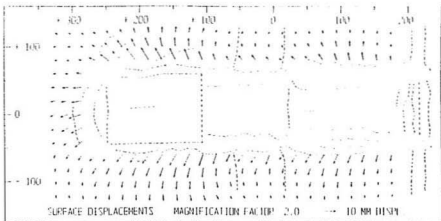


Figure 4.24 Top : Test 04 plan view drawing of surface displacement vectors; Bottom : Average axial and lateral surface displacements versus distance from the scour axis

150 mm from the scour axis at model scale). The movement of surface markers within the scour may be qualitatively assessed based on the radiographic evidence, as displayed in Figure 4F.1. Some of the internal markers were displaced horizontally and laterally during the event, and were deposited at the sides of the scour incision; other markers were displaced horizontally and vertically below the scour, and experienced only limited

lateral movement. Quantitative evaluation of these displacements was impracticable because of the difficulty of positively identifying particular markers after very large movements had occurred.

The displaced configurations of soil deformation grids, and the locations of pore pressure transducers and model pipeline segments, are shown in plan view in the trace compiled from Test 04 radiographs presented in Figure 4F.1. Figure 4F.2 displays similar information acquired from cross - sectional radiographs at two separate horizontal positions, coinciding with the lateral grid and model pipeline locations. The traces of the axial section radiographs situated near to the initial portion of the scour, and at the final horizontal position of the model iceberg, are shown in Figures 4F.3 and 4F.4 respectively. Figure 4F.4 also includes a view of the displaced grid with the apparent final model iceberg position superimposed on the axial trace.

Figure 4F.5 gives details of Test 04 sub - surface displacements in terms of both initial / displaced plots and displacement vector plots for each of the soil deformation grids installed within the clay specimen. The initial and displaced configuration of the first lateral grid ($x = -19$ mm) is shown in cross - sectional and plan view in Figure 4.25. Soil displacements generated by the scouring event included lateral, vertical, and horizontal components. The lateral component of displacement was more extensive in this test than in preceding tests; although, significant lateral movements were generally restricted to a shallow region adjacent to the edges of the scour, corresponding with the measured surface heave. The vertical component of displacement was relatively consistent across the scour width, but decreased at the edges of the incision where lateral movements increased. In general, vertical soil displacements occurred in a pattern similar

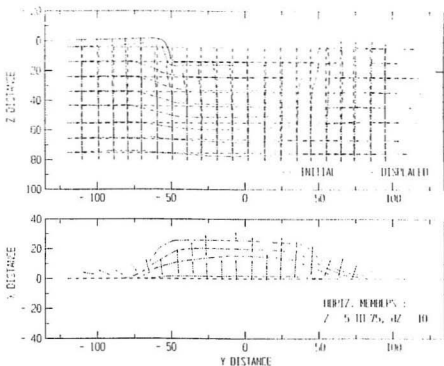


Figure 4.25 Test 04 initial / displaced plot of lateral grid at $x = -19$ shown in cross-section and plan view

to the morphology of the scoured surface and decreased gradually with depth below the scour. The horizontal component of displacement, in the direction of travel of the model iceberg, was larger in magnitude than the associated vertical component; however, large horizontal soil movements were limited to shallower depths. Figure 4.26 shows the initial / displaced plot for the axial grid at the final position of the model iceberg. The soil displacements measured at this particular location include some effects of a bearing capacity failure coinciding with the cessation of movement and the consequent change in forces acting on the model. To reduce effects extraneous to scouring, equipment

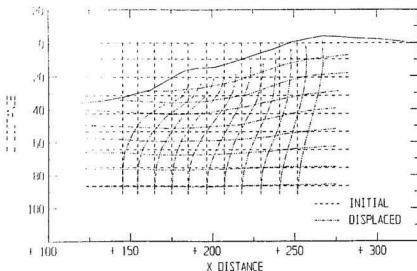


Figure 4.26 Test 04 initial / displaced plot of axial grid located at final horizontal position of model iceberg

modifications to provide vertical support for the model at the end of the scour path were implemented in subsequent tests.

A summary of the Test 04 displacement records is provided in Figure 4.27, in which values of the vertical and horizontal components are plotted against depth below the base of the scour. The horizontal displacements shown in this plot were evaluated using the results from the initial axial grid at horizontal positions within the apparent steady - state region of scouring. Measurements acquired from the axial grid were considered to be more accurate due to distortion in plan view radiographs; however, larger horizontal soil displacements determined from lateral grid results were more consistent with measured model pipeline deformations, described below. The plotted vertical displacement results were derived from well - defined lateral grid movements.

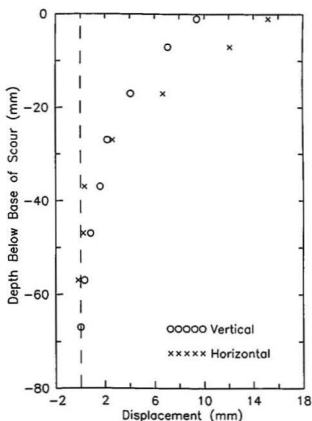


Figure 4.27 Test 04 values of vertical and horizontal components of soil displacement versus depth below scour base

The measured maximum values of vertical and horizontal displacement immediately below the base of the scour (interpolated at a depth below base = 0.1 m) were 0.94 and 1.52 m respectively at prototype scale; however, there was notable variation in the results as obtained from different grids. The maximum depths below the base of the scour at which vertical and horizontal displacements were measured, as estimated for

a lower bound displacement magnitude of 0.2 m, were 3.2 and 3.1 m respectively at prototype scale. The vertical and horizontal displacements extended to normalized values of 2.1 and 2.0 scour depths beneath the scour base.

Model pipeline segments placed at two different depths in the Test 04 clay specimen experienced plastic deformation due to the effects of scouring. The depths of pipeline segments shown in Figure 4F.2 represent apparent final levels measured subsequent to completion of the test. Initial depths for the first and second pipeline segments were approximately 21 and 15 mm respectively as measured from the crown of the segment to the original clay surface (i.e. approximately 0.6 and 0.0 m below the scour base at prototype scale). Both pipeline segments were severely bent or bowed in the forward horizontal direction and also exhibited a smaller vertical component of plastic deformation. The maximum centre - line deflections measured in the vertical and horizontal directions for the first segment, were about 0.22 and 2.35 m respectively at prototype scale. Similarly, the shallower second segment, situated immediately beneath the scour base, sustained prototype vertical and horizontal deflections on the order of 0.09 and 2.83 m at the pipe centre - line (scour axis). The observed pipeline distress in this test was not indicative of any direct contact with the model keel.

4.3.5 Scour Test 05

Model Input Conditions

Test 05 represented baseline conditions for the experimental programme. The test inputs are displayed in Figure 5A.1 in the corresponding section of Appendix A. The model

iceberg configuration was identical to that used in Test 04. The width of the model was 100 mm, the attack angle was 15 degrees, and the model vertical stiffness was 61 N/mm in free water of nominal 80 mm depth. The clay was consolidated in the laboratory under a uniform vertical effective stress of 140 kPa, coinciding with the initial stress state for the Test 01 specimen. The test date was delayed due to unanticipated repairs of the beam centrifuge. As a result, the time period for laboratory pre - consolidation in Test 05 had to be extended by about three weeks over the typical duration allowed for this procedure. The measured compression of the specimen during this supplementary interval of laboratory consolidation was negligible.

The Test 05 layout of instrumentation, deformation markers, and model pipeline segments is shown in elevation and plan view in Figure 5A.2. The arrangement was similar to that of Test 04; however, lateral grid positions were altered slightly to expedite post - test investigation of the clay specimen. In addition, the horizontal length of the second axial grid was extended, to improve measurements of soil displacement in the vicinity of the final position of the model iceberg. In this test, equipment modifications were also implemented to provide immediate support for the model at the end of the scouring event. The support apparatus is described in Section 3.3.2.

Experimental determinations of the undrained shear strength in Test 05 were restricted to values based on post - test moisture content measurements. No meaningful data were acquired from the vane shear test device due to malfunction of the load cell used to measure the applied torque. Figure 5B.1 gives a comparison of experimental values with c_u profiles estimated in accordance with Equations 4.2 and 4.3. The values assessed from moisture content measurements are in apparent agreement with the

Modified Cam Clay strength profile. The strength predictions were larger than anticipated for post - test conditions, as it may be expected that free water was drawn into the clay specimen due to pore suction set - up with stoppage of the centrifuge.

Test Results

The consolidation records for Test 05 are given in Figure 5C.1, including plots of pore pressure against time, and clay surface settlement versus the square root of time. PPT Channel 03 did not function during the test and, therefore, seven transducers were available to monitor pore water stress conditions in the clay specimen. The centrifuge time required to complete greater than 95 percent of primary consolidation was about 4.7 hours, and the apparent initial clay surface settlement was 1.4 mm in this test. A summary of the test instrumentation outputs plotted against time and horizontal position during the scouring event is given in Figure 5C.2. The event was completed in 6.0 seconds, in which the model iceberg travelled a total horizontal distance of 448 mm. The average scouring rate was 72.1 mm/s, as evaluated from the data records of the position transducer and rotary potentiometer.

Figure 4.28 shows a plan view radiograph and related drawing depicting surface features of the Test 05 scour. Figure 4.29 displays an average cross - section surface profile of the scour, together with an axial plot of scour depths and berm elevations. Further details of the overall surface profile are given in Figure 5D.1 as cross - sectional plots at 50 mm intervals of horizontal position. The initial period of uprise to an apparent steady - state scouring level was relatively rapid in this test, similar to the Test 04 event. The average scour depth for equilibrium conditions was 12.1 mm or 1.21 m at prototype

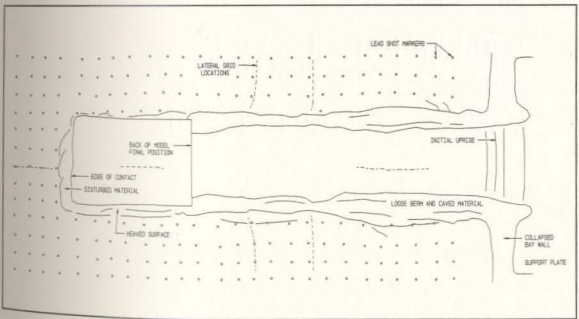
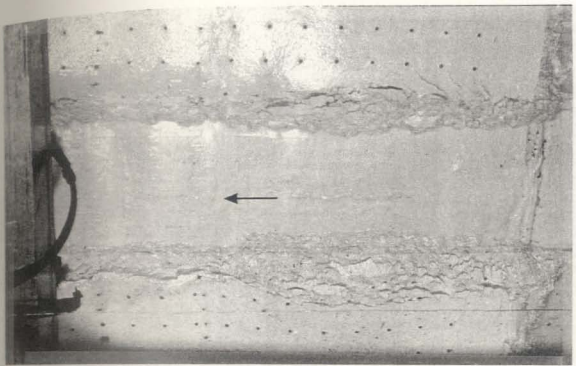


Figure 4.28 Top : Plan view photograph of model scour created in Test 05; Bottom : Plan view drawing illustrating scour surface features

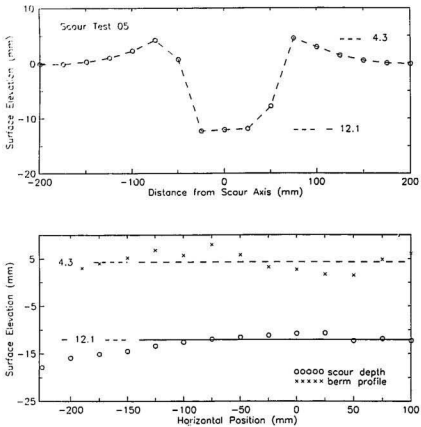


Figure 4.29 Top : Average cross - section surface profile for steady - state region of Test 05 scour; Bottom : Axial section plot of measured scour depths and berm elevations

scale. The corresponding average berm elevation was 4.3 mm. The sidewalls were caved along the entire length of the scour, and considerable surface heave was measured adjacent to the incision. Loose or remoulded material due to berm formation and caving was observed to a maximum distance of approximately 20 mm from the scour edges, and decreased in lateral extent beyond the first model pipeline cross - section. A linear

depression was associated with the trench location of the shallower second model pipeline, suggesting some local movement of the segment during the scouring event. A frontal mound of spoil material extended to a maximum distance on the order of 20 mm beyond the final point of contact with the scouring face of the model iceberg. The support apparatus served to limit vertical movement of the model to less than approximately 4 mm below the scouring level at the end of the event.

Figure 4.30 provides a summary of the pore water pressure responses recorded during the Test 05 scouring event. The measured locations of the transducers are given in Table 4.9, along with the peak and minimum pore pressures developed as scouring progressed. Figure 5E.1 displays the spatial distribution of the excess pore pressures at 50 mm intervals of horizontal movement along the scour path. The effects of the scouring event were initially recorded as negative excess pore pressures at a prototype horizontal distance on the order of 25 m from the current position of the model iceberg. The maximum rise in pore pressure measured within the apparent steady - state region of scouring was 108 kPa for a transducer (PPT 07) located 2.5 m below the initial clay surface, and 4.1 m laterally outward from the scour axis (at prototype scale). The peak response was recorded when the model was at a horizontal distance of 3.5 m ($dx = - 35$ mm) from the transducer position. The maximum pore suction measured was 44 kPa for the same device, when the model was at a horizontal distance of 10.6 m ($dx = - 106$ mm) from the transducer position.

Figure 4.31 shows a plot of the resultant forces acting at the model iceberg - soil interface versus the horizontal position of the model. The Test 05 force data are also listed in Table 4.10 at 50 mm intervals of model horizontal movement. In addition, the

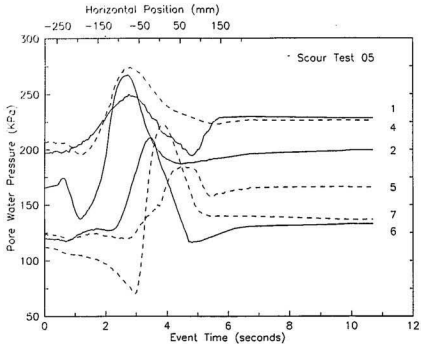


Figure 4.30 Test 05 pore pressure responses during event for seven transducer channels

results are presented graphically in Figure 4.32, which displays the model iceberg orientation and the system of forces acting on the model at various horizontal positions. In this test, the vertical force component was about 3.4 times as large as the horizontal component, and the resultant forces remained relatively constant within the apparent steady - state region of scouring. The average magnitudes of the vertical and horizontal components in this region were 16.9 and 5.0 MN respectively at prototype scale. The effective attack angle of the model increased at the beginning of the event to a maximum value of 17.8 degrees, and then decreased to an approximate steady value of about

Table 4.9 Top : Test 05 measured pore pressure transducer locations; Bottom : Maximum and minimum excess pore pressures and horizontal distance from model

PPT No.	x (mm)	y (mm)	z (mm)	w (mm) ¹
1	0	- 11	122	80.0
2	- 131	- 7	89	79.9
3	- 14	- 1	94	80.0
4	- 134	- 9	133	79.9
5	6	- 8	60	80.0
6	- 6	- 57	45	80.4
7	23	41	25	80.2
8	3	- 152	35	83.0
9	0	407	- 3	101.3

¹ w = free water depth at position

PPT No.	u_1 (KPa)	max. du (KPa)	dx (mm)	min. du (KPa)	dx (mm)
1	196	53	- 100	- 2	+ 75
2	165	102	+ 27	- 28	- 90
4	206	68	+ 38	- 11	- 87
5	127	57	+ 34	- 8	- 252
6	120	90	- 36	- 4	+ 81
7	114	108	- 35	- 44	- 106
8	121	43	- 58	- 2	+ 105

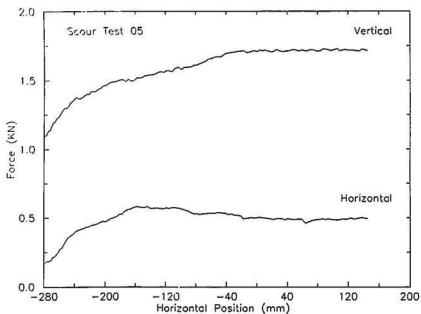


Figure 4.31 Test 05 horizontal and vertical components of the resultant force plotted against model horizontal position

16.4 degrees, on average, over the latter portion of the scouring event. The inclination of the resultant force vector did not vary significantly from the perpendicular to the inclined face of the model, as scouring progressed. The position of the force vector increased at the start of the event to a peak distance of 30 mm or 3.0 m at prototype scale from the model iceberg inflection line, and then reduced toward an average value of about 2.6 m near to the end of the event.

Interface pressures measured at the horizontal base (IPT 18) and inclined scouring face (IPT 19 and 20) of the model iceberg are shown in Figure 5C.2. The data acquired from the transducers situated at the scouring face of the model, described an irregularly

Table 4.10 Test 05 resultant force data tabulated for different model horizontal positions

Horiz. Pos. (mm)	Horiz. Force (N)	Vert. Force (N)	Total Force (N)	Vector Angle (deg)	Attack Angle (deg)
- 250	338.2	1302	1345	75.4	16.9
- 200	472.2	1464	1538	72.2	17.4
- 150	574.5	1526	1631	69.4	17.8
- 100	566.4	1580	1679	70.3	17.0
- 50	538.2	1672	1756	72.1	16.8
0	499.8	1706	1778	73.7	16.4
+ 50	487.3	1720	1788	74.2	16.3
+ 100	486.6	1720	1787	74.1	16.3
+ 145	491.9	1713	1783	74.0	16.3
Average ¹	504.9	1694	1768	73.4	16.4

¹ Average values for approx. steady state region : $x = - 100$ to 150 .

varying response with a peak recorded pressure of 256 kPa. The pressure acting on the inclined face decreased to a constant value of about 173 kPa near to the end of the event. The pressure record for the transducer located at the base of the model indicated a relatively steady response over the duration of the event, with minor fluctuations about an average pressure of approximately 151 kPa. It should be noted that due to angular rotation experienced by the model, the bottom face was slightly inclined relative to the horizontal, as illustrated in Figure 4.32.

A plan view drawing of surface displacement vectors at positions external to the Test 05 scour incision is displayed in Figure 4.33, together with a summary plot showing the average values of the horizontal and lateral components of displacement for the

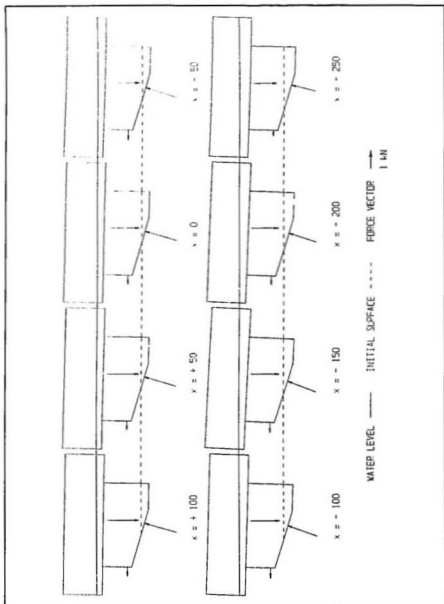


Figure 4.32 Test 05 model iceberg orientation and resultant force vectors

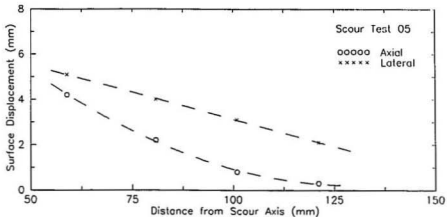
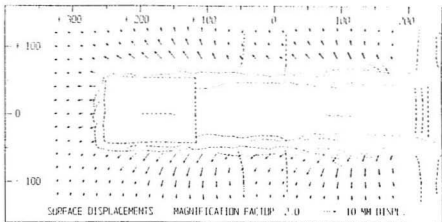


Figure 4.33 Top : Test 05 plan view drawing of surface displacement vectors; Bottom : Average axial and lateral surface displacements versus distance from the scour axis

apparent steady - state region of scouring. At lateral positions about 1 m from the edge of the scour, the average horizontal and lateral displacements were 0.42 and 0.51 m respectively at prototype scale. The surface displacements diminished with distance from the scour axis to values of 0.03 and 0.21 m at lateral positions approximately 7 m from the scour edge (i.e. 120 mm from the scour axis at model scale). Qualitative evaluation

of radiographic evidence, as presented in Figure 5F.1, indicated that the majority of surface markers within the scour were displaced horizontally forward and vertically downward below the scour, and underwent relatively limited lateral movement. Quantitative assessment of these displacements was precluded by the large movements experienced by some of the internal markers.

Figure 5F.1 provides a trace from plan view radiographs of the clay specimen, which displays the locations of pore pressure transducers, model pipeline segments, and the displaced configuration of soil deformation grids. The traces of cross - sectional radiographs are given in Figure 5F.2, at two horizontal positions corresponding with the lateral grid and model pipeline locations. Figures 5F.3 and 5F.4 show traces of the axial section grids situated near to the beginning of the scour, and at the final horizontal position of the model iceberg.

Test 05 sub - surface displacements are illustrated in Figure 5F.5 including initial / displaced plots and displacement vector plots for each of the grids installed within the clay specimen. Figure 4.34 shows the initial and displaced configuration of the second lateral grid ($x = + 41$ mm) in both cross - sectional and plan view. The lateral component of soil displacement was small in this test, and significant movements were limited to the vicinity of the edges of the scour. The vertical component of displacement was relatively extensive; downward movements were recorded over the entire depth of the emplaced grids, at positions directly below the scour incision. The vertical displacements were consistent across the width of the scour and gradually attenuated with depth beneath the incision. The horizontal displacement component was larger than the vertical component immediately below the scour; however, the horizontal

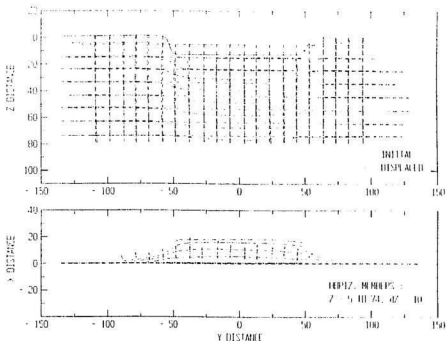


Figure 4.34 Test 05 initial / displaced plot of lateral grid at $x = + 41$ shown in cross - section and plan view

displacement gradient was also steeper, and movements were restricted to shallower depths. The initial / displaced plot for the axial grid situated at the final position of the model iceberg is shown in Figure 4.35. The results from this grid also suggest a dominant vertical direction of displacement; although, this may be partially attributable to the effects of limited vertical movement of the model associated with the discontinuation of scouring.

Figure 4.36 provides a summary of the sub - surface displacement measurements for Test 05, presented as profiles of the maximum (below scour) values of the vertical and horizontal displacement components. The displacements shown in this plot were

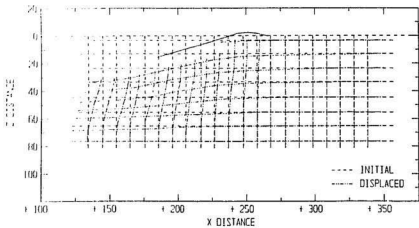


Figure 4.35 Test 05 initial / displaced plot of axial grid located at final horizontal position of model iceberg

evaluated as the average of results from both axial and lateral grids within the apparent steady - state region of scouring. The horizontal displacement results derived from axial and lateral grid measurements were relatively consistent in this test. The maximum values of vertical and horizontal displacement immediately below the base of the scour (interpolated at a depth below base = 0.1 m) were 0.88 and 1.29 m respectively at prototype scale. The limiting depths at which vertical and horizontal components of displacement were measured, determined for a lower bound displacement magnitude of 0.2 m, were 6.2 and 3.0 m respectively at prototype scale. The vertical and horizontal displacements extended to normalized values on the order of 5.1 and 2.5 scour depths below the base of the scour. Model pipeline segments situated at prototype depths of approximately 1.5 and 0.6 m beneath the scour base, did not experience any measurable plastic deformation in this test.

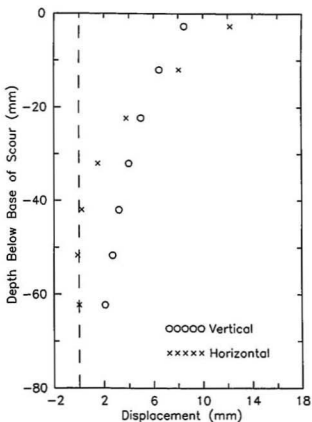


Figure 4.36 Test 05 maximum vertical and horizontal components of soil displacement versus depth below scour base

4.3.6 Scour Test 06

Model Input Conditions

The Test 06 input conditions, summarized in Figure 6A.1 in the corresponding section of Appendix A, were identical to the Test 05 case, with the exception of the initial stress

state of the clay specimen. In Test 06, the clay was consolidated in the laboratory under an increased vertical effective stress of 200 kPa. The width of the model iceberg was 100 mm, the attack angle was 15 degrees, and the model vertical stiffness was 61 N/mm, coinciding with the Test 04 and 05 configuration. The nominal depth of free surface water was also retained at 80 mm in this test. In addition, the Test 06 arrangement of instrumentation, deformation markers, and model pipeline segments, shown in Figure 6A.2, was not altered from the layout used in the succeeding test. The elevation of the support apparatus was changed slightly to accommodate the expected model vertical position at the end of the scouring event.

The experimental methods employed to assess undrained shear strength included both in - flight vane shear testing and post - test moisture content measurements. In Figure 6B.1, the experimentally derived c_u values are compared with strength estimates based on Equations 4.2 and 4.3. Vane tests were performed at three horizons : 30, 60, and 90 mm below the clay surface. Test results are given in Figure 6B.2, which shows plots of vertical displacement, rotation, and torque against time, in addition to torque versus rotation curves evaluated for each level. As depicted in Figure 6B.1, the vane test data implied a more rapid increase in strength with depth in comparison against other predictions. The measured vane strength was 20.1 kPa at a prototype depth of 3.0 m, as compared with an estimate of 22.3 kPa derived in accordance with the empirical relation given by Equation 4.2. At a prototype depth of 9.0 m, the vane strength increased to an apparent value of 40.7 kPa, whereas the corresponding empirical strength estimate was 30.9 kPa for this test level. Surface water access to the vane head may have diminished with depth below the clay surface, resulting in more realistic determinations of the peak

undrained shear strength. Furthermore, the shaft resistance of the vane apparatus, deducted in the assessment of the vane shear strength, may have been more significantly underestimated for tests undertaken at greater depths. In contrast, the undrained shear strength predictions based on moisture content measurements were relatively consistent with depth but were also larger than anticipated for post - test conditions.

Test Results

Figure 6C.1 displays the consolidation records for Test 06, as plots of pore pressure against time and clay surface settlement versus the square root of time. Some electrical noise was evident on consolidation pore pressure transducer signals; however, this problem was resolved prior to the inception of the scouring event. A time period of about 5.2 hours was required to complete greater than 95 percent of primary consolidation, preceding vane test implementation. The apparent initial clay surface settlement was 2.3 mm during the consolidation phase of the test.

The model scouring event was initiated subsequent to the completion of vane testing. Malfunction of the drive system produced an interruption in model motion during the event, followed by movement at a substantially reduced rate. The model iceberg was initially advanced over a horizontal distance of 161 mm in a time period of 3.1 seconds, at an average scouring rate of 60.3 mm/s. The instrument outputs recorded during this initial section of the event are shown plotted versus time in Figure 6C.2A. Model movement was then resumed at a diminished rate of 0.53 mm/s after a delay of about 33 seconds. The additional time required to complete the event was about 468 seconds during which the model traversed a further distance of 257 mm. Figure 6C.2B provides

a summary of the test instrumentation outputs for this final section of the event, plotted against time and horizontal position. Due to the decreased scouring velocity, the effects of drainage must be given consideration in the interpretation of test results.

A photograph and corresponding plan view drawing of the scour created in Test 06 are presented in Figure 4.37. An average cross - section surface profile for the apparent steady - state region, and an axial plot of scour depths and berm elevations are given in Figure 4.38. Surface profile data are also displayed in Figure 6D.1, as cross - sectional plots at 50 mm intervals of horizontal position. The Test 06 scour was characterized by extensive loose berm and caved sidewall material. A large amount of surcharge was built - up at the front and sides of the advancing model iceberg. This material was displaced horizontally during the event and deposited as a mound which extended to about 55 mm in front of the final model position. The scour incision was relatively uniform in appearance after an equilibrium scour depth of 16.3 mm or 1.63 m at prototype scale had been established. The corresponding berm elevations averaged 5.8 mm above the original surface level; peak elevations coincided with an initial region of significant surface heave adjacent to the scour, possibly attributable to effects associated with the transition to a reduced scouring rate. The sidewalls were caved along the entire length of the scour, and surface soil disturbance was evident to a maximum distance of about 25 mm laterally outward from the edges of the scour incision.

The Test 06 pore water pressure responses are shown in Figure 4.39, as recorded during the final section of the scouring event at the reduced rate of model iceberg movement. Table 4.11 lists the measured locations of the pore pressure transducers, together with the corresponding peak and minimum pore pressure values, as recorded

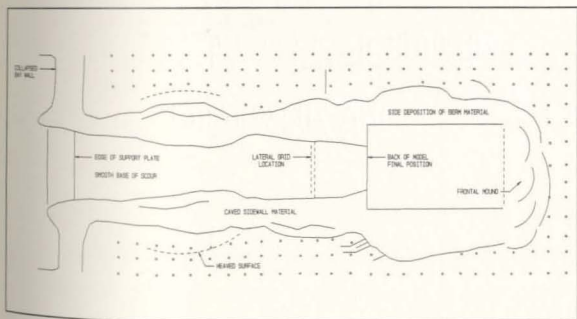
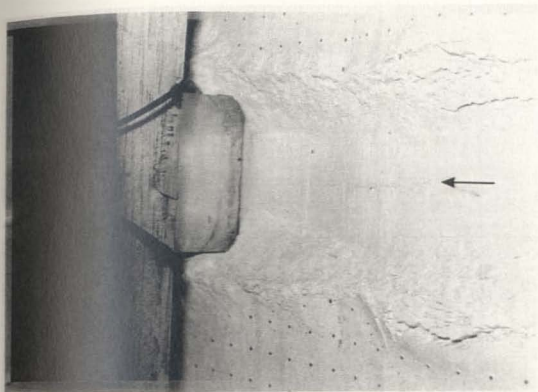


Figure 4.37 Top : Photograph of model scour created in Test 06 - view in direction of travel;
 Bottom : Plan view drawing illustrating scour surface features

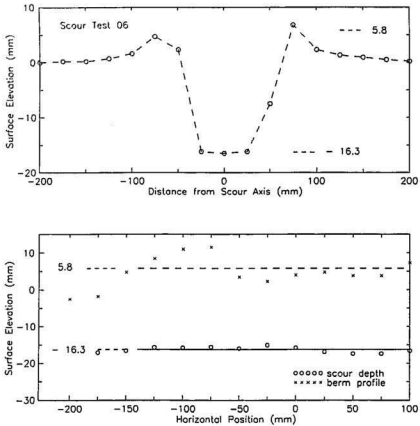


Figure 4.38 Top : Average cross - section surface profile for steady - state region of Test 06 scour; Bottom : Axial section plot of measured scour depths and berm elevations

over the entire duration of the scouring episode. The spatial distribution of pore pressure change is depicted in Figure GE.1 at 50 mm intervals of model horizontal movement. PPT Channel 06 and 08 responses at the completion of consolidation were inconsistent with expected equilibrium pore pressures and, therefore, the test records for these transducers were deemed unreliable. The effects of scouring were initially observed at

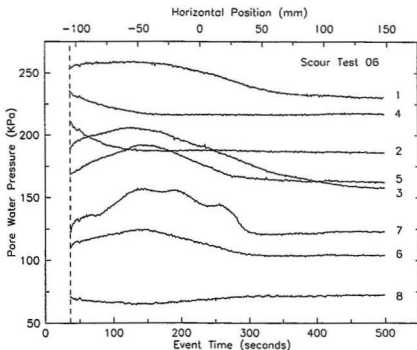


Figure 4.39 Test 06 pore pressure responses plotted for final section at reduced rate

a prototype horizontal distance approximately 25 m from the current model position. In the apparent steady - state region associated with the final section of the event at reduced scouring rate, the maximum recorded increase in pore pressure was 43 kPa for a transducer (PPT 07) located at a depth 3.8 m below the initial clay surface, and 2.2 m laterally outward from the scour axis (at prototype scale). The maximum excess pore pressure was observed when the model was at a horizontal distance of approximately 3.5 m ($dx = -35$ mm) from the transducer position. A similar peak response was recorded by a transducer (PPT 05) situated at a depth of 6.9 m and 0.8 m laterally

Table 4.11 Top : Test 06 measured pore pressure transducer locations; Bottom : Maximum and minimum excess pore pressures and horizontal distance from model

PPT No.	x (mm)	y (mm)	z (mm)	w (mm) ¹
1	- 3	0	142	80.0
2	- 132	- 2	90	79.9
3	- 10	1	87	80.0
4	- 132	- 2	132	79.9
5	0	- 8	69	80.0
6	1	- 40	70	80.2
7	- 9	22	38	80.1
8	8	- 239	40	87.3
9	0	407	- 3	101.3

¹ w = free water depth at position

PPT No.	u_i (KPa)	max. du (KPa)	dx (mm)	min. du (KPa)	dx (mm)
1	226	34	- 53	-	-
2	175	91	+ 10	- 39	- 73
3	166	40	- 39	-	-
4	213	36	+ 5	-	-
5	149	43	- 40	- 17	- 135
6	96	29	- 45	-	-
7	114	43	- 35	- 2	- 242
8	76	3	- 171	- 12	- 54

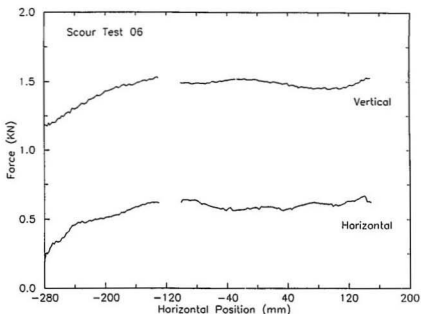


Figure 4.40 Test 06 horizontal and vertical components of the resultant force plotted against model horizontal position

outward from the scour axis (at prototype scale). A maximum pore suction of about 17 kPa was measured at this same transducer position, when the model was at a horizontal distance of 13.5 m ($dx = -135$ mm).

The resultant forces acting at the model iceberg - soil interface during the scouring event are plotted against the model horizontal position in Figure 4.40. The break in plotted data is associated with the interruption in model motion and the transition to a reduced scouring rate over the final section of the event. Table 4.12 provides a listing of the force data at 50 mm intervals of model horizontal movement. Figure 4.41 illustrates the model iceberg orientation and the system of forces acting on the model at

Table 4.12 Test 06 resultant force data tabulated for different model horizontal positions

Horiz. Pos. (mm)	Horiz. Force (N)	Vert. Force (N)	Total Force (N)	Vector Angle (deg)	Attack Angle (deg)
- 250	399.0	1270	1331	72.6	16.1
- 200	512.8	1430	1520	70.3	16.0
- 150	604.9	1504	1621	68.1	15.9
- 100	626.1	1488	1615	67.2	15.5
- 50	572.9	1506	1611	69.2	15.5
0	583.6	1513	1622	68.9	15.4
+ 50	591.8	1471	1585	68.1	15.4
+ 100	592.3	1460	1576	67.9	15.8
+ 150	621.8	1529	1650	67.9	15.7
Average ¹	604.2	1487	1605	67.9	15.6

¹ Average values for approx. steady state region : $x = - 100$ to 150 .

different horizontal positions along the scour path. In this test, a substantial quantity of surcharge material was developed at the front and sides of the model, and was displaced horizontally with the model during the event. The resultant forces did not vary significantly over the final section of the event, and the vertical component of the force was about 2.5 times as large as the measured horizontal component. The average prototype magnitudes of the vertical and horizontal components were 14.9 and 6.0 MN respectively for the apparent steady - state region of scouring. The effective attack angle increased initially to a maximum value of 16.5 degrees, and then reduced to a relatively consistent orientation with an average angle of 15.6 degrees during the final section of the event. The inclination of the resultant force vector also remained relatively constant at an angle approximately 6 degrees from the perpendicular to the scouring face. The

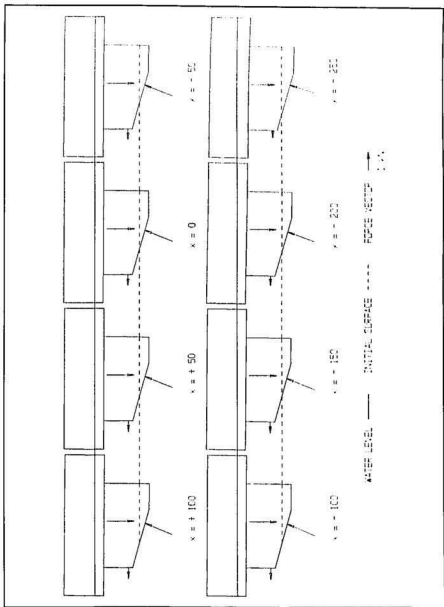


Figure 4.41 Test 06 model iceberg orientation and resultant force vectors

position of the force vector increased initially and then retained a steady value during the final section of the event, at a prototype distance of 2.5 m from the model iceberg inflection line.

The interface pressure responses at the horizontal base (IPT 18) and inclined scouring face (IPT 19 and 20) of the model iceberg are shown in Figures 6C.2A and 6C.2B. The maximum total pressures acting at these locations were approximately 207 and 230 kPa respectively, as measured at the completion of the initial section of rapid model movement. The pressures recorded during subsequent scouring at the reduced rate were irregularly varying, conceivably as the result of surcharge build-up in front of the advancing model, and the intermittent deposition of berm material. Over the final section of the event, the average pressure was 172 kPa at the base of the model. The average pressure at the scouring face of the model was 189 kPa, with recorded variations as large as 15 percent of the mean value. The period of fluctuation of the pressure response also corresponded approximately with changes in the horizontal force record for the event.

Figure 4.42 shows a plan view drawing of surface displacement vectors at positions external to the Test 06 scour incision, and also displays a plot of the average magnitudes of horizontal and lateral components of displacement for the apparent steady-state region. In this test, surface displacement magnitudes varied considerably for different horizontal positions along the scour path. Maximum lateral movements coincided with the region at which model iceberg movement was suspended prior to transition to the reduced scouring rate. Most surface markers situated at a lateral position 1 m from the edge of the scour incision were obscured by berm deposition or caved

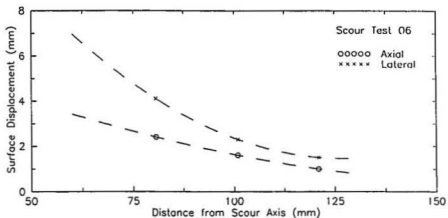
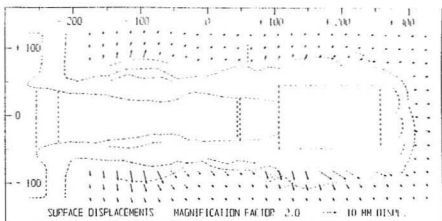


Figure 4.42 Top : Test 06 plan view drawing of surface displacement vectors; Bottom : Average axial and lateral surface displacements versus distance from the scour axis

sidewall material. The average horizontal and lateral surface displacements recorded at a distance of about 3 m from the scour edge were 0.24 and 0.41 m respectively at prototype scale. At lateral positions approximately 7 m from the scour edge (120 mm from the scour axis at model scale) the horizontal and lateral displacements declined to average values of 0.10 and 0.15 m respectively. The movement of surface markers

within the scour may be qualitatively evaluated from radiographic evidence, as shown in Figure 6F.1. Some of the internal markers, located within the initial region of model movement preceding the reduction in scouring rate, underwent large lateral movements and were deposited along the sides of the scour incision. However, the majority of the internal markers were displaced horizontally with surcharge material amassed in front of the advancing model, and were deposited within the mound of material in front of the model at its final position.

The plan view trace compiled from radiographs of the Test 06 scour is shown in Figure 6F.1, including the displaced configuration of soil deformation grids and the locations of pore pressure transducers and model pipeline segments. Figure 6F.2 displays the traces of cross-sectional radiographs at two different horizontal positions, which convey similar information at each of the lateral grid and model pipeline locations. The radiograph trace of the axial grid situated near to the beginning of the scour is shown in Figure 6F.3. Due to its location, the displaced configuration of the grid shown in this trace was influenced in part by the initial section of rapid model iceberg movement. The trace of an axial radiograph showing the grid located at the final horizontal position of the model is presented in Figure 6F.4.

The initial / displaced plots and displacement vector plots derived from the soil deformation grids installed within the Test 06 specimen are given in Figure 6F.5. Similar plots were not presented for the initial axial grid (Figure 6F.3); quantitative assessment of displacements from this grid was impeded by the reliability of the radiographic evidence, since final locations of the surface level and top horizontal member of the grid were unclear. The sub-surface displacements evaluated from other grids represented the

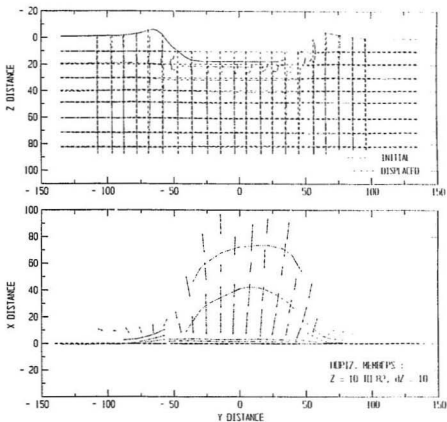


Figure 4.43 Test 06 initial / displaced plot of lateral grid at $x = +54$ shown in cross - section and plan view

effects of a drained or partially drained scouring condition due to the reduced rate of model movement over the final section of the event.

In general, the displacement patterns observed in this test were dissimilar to the results from preceding experiments. Figure 4.43 shows the initial and displaced configuration of the second lateral grid ($x = +54$ mm) in both cross - sectional and plan view. The lateral component of displacement was large within a relatively shallow region

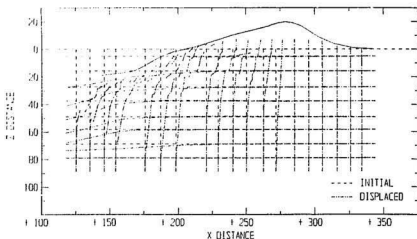


Figure 4.44 Test 06 initial / displaced plot of axial grid located at final horizontal position of model iceberg

immediately beneath the scour incision, and also at positions adjacent to the scour edges. In contrast with prior test observations, the vertical component of displacement measured below the scour was relatively small or negligible. The horizontal component of displacement was very large at positions above or immediately below the base of the scour; however, significant horizontal movements were also limited to shallow depths. It should be noted that the top horizontal member shown in the plan view plot of Figure 4.43 was displaced horizontally from the first lateral grid at $x = -23$ mm. This evidence suggests the development of a relatively stable region of frontal material which moved concurrently with the advancing model iceberg. Figure 4.44 shows the initial / displaced plot for the axial grid located at the final position of the model iceberg. Local vertical displacement of horizontal members at the beginning of the grid was inconsistent with other deformation data, and may be attributable in part to manual

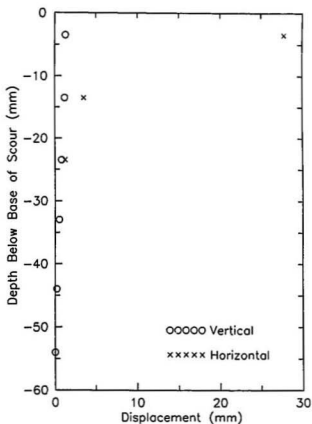


Figure 4.45 Test 06 maximum vertical and horizontal components of soil displacement versus depth below scour base

disturbance during placement. The assessment of displacement vectors indicated a shallow region of large horizontal movements; however, the displaced configuration of vertical members displayed the development of thin zones of shearing or failure surfaces which may be indicative of deep - seated soil deformation.

The sub - surface displacement records for Test 06 are summarized in Figure 4.45

as profiles of the maximum values of vertical and horizontal components of displacement. The plotted magnitudes were evaluated as the average of results from the two lateral grids, which were located within the apparent steady - state region of scouring. The maximum values of vertical and horizontal displacement immediately below the base of the scour (interpolated at a depth below base = 0.1 m) were 0.15 and 3.39 m respectively at prototype scale. The maximum depth below the base of the scour at which horizontal displacements were recorded, evaluated for a lower bound displacement magnitude of 0.2 m, was 2.0 m at prototype scale. The magnitudes of vertical displacement were less than 0.2 m at all measured positions below the scour base. Therefore, for an assumed lower bound of 0.2 m, the vertical and horizontal displacements extended to normalized values of zero and 1.3 scour depths below the base of the scour. Model pipeline segments situated at prototype depths of approximately 1.3 and 0.4 m beneath the scour base, did not undergo any measurable plastic deformation in this test.

4.3.7 Scour Test 07

Model Input Conditions

The Test 07 model iceberg configuration and input parameters are presented in Figure 7A.1 in the corresponding section of Appendix A. A photograph of the instrumented model iceberg used in this test is shown in Figure 3.8. As described in Section 3.3.2, two linear position sensors were installed on the model to allow for redundant measurements of vertical position during the scouring event. The input

conditions were altered from the Test 05 baseline case by reduction of the model width to a value of 50 mm or 5 m at prototype scale. The buoyant weight and vertical stiffness of the model were also reduced by half relative to baseline conditions, in order to maintain similar applied stress levels to ensure a comparable depth of scouring. The attack angle of the model was set at 15 degrees, and the model vertical stiffness was 31 N/mm in free water of nominal 80 mm depth. The clay laboratory pre - consolidation stress was 140 kPa, coinciding with the initial stress state for the Test 05 specimen.

Figure 7A.2 shows elevation and plan view drawings of the Test 07 layout of instrumentation, deformation markers, and model pipeline segments. The arrangement was modified to include only one lateral soil deformation grid and model pipeline segment, at a horizontal position within the expected steady - state region of scouring. In addition, the length of the axial grid at the final location of the model iceberg was extended. These changes were implemented in order to reduce disturbance associated with excavation and backfill of two cross - sectional trenches, and to facilitate improved investigation of deformation fields at both the axial and lateral grid locations.

Estimated undrained shear strength profiles for the Test 07 specimen are presented in Figure 7B.1. In - flight vane shear tests were conducted at three depths : 30, 60, and 90 mm below the clay surface. The vane test data are shown in Figure B.2, including vertical displacement, rotation, and torque history plots, in addition to the torque versus rotation curves for each level. In Figure 7B.1, c_u values derived from experimental methods are compared with strength estimates based on Equations 4.2 and 4.3. A higher gradient of undrained shear strength with depth was predicted in accordance with the results from vane testing. At a prototype depth of 3.0 m, the measured vane strength was

20.1 kPa, as compared with the strength value of 17.3 kPa based on the empirical relation given by Equation 4.2. At greater depths, significantly higher strength magnitudes were predicted from vane test results. The vane shaft resistance appeared to be underestimated, which implied higher predicted peak torque values due to the vane head alone, than were actually mobilized during testing. The undrained shear strength estimates from moisture content measurements were also higher than expected for post - test conditions, and exceeded the strength values determined using Equations 4.2 and 4.3.

Test Results

The consolidation records for Test 07 are given in Figure 7C.1 as plots of pore pressure against time and clay surface settlement versus the square root of time. The clay specimen was permitted to consolidate over a time period of about 5.1 hours in order to ensure the establishment of equilibrium conditions. The apparent initial clay surface settlement was 1.9 mm, following the completion of greater than 95 percent of primary consolidation. The instrumentation outputs for the scouring event are presented in Figure 7C.2, plotted against time and horizontal position. The model iceberg travelled a total horizontal distance of 372 mm in a time period of 4.8 seconds, at an average scouring rate of 77.8 mm/s. The model became laterally unstable from the outset of the event, resulting in rotational movement (roll) about the x - axis. The resultant lateral inclination of the scour incision increased gradually with the horizontal distance travelled by the model.

Figure 4.46 shows a plan view photograph and related drawing illustrating surface features of the scour created in Test 07. Figure 4.47 displays an average cross - section

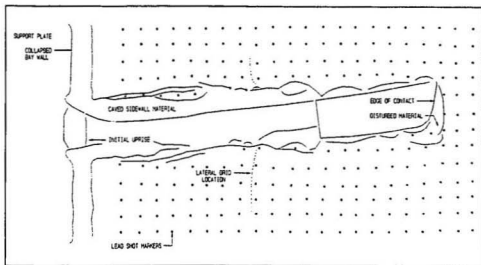
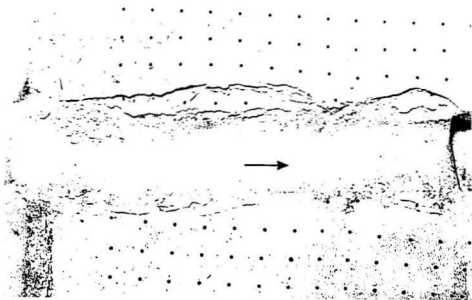


Figure 4.46 Top : Plan view photograph of model scour created in Test 07; Bottom : Plan view drawing illustrating scour surface features

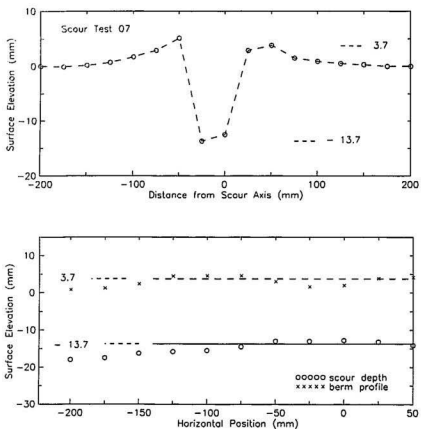


Figure 4.47 Top : Average cross - section surface profile for steady - state region of Test 07 scour; Bottom : Axial section plot of measured scour depths and berm elevations

surface profile of the scour, as well as an axial plot of scour depths and berm elevations. The surface relief in the vicinity of the scour is further described in Figure 7D.1, which depicts cross - sectional profiles at 50 mm intervals of horizontal position. The assessment of scour depths was hindered by the narrow scour width and caved sidewall material within the incision, as well the lateral inclination of the scour base due to tilt of

the model. The average scour depth was 13.7 mm or 1.37 m at prototype scale, as estimated for the apparent steady - state region of scouring. The corresponding average berm elevation was 3.7 mm, including heave of the surface adjacent to the scour and limited remoulded berm material. The lateral inclination of the scour base was about 3 to 5 degrees on average, at measured cross - sections. The sidewalls of the incision were caved along the entire length of the deeper scour edge, and over segments of the shallow edge near to the beginning and end of the scour. Surface soil disturbance was observed to a maximum distance of about 17 mm from the scour edges. A local depression and associated reduction in berm elevation were evident in the vicinity of the model pipeline segment, indicative of displacement of the segment during the event. The model was unsupported at the completion of the event, and experienced large vertical movement as would be associated with bearing failure of the underlying material. At the shallow edge of the incision, surface soil disturbance extended to approximately 30 mm beyond the final boundary of contact with the inclined face of the model. A limited amount of loose berm material was also deposited along the sides of the model at the final horizontal position.

The pore water pressure responses recorded during the Test 07 scouring event are summarized in Figure 4.48. PPT Channel 06 and 08 pore pressures were inconsistent with expected equilibrium values and, therefore, test records acquired from these devices may be unreliable. Furthermore, the results from PPT 05, which implied a relatively limited response over the duration of the event, were incompatible with the measurements from other devices. The final locations of the transducers are indicated in Table 4.13, as well as the peak and minimum pore pressure changes developed as scouring progressed.

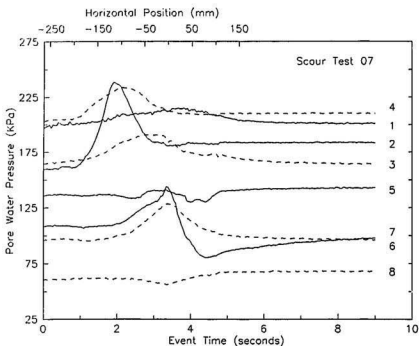


Figure 4.48 Test 07 pore pressure responses during event - transducer channels 01 to 08

Figure 7E.1 displays the spatial distribution of excess pore pressures at 50 mm intervals of model horizontal movement. The effects of scouring were initially recorded at a prototype horizontal distance on the order of 20 m in front of the current model iceberg position. The scour - induced pore pressure response was small or negligible for a transducer (PPT 08) situated at lateral distance of 15.0 m from the scour axis. The maximum rise in pore pressure measured within the apparent steady - state region of scouring was 35 kPa for a transducer (PPT 07) located 3.0 m below the initial clay surface, and 5.1 m laterally outward from the scour axis (at prototype scale). The peak

Table 4.13 *Top : Test 07 measured pore water pressure transducer locations; Bottom : Maximum and minimum excess pore pressures and horizontal distance from model*

PPT No.	x (mm)	y (mm)	z (mm)	w (mm)
1	- 13	- 13	126	80.0
2	- 156	5	79	79.9
3	- 11	6	91	80.0
4	- 123	4	131	79.9
5	- 1	- 6	60	80.0
6	- 5	- 33	70	80.1
7	- 5	51	30	80.3
8	0	- 150	38	82.9
9	0	403	- 3	100.9

¹ w = free water depth at position

PPT No.	u_1 (KPa)	max. du (KPa)	dx (mm)	min. du (KPa)	dx (mm)
1	197	18	+ 53	-	-
2	159	79	+ 22	-	-
3	165	26	- 52	-	-
4	203	31	+ 6	-	-
5	136	5	- 7	- 6	- 59
6	95	33	+ 6	-	-
7	108	35	+ 4	- 28	+ 97
8	61	-	-	- 5	- 1

response was recorded when the model was at a horizontal position ($dx = + 4 \text{ mm}$) which was approximately coincident with the location of the transducer. The maximum pore suction measured was 28.0 kPa for the same device, following movement of the model to a horizontal distance of 9.7 m ($dx = + 97 \text{ mm}$) beyond the transducer position.

Figure 4.49 shows a plot of the vertical component of the resultant forces acting at the model iceberg - soil interface versus the horizontal position of the model during the Test 07 scouring event. The average magnitude of the vertical component within the apparent steady - state region of scouring was 7.8 MN at prototype scale. The linear position sensors installed to measure the model vertical position in this test, did not retain contact with the reference guide rail, due to compression at the test acceleration level and the unanticipated lateral tilt of the model. In addition, the tension load cell, used to measure the horizontal component of the resultant scour force, malfunctioned as the result of apparent water damage to the sensor (see Figure 7C.2). Therefore, the available data on model orientation and resultant forces were limited to the vertical position and the associated vertical component of the resultant force developed during the event.

Interface pressures measured at the horizontal base (IPT 18) and at the inclined scouring face (IPT 19) of the model iceberg are shown in Figure 7C.2. The response at the base of the model indicated relatively low total pressures of about 115 kPa on average, with irregular fluctuations as large as 35 percent of the mean value. The average total pressure measured at one side of the scouring face of the model was approximately 200 kPa over the initial 260 mm of model horizontal movement, with a maximum recorded value of 254 kPa. The pressure response along this side of the scouring face

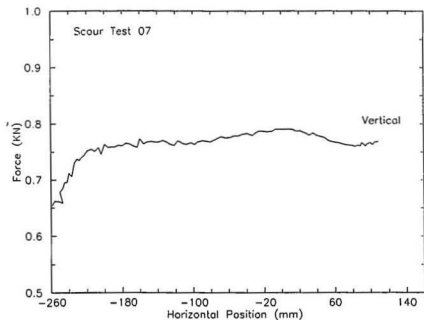


Figure 4.49 Test 07 vertical component of the resultant force plotted against model horizontal position; approx. steady - state region : $x = -100$ to 50 .

declined significantly over the final portion of the scouring event as a result of the lateral inclination of the model.

A plan view drawing of surface displacement vectors at positions external to the Test 07 scour is presented in Figure 4.50, together with a plot of the average values of the horizontal and lateral components of displacement for the apparent steady - state region of scouring. The surface displacement field was not symmetric about the scour axis, and larger lateral movements were measured at positions adjacent to the shallow edge of the scour. The average horizontal and lateral displacements were approximately 0.46 and 0.56 m respectively at prototype scale, at lateral positions about 1 m from the

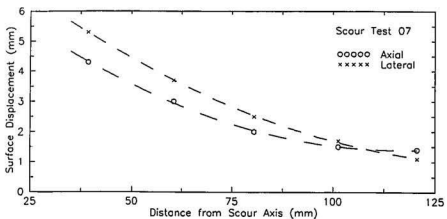
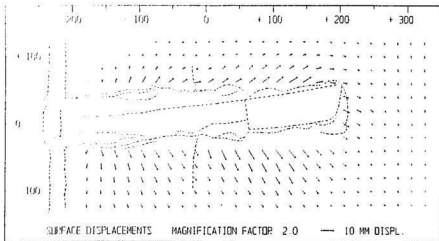


Figure 4.50 Top : Test 07 plan view drawing of surface displacement vectors; Bottom : Average axial and lateral surface displacements versus distance from the scour axis. The surface displacements reduced with distance from the scour axis to prototype magnitudes of 0.14 and 0.11 m, at lateral positions about 9.5 m from the scour edge (i.e. 120 mm from the scour axis at model scale). Qualitative assessment of the plan view radiograph trace shown in Figure 7F.1 implied that the majority of internal markers

were displaced vertically to positions beneath the scour and horizontally in the direction of travel, with only limited lateral movement.

Figure 7F.1 displays a trace assembled from plan view radiographs of the clay specimen, illustrating the locations of pore pressure transducers, the model pipeline segment, and the displaced configuration of soil deformation grids. The trace of a cross-sectional radiograph at the location of the lateral grid and model pipeline segment, is presented in Figure 7F.2. As shown in this figure, horizontal grid members were divided into smaller segments in this test in order to reduce influence on displacement patterns imposed by the measurement technique. Figure 7F.3 presents the trace of a radiograph which shows the axial grid situated near to the beginning of the scour. The axial grid at the final model iceberg position provided limited relevant data due to lateral deviation of the scour path resulting from tilt of the model.

Test 07 sub-surface displacement records are shown in Figure 7F.5 as initial / displaced plots and displacement vector plots for grids placed at different locations within the clay specimen. Figure 4.51 displays cross-sectional and plan views of the displaced configuration of the lateral soil deformation grid ($x = -25$ mm). In cross-section, the displacement pattern was comparable to a circular failure mechanism, with apparent rotational movement toward the shallow edge of the scour. The magnitude of the lateral component of soil displacement associated with the inclination of the scour may have been underestimated, as vertical grid members were unclear at near-surface positions. Both lateral and vertical movements were evident to within a shallow region below the base of the scour. Vertical movements varied with lateral position, from downward displacements at the deep edge of the scour, to upward heave adjacent to the

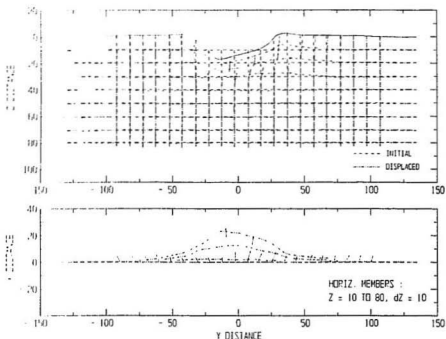


Figure 4.51 Test 07 initial / displaced plot of lateral grid at $x = -25$ shown in cross - section and plan view

shallow edge. The horizontal component of displacement was significantly larger than the vertical component; however, measurable horizontal and vertical displacements extended to similar depths beneath the scour base. The initial / displaced plot for the axial grid located near to the beginning of the scour is shown in Figure 4.52. The near - surface vertical displacements evaluated from the axial grid were inconsistent with measured scour depths, and may have been underestimated due to inaccurate definition of the surface level based on the radiographic evidence.

Figure 4.53 provides a summary of the Test 07 sub - surface displacement measurements, including profiles of the maximum values of the vertical and horizontal

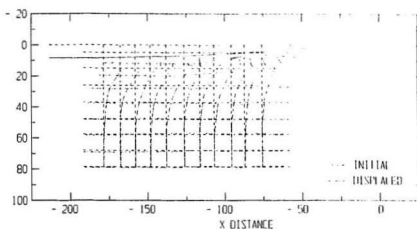


Figure 4.52 *Test 07 initial / displaced plot of axial grid located near beginning of scour*

displacement components. The displacements shown in this plot were assessed as the average of the limited available results from the lateral and axial grids, described above. The maximum values of vertical and horizontal displacement immediately below the base of the scour (interpolated at a depth below base = 0.1 m) were 0.62 and 1.46 m respectively at prototype scale. The limiting depths at which vertical and horizontal components of displacement were measured, evaluated for a lower bound displacement magnitude of 0.2 m, were 1.5 and 2.3 m respectively at prototype scale. The vertical and horizontal displacements extended to normalized values on the order of 1.0 and 1.6 scour depths below the base of the scour. The model pipeline segment located at a prototype depth of 0.63 m beneath the scour base exhibited modest vertical curvature following completion of the test, with a maximum centre - line deflection of approximately 1.3 mm at model scale.

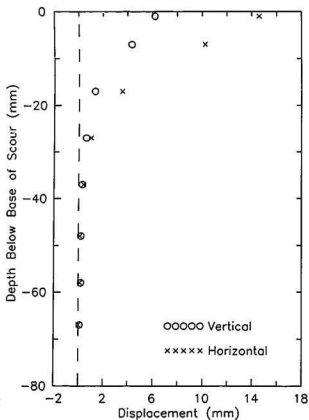


Figure 4.53 Test 07 maximum vertical and horizontal components of soil displacement versus depth below scour base

4.3.8 Scour Test 08

Model Input Conditions

In Test 08, the attack angle of the model iceberg was increased to 25 degrees, and this was the only proposed variation relative to Test 05 baseline conditions. The model

iceberg configuration and input parameters are summarized in Figure 8A.1, in the corresponding section of Appendix A. The width of the model was 100 mm, and the model vertical stiffness was 61 N/mm in free water of nominal 80 mm depth. The clay was consolidated in the laboratory under a uniform vertical effective stress of 140 kPa, to establish the same initial stress state as for the Test 05 specimen. The arrangement of instrumentation, deformation markers, and model pipeline segments, shown in Figure 8A.2, was not altered from the layout used in Test 07. The elevation of the support apparatus was reset in accordance with the expected vertical position of the model at the end of the scouring event.

Figure 3.8 shows a photograph of the instrumented model iceberg used in Test 08. It was required to compensate for the effects of the change in model geometry, to ensure that the values of other test variables were identical to baseline conditions. In order to retain a consistent magnitude and point of action of the buoyant weight, the mass distribution of the model was altered through re - design of the aluminum shell, and balsa wood pieces of prescribed dimensions were attached to the exterior of the model. In addition, the drive system pulling cable was connected to the inclined face of the model at a specified elevation, in order to preserve an identical point of action of the applied horizontal force. A further equipment modification was implemented to provide a redundant record of model vertical movements during the scouring event. To allow for measurements of vertical position, two displacement transducers were attached to the model and were placed in contact with a reference guide rail, as described in Section 3.3.2.

Figure 8B.1 shows estimated undrained shear strength profiles for the Test 08

clay specimen. In - flight vane shear test data were not acquired due to malfunction of the rotational drive motor of the device at the test acceleration level. The c_u values derived from moisture content determinations were significantly higher than strength estimates based on Equation 4.2, likely as the result of moisture content measurement inaccuracies. Undrained shear strengths evaluated by the use of a hand - operated vane (19 mm diameter by 30 mm length) after the completion of the test, were an average of 42 percent lower than values associated with the empirical relationship. The large discrepancy between post - test hand - vane predictions and the proposed in - flight strength profile may be expected due to possible air entry to the region of the vane test, shear distortion on unloading of the specimen, and water drawn into the clay to relieve pore suction set - up by stoppage of the centrifuge (Britto et al., 1981).

Test Results

Figure 8C.1 displays data acquired during consolidation of the Test 08 clay specimen, including plots of pore pressure against time and surface settlement versus the square root of time. A time period of 5.2 hours was required to achieve greater than 95 percent of primary consolidation. The apparent initial clay surface settlement was 0.4 mm during the consolidation phase of the test. The relatively small magnitude of consolidation settlement recorded in this test may be attributable to initial disturbance or local bearing failure at the position of displacement transducer contact with the specimen surface.

The fabrication of the Test 08 model iceberg was deficient due to porosity in the welds, which permitted water leakage to the interior of the aluminum shell. The model was verified as watertight at normal gravity levels in the laboratory; however, water

entry resulted under elevated pressures during centrifuge flight. Water leakage increased the buoyant weight of the model, and thereby altered the specified input conditions for the test. Increased scour depths resulted in the development of forces which exceeded drive system capabilities, causing an interruption of model motion and subsequent movement at a substantially reduced rate. The model was initially advanced over a horizontal distance of 171 mm in a time period of 3.1 seconds, at an average scouring rate of 61.0 mm/s. Figure 8C.2A displays the test instrumentation outputs measured during this initial section of the scouring event. The model motion was suspended over a time interval of approximately 160 seconds, and then restarted with irregular movement at an average rate of 0.52 mm/s. The model was advanced over an additional distance of 174 mm within a time duration of about 325 seconds. The test instrumentation outputs recorded during this final section of the event are shown in Figure 8C.2B. As a result of the significant reduction in velocity, the model event effectively represented a drained scouring condition.

A photograph and corresponding plan view drawing of the Test 08 scour are shown in Figure 4.54. An average cross - section surface profile for the apparent steady - state region is presented in Figure 4.55, together with an axial plot of measured scour depths and berm elevations. Figure 8D.1 displays additional cross - section surface profile data, plotted at 50 mm intervals of horizontal position. The scour depth increased gradually from an initial value of approximately 24.5 mm to an average equilibrium scour depth of 22.3 mm or 2.23 m at prototype scale. Berm elevations also increased with horizontal distance along the scour path, presumably as the result of surcharge build - up over the duration of the event. The average berm elevation was 7.7 mm above

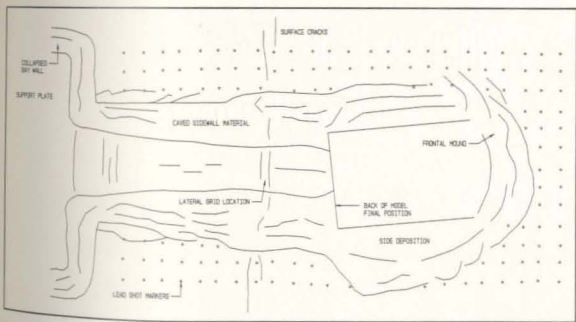
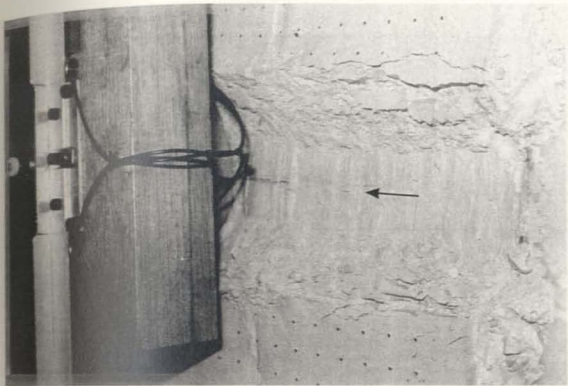


Figure 4.54 Top : Photograph of model scour created in Test 08 - view in direction of travel;
 Bottom : Plan view drawing illustrating scour surface features

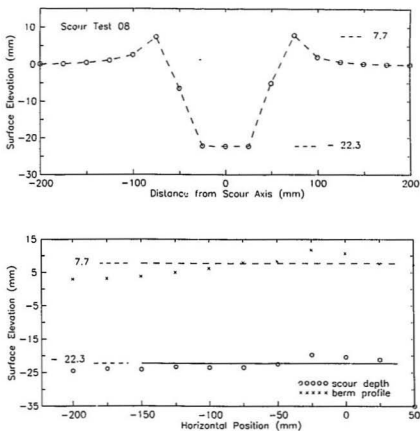


Figure 4.55 Top : Average cross - section surface profile for steady - state region of Test 08 scour; Bottom : Axial section plot of measured scour depths and berm elevations

the original surface level. A local reduction in scour depth and corresponding increase in berm elevation was evident at a horizontal position coincident with the location of the model pipeline segment. A linear depression and soil surface fractures formed in the vicinity of the pipeline segment, indicative of movement over the majority of its lateral extent. The sidewalls of the incision were characterized by extensive loose berm and

caved material along the entire length of the scour, in addition to longitudinal surface fractures. The surface soil disturbance increased with the horizontal distance travelled, to a maximum lateral extent of approximately 35 mm from the edges of the scour. A massive quantity of remoulded material was displaced concurrently at the front and sides of the advancing model iceberg. The resultant frontal spoil mound extended to a horizontal distance of about 60 mm beyond the final model position, with a maximum elevation on the order of 35 mm above the initial surface level.

Figure 4.56 provides a summary of the Test 08 pore pressure responses, as recorded over the final section of the scouring event. Table 4.14 lists the measured locations of the pore pressure transducers, as well as the corresponding peak and minimum excess pore pressure magnitudes. Figure 8E.1 displays the spatial distribution of pore pressure changes at 50 mm intervals of horizontal position. The discontinuity of model iceberg movements and associated drainage effects, produced irregular pore pressure responses during the final section of the event. Excess pore pressures induced by the event were first measured at a prototype horizontal distance approximately 20 m from the current model position. The maximum recorded increase in pore pressure was 47 kPa for a transducer (PPT 03) located near to the scour axis, at a depth of 7.2 m below the initial clay surface (at prototype scale). The peak value was measured during the final section of the event when the model was situated almost directly above the transducer position ($dx = -3$ mm). PPT Channel 07, located at a prototype depth of 1.6 m (i.e. approximately 0.6 m above the scour base) and immediately adjacent to the scour edge, developed negative excess pore pressures and displayed a relatively erratic response during the event. A maximum pore suction of 31 kPa was recorded at PPT 07,

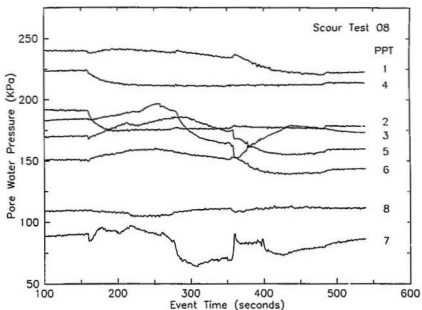


Figure 4.56 Test 08 pore pressure responses plotted for final section at reduced rate

for a model location which was nearly coincident with the position of the transducer ($dx = -2$ mm).

The resultant scour forces are shown plotted against the horizontal position of the model iceberg in Figure 4.57. The break in the force records shown, corresponds with the suspension of model movement and transition to the reduced rate of scouring. In addition, an extreme increase in the measured horizontal force near to the completion of the event, was indicative of load cell contact with the frontal surcharge material or instrument malfunction arising from this contact. The results preceding this apparent deviation in horizontal loading are presented in the figure. Table 4.15 gives a listing of

Table 4.14 Top : Test 08 measured pore pressure transducer locations; Bottom : Maximum and minimum excess pore pressures and horizontal distance from model

PPT No.	x (mm)	y (mm)	z (mm)	w (mm) ¹
1	- 13	- 3	141	80.0
2	- 140	0	85	79.9
3	- 16	- 4	72	80.0
4	- 141	1	133	79.9
5	- 2	- 3	64	80.0
6	- 2	- 45	65	80.3
7	9	55	16	80.4
8	- 2	- 147	37	82.8
9	0	407	- 3	101.3

¹ w = free water depth at position

PPT No.	u_i (KPa)	max. du (KPa)	dx (mm)	min. du (KPa)	dx (mm)
1	215	27	- 33	- 1	- 257
2	160	73	+ 22	- 46	- 67
3	150	47	- 3	-	-
4	204	36	+ 29	- 6	- 108
5	141	45	- 2	- 11	- 141
6	130	30	- 18	- 4	- 192
7	95	2	- 44	- 31	- 2
8	119	6	- 144	- 15	- 16

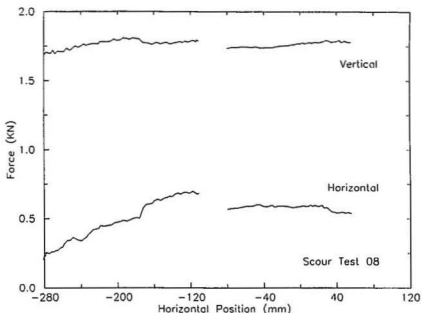


Figure 4.57 Test 08 horizontal and vertical components of the resultant force plotted against model horizontal position

the force data at 50 mm intervals of model horizontal movement. Figure 4.58 provides a graphical illustration of the model orientation and the acting system of forces at different horizontal positions.

The Test 08 horizontal force records were unreliable, as load cell measurements were lower than expected force magnitudes in consideration of the model geometry, scour depth, and extent of surcharge displaced with the model. Based on the available data, the vertical component of the resultant force was about 3.0 times as large as the horizontal component, and the average prototype magnitudes of the vertical and horizontal components were 17.6 and 5.9 MN respectively over the final section of the

Table 4.15 Test 08 resultant force data tabulated for different model horizontal positions

Horiz. Pos. (mm)	Horiz. Force (N)	Vert. Force (N)	Total Force (N)	Vector Angle (deg)	Attack Angle (deg)
- 250	362.4	1734	1771	78.2	22.4
- 200	471.4	1792	1853	75.3	23.2
- 150	646.7	1774	1888	70.0	24.9
- 100	587.8	1761	1857	71.5	25.6
- 50	598.8	1747	1847	71.1	25.6
0	586.4	1768	1862	71.6	25.2
+ 50	540.9	1788	1868	73.2	25.0
Average ¹	586.4	1756	1852	71.5	25.3

¹ Average values for approx. steady state region : $x = - 100$ to 25.

event. The effective attack angle of the model increased from a minimum value of approximately 22 degrees to an average value of 25.3 degrees within the apparent steady - state region of scouring. The corresponding inclination of the resultant force vector was offset by about 7 degrees from the perpendicular to the scouring face, conceivably due to underestimation of the horizontal force component. The position of the force vector increased initially and maintained a relatively steady value during the final section of the event, at an average prototype distance of 2.0 m from the model inflection line. As the result of water leakage into the model during testing, inductive pressure transducer measurements of interface pressures were not acquired in this test.

Figure 4.59 displays a plan view drawing of surface displacement vectors at positions external to the model scour created in Test 08, as well as a plot of the average magnitudes of horizontal and lateral components of displacement. Surface markers

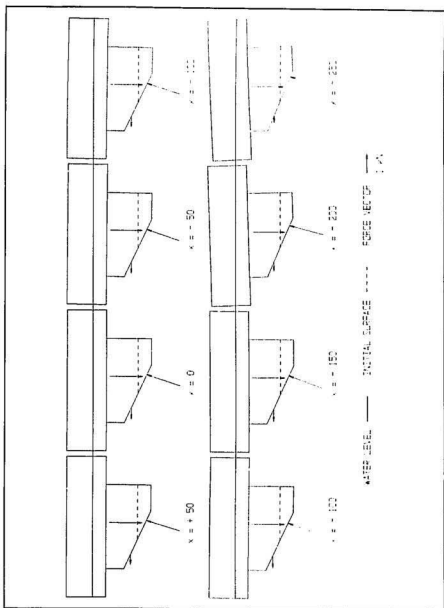


Figure 4.58 Test 08 model iceberg orientation and resultant force vectors

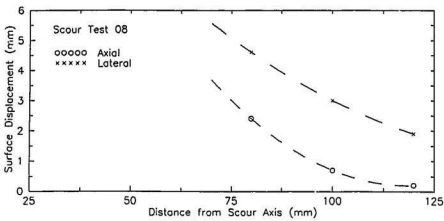
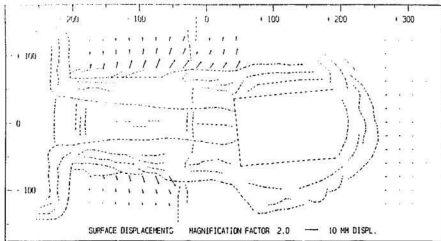


Figure 4.59 Top : Test 08 plan view drawing of surface displacement vectors; Bottom : Average axial and lateral surface displacements versus distance from the scour axis

located at lateral positions approximately 1 m from the edge of the incision were obscured by extensive surficial disturbance due to caving and berm deposition. Based on the available data, the average horizontal and lateral surface displacements measured at a prototype distance of about 3 m from the scour edge, were 0.24 and 0.46 m

respectively. The surface displacements decreased with distance from the scour axis to values of 0.02 and 0.19 m at lateral positions approximately 7 m from the scour edge (i.e. 120 mm from the scour axis at model scale). The radiograph traces presented in Figures 8F.1 and 8F.4, display an accumulation of surface markers within the mound of material at the front and sides of the final position of the model iceberg. The majority of the surface markers situated within the scour path or immediately adjacent to the scour edges were displaced concurrently with the model to its final position. This evidence implied the formation of a region of frontal material which remained relatively stable in relation to the model, throughout the scouring event.

The plan view radiograph trace of the Test 08 scour presented in Figure 8F.1, shows the locations of pore pressure transducers, the model pipeline segment, and the displaced configuration of soil deformation grids. The boundaries of the scour were poorly - defined in this view, due to extensive disturbance of surficial material adjacent to the incision. Figure 8F.2 displays the trace of a radiograph which provides a cross - sectional view of the deformed lateral grid and model pipeline segment. The radiograph traces of the axial grids situated near to the beginning of the scour and at the final horizontal position of the model, are presented in Figures 8F.3 and 8F.4 respectively. The model was not supported effectively at the completion of movement in this test, resulting in some additional displacement of the final axial grid which was unrelated to the scouring event.

Initial / displaced plots and displacement vectors plots obtained from the soil deformation grids installed within the Test 08 specimen are given in Figure 8F.5. With the exception of results from the initial axial grid, the measured sub - surface

displacements represented the effects of a drained or partially drained scouring condition due to the diminished rate of advance of the model iceberg. The displacement patterns witnessed in this test were comparable to the results from Test 06, where the rate of model movement was also reduced over the final section of the event.

The initial and displaced configuration of the lateral grid ($x = -20$ mm) is depicted in cross-sectional and plan view in Figure 4.60. Some lateral movements were observed; however, the lateral component of displacement was limited to shallow depths, with increasing magnitudes toward the edges of the scour. The measured vertical component of displacement was relatively small or negligible. The vertical movement of the horizontal grid member immediately below the base of the scour indicated cumulative upward displacements, which may be attributable to sidewall failure or caving following the passage of the model iceberg. Upward vertical movements corresponding with surface heave adjacent to the scour edges were also noted; although, displacement patterns in this region included the effects of both the scouring event and subsequent failure of the sidewalls of the incision. The horizontal component of displacement was very large at positions above or immediately below the scour base. A portion of the upper horizontal grid member within the scour path, was displaced from the initial grid location to the final position of the model iceberg. The horizontal displacement gradient with depth was also relatively high, such that large horizontal movements were restricted to a shallow region beneath the scour.

Figure 4.61 shows the initial / displaced plot for the axial grid located near to the beginning of the scour. This axial grid extended over the horizontal region associated with the initial rate of advance of the model iceberg and the transition to a reduced rate.

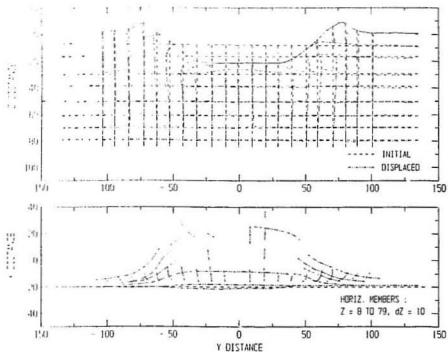


Figure 4.60 Test 08 initial / displaced plot of lateral grid at $x = -20$ shown in cross-section and plan view

The measurements from this grid indicated a shallow region of very large horizontal movements, and small vertical displacements at positions below the scour base. In addition, the displaced configuration of the vertical members of the grid displayed a thin zone of shearing or a failure surface, which suggested the development of a deeper zone of sub-scour displacement. The initial / displaced plot for the axial grid at the final model position, shown in Figure 8F.5, provided comparable information; however, the measured vertical component of displacement was larger, as was consistent with a bearing capacity failure beneath the model following the completion of the event.

The sub-surface displacement records for Test 08 are summarized in Figure 4.62

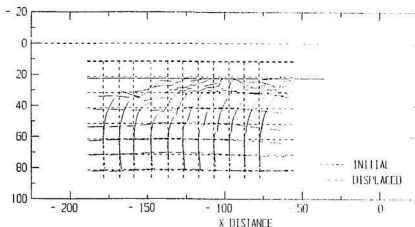


Figure 4.61 Test 08 initial / displaced plot of axial grid located near beginning of scour

which displays profiles of the maximum values of vertical and horizontal components of displacement. The displacements shown in this plot were averages, based on the available data from lateral and initial axial grids. The very large horizontal movements at positions above and immediately below the base of the scour, limited the accuracy of measurements in this vicinity. The approximate maximum values of vertical and horizontal displacement immediately below the scour base (interpolated at a depth below base = 0.1 m) were 0.44 and 2.84 m respectively at prototype scale. The maximum depths below the base of the scour at which vertical and horizontal displacements were recorded, evaluated for a lower bound displacement magnitude of 0.2 m, were 0.7 and 2.8 m respectively at prototype scale. The vertical and horizontal displacements extended to normalized values of 0.3 and 1.4 scour depths below the scour base.

The model pipeline segment, initially located at a prototype depth of approximately 0.3 m above the base of the scour (19 mm below the original clay surface

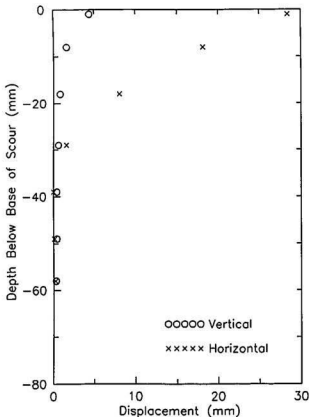


Figure 4.62 Test 08 maximum vertical and horizontal components of soil displacement versus depth below scour base

at model scale), was displaced vertically during the scouring event to a final position beneath the scour. Void space observed in front of the pipeline segment during excavation, suggested that forward horizontal movement was followed by limited rebound of the segment. Scrape markings at positions coinciding with the edges of the scour incision, provided evidence of direct contact with the model keel. The segment

experienced plastic bending, with maximum centre - line vertical and horizontal deflections of approximately 0.18 and 0.32 m respectively at prototype scale. The measured horizontal curvature of the segment was not symmetric in relation to the pipe centre - line (scour axis).

4.3.9 Scour Test 09

Model Input Conditions

In Test 09, the identical prototype scouring event to that represented in Test 05, was modelled at a reduced scale of 1/125, and at an increased acceleration level of 125 gravities. The model iceberg configuration and input parameters for this test are given in Figure 9A.1 in the corresponding section of Appendix A. The model iceberg used in Test 09 was geometrically similar to the Test 05 model, with all dimensions reduced in proportion to the ratio of the linear scale factors, 100/125. The keel width was 80 mm or 10 m at prototype scale, the horizontal base length was 40 mm, and the attack angle was set at 15 degrees. The waterplane area of the model was 200 by 200 mm² which corresponded with a vertical stiffness of 49 N/mm or 6.1 MN/m at prototype scale. In accordance with the scaling relationships presented in Table 3.1, the mass of the Test 09 model was reduced by the ratio of (100/125)³ from the Test 05 model mass, to ensure that the magnitude of the buoyant weight of the model was scaled appropriately. In addition, the mass distribution of the reduced scale model, including attached instrumentation, was designed such that the buoyant weight acted at corresponding positions in both tests.

The Test 09 clay specimen was subjected to a laboratory pre - consolidation stress of 140 kPa, coinciding with the initial stress state for the Test 05 specimen. At the test acceleration level in - flight, identical vertical stresses were induced at corresponding positions in both specimens. The consolidated thickness of the Test 09 specimen was reduced by the ratio of the linear scale factors to 144 mm, representing a full scale prototype stratum of saturated clay which was 18 m in depth. The thickness of the base drainage region was increased by the installation of a 36 mm deep saturated sand layer below the clay specimen. Due to the additional thickness of the sand layer, the upper clay surface was situated at the same radius in both tests, and this served to minimize differences in stress levels resulting from the radial divergence of the centrifuge acceleration field. The nominal depth of free surface water at the location of the model was reduced to 64 mm, representing an 8 m water depth at prototype scale.

Figure 9A.2 shows elevation and plan view drawings of the Test 09 layout of instrumentation, deformation markers, and model pipeline segments. The model iceberg was supported at an initial depth 16 mm below the clay surface, and equipment elevations were modified to accommodate the reduced scale of the model. The pore pressure transducers were installed at the same depths as in Test 05, as constrained by available ports in the tub which contained the clay specimen; however, lateral distances from the scour axis were reduced in accordance with the model scale. The soil deformation grids used in Test 09 were placed at geometrically similar locations in relation to Test 05, and the mesh sizing was also reduced by the ratio of the linear scale factors to 8 mm. The prototype length of travel was increased, and the location of the final axial grid was altered to coincide with the expected model position at the completion of the event. The

positions of surface markers were also changed to model the Test 05 layout at the reduced scale. In Test 09, a rectangular pattern of surface markers (192 mm width, 528 mm length) was established at 16 mm spacings centred on the scour axis. The identical lead shot were used in both tests, such that the mass and diameter of the individual markers were not modelled.

The selection of stainless steel sections to model Test 05 pipeline segments at reduced scale, was restricted by commercial availability of appropriate tubing sizes. The model pipelines employed in Test 09 had an outside diameter of 4.80 mm and a wall thickness of 0.20 mm, and represented prototype segments comprised of an identical material with an outside diameter of 600 mm and a wall thickness of 25 mm. The tubular sections used in Test 05 modelled prototype segments having the same wall thickness, but represented pipelines with a somewhat larger outside diameter of 635 mm.

The experimental methods used to estimate undrained shear strength in Test 09 included both in - flight vane shear testing, and post - test hand - vane and moisture content measurements. In - flight vane shear tests were carried out at three levels : 30, 60, and 90 mm below the clay surface. The vane test data are presented in Figure B.2, including plots of vertical displacement, rotation, and torque against time, as well as the torque versus rotation curves for each level. In Figure 9B.1, c_u values determined by the use of experimental methods are compared with strength profiles based on Equations 4.2 and 4.3. Similar to preceding test observations, the in - flight vane results predicted a higher strength gradient and larger strength magnitudes at greater depths, in relation to expected values. The measured vane strength was 24.9 kPa at a prototype depth of 3.75 m, as compared with a value of 18.5 kPa derived in accordance with the empirical

relation given by Equation 4.2. At a prototype depth of 7.5 m, the vane strength increased to 36.0 kPa, whereas the corresponding empirical strength estimate was 22.8 kPa for this test level. The apparent large discrepancies with predicted vane strength magnitudes at greater depths, may be partly attributable to reduced surface water access to the vane head, underestimation of the vane shaft resistance, or change in calibration of the torque load cell. Inadequate rate of rotation and associated increased drainage, may also account for larger than anticipated strength measurements; however, the vane testing protocol was generally consistent with that employed by previous researchers (Section 3.5). Undrained shear strengths evaluated from hand - vane measurements were an average of 54 percent lower than estimates from the empirical relation, as expected for conditions following the completion of the centrifuge test. In contrast, the strength values based on post - test moisture content determinations exceeded the estimates from Equation 4.2. Lower than expected moisture contents and implied larger strengths were also noted in preceding tests, and may be indicative of moisture content measurement inaccuracies.

Test Results

The consolidation records for Test 09 are presented in Figure 9C.1 as plots of pore pressure against time and clay surface settlement versus the square root of time. The time duration allowed for consolidation of the reduced scale specimen was about 4.5 hours. The apparent initial clay surface settlement was 1.9 mm, following the completion of greater than 95 percent of primary consolidation. Figure 9C.2 provides a summary of the test instrumentation outputs plotted against time and horizontal position during the

scouring event. The event was completed in 5.9 seconds, in which the model iceberg travelled a total horizontal distance of 461 mm or 57.6 m at the corresponding prototype scale. The average rate of advance of the model was 77.6 mm/s, as assessed from the data records of the position transducer and rotary potentiometer.

Figure 4.63 provides a plan view photograph and related drawing to illustrate surface features of the Test 09 scour. Figure 4.64 shows an average cross - section surface profile of the scour, together with an axial plot of scour depths and berm elevations. Additional surface profile data are presented in Figure 9D.1, as cross - sectional plots at 50 mm intervals of horizontal position along the scour path. The model iceberg experienced an initial period of relatively rapid uprise to an apparent steady - state level, corresponding with an average scour depth of 8.8 mm or 1.10 m at prototype scale. The average berm elevation in this region was 3.8 mm, attributable primarily to surface heave adjacent to the incision. Shallower scour depths were evident at positions coincident with the trench locations of the model pipeline segments; the depth of scouring increased slightly over the latter portion of the event to values on the order of 10 mm, at positions beyond the model pipeline cross - sections. Loose or remoulded material arising from caving of the sidewalls of the incision and limited berm formation, was observed to a maximum lateral distance of approximately 15 mm from the scour edges, with some additional local disturbance. Surface disturbance also extended to a horizontal distance of about 15 mm in front of the final position of the model, and a relatively small amount of frontal spoil material was evident at this location.

The pore pressure responses measured during the Test 09 scouring event are summarized in Figure 4.65. The final locations of the transducers are listed in Table 4.16

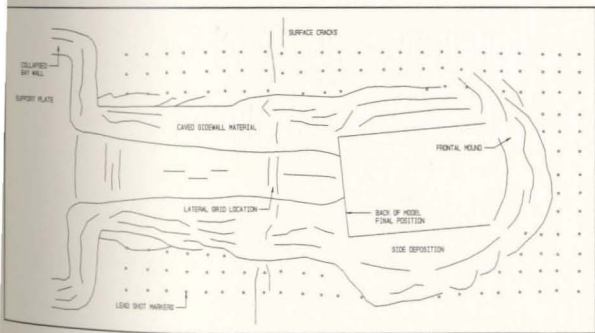
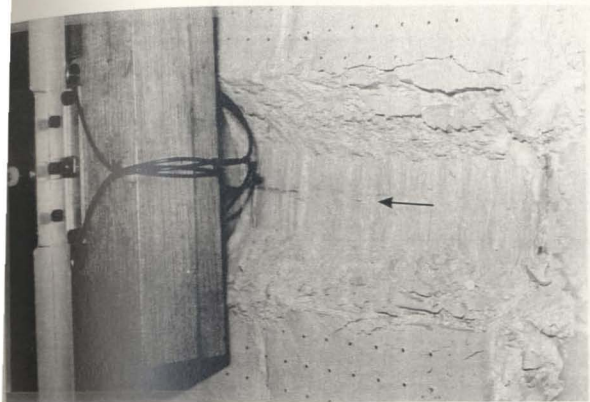


Figure 4.54 Top : Photograph of model scour created in Test 08 - view in direction of travel;
 Bottom : Plan view drawing illustrating scour surface features

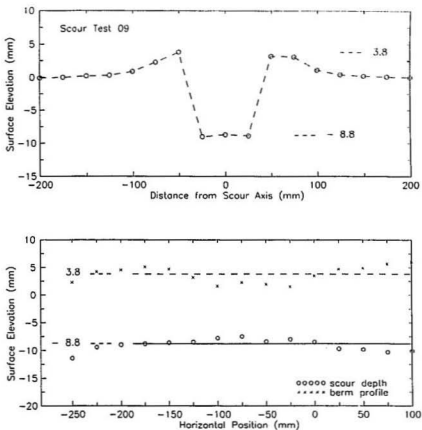


Figure 4.64 Top : Average cross - section surface profile for steady - state region of Test 09 scour; Bottom : Axial section plot of measured scour depths and berm elevations

together with the peak and minimum excess pore pressures developed during the event. The spatial distribution of the pore pressure changes at 50 mm intervals of model horizontal movement is illustrated in Figure 9E.1. The effects of scouring were initially recorded at a prototype horizontal distance on the order of 25 m from the current position of the model iceberg. The maximum rise in pore pressure measured within the apparent

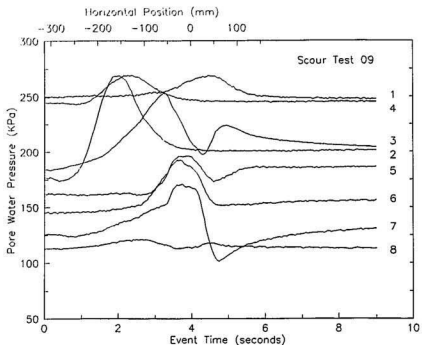


Figure 4.65 Test 09 pore pressure responses during event - transducer channels 01 to 08

steady - state region of scouring was 70.1 kPa for a transducer (PPT 03) located 10.5 m below the initial clay surface (at prototype scale), and at a lateral position coincident with the scour axis. The peak response was recorded when the model was at a horizontal distance of 7.9 m ($dx = -63$ mm) from the transducer position. The maximum measured pore suction was 23.9 kPa, for a transducer (PPT 07) situated at a prototype depth of 4.5 m, and adjacent to one edge of the scour incision. The negative pore pressure response was recorded following movement of the model to a horizontal distance of 7.5 m ($dx = +60$ mm) beyond the transducer position.

Table 4.16 Test 09 measured pore pressure transducer locations; Bottom : Maximum and minimum excess pore pressures and horizontal distance from model

PPT No.	x (mm)	y (mm)	z (mm)	w (mm) ¹
1	- 11	- 3	137	64.0
2	- 197	5	82	63.4
3	- 14	0	84	64.0
4	- 183	0	135	63.5
5	- 2	- 2	66	64.0
6	- 7	- 44	64	64.2
7	- 6	36	36	64.1
8	- 3	- 125	30	66.0
9	0	405	- 3	85.1

¹ w = free water depth at position

PPT No.	u_1 (KPa)	max. du (KPa)	dx (mm)	min. du (KPa)	dx (mm)
1	250	19	+ 39	-	-
2	177	92	+ 14	- 3	- 103
3	184	70	- 63	-	-
4	245	24	+ 26	- 2	- 94
5	162	34	- 18	- 2	- 254
6	145	48	- 31	-	-
7	125	45	- 27	- 24	+ 60
8	113	9	- 128	-	-

Figure 4.66 shows the resultant forces acting at the model iceberg - soil interface plotted against the horizontal position of the model. The Test 09 force data are also listed at 40 mm intervals of model horizontal movement in Table 4.17. In addition, Figure 4.67 displays the model orientation and the related system of forces for different horizontal positions along the scour path. The vertical component of force developed during the event was about 3.8 times as large as the measured horizontal component. A region of higher vertical force may be associated with the trench locations of the model pipeline segments. The average magnitudes of the vertical and horizontal components over the apparent steady - state region of scouring were 17.6 and 4.6 MN respectively at prototype scale. The effective attack angle increased initially to a maximum value of 17.8 degrees, and then declined to an average steady value of 15.6 degrees over the final section of the event. The inclination of the resultant force vector was approximately perpendicular to the scouring face of the model, and remained relatively constant throughout the event. The position of the force vector did not vary significantly as scouring progressed; the force vector acted at a peak distance of 2.5 m (at prototype scale) from the model iceberg inflection line, and then decreased to an average value of about 2.2 m at near to the completion of the event.

The interface pressure records for transducers situated at the base (IPT 18) and inclined scouring face (IPT 19 and 20) of the model iceberg are displayed in Figure 9C.2. The data acquired from the transducer located at the base of the model indicated a regularly fluctuating response over the final section of the event, with an average pressure of 145 kPa and recorded variations as large as 21 percent of the mean value. The total pressure response measured at the scouring face of the model was irregularly

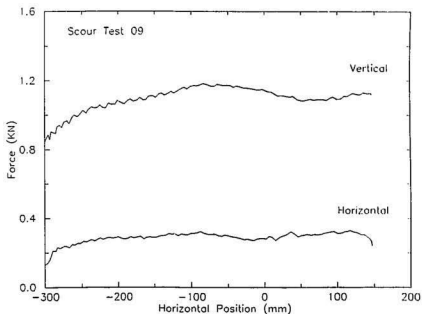


Figure 4.66 Test 09 horizontal and vertical components of the resultant force plotted against model horizontal position

varying with extreme fluctuations. Maximum pressures were measured at positions coincident with the trench locations of the model pipeline segments; the peak recorded magnitude was 229 kPa. The average pressure acting on the inclined face within the apparent steady - state region of scouring was 171 kPa.

A plan view drawing of surface displacement vectors at positions outside of the Test 09 scour incision is displayed in Figure 4.68, along with a plot of the average values of horizontal and vertical components of displacement for the apparent steady - state region of scouring. The external displacements varied with horizontal distance along the scour path; movements near to the initial model position were predominantly lateral

Table 4.17 Test 09 resultant force data tabulated for different model horizontal positions

Horiz. Pos. (mm)	Horiz. Force (N)	Vert. Force (N)	Total Force (N)	Vector Angle (deg)	Attack Angle (deg)
- 300	129.9	840	850	81.2	17.1
- 260	243.6	1000	1029	76.3	17.8
- 220	276.9	1044	1080	75.2	17.0
- 180	283.8	1079	1116	75.3	16.6
- 140	296.6	1126	1164	75.2	15.7
- 100	312.3	1165	1207	75.0	15.3
- 60	295.8	1174	1211	75.9	14.6
- 20	275.3	1155	1187	76.6	14.8
+ 20	285.5	1111	1147	75.6	15.5
+ 60	303.6	1088	1130	74.4	15.9
+ 100	311.5	1091	1135	74.1	16.0
+ 140	295.3	1126	1164	75.3	15.5
Average ¹	297.1	1125	1164	75.2	15.6

¹ Average values for approx. steady state region : $x = -200$ to 100 .

in direction, and the horizontal component of displacement increased over the final section of the scour. The average horizontal and lateral displacements recorded at lateral positions approximately 1 m from the edge of the scour, were 0.30 and 0.45 m respectively at prototype scale. The surface displacements declined to average magnitudes of 0.08 and 0.18 m respectively at lateral positions about 7 m from the scour edge (i.e. 96 mm from the scour axis at model scale). As illustrated in the radiograph trace given in Figure 9F.1, the majority of the surface markers in the path of the advancing model were displaced vertically to positions beneath the scour and forward

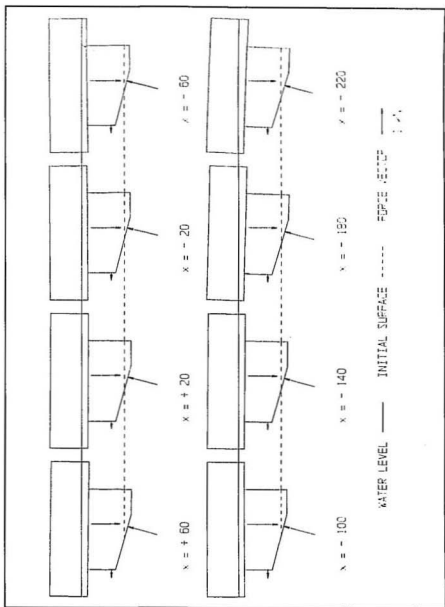


Figure 4.67 Test 09 model iceberg orientation and resultant force vectors

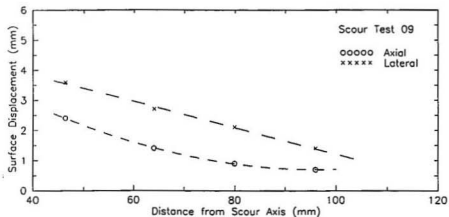
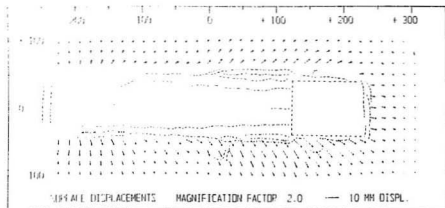


Figure 4.68 Top : Test 09 plan view drawing of surface displacement vectors; Bottom : Average axial and lateral surface displacements versus distance from the scour axis over a limited horizontal distance, with negligible lateral movement.

Figure 9F.1 presents a trace compiled from plan view radiographs of the clay specimen, which displays the locations of pore pressure transducers, model pipeline segments, and the displaced configuration of soil deformation grids. Figure 9F.2 provides similar information in cross-sectional view, at two horizontal positions corresponding

with the lateral grid and model pipeline locations. The traces of axial section radiographs at grid locations near to the beginning of the scour and at the final horizontal position of the model iceberg, are given in Figures 9F.3 and 9F.4 respectively.

The sub - surface displacement records for Test 09 are displayed in Figure 9F.5 as initial / displaced plots and displacement vector plots for each of the grids installed within the clay specimen. Figure 4.69 shows cross - sectional and plan views of the initial and displaced configuration of the second lateral grid ($x = -40$ mm). The observed displacement patterns in this test were comparable with the results from Test 05. The accuracy of near - surface displacement measurements was reduced due to poor definition of the upper portion of vertical grid members in site investigation radiographs. The lateral component of soil displacement was small, and movements were limited to shallow depths in the vicinity of the edges of the scour. The vertical component of displacement was relatively uniform across the scour width, and decreased gradually with depth below the scour. Vertical displacements were measured over the entire depth of the second lateral grid; however, movements recorded at the first lateral grid ($x = -97$ mm) were less extensive, and displacement magnitudes were smaller at this location. The horizontal component of displacement was larger in magnitude than the corresponding vertical component at shallow depths; however, the horizontal movements attenuated more rapidly, and apparent small negative displacements were evident below a given depth.

The initial / displaced plot for the axial grid located at the final position of the model iceberg is shown in Figure 4.70. The vertical movements of the model associated with the discontinuation of scouring were reduced to approximately 3 mm, as the result

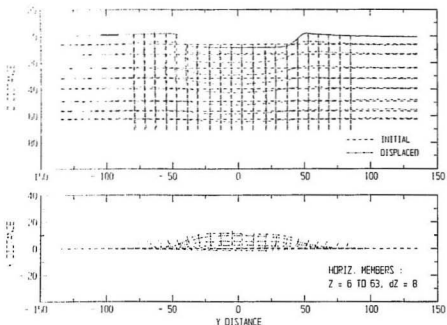


Figure 4.69 Test 09 initial / displaced plot of lateral grid at $x = -40$ shown in cross-section and plan view

of support provided at the completion of the event. Vertical and horizontal displacement magnitudes were similar at this grid location; however, the vertical component of displacement was more extensive over the depth of the grid. The displacement record for this grid also provided information on the pattern of movements developed in front of the advancing model. The grid measurements at this location suggested that soil in front of the model was displaced upward and forward at vertical positions beneath the scour base, within an apparent zone of large displacement.

Figure 4.71 presents a summary plot of the Test 09 sub - surface displacement records, which shows profiles of the maximum values of the vertical and horizontal

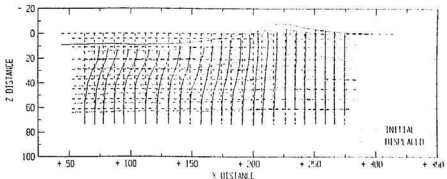


Figure 4.70 Test 09 initial / displaced plot of axial grid located at final horizontal position of model iceberg

displacement components within the apparent steady - state region of scouring. The horizontal displacement measurements from the initial axial grid were consistent with lateral grid estimates in this test, and the plotted magnitudes were evaluated based on both sets of results. The vertical displacements shown in Figure 4.71 were assessed as the average of well - defined lateral grid movements. The maximum values of vertical and horizontal displacement immediately below the base of the scour (interpolated at a depth below base = 0.1 m) were 0.68 and 1.08 m respectively at prototype scale. The limiting depths at which vertical and horizontal displacements were measured, evaluated for a lower bound displacement magnitude of 0.2 m, were 4.2 and 2.8 m respectively at prototype scale. The vertical and horizontal displacements extended to normalized values on the order of 3.8 and 2.5 scour depths below the base of the scour. Model pipeline segments located at depths of 1.5 and 2.2 m beneath the scour base at prototype scale, did not exhibit any measurable plastic deformation due to the effects of the scouring event.

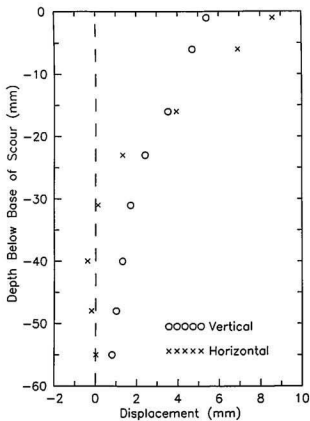


Figure 4.71 Test 09 maximum vertical and horizontal components of soil displacement versus depth below scour base

Chapter 5

Numerical Analysis

5.1 Introduction

Theoretical modelling and centrifuge physical modelling are complementary approaches by which to predict performance in geotechnical boundary value problems, as illustrated schematically in Figure 5.1. Centrifuge model test data are well suited for the development and verification of theoretical models of the ice - soil interaction during a scouring event. After such verification, the theoretical model may then be exploited as an effective method for the analysis of comparable full scale conditions of interest. Any design methodology formulated in this manner, however, will incorporate the various common simplifying assumptions which are inherent to the modelling techniques. Direct calibration of the model against field data, where available, is required in order to address the limitations of the idealization, to ensure reliable predictions of prototype behaviour.

The accurate evaluation of soil disturbance effects during a scouring event is complicated by the following factors.

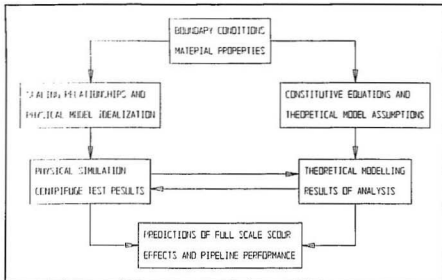


Figure 5.1 Relationship between theoretical modelling and centrifuge physical model study of ice scouring

(1) The interacting system is characterized by continuous movement of the ice feature, and large deformations and strains are developed within the soil mass.

(2) Soil behaviour is usually highly nonlinear and depends on the complete geological history of the deposit as represented by the size, shape, packing, and mineral composition of the particles, the stress history that has been sustained, the pore fluid and other considerations.

(3) The ice - soil interface conditions are not well - defined, and include characteristics that cannot be adequately simulated by linear modelling, e.g. Coulomb friction.

At the current level of understanding of the process of ice scouring, closed form analytical solutions which provide reliable predictions of soil displacements are intractable. On the other hand, numerical techniques such as the finite element method have been adequately developed to overcome the aforementioned difficulties, and may generate approximate solutions of sufficient accuracy. However, numerical analyses which replicate all aspects of the phenomenon of disturbance are considered beyond the current state - of - the - art. The present study attempted to evaluate the practical validity of the finite element method as a theoretical means for the determination of soil performance under idealized scouring conditions. This entailed a comparative examination of the results of centrifuge model tests and preliminary numerical analyses which embraced important aspects of the physical problem.

Related Research

Finite element models have been used effectively in the solution of other classes of large strain geomechanical problems. In particular, numerical analyses have been performed to predict disturbance effects induced by the penetration of foundation elements and devices into a soil medium, as during the installation of piles, penetrometers, and sampling tubes (e.g. Baligh and Scott, 1976; Kioussis et al., 1988; van den Berg et al., 1991, 1992). Despite notable dissimilarity of boundary conditions in relation to representations of ice scouring, these studies have demonstrated the applicability of the finite element technique in modelling the effects of large deformations and large strains, as well as material nonlinearities and soil - structure interface conditions. The finite element method has also been applied to the problem of soil cutting in the context of

tillage tools, including both two - dimensional plane strain analyses for a wide cutting blade (Yong and Hanna, 1977) and three - dimensional analyses for a narrow cutting blade (Desai and Phan, 1980; Desai et al., 1982; Chi and Kushwaha, 1988). Ice scouring may be thought of as a soil cutting process; however, it differs from soil cutting by earth - moving and agricultural machinery which involves sharp, positively - raked blades rather than the blunt, negatively - raked geometries that are most commonly associated with ice keels (Palmer, 1990).

Successful and economically viable analysis of the foregoing problems required not only correct theoretical formulations, but also efficient analysis procedures and numerical algorithms to accommodate large strain effects. Furthermore, adequate modelling of nonlinear boundary effects through the provision of suitable interface elements was necessary in order to obtain reasonable correspondence between theoretically computed displacement fields and experimentally measured values. Experimental or field verification was essential to ensure the accuracy of the calculated predictions of soil behaviour. The finite element models were successively improved through repeated practical application and empirical modification of input conditions or modelling assumptions.

More recently, research was initiated in which the finite element method was applied in the development of numerical models of ice scouring. Poorooshasb and Yang (1993) summarized the results of initial analyses which were implemented through use of the general purpose finite element code ANSYS (Swanson Analysis Systems Inc., 1989). The finite element analyses allowed for large deformation conditions, including large translational and rotational movements; however, a large strain

formulation was not adopted. An extended form of the Drucker - Prager constitutive model was used to define an elastic - perfectly plastic material response, and both drained and undrained total stress analyses were performed. The scouring event was simulated by direct application of horizontal displacements at nodes delineating the ice - soil interface. Two - dimensional plane strain conditions were initially investigated.

The analysis (Poorooshasb and Yang, 1993; Yang et al., 1993) was extended to consider a preliminary three - dimensional representation of the problem, including a simplified beam - element model of a buried pipeline. Based on correspondence of the results from two - and three - dimensional models, the authors concluded that a plane strain idealization may serve as an adequate representation of the ice - soil interaction during a scouring event. Furthermore, it was found that the presence of the model pipeline within the soil domain did not significantly alter the resultant forces or the predicted soil stress and displacement fields. The authors inferred, therefore, that a separate soil - pipeline interaction analysis may be carried out to investigate load transfer to the pipeline from computed free - field soil displacements (i.e. displacements not influenced by the rigidity of any embedded pipeline) in place of a comprehensive three - dimensional finite element analysis of the ice - soil - pipeline interaction.

Yang et al. (1994) described the plane strain finite element model and compared the results of the analysis with centrifuge model test data acquired as part of the present study (Scour Test 02). The analysis provided information on the resultant forces and the stress and displacement fields in the soil. The predicted soil displacement magnitudes markedly exceeded the experimental values at positions immediately below the base of the scour; however, the pattern and vertical extent of the computed and measured soil

movements was found to be similar. Although the representation of the model iceberg advancement and the material response were relatively crude, the comparisons with centrifuge test data suggested that realistic quantitative predictions of scour effects might be obtained through refinement of the preliminary analysis. More current research (C - CORE, 1995) demonstrated inadequacies in realistic representation of a steady - state scouring condition for the limited range of horizontal movement which was simulated.

In the present study, it was proposed to address deficiencies in the existing numerical analysis procedures in order to resolve unexplained discrepancies in comparison with physical evidence, and to enhance predictive capabilities. This research was undertaken in parallel with similar numerical investigations of the effects of ice scouring on buried pipelines (C - CORE, 1995). In particular, modifications were made in relation to the following attributes of the numerical model.

(1) A finite strain formulation was adopted in the analysis to account for the development of both large deformations and large strains, as characteristic effects of the scouring process.

(2) Effective stress consolidation analyses were performed by application of an algorithm for the solution of coupled fluid - solid equations, so as to include the effects of the pore water response.

(3) The elastic - perfectly plastic constitutive model was replaced with a more realistic representation of the soil as a nonlinear elastic - plastic material which may exhibit both strain hardening or softening behaviour.

(4) Simulation of the ice - soil interface was refined through use of suitable interface elements which allowed for inherent nonlinear boundary effects.

The numerical analyses were implemented through use of the general purpose finite element code ABAQUS (Hibbit et al., 1994) which incorporated the necessary capabilities to accommodate the above - stated modelling refinements. In this chapter, features of the analysis which are relevant to the simulation of an idealized scouring condition are described, and limitations of the proposed numerical representation are presented. Preliminary verification of the approach is provided through comparison with experimental data from representative centrifuge tests, as detailed in Chapter 6.

5.2 Finite Element Modelling

Nonlinear behaviour in the mechanics of deformable solids may be assumed to occur due to one or more of the following three factors : (1) geometric nonlinearity, which arises from the nonlinear terms in the kinematic equations or the expressions describing the state variables such as strains; (2) material nonlinearity, which reflects the nonlinear terms in the constitutive equations, and; (3) boundary nonlinearity, which is caused by the interaction between two adjacent bodies with different material properties. The utility of the finite element method for the investigation of ice scouring derives mainly from its capability of solving problems which involve each of these forms of nonlinearity. Furthermore, the method allows for consideration of arbitrary geometries, soil stratigraphies, and applied loads, as may be necessary to ensure realistic representation of a range of field conditions.

5.2.1 Geometric Nonlinearity

Stress and Strain Measures

Classical finite element algorithms assume that strains, both elastic and plastic, are infinitesimal, and that the initial geometry of a deforming body is not appreciably altered during the deformation process. The errors associated with this approximation are of the order of the strains and rotations compared to unity (Nagtegaal, 1982). As a result, the infinitesimal strain definition is only useful for small displacement gradients; that is, both strains and rotations must be small for this definition to be appropriate. The large movements of the soil medium in the vicinity of an ice keel during a scouring event cause significant modification of the geometry of the solution domain. The resulting strains are no longer linearly related to displacement gradients, and the finite element formulation must account for the changes in geometry which are inherent to the problem. In the present study, it was therefore necessary to carry out the analysis using a code developed in accordance with large strain theory, in order to yield realistic quantitative predictions of soil displacements.

When the small strain approximation is no longer valid the correct formalism of stresses and strains must be established, and the constitutive relations must also be generalized to accommodate the revised definitions of the large strain formulation. Hibbitt et al. (1994) presented detailed derivations relevant to the large strain theory and solution methods adopted within the code used in the finite element analysis. An elastic reference state was identified for the material, and the stress and strain measures that provided a work conjugate pairing were defined. The internal virtual work rate was

written in terms of the Cauchy or true stress σ and as an integral over the natural reference volume, as follows

$$\int_V \sigma : \mathbf{D} \, dV = \int_{V_0} J \sigma : \mathbf{D} \, dV_0 \quad (5.1)$$

where $J = dV / dV_0$ is the Jacobian of the elastic deformation between the natural reference and the current volume. In accordance with the work conjugacy concept, the Kirchoff stress, defined as

$$\tau = J \sigma \quad (5.2)$$

was therefore the conjugate to the strain measure for which the associated strain rate is equivalent to the rate of deformation, given by the symmetric part of the spatial gradient

$$\mathbf{D} = \text{sym} \left[\frac{\partial \mathbf{v}}{\partial \mathbf{x}} \right] \quad (5.3)$$

where \mathbf{v} is the velocity of a material point and \mathbf{x} are the current spatial coordinates of the point. The stress measure expressed in Equation 5.2 was useful in the development of constitutive models at large strains, since it is the most direct measure with respect to an elastic reference state for which the conjugate strain rate is given by the rate of deformation. The corresponding strain measure was identified in one - dimension as the logarithmic strain, and provided the most appropriate definition for elastic - plastic materials where the elastic part of the strain can be assumed to be small.

The solid (continuum) elements available within the code used a fully nonlinear formulation and allowed for finite strain and rotation. The strains were computed by approximate integration of the rate of deformation (Equation 5.3) over a given increment, through use of a central difference algorithm. The strain components were referred to a

fixed coordinate basis, such that the strain at the start of the increment must be rotated to account for the rigid body motion during the increment. The rigid body rotation relative to the coordinate system was addressed by application of the approximate method proposed by Hughes and Winget (1980). In accordance with this approach, the stress state was integrated as follows

$$\tau_{t+\Delta t} = \Delta \mathbf{R} \cdot \tau_t \cdot \Delta \mathbf{R}^T + \Delta \tau (\Delta \mathbf{D}) \quad (5.4)$$

where τ is the Kirchoff stress tensor defined with respect to the elastic reference configuration, and the subscripts t and $t + \Delta t$ refer to the beginning and end of the time increment, respectively. The stress increment $\Delta \tau$ ($\Delta \mathbf{D}$) caused by the straining of the material during the time increment Δt was dependent on the strain increment $\Delta \mathbf{D}$ defined by the central difference operator as

$$\Delta \mathbf{D} = \text{sym} \left[\frac{\partial \Delta \mathbf{u}}{\partial \mathbf{x}_{t+\Delta t/2}} \right] \quad (5.5)$$

in which $\Delta \mathbf{u}$ is the displacement increment, and \mathbf{x} refers to the current spatial position of the point under consideration. The increment in rotation $\Delta \mathbf{R}$ which occurred within the time increment Δt was approximated as

$$\Delta \mathbf{R} = \left[\mathbf{I} - \frac{1}{2} \Delta \omega \right]^{-1} \cdot \left[\mathbf{I} + \frac{1}{2} \Delta \omega \right] \quad (5.6)$$

where $\Delta \omega$ is the central difference integration of the rate of spin, given by

$$\Delta \omega = \text{asym} \left[\frac{\partial \Delta \mathbf{u}}{\partial \mathbf{x}_{t+\Delta t/2}} \right] \quad (5.7)$$

The approximate integration techniques used to define the strain and rotation measures were deemed inappropriate for applications in which both strains and rotations are large and the material exhibits significant anisotropic behaviour. This condition may arise for finite strain analyses using kinematic hardening plasticity models with the induction of anisotropy through straining. For practical purposes with typical material parameters, inaccurate solutions may be anticipated for such material models when strain magnitudes exceed values of 20 to 30 percent (Hibbitt et al., 1994). An isotropic hardening constitutive model, described in Section 5.2.3, was implemented in the present study, where peak strain levels of the order of 100 percent were developed in the simulation of a scouring event.

Updated Lagrangian (relative) Formulation

In the finite element approach to continuum mechanics problems, there are three alternative methods by which to describe the deformation of a continuous medium; these are termed spatial, referential and relative formulations (Gadala et al. 1983; Gadala and Oravas, 1984). In the spatial or Eulerian formulation, a condition of flow is modelled within a fixed region of space, and the current position of a material point in motion is implicitly dependent on the variable time. This approach is inappropriate for the representation of moving boundaries and history - dependent materials, as required in the analysis of ice scouring. In the referential formulation, the motion of a material point is described in relation to an arbitrarily selected reference configuration. The total Lagrangian formulation is a particular referential description where the initial state is selected as the reference configuration. The relative or updated Lagrangian formulation

is also referential in nature however, in this case, the current state is selected as a time - dependent reference configuration.

An updated Lagrangian formulation was implicit to the analysis performed as part of the present study. This approach facilitated the accurate definition of the material stress history, the boundary conditions, and the stress and strain states, as material points were coincident with the finite element mesh throughout the deformation process. The incremental analysis procedure was based upon the following concepts (Nagtegaal and De Jong, 1981).

(1) During each increment, a Lagrangian formulation was used : the state variables were defined with respect to the state at the start of the increment.

(2) At the end of each increment, the state variables were revised (updated) with respect to the state at the end of the increment.

A computational limit may be exceeded where very large local deformations occur, as severe distortion of the elements may lead to loss of accuracy and eventually to numerical divergence. This condition may be partially alleviated by the implementation of a method of description which incorporates aspects of both the Lagrangian and Eulerian formulations. In this approach, referred to as an Arbitrary Lagrangian - Eulerian (ALE) formulation, the mesh boundaries coincide with the material boundaries; however, the deformations of the mesh and the material are independent of each other. The application of this method to the analysis of ice scouring was considered impractical in the present study, owing to the history - dependence of the material behaviour which introduces additional convective terms in the formulation (Liu et al., 1987). However, recent ALE finite element models circumvent some of these numerical difficulties

(e.g. Huetink et al., 1990; van den Berg et al., 1991, 1992) and may represent a viable alternative for further investigation of the scour problem.

Interactive mesh rezoning techniques may also be introduced into Lagrangian codes to address the condition of mesh degeneration associated with very large local deformations (e.g. Flower and Hallquist, 1986; Shih et al., 1990). The criterion for rezoning is extreme element distortion in regions of high strain gradients, since elements may represent states of uniform strain accurately irrespective of the strain magnitudes experienced. The procedure involves definition of a new mesh for the deformed continuum, and transfer of the current state of the material onto the revised mesh. In the general case, the elemental and nodal data, including the stress and strain states, may be interpolated, deleted, added, or translated during each displacement increment. The code implemented in the present study provided a limited rezoning capability for use with two - dimensional first - order elements. This capability was not employed in the analysis, as it was insufficient to allow for adaptive mesh refinement throughout the simulation of an idealized scouring event.

Element Selection

An important aspect of the behaviour of soils is that discontinuities may form under certain conditions. Discontinuities which are pre - existing in the soil mass are relatively straightforward to deal with numerically, in that their position is known *a priori*. On the other hand, discontinuities which form in an indeterminate manner during the course of soil deformation, such as failure surfaces during a scouring event, are more difficult to deal with in an analysis. In the finite element method, element shape functions are

defined such that displacements vary continuously, and discontinuities may only be approximated by zones of elements undergoing intense shear deformation. In the analysis of the corresponding large strain problems, the element types used must therefore be tolerant to localized mesh distortion. Lower - order elements were recommended for cases in which large strains and high strain gradients are anticipated (Nagtegaal et al., 1974; Nagtegaal and De Jong, 1981). For a given number of nodes, lower - order elements were noted to provide the greatest number of locations at which some component of the gradient of the solution may be discontinuous.

The condition of zero volume change throughout an element leads to constraints on the deformation of the element (Nagtegaal et al., 1974; Sloan and Randolph, 1982). For incompressible or nearly incompressible cases, the predicted response of the finite element model may be too stiff, due to the restriction imposed on the modes of deformation which assemblages of elements are capable of exhibiting. In order to obtain accurate solutions for undrained problems, the number of degrees of freedom within each element must exceed the number of constraints imposed by the condition of zero volume change. In accordance with this requirement, first - order (4 - noded quadrilateral) elements were found to be inadequate for use in the analysis of undrained problems in plane strain configurations (Sloan and Randolph, 1982). This improper behaviour may be avoided by amendment of the element formulation to address the incompressibility constraint, or through the implementation of higher - order elements in the analysis.

In the selection of element types for the present study, it was necessary to accommodate large strain and essentially undrained conditions, as were relevant to the analysis of ice scouring. Rectangular 8 - noded isoparametric elements with biquadratic

displacement and bilinear pore pressure description were employed in the plane strain discretization of the soil domain. This element type was amenable to fully - coupled effective stress analysis, and allowed for the incompressibility constraint imposed by undrained conditions. A reduced integration scheme was used in forming the stiffness matrices and internal forces for the element, and this served to increase the solution accuracy and also to decrease the associated computational costs. Since an updated Lagrangian formulation was used, the element stiffness was formed in the current deformed configuration of the element. It was noted that 8 - noded isoparametric elements are sensitive to the positions of the mid - side nodes, and severe distortion may inhibit linear strain variation over the element and decrease the rate of solution convergence (Nagtegaal and De Jong, 1981).

5.2.2 Material Nonlinearity

Effective Stress Analysis

The soil was modelled as a two - phase material in accordance with the principle of effective stress. Only time effects due to primary consolidation were considered; the behaviour of the soil skeleton was assumed to be rate and time independent. The finite element mesh was associated with the solid phase or soil skeleton, and pore fluid flow was permitted throughout the mesh. A continuity relationship was defined for the pore fluid based on the principle of conservation of mass, in which the viscous flow of the fluid was described according to Darcy's law. The pore fluid continuity and the stress equilibrium equations formed the basis for the coupled deformation / diffusion solution.

The coupled problem was nonlinear and unsymmetric with the inclusion of the effects of material and geometric nonlinearities, and permeability dependence on the void ratio.

Modified Cam - Clay

The constitutive model adopted for use in the present study was the Modified Cam - clay model (Burland, 1967; Roscoe and Burland, 1968). The model is based on the concepts of critical state theory (Schofield and Wroth, 1968; Wood, 1990) and is known to successfully reproduce well - established experimentally determined behaviour for soft clays. Modified Cam - clay is an elastic - plastic model, and includes the following attributes for the description of the soil response : (1) an elasticity theory which characterizes the elastic, recoverable deformations of the soil; (2) a yield surface which delineates a boundary in a general stress space, within which deformations may be considered to be elastic and recoverable; (3) a flow rule or plastic potential which specifies the mode of plastic deformation that occurs when the soil is yielding, and (4) a hardening law which defines the expansion of the yield surface and the absolute magnitude of the plastic deformation. The assumptions of the model in relation to each of these attributes are reported briefly in this section, with discussion entirely in terms of effective stresses. The model was implemented numerically through backward Euler integration of both the flow rule and the hardening law, as presented in detail by Hibbitt et al. (1994).

In the formulation of the model, the state of stress is defined by the effective stress quantities p and q , which represent the mean normal stress and the deviatoric

stress, respectively. The corresponding incremental strain variables are $\delta \varepsilon_p$ and $\delta \varepsilon_q$, which represent the volumetric and deviatoric components of the strain. In terms of the principal effective stresses and strains, the volumetric and deviatoric stresses and strain increments are given by the following general expressions :

$$\begin{aligned}
 p &= \frac{1}{3} (\sigma_1 + \sigma_2 + \sigma_3) \\
 q &= \frac{1}{\sqrt{2}} [(\sigma_1 - \sigma_2)^2 + (\sigma_2 - \sigma_3)^2 + (\sigma_3 - \sigma_1)^2]^{1/2} \\
 \delta \varepsilon_p &= \delta \varepsilon_1 + \delta \varepsilon_2 + \delta \varepsilon_3 \\
 \delta \varepsilon_q &= \frac{2}{3} [(\delta \varepsilon_1 - \delta \varepsilon_2)^2 + (\delta \varepsilon_2 - \delta \varepsilon_3)^2 + (\delta \varepsilon_3 - \delta \varepsilon_1)^2]^{1/2}
 \end{aligned} \tag{5.8}$$

These quantities are related to the first and second invariants of the stress tensor and the strain increment tensor.

The elastic and plastic responses of the soil are distinguished by separation of the mechanical deformation into recoverable (elastic) and nonrecoverable (plastic) components. For large strain problems, definition of the strain rate measure in accordance with Equation 5.3 and the assumption of small elastic strains (negligible compared to unity), results in the usual additive strain rate decomposition for incremental plasticity models, expressed as

$$\delta \varepsilon = \delta \varepsilon^e + \delta \varepsilon^p \tag{5.9}$$

in which $\delta \varepsilon$ are the total strain rates, and the superscripts e and p refer to the elastic and plastic components, respectively.

The soil is assumed to behave as an isotropic elastic material within the yield surface, and recoverable changes in volume are associated only with changes in mean

effective stress. An unloading - reloading line for a particular stress state within the yield surface represents the elastically attainable combinations of the specific volume v and the mean effective stress p . The equation for the unloading - reloading line (denoted URL in Figure 5.2) is described as a linear relationship between the specific volume and the logarithm of the mean effective stress in the form

$$v = v_x - \kappa \ln p \quad (5.10)$$

where the parameter κ describes the gradient of the line and v_x is the specific volume associated with a unit value of the mean effective stress. Since a change in specific volume δv produces an increment of volumetric strain $\delta \epsilon_p$, Equation 5.10 can be written as an incremental relationship, given by

$$\delta \epsilon_p^e = \kappa \frac{\delta p}{v p} \quad (5.11)$$

in which the superscript e again indicates an elastic strain increment. The definition of a constant slope κ of an unloading - reloading line in the compression plane implies an elastic bulk modulus K that increases with the mean effective stress according to :

$$K = \frac{v p}{\kappa} \quad (5.12)$$

It is also assumed that recoverable shear strain increments $\delta \epsilon_q^e$ are induced by changes in the deviator stress q such that

$$\delta \epsilon_q^e = \frac{\delta q}{3G} \quad (5.13)$$

where G denotes an elastic shear modulus. With the bulk modulus given as a function of the mean effective stress, limitations are imposed on the permitted selection of a variable

or constant shear modulus (Zytynski et al., 1978). In practice, the value of G might be deduced through a specified constant value of the Poisson's ratio ν , leading to a shear modulus that is dependent on the mean stress in the same manner as the bulk modulus (Britto and Gunn, 1987).

The Modified Cam - clay yield surface describes an elliptical shape in effective stress $p : q$ space, as depicted in Figure 5.2. The yield surface is centred on the p axis and passes through the origin, with size defined by p_c , the maximum mean effective stress to which the soil has been subjected in its past history. An equation defining the yield surface may be written in the following form :

$$\frac{p}{p_c} = \frac{M^2}{M^2 + \eta^2} \quad (5.14)$$

in which $\eta = q/p$ is the ratio of the deviator and mean effective stresses, and M is a constant model parameter equal to the slope of the critical state line, as described below. The change in size of the yield surface p_c is dependent upon changes in the effective stresses p and q as the soil yields, in accordance with the differential form of Equation 5.14. In order to specify the yield surface within a general framework for elastic - plastic models as presented by Wood (1990), Equation 5.14 can also be expressed as

$$f(p, q, p_c) = q^2 - M^2 [p(p_c - p)] = 0 \quad (5.15)$$

where the yield function f delineates the boundary of elastically attainable combinations of the effective stresses.

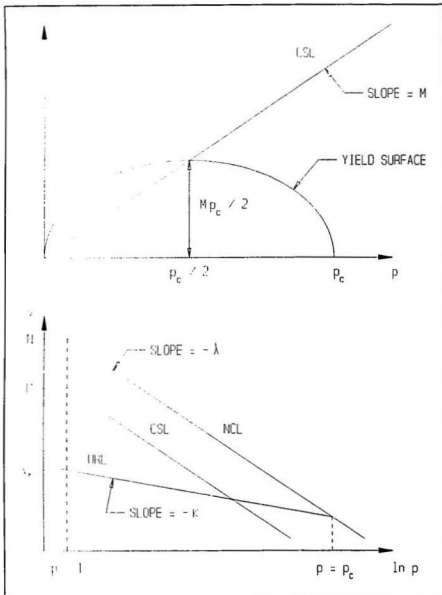


Figure 5.2 Top : Modified Cam - clay yield surface and critical state line in effective stress space; Bottom : Normal compression (NCL), unload - reload (URL), and critical state lines (CSL) in compression plane

The concept of normality of associated plastic strain increments is adopted to deduce the change of plastic volumetric strain which must accompany an increment of plastic shear strain, as the soil yields. For associated flow, the yield function f and the plastic potential g are identical, and the vector of plastic strain increments acts in the direction of the outward normal to the yield surface, such that

$$\frac{\delta \varepsilon_p^p}{\delta \varepsilon_q^p} = \frac{\partial g / \partial p}{\partial g / \partial q} = \frac{M^2(2p - p_c)}{2q} = \frac{M^2 - \eta^2}{2\eta} \quad (5.16)$$

The flow rule given by Equation 5.16 provides an indication of the relative magnitudes of the individual components of plastic strain, when plastic deformations occur.

The isotropic hardening or expansion of the yield surface at constant shape, is assumed to depend upon the normal compression of the soil. The normal compression stress p_c provides a link, through the hardening law, between the size of the yield surface in effective stress space and the isotropic normal compression line in the compression plane (denoted NCL in Figure 5.2). A linear relationship between the specific volume v and the logarithm of the mean effective stress is employed to describe the isotropic normal compression, in the form

$$v = N - \lambda \ln p_c \quad (5.17)$$

where λ is the gradient of the line and the parameter N defines the position of the line in $p : v$ space, being the specific volume associated with a unit value of the mean effective stress. The plastic volumetric strain increments are defined by the change in size of the yield surface in accordance with the following relationship :

$$\delta \varepsilon_p^p = (\lambda - \kappa) \frac{\delta p_e}{v p_e} \quad (5.18)$$

which serves as the hardening law for the model, and allows for the assessment of the magnitude of the plastic strain.

The model includes the concept of a critical state for the soil in which plastic shear distortion may continue indefinitely without changes in volume or effective stresses. The critical state condition may be expressed as

$$\frac{\partial p}{\partial \varepsilon} = \frac{\partial q}{\partial \varepsilon_q} = \frac{\partial v}{\partial \varepsilon_q} = 0 \quad (5.19)$$

In effective stress $p : q$ space, the locus of ultimate states, referred to as the critical state line (denoted CSL in Figure 5.2), is defined according to

$$q_{cs} = M p_{cs} \quad (5.20)$$

where the parameter M , the slope of the line, can be thought of as a frictional constant relating the shear strength to the effective stress level. In the compression plane, the critical state line is parallel to the isotropic normal compression line, given by a linear relationship of a similar form :

$$v_{cs} = \Gamma - \lambda \ln p_{cs} \quad (5.21)$$

in which the parameter Γ defines the specific volume associated with a unit value of the mean effective stress at critical state.

In drained or undrained deformation of normally or lightly overconsolidated soil, yielding initially occurs with stress ratio $\eta < M$ on the wet side of critical state, as

illustrated in Figure 5.3 (a). For yielding within this region, the plastic volumetric strain component is compressive, and continued deformation is associated with expansion of the yield surface, and plastic hardening of the soil. Conversely, in drained or undrained deformation of heavily overconsolidated soil, yielding initially occurs with stress ratio $\eta > M$ on the dry side of critical state, as illustrated in Figure 5.3 (b). For yielding within this region, the plastic volumetric strain component is dilative, and continued deformation is associated with contraction of the yield surface, and plastic softening of the soil. Although the model provides predictions of plastic strain for stress paths which reach yield on the dry side of critical state, softening is an unstable process which fails to satisfy the condition of normality of plastic strain increments. In this region, failure involves the localization of shear distortion within distinct rupture bands prior to reaching the yield surface as defined for the model.

The idealized stress - strain behaviour under states of constant mean effective stress, with increasing deviatoric strain, is also shown in Figure 5.3. Following initial yield, which is dependent upon the extent of overconsolidation, the soil experiences hardening or softening until the effective stress state reaches the top of the current yield surface with stress ratio $\eta = M$, where unrestricted plastic shear distortion can occur without further expansion or contraction of the yield surface. The critical state line provides a division between stress states for which positive excess pore pressures and volumetric compression may be expected to develop and those associated with negative excess pore pressures and volumetric expansion. The particular response exhibited will depend upon the initial state and the total stress path to which the soil is subjected.

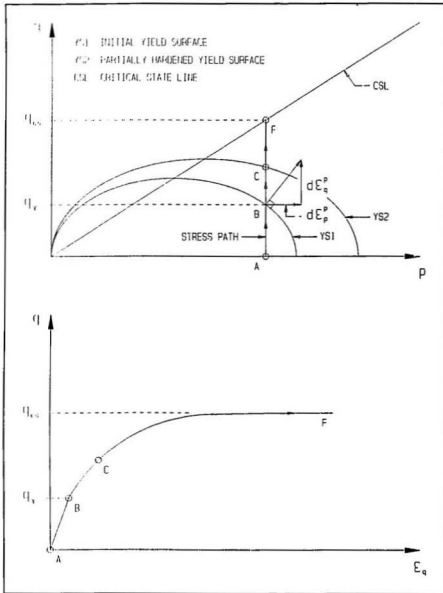


Figure 5.3 (a) Modified Cam-clay strain hardening behaviour on wet side of critical state : predicted stress-strain response for shear test at constant mean effective stress

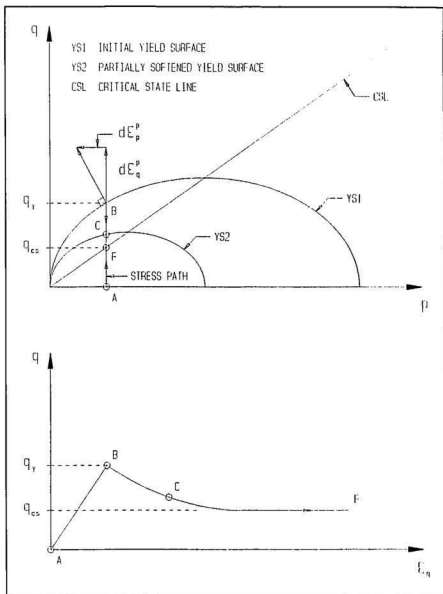


Figure 5.3 (b) Modified Cam - clay strain softening behaviour on dry side of critical state : predicted stress - strain response for shear test at constant mean effective stress

5.2.3 Boundary Nonlinearity

Rigid Surface - Soil Interaction

A rational simulation of ice scouring required modelling of the interaction between the deformable soil medium and a rigid body idealization of the model keel, under prescribed motion. A finite - sliding formulation was adopted which allowed for separation and relative displacement of finite magnitude, and arbitrary rotation of the contacting surfaces. The finite - sliding capability was implemented by means of rigid surface interface elements which model contact between an element face, attached to the deforming medium, and a rigid body. The elements used were compatible with the discretized soil domain and incorporated the corresponding nodes at the contact surface, as illustrated in Figure 5.4. Three nodes of each element formed part of the deforming mesh, and a final node acted as a reference node for the rigid body. The reference node was common to each of the interface elements employed to detect contact with the rigid body. The surface geometry of the rigid body was described analytically in two - dimensions in terms of a series of interconnected straight line segments. The rigid body reference node was allowed both translational and rotational degrees of freedom, and boundary conditions were applied to the node to define the motion of the rigid body during the event.

The interface elements were required to satisfy the conditions of equilibrium and continuity of displacements in the normal contact direction. In Figure 5.4, point A is a node on the contact surface of the deforming mesh with current coordinates x_A , and point C is the rigid body reference node with current coordinates x_C . Point B is the

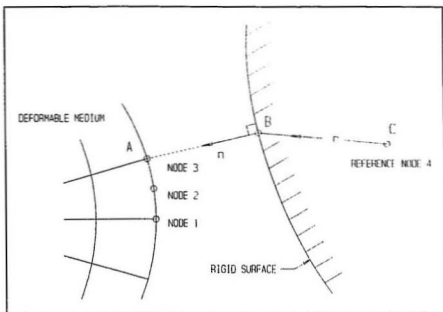


Figure 5.4 Node ordering for interface elements and definition of rigid surface geometry

nearest position to A on the rigid surface, at which the normal to the surface n is directed through A. The variable h then provides a measure of the overclosure of the interacting surfaces, given as the distance from B to A along $-n$, such that

$$n h = -x_A + x_C + r \quad (5.22)$$

where r is defined as the vector from C to B. If the value of h was less than a specified clearance below which contact occurred, a contact constraint was enforced through Lagrange multiplier techniques, as detailed by Hibbitt et al. (1994). The kinematic measures of overclosure and relative shear sliding, constructed at each integration point of the elements, were used to introduce constitutive relations which define the local material response at the contacting surfaces.

Surface Constitutive Behaviour

The surfaces in contact transmitted shear stress as well as normal pressure, and the contact tractions depended upon the relative motions at the interface. In the direction of the local normal, the pressure stress - clearance relationship was defined as a perfectly hard contact condition, for which the contact pressure stress σ_n at a point was given as a function of the overclosure h of the surfaces. The surfaces separated if the pressure stress was reduced to zero, and separated surfaces came into contact when the clearance between them was reduced to zero. During contact, any pressure stress could be transmitted between the surfaces, with no interpenetration.

The tangential shear stress tractions were coupled to the normal pressure stress through frictional effects. The standard Coulomb friction model was used to describe the shear response at the interface. As illustrated in Figure 5.5, relative motion or slip was not permitted if the equivalent shear stress τ_{eq} was less than the critical stress τ_{cr} , or

$$\tau_{eq} = \{ \tau_1^2 + \tau_2^2 \}^{1/2} < \tau_{cr} \quad (5.24)$$

where the critical stress was proportional to the contact pressure σ_n , according to :

$$\tau_{cr} = \sigma_n \tan \delta = \mu \sigma_n \quad (5.25)$$

in which δ is the angle of friction at the interface, and μ is the corresponding Coulomb friction coefficient. For two - dimensional models adopted in the present study, an isotropic friction condition was implicit. Frictional slip occurred when the equivalent stress reached the critical stress value. For isotropic friction, the direction of the slip and

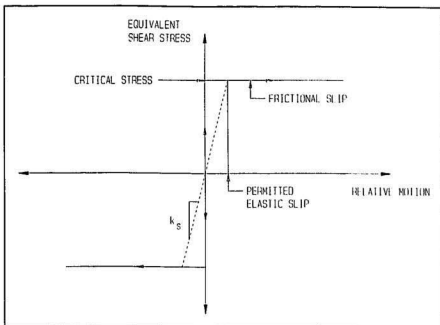


Figure 5.5 Non - local interface friction model, for which the condition of no relative motion was approximated by stiff elastic behaviour, as shown by the dashed line

the frictional shear stress coincide, which may be expressed in the form

$$\frac{\tau_i}{\tau_{eq}} = \frac{\delta \gamma_i}{\delta \gamma_{eq}} \quad (5.26)$$

where $\delta \gamma_i$ is the slip rate in the i - direction, and $\delta \gamma_{eq}$ is the equivalent slip rate, given by

$$\delta \gamma_{eq} = \{ \delta \gamma_1^2 + \delta \gamma_2^2 \}^{1/2} \quad (5.27)$$

In the numerical implementation of the friction model, the condition of no relative motion or sticking response, was approximated by stiff elastic behaviour. The elastic stiffness k_s was defined such that the relative motion was bounded by an allowable

maximum elastic slip, permitted before frictional slip occurred. This approximate approach may be viewed as an implementation of a non - local friction model, in which the Coulomb condition was not applied at a point, but was weighted over a small area of the interface (Oden and Pires, 1983).

5.3 Implementation of Analysis

The theoretical approach should be equally valid in predicting the response of both the small scale centrifuge model and the corresponding full scale event. In the present study, the prototype full scale conditions were simulated directly in the finite element analysis. The centrifuge model test and the numerical analysis both provided data which were used to compare numerical predictions and experimental observations, in accordance with the relationship presented in Figure 5.1.

5.3.1 *In situ* Stress State

The numerical analysis was implemented through the specification of history data which defined the sequence of events or loadings for which the response of the model was sought. For the physical model, the reconsolidation phase on the centrifuge altered the initially uniform effective stress field of the specimen to a distribution of effective stresses which were in equilibrium with the prescribed acceleration field and boundary conditions. This *in situ* effective stress state and the corresponding specific volume conditions were established in the initial step of the analysis, through the application of user subroutines, defined in accordance with the following assumptions.

The predicted response of the soil was dependent upon the stress history and the unloading relation assumed for conditions prior to the initial state defined in the analysis. Soil loading and unloading were taken to be one - dimensional such that the principal stress directions were vertical and horizontal. The *in situ* horizontal effective stresses were computed from the *in situ* vertical effective stresses and the coefficient of lateral earth pressure at rest K_0 . The K_0 values were defined based on the semi - empirical relationships proposed by Wroth (1975) (Equation 4.4) for initial one - dimensional unloading following one - dimensional normal consolidation, and were bounded by the coefficients of passive and active earth pressure. The initial values of the specific volume were computed from the corresponding *in situ* mean effective stresses and the known history of overconsolidation of the soil, in accordance with Equations 5.10 and 5.17. The initial size of the yield surface p_c for a given soil element was determined from the maximum effective stresses, using the expression for the yield surface given by Equation 5.14. The imposed laboratory pre - consolidation stresses defined the maximum effective stress values at near surface depths, such that the initial stress state laid within the initial yield surface.

5.3.2 Material Parameters

Theoretical modelling carried out with complex constitutive relationships and numerical procedures may be susceptible to hidden inaccuracies, numerical instabilities, lack of unique solutions, and other errors. The material parameters used in the analyses were therefore derived from an existing base of data, such that validation of the analysis

methods was not compromised by empirical modification of the selected input values. Typical material properties data for Speswhite kaolin clay were presented in Section 2.4.1. The Modified Cam - clay model, as implemented in the present study, involved specification of five parameters, each of which has identifiable physical significance. To allow for a coupled pore fluid diffusion and deformation solution, values of the vertical and horizontal permeabilities were also defined for the material. Furthermore, selection of the interface angle of friction was required, with use of the Coulomb friction model to describe the surface interaction.

The critical state stress ratio, M

The critical state is approached asymptotically by a normally consolidated or lightly overconsolidated specimen as it is sheared monotonically, and represents the state at which the soil experiences continued shear distortion without further changes in volume or effective stresses. It is found from empirical evidence that, at the critical state, the stress ratio $M = q_{cs} / p_{cs}$ is independent of the mean effective stress, defined in accordance with Equation 5.20. The value of M may be determined by plotting the stress paths of appropriate shear tests in $p : q$ space, and computing the stress ratio associated with large strains at the ultimate or failure conditions in the tests. The results are, in some cases, observed to differ between triaxial compression and extension tests, and this effect could be incorporated within the constitutive model by adopting a non - circular generalization of the yield locus in the octahedral plane. A direct relationship also exists between the critical state stress ratio and the effective angle of friction at constant

volume ϕ_{cv} , given by the following expression for triaxial compression :

$$M = \frac{6 \sin \phi_{cv}}{3 - \sin \phi_{cv}} \quad (5.28)$$

A series of undrained triaxial compression tests with pore pressure measurement were conducted by Davidson (1980) on isotropically compressed specimens of Speswhite kaolin, encompassing a range of overconsolidation ratios from 1.0 to 7.0. Davies (1981) performed tests on specimens subjected to one - dimensional compression, as relevant to the stress state imposed during laboratory pre - consolidation of centrifuge models. The results of both test series were used to define a unique locus of end points in effective stress space, described by a straight line passing through the origin with gradient $M = 0.88$. Al - Tabbaa (1984) presented data from drained triaxial tests on one - dimensionally compressed specimens with an overconsolidation ratio of 2.0. The critical state stress ratio in triaxial compression was higher in comparison with the result obtained in triaxial extension, with average values of $M = 0.90$ and 0.68 respectively. Values of the parameter M for Speswhite kaolin, as reported by other research workers included the following : 0.8 (Knogle, 1979); 0.88 (Houlsby, 1981); 0.90 (Clegg, 1981), and; 0.84 (Powrie, 1986).

A critical state stress ratio of $M = 0.9$ was specified for use in analyses carried out as part of the present study, corresponding with a value of the effective angle of friction $\phi_{cv} = 23^\circ$ in triaxial compression, as given by Equation 5.28. For simplicity, a circular generalization of the yield locus in the octahedral plane was adopted, implying an assumption of equal M in compression and extension.

The gradient of normal consolidation lines, λ

It is observed empirically that, for clay specimens undergoing normal compression, the relationship between the specific volume v and the logarithm of the mean effective stress p is approximately linear for a constant stress ratio path, and that the gradient λ is independent of the stress ratio. A linear relationship, as given by Equation 5.17, provides a reasonable representation of the soil behaviour over a range of effective stresses of engineering interest. The value of λ may be determined from that portion of an instrumented oedometer or drained triaxial compression test which exceeds the initial pre - consolidation pressure.

The consolidation characteristics of Speswhite kaolin were investigated by Knoyle (1979) under both one - dimensional and isotropic conditions. Mair (1979) and Davies (1981) compiled the data from one - dimensional compression tests as reported by several research workers, and the results were consistent with those presented by Knoyle (1979), indicating an average gradient of $\lambda = 0.25$ over an approximate range of mean effective stresses from 100 to 600 kPa. Powrie (1986) specified a value of $\lambda = 0.26$ for Speswhite kaolin, based on the results from a series of isotropic and one - dimensional compression tests performed by Al - Tabbaa (1987). The test results displayed a reduction of the value of λ by 10 percent as the mean effective stress was increased from 60 to 600 kPa. Airey (1984) also reported a dependency on stress level, with the value of λ decreasing from 0.38 at a vertical effective stress of 25 kPa to 0.21 at 250 kPa in one - dimensional compression. A linear normal compression relationship with a constant value of the gradient of $\lambda = 0.25$, was assumed to provide an adequate

representation over the range of effective stresses which were relevant in the present study.

The gradient of swelling lines, κ

The relationship between the specific volume v and the logarithm of the mean effective stress p during swelling and recompression is also observed to be approximately linear, with gradient κ , for clay specimens subjected to constant stress ratio paths, as indicated by Equation 5.10. Since the coefficient of lateral earth pressure at rest K_0 varies with one - dimensional unloading, an oedometer capable of horizontal stress measurement is required if the value of κ is to be assessed for one - dimensional unloading rather than isotropic unloading. The empirical evidence indicates that the stress - strain behaviour on an unloading - reloading path is hysteretic, such that a single value of the parameter κ is insufficient to define the gradient. Immediately following strain path reversal the soil stiffness is higher and the value of κ is locally small, with decreasing stiffness during continued unloading / reloading.

The gradient of swelling lines for Speswhite kaolin was characterized by a value of $\kappa = 0.045$, from one - dimensional compression test data obtained by Knoyle (1979). Al - Tabbaa (1987) investigated both one - dimensional and isotropic unloading and reloading, and presented values of κ as a function of the overconsolidation ratio. The measured local gradients were given by $\kappa \approx 0.01$ on first strain reversal whereas, at an overconsolidation ratio of about 6, average values of $\kappa \approx 0.06$ were obtained. An overall result of $\kappa = 0.028$ was reported, for the complete range of overconsolidation ratios

investigated. Powrie (1986) adopted an average gradient of $\kappa = 0.05$, based on the data given by Al - Tabbaa (1987), and consistent with values assumed in preceding research on Speswhite kaolin (e.g. Davies, 1981; Almeida, 1984). Stewart (1989) found lower average values of $\kappa = 0.034$ and 0.038 for one - dimensional unloading of heavily overconsolidated specimens. In consideration of the available experimental evidence, a constant value of $\kappa = 0.04$ was considered to provide the most appropriate representation over the range of unloading / reloading conditions anticipated in the present study.

The critical state reference specific volume, Γ

As illustrated in Figure 5.2, the isotropic normal compression line and the critical state line have parallel projections in the compression plane with reference values of specific volume denoted by N and Γ respectively, where

$$\Gamma = N - (\lambda - \kappa) \ln 2 \quad (5.29)$$

in accordance with Modified Cam - clay theory. The value of Γ , representing the specific volume intercept at $p_{cs} = 1 \text{ kPa}$, is commonly taken as the single parameter required to describe the location of the lines of plastic compression in $v : \ln p$ space.

The critical state reference specific volume derived from the tests conducted by Knoyle (1979) on Speswhite kaolin was $\Gamma = 3.39$. Clegg (1981) obtained a comparable value of $\Gamma = 3.44$ and this result was also adopted in analyses performed by Davies (1981) and Almeida (1984). The extrapolation of normal compression data presented by Al - Tabbaa (1987) indicated a lower average intercept, given by $\Gamma = 3.00$. In the present study, a reference specific volume of $\Gamma = 3.44$ was used to locate the

critical state line in the compression plane, in accordance with the bulk of available experimental evidence for Speswhite kaolin.

The Poisson's ratio, ν

Changes in the deviator stress q within the yield locus, for an isotropic elastic soil, produce elastic shear strain increments which can be calculated from Equation 5.13 with an appropriate value of the shear modulus G . The empirical evidence indicates that the value of G is dependent upon stress level, and is most strongly correlated with the mean effective stress (Wroth et al., 1979). Al - Tabbaa (1987) investigated the relationship between the shear modulus and the mean effective stress, for values obtained from initial unloading / reloading in shear tests on Speswhite kaolin, and compared the results with data presented by Davidson (1980). The variation of the shear modulus with stress level was described according to the approximate relation given by $G = 62 p$, based on a least square fit to the experimental data. The introduction of the shear modulus as a function of the value of p results in non - conservative elasticity if the bulk modulus is independent of the shear stress. However, the assumption of a constant value of the shear modulus to address this theoretical requirement is inconsistent with the observed behaviour, and generally leads to greater inaccuracies in the solution.

The selection of a constant value of the Poisson's ratio ν was adopted as an alternative method by which to specify G where, from elasticity theory,

$$G = \frac{3 (1 - 2 \nu)}{2 (1 + \nu)} K \quad (5.30)$$

which implied that the shear modulus was proportional to the mean effective stress in the same way as the bulk modulus. This approach was considered to provide reasonable results where elastic behaviour does not dominate the solution, and where there is a significant variation in stress level in the soil. Al - Tabbaa (1987) observed that Poisson's ratio was constant on initial unloading and independent of the mean effective stress. For Speswhite kaolin, an average result of $\nu = 0.3$ was derived from the initial slope of one - dimensional unloading / reloading paths in $\sigma_v : \sigma_h$ space. Wroth (1975) reported a constant value of $\nu = 0.33$ for lightly overconsolidated kaolin based on the one - dimensional consolidation test data from Nadarajah (1973). This result was used in the idealization of the elastic behaviour of Speswhite kaolin for analyses performed in the present study.

The vertical and horizontal permeabilities, k_v and k_h

The permeability of the soil must be specified to model the flow of water through the soil as part of a coupled deformation / diffusion solution. An orthotropic definition is required for one - dimensionally compressed specimens, in which the value of the horizontal permeability differs from the value of the vertical permeability. The empirical evidence indicates that permeability varies with the current volumetric state of the soil. A decrease in void ratio associated with smaller void passages, will lead to a reduction in permeability, since resistance to fluid flow is primarily due to viscous effects.

Al - Tabbaa (1987) investigated the variation of permeability with void ratio for Speswhite kaolin subjected to one - dimensional normal compression. Values of

permeability were obtained from both falling - head and consolidation tests conducted using a modified oedometer which permitted radial drainage. Unique relationships between the vertical and horizontal permeability (k_v and k_h) and the void ratio e were established, in the form :

$$\begin{aligned}k_v &= 0.50 e^{3.25} * 10^{-6} \text{ mm/s} \\k_h &= 1.43 e^{2.09} * 10^{-6} \text{ mm/s}\end{aligned}\tag{5.31}$$

which described a linear dependency of the logarithm of permeability on the logarithm of void ratio. The expressions provided an acceptable fit to the experimental data for both normally consolidated and overconsolidated specimens, within a range of void ratios from 2.2 to 0.98. Comparison with the results obtained by other research workers for the vertical permeability of Speswhite kaolin (Manson, 1980; Davies, 1981; Kusakabe, 1982; Savvidou, 1984) showed limited scatter, and Equation 5.31 formed a lower bound at higher values of the void ratio. In the present study, the variation of vertical and horizontal permeabilities with the current state was accounted for through implementation of Equation 5.31 within the analysis.

The interface angle of friction, δ

The surface constitutive model implemented in the analysis required specification of the interface angle of friction δ as a material parameter, with the assumption that the soil had no effective cohesion. The frictional resistances between kaolin and different structural materials treated with various lubricants, were measured in laboratory direct shear tests, as summarized in Table 5.1. The recorded values of interface friction were low, ranging

Table 5.1 Values of the interface angle of friction between kaolin and other materials (data assembled from : Hambly, 1969; Powrie, 1986, and; Waggett, 1989)

Surface in contact with kaolin	Lubricant at interface	Contact pressure (kN / m ²)	Rate of shearing (mm / hr)	Angle of friction (deg.)
aluminum	silicone grease	70	24.0	0.57 to 0.80
stainless steel	silicone grease	100	0.33	1.13
brass	silicone grease	70	24.0	0.52 to 0.80
rubber	silicone grease	70	24.0	0.57
rubber	silicone grease	70	2.40	0.92
rubber	silicone grease	70	0.50	1.20
perspex	no lubricant	-	-	11.9
perspex	Adsil silicone spray	-	-	6.3
perspex	silicone grease	-	-	2.3

from 0.6 to 0.8° for an aluminum contact surface at which silicone grease was applied as a lubricant. The results also indicated dependency of the value of δ on the rate of shearing, where decreasing rates were associated with increasing frictional resistance. In addition, Waggett (1989) observed variation of the parameter with the degree of overconsolidation of the soil, and reported higher values of residual friction with increasing overconsolidation ratio at a kaolin / perspex interface.

A well - defined model keel / soil interface condition was provided in the experimental investigation, through use of a polished aluminum contact surface and application of Adsil silicone spray as a lubricant. The effectiveness of the lubricant was reduced, however, due to submergence of the contact surface during the event. The specified velocity of the model iceberg exceeded rates of deformation imposed in laboratory direct shear testing by several orders of magnitude. The contact surface represented a practically smooth interface under test conditions, and the effects of low values of the soil / rigid surface friction angle within the range of 2.9 to 8.5° were investigated in the analysis, as considered relevant to the interface condition prescribed in the physical model study.

5.3.3 Model Development

Finite Element Mesh

Figure 5.6 shows the general mesh configuration and the boundary conditions which were adopted in the two - dimensional plane strain idealization of the scouring process. As discussed in Section 5.2.1, rectangular 8 - noded isoparametric elements with biquadratic displacement and bilinear pore pressure description were selected for the discretization of the soil domain. The compatible rigid surface interface elements (Section 5.2.2) incorporated the nodes at the surface of the deforming soil, in addition to a common reference node associated with the interacting rigid body. The initial configuration of the rigid body was specified in terms of coordinates which connected a series of straight line segments, conforming to the geometry and prototype dimensions of the model keel.

The finite element mesh was required to accommodate high strain gradients associated with severe deformation adjacent to the rigid body. It was necessary to provide appropriate mesh refinement, such that displacement models of the selected elements could adequately approximate the solution in this region. The simulation of a scouring event also required sufficient rigid body movement to approach a relevant steady - state condition, for comparison with experimental observations. Preliminary trial - and - error analyses were conducted to determine the maximum movement of the rigid body, as dependent on the selected mesh configuration. Severe element distortion restricted allowable refinement of the mesh for which convergence was attained at large movements, and it was necessary to adopt a relatively coarse discretization over the depth of the scour cut. The achievable movement of the rigid body was directly related to the assumed mesh configuration. Comparison with the results from analyses which included finer mesh subdivisions within the scour cut depth, indicated negligible dependence on the mesh configuration over a limited range of movement of the rigid body. In the analysis of individual scouring events, the general mesh configuration was adapted as a function of the particular scour depth and keel geometry.

Boundary Conditions

The boundary conditions assumed in the analysis (Figure 5.6) approximated those imposed by the centrifuge model container (Section 3.2.1). The walls of the container provided a condition of high lateral stiffness and were coated with water - resistant grease to reduce friction. The interface at the end boundaries was treated as frictionless with consideration of the data presented in Table 5.1. The movement of nodal points

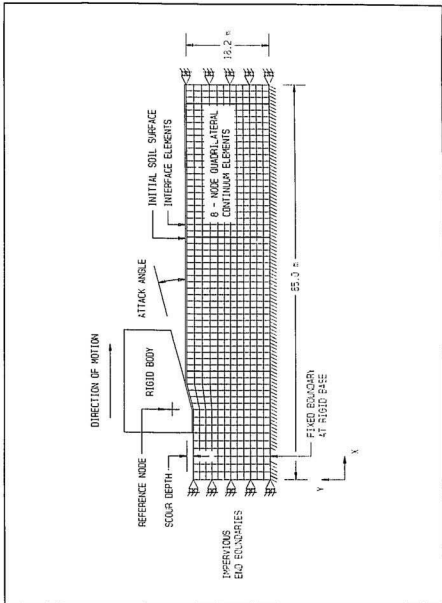


Figure 5.6 Two - dimensional plane strain idealization of scouring process : finite element mesh configuration and boundary conditions adopted in analysis

along the end boundaries was restrained in the horizontal direction. The boundary at the base of the soil specimen was interpreted as completely fixed. The nodal point displacements at the bottom boundary were restrained in both vertical and horizontal directions. During a centrifuge model test, allowance was made for two - way drainage at the top and bottom of the soil specimen. In the initial analyses performed, the soil domain was confined by impervious end boundaries and drainage was permitted at the top and bottom surfaces.

The numerical algorithm for consolidation introduces a relationship between a minimum allowable time increment and the element dimensions at a drainage boundary. Initially, consolidation is a surface phenomenon, with a singularity in the derivative of the excess pore pressures at the draining surface. A reasonable approximation with a linear pore pressure representation can only be expected when consolidation has extended deep enough to affect the first row of nodes in the interior of the soil domain. In order to accurately model the surface condition which occurs at very small times at a drainage boundary, the mesh size adjacent to the boundary and the time increment must be selected accordingly (e.g. Vermeer and Verruijt, 1981).

In the present study, the solution encompassed a significant volume of soil and an essentially undrained response was anticipated during the simulation of an event. The specification of impervious boundaries at the top and bottom surfaces was consistent with the type of analysis undertaken and the degree of refinement of the mesh, where detailed representation of the surface condition was not relevant. Comparison with analyses that made allowance for surface drainage, indicated that results were not significantly altered by the drainage boundary condition assumed at the free surface. Following very large

movement, the surface elements immediately in front of the rigid body were more irregularly distorted in analyses where a surface drainage boundary was adopted. The pore pressure tolerance that controlled the automatic time incrementation was set to a relatively large value since the nonlinearity of the material restricted the size of the increments during the transient analysis.

Sequence of Analysis

The simulation of an event was divided into a series of steps, and the state of the model evolved throughout the analysis as it responded to the history of loading. In the first step of the analysis, the *in situ* effective stress and volumetric conditions, corresponding with the equilibrium state of the physical model, were established in accordance with the assumptions presented in Section 5.3.1. This step included a process of iteration, as required to ensure a stress state which equilibrated the prescribed boundary conditions and geostatic loadings. The size of the initial yield surface was then adjusted at any material point where the yield function was violated, such that the initial stress state laid on a current yield surface.

During a physical model event, a steady - state scour depth was established following a brief period of uplift of the model iceberg from a prescribed initial position. In addition to changes in the scour depth experienced by the model iceberg, rotations about a transverse axis through the model produced small changes in the attack angle during the event. It was impractical to simulate the entire scouring episode numerically. Therefore, a uniform scour depth and a fixed value of the attack angle were adopted in the analysis. The constant scour depth used in the analysis was selected to represent the

steady - state condition. The simulation of the event was carried out as a perturbation step following the set - up of the *in situ* effective stress and volumetric conditions in the first step of the analysis. The rotation and vertical translation degrees of freedom of the rigid body reference node were restrained, and the motion of the model iceberg was idealized as a horizontal translation of the rigid body. The translation was specified over a fixed time interval such that the analysis step time corresponded with the physical model event time, and an identical rate of scouring was defined for the numerical model.

The measurements of scour - induced subsurface soil deformation presented in Chapter 4 were acquired following unloading of the imposed scour forces and self - weight stresses at the completion of a centrifuge model test. The recorded values embodied the cumulative plastic soil deformation, with expected relaxation and recovery of the elastic component of the soil response. To allow for comparison with the centrifuge test measurements, a final unloading step was included in the analysis, following the simulation of an event. A vertical translation was prescribed in this step, such that the rigid body was separated from the soil domain. With the removal of the recoverable component of the soil response as a result of the unloading step, it was anticipated that the analysis solution would correspond more closely with the deformed state exhibited during site investigation of the physical model.

5.3.4 Representation of Scouring Mechanisms

The model scours created in the experimental programme were wide in relation to their depth, corresponding to the high width / depth ratios characteristic of typical field scour

geometries. A two - dimensional plane strain idealization of the scouring process was adopted in the numerical analysis. The implementation of a two - dimensional representation imposed certain restrictions on potential mechanisms of scouring, and these limitations were evaluated with consideration of the available evidence from physical modelling.

Physical Modelling

During a scouring event, a material point initially situated at some distance in front of the advancing keel was first displaced forward and upward, as associated with the formation of a raised mound in front of the keel. The attainment of a stable configuration of the frontal mound with continued scouring involved subsequent lateral displacement of the material point, related to berm formation on both sides of the resulting incision. A common feature of the measured scour profiles was berm dimensions that were small in relation to the size of the scour created. The cross - sectional area of berm material above the initial level of the soil surface was typically found to be less than the cross - sectional area of the scour incision.

A material point in the path of the advancing keel, which initially underwent upward movement, may also experience subsequent downward displacement toward the base of the scour, with negligible lateral movement. The experimental programme provided evidence of surface material markers which were displaced to positions at the scour base, following forward movement over a limited horizontal distance. The downward displacement of surface material corresponded with compatible vertical sub -

scour displacements, which occurred in a pattern similar to the morphology of the scoured surface and attenuated with depth below the scour.

In the assessment of potential mechanisms of scouring, the requirement of volume constancy for undrained conditions must be addressed. Figure 5.7 illustrates modes of deformation during an event, as necessary to balance the volume change associated with loss of material in the scour path. The upward displacement ahead of the advancing keel represented only a transient accommodation for this volume loss, since development of the frontal mound was limited to a stable configuration with continued scouring. Lateral movement of the material provided a clearing mechanism, as required to allow for additional upward movement into the frontal mound. The material included in berm formation through lateral movement was, however, insufficient to account for the complete volume loss during scouring, and the remainder of the volume change was developed through sub - scour displacement.

The measured downward vertical displacement at positions beneath the scour must also be compensated through a mechanism which involved backward or lateral movement at depth, together with remote upward displacement. Limited evidence, as obtained for a single event (Test 02), was provided in support the former pattern of deformation; however, backward horizontal displacements as recorded for this event, diminished with the establishment of steady conditions. Furthermore, upward movement in back of the keel, associated with infilling of the scour path, was not observed. It may be inferred that the downward vertical sub - scour displacement was compensated through lateral movement at depth, and upward displacement across a wide lateral extent; however, a mechanism which involved deep - seated lateral movement was not identified explicitly

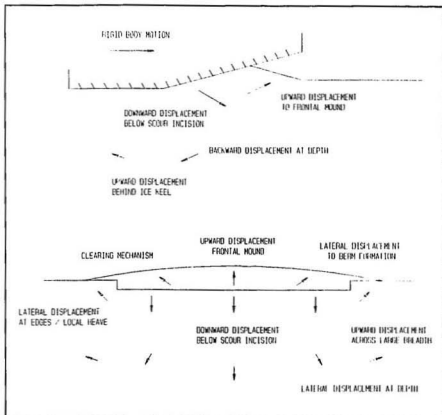


Figure 5.7 *Potential soil deformation patterns during a scouring event. Top : Side elevation view; Bottom : View in direction of motion*

in test measurements. The recorded lateral displacements were generally confined to shallow depths, corresponding with local heave of the surface adjacent to the edges of the scour. Dissipation of the material movement over an extensive area may account for the lack of correlation of the observed volume change with a characteristic mechanism. In addition, as discussed in Section 2.4.2, the effects of consolidation progressed into the material from the surface drainage boundary much more rapidly in the model than in the

corresponding prototype. Therefore, it may be concluded that the observed compression of material beneath the keel was partially accommodated through pore water drainage within a region near to the surface.

Numerical Analysis

The two - dimensional numerical model of the scouring process neglected the effects of soil displacement directed laterally outward from the scour axis. The continuum idealization did not allow for a lateral clearing mechanism of failed material within the frontal mound. The numerical model therefore represented a progressive build - up of the frontal mound, and this restricted the range of motion of the rigid body over which realistic predictions of the material response could be expected. In particular, the absence of a clearing mechanism must be taken into consideration in the evaluation of predicted resultant forces in relation to test measurements, as discussed in Chapter 6. The numerical model was also unable to account for edge effects associated with observed near - surface lateral sub - scour soil movements. Sub - scour displacement against the direction of motion of the rigid body was permitted; however, preliminary analyses indicated that this pattern of deformation was not a predominant component of the material response, with allowance for continued upward displacement in front of the rigid body.

The numerical model provided a direct representation of a full scale prototype related to the physical model scouring event through scaling laws presented in Chapter 2. An identical rate of scouring was defined for the physical model and numerical prototype events, in accordance with Equation 2.10. This implied that surficial drainage during the

physical model event, associated with the reduction of the linear scale, was not replicated in the numerical analysis. The anticipated extent of drainage and the effects of pore pressure dissipation during the physical model event were discussed in Section 2.4.2.

Chapter 6

Analysis Results and Discussion

6.1 Introduction

Comparison between the physical model event data and the finite element analysis results permitted a preliminary assessment of the admissibility and viability of the adopted numerical approach for prediction of the effects of scouring. For a mixed boundary value problem, with boundary conditions specified in terms of both displacement and stress, the stress and velocity fields must be compatible as there is no apparent independence between the two fields. Therefore, separate agreement for both the resultant forces developed and the soil deformation between theoretically computed values and experimental measurements was required for verification of the analysis methods.

The limitations of the numerical representation were described in Chapter 5. The analysis provided information on the resultant forces and the stress and displacement fields in the soil for conditions approximating a steady - state, established following limited ice movement at a uniform depth of scouring. The data acquired from each centrifuge test were applicable to a well - defined scouring event; however, the permitted degrees of freedom of the model iceberg restricted the expected range of motion over

which steady - state conditions were relevant. Equipment and instrumentation malfunction imposed further variation in some tests, which must also be accounted for in the interpretation of results. The selection of tests for comparison was therefore made so as to lessen departures from the idealized conditions adopted in the analysis.

Scour Tests 04, 05 and 09 were chosen as representative tests from the experimental programme for correlation with numerical simulations of the corresponding prototype scouring events. A realistic vertical stiffness was defined in these tests, and uniform scouring conditions were therefore established following limited initial unsteady motion. The design rate of advance was also achieved during testing, such that approximate undrained conditions were modelled in each event. Furthermore, in these tests, the accurate definition of the event was not hindered by equipment or instrumentation malfunction. Comparisons based on the data from Tests 05 and 09, which represented an identical prototype scouring event, additionally permitted assessment of the internal consistency of the physical modelling methods.

In this chapter, a comparative examination of the data acquired in representative tests with analysis results is presented. The effectiveness of the numerical representation for characterization of the effects of scouring is discussed. The implementation of the analysis to study a range of parametric variations is also required to evaluate the relative significance of test parameters and analysis restrictions; however, in the present study, practical considerations limited the scope of this objective to a direct assessment of the effects of parameters from the results of the incomplete experimental programme. Finally, a methodology through which the numerical approach may be applied in design

of buried pipelines to accommodate the loadings imposed by sub - scour movements is introduced, and associated practical implications of the study are discussed.

6.2 Analysis of Test 04

6.2.1 Input Conditions

Numerical analyses were undertaken to investigate the prototype scouring event corresponding to Test 04, described in Section 4.3.4. Table 6.1 provides a summary of input conditions employed in the analyses, including the parameters chosen to describe the behaviour of Speswhite kaolin. The procedures adopted for implementation of the analyses were outlined in Section 5.3. The prototype depth of scouring was specified as a constant value of 1.46 m, in accordance with the average equilibrium vertical position established in the experiment. The prototype rate of horizontal translation of the rigid body was set equal to the average test scouring rate of 0.073 m/s, on the basis of the scaling relationship given by Equation 2.10.

A series of initial analyses were conducted to define the finite element mesh configuration, as depicted in Figure 5.6. The coarse discretization permitted severe deformation adjacent to the rigid keel surface associated with large movements required to approach a relevant steady - state condition. The mesh configuration assumed in the final analysis of the Test 04 problem comprised 2524 nodes and 774 elements, which included both rectangular 8 - noded isoparametric elements and compatible rigid surface interface elements. The total number of variables in the model was 5624, which

Table 6.1 Summary of material parameters for Speswhite kaolin and additional input conditions, as specified in numerical analyses of representative tests

Input condition / material parameter	Values for analysis of Test 04 event	Values for analysis of Test 05 / 09 event
prototype scour depth (m)	1.46	1.21
rate of keel advance (m / s)	0.073	0.072
preconsolid. effective vert. stress σ'_{v0} (kPa)	110.	140.
normally consolidated K_{nc}	0.69	0.69
K_a variation with overconsolidation ratio	Eqn. 4.4	Eqn. 4.4
critical state stress ratio M	0.90	0.90
gradient of normal consolidation lines λ	0.25	0.25
gradient of swelling lines κ	0.04	0.04
critical reference specific volume Γ	3.44	3.44
Poisson's ratio ν	0.33	0.33
permeability coefficients k_v, k_h	Eqn. 5.31	Eqn. 5.31
interface angle of friction δ (deg.)	2.9	2.9

encompassed the degrees of freedom of the model in addition to the Lagrange multiplier variables. A total of 338 increments were needed to achieve an equivalent prototype rigid body movement of 14.5 m, and the analysis was terminated when the incremental displacement was less than 10^{-6} times the total prescribed value.

6.2.2 Analysis Results

The results of numerical analyses for the Test 04 event are presented in this section, and compared with the experimental measurements reported in Chapter 4.

Local Element Behaviour

Figure 6.1 indicates positions of reference elements in the finite element mesh, selected to illustrate patterns of local behaviour during simulation of the event. Elements EL 20, 80, and 140 were situated at a horizontal position $x = 14.4$ m in front of the initial location of the rigid body, at average depths below surface of 0.9, 2.6, and 4.3 m, respectively. Figure 6.2 displays the effective stress paths experienced by the reference elements, and the associated deviatoric stress - strain responses. In addition, the computed centroidal element excess pore pressures developed during the event are shown plotted against deviatoric strain in Figure 6.3.

For an initially overconsolidated state and deformation under essentially undrained conditions, the elastic portion of the element response was characterized by a constant value of the mean effective stress, until the deviator stress had increased sufficiently to bring the effective stress state to the initial yield surface. The computed isotropic elastic

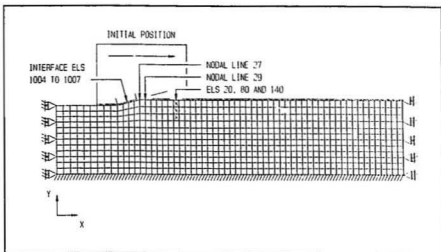


Figure 6.1 Test 04 analysis mesh configuration illustrating reference elements and nodes

response therefore involved only elastic shear strains and the pore pressures generated were equal to the changes in total mean stress. With the inception of yield, plastic shear strains developed and there was a corresponding decrease in stiffness. Yielding at near surface element positions, with initial stress ratio $\eta > M$ on the dry side of critical state, was associated with plastic softening and contraction of the yield surface. The mean effective stress increased with continued yielding until the effective stress state reached the top of the current yield surface with stress ratio $\eta = M$. The excess pore pressure decreased from an initial maximum value, attained with the onset of yield, to a minimum value at critical state. For the surface element EL 20, suppressed volumetric dilation of the soil resulted in the development of negative excess pore pressures, whereas the magnitude of pore pressure reduction following yield was less severe for the elements situated at increased depth.

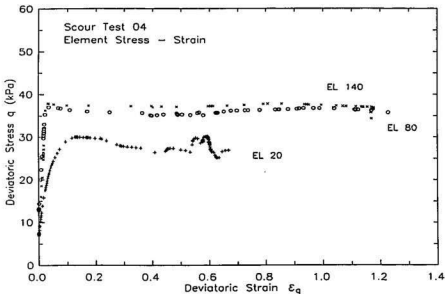
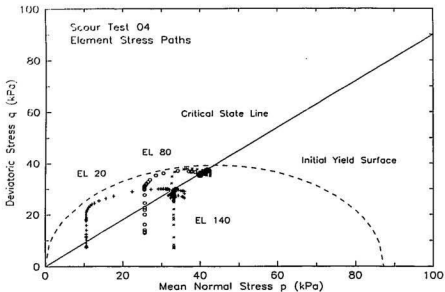


Figure 6.2 Top : Computed effective stress paths for reference elements (EL 20, 80, and 140) during event simulation; Bottom : Element deviatoric stress against strain

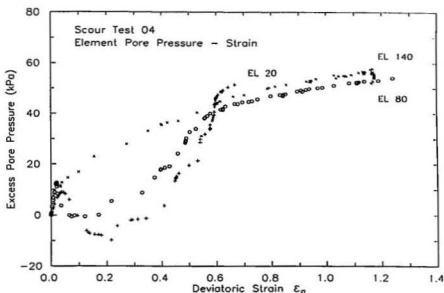


Figure 6.3 *Computed excess pore pressures during event simulation plotted against deviatoric strain for reference elements (EL 20, 80, and 140)*

The beginning of yielding corresponded with a decrease in stiffness of the soil and a kink in the pore pressure - strain relationship; however, the passage of the effective stress path through the initial yield surface was not relevant to soil failure or stability. Whereas a laboratory test on a single element of soil reaches completion as the effective stress path approaches the critical state line, field loading and numerical simulation for an element in the scour path was continued. As the effective stress path for the element progressed toward critical states, the incremental shear stiffness local to the point approached zero, and the soil was incapable of resisting any additional shear stress. The local attainment of critical states, or local failure, was initially contained or supported by surrounding soil which had not yet failed.

At critical states, deformation continued without further change in the deviator or mean effective stresses, and this implied that excess pore pressures generated were equal to the changes in total mean stress. The effective stress state remained constant; however, the total stress path moved sideways in $p : q$ space with increased total mean stress at a constant value of the deviator stress. The surface element EL 20 exhibited a sharp increase in excess pore pressure at a critical state, with notable periods of fluctuation in the rate of pore pressure development, as may be attributed to variation in load transfer associated with a stick - slip response at the rigid body - soil interface. Element EL 140, at greater depth, displayed a more uniform excess pore pressure response, with a gradual decrease in the rate of development during deformation at a critical state. Despite dissimilar initial stress states and character of response for the elements situated at different depths, comparable pore pressure magnitudes were obtained at the completion of the simulation, with higher rates of total stress change and excess pore pressure development at shallow depths. A reduction in pore pressure and the development of negative excess pore pressure values due to the suppression of volumetric expansion, was predicted for elements which experienced unloading with passage of the rigid body beyond the material point during simulation of the event. The rigid body movement was not extended over sufficient range to represent this unloading condition at the horizontal position of the selected reference elements.

The cumulative shear strains established at the termination of movement were significantly larger for elements EL 80 and 140 ($\epsilon_q = 1.24$ and 1.17 , respectively) below the depth of the scour cut, relative to the surface element EL 20 ($\epsilon_q = 0.67$) situated above the base of the rigid body. The deviatoric stress : strain response for

element EL 20 became erratic or variable at high strain levels, and may be related to the effects of extreme element distortion, associated with high strain gradients in this region.

Excess Pore Pressures

The contours of computed excess pore pressures are shown plotted in Figure 6.4 for different horizontal positions of the rigid body over the limited range of movement simulated in the analysis; results are presented for increments 50, 100, 200, and 338, corresponding with horizontal movements of 1.8, 4.1, 8.6, and 14.5 m, respectively. The spatial distribution of the experimentally recorded pore pressure changes was displayed in Figure 4E.1 for different intervals of model horizontal movement. In comparison, general agreement with the test measurements was found; the recorded pore pressures ranged between extreme values of - 37 and 88 kPa at the transducer locations, which showed reasonable correspondence with the predicted bounds illustrated in Figure 6.4. The horizontal and vertical extent of the computed excess pore pressure field also coincided with the zone of influence inferred from the transducer records; pore pressure changes were predicted at horizontal distances on the order of 25 m in front of the current model position, and at vertical distances which extended to the bottom boundary of the soil domain. In addition, the development of negative excess pore pressures within shallow regions both in front of and behind the advancing rigid body, was comparable with measured pore suctions both preceding and following passage of the model keel over a particular location.

The specification of impervious surface boundaries was consistent with the implementation of an essentially undrained consolidation analysis, as discussed in

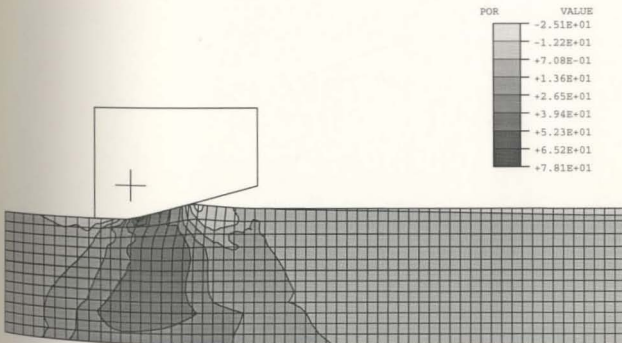
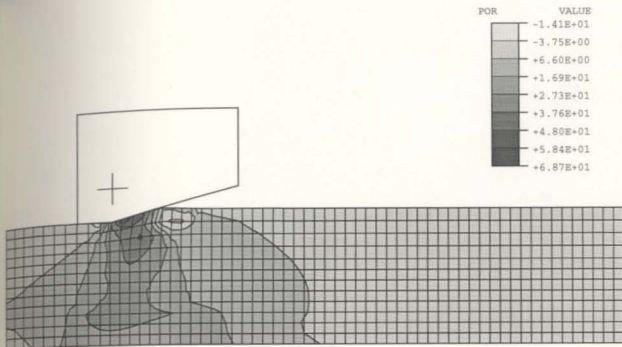


Figure 6.4 Test 04 analysis contour plots of excess pore pressure (kPa) for different rigid body positions. Top : $x = 1.8$ m; Bottom : $x = 4.1$ m

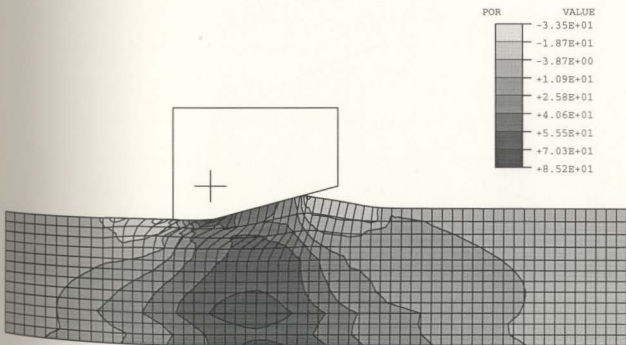
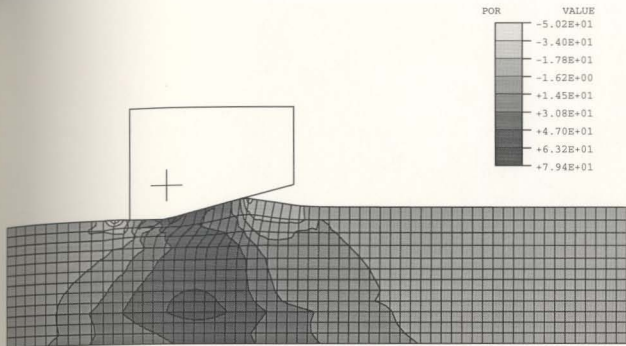


Figure 6.4 (continued) Test 04 analysis contour plots of excess pore pressure (kPa) for different rigid body positions. Top : $x = 8.6$ m; Bottom : $x = 14.5$ m

Section 5.3.3. At these boundaries, the computed excess pore pressures reached constant values with no physical significance which depended upon the loading and geometry of the solution domain.

The analysis results provided an adequate representation of the character of the local pore pressure responses, as acquired through transducer measurements during the event. Figure 6.5 presents comparisons for individual transducer records with values computed at corresponding prototype depths in the numerical model. The model predictions were provided for reference integration points located at different horizontal distances in front of the initial rigid body position, to illustrate the effect of the range of movement simulated in the analysis. The magnitude of excess pore pressure development increased with the initial horizontal distance from the reference point; however, the difference diminished as a far - field initial distance was approached and an apparent steady - state response was simulated. The computed values were compared with the measurements from transducer Channels 05, 06, 07, 04, and 01, with model locations as specified in Table 4.7. The two - dimensional analysis representation was unable to account for the measured distribution of excess pore pressures with lateral distance from the scour axis.

Comparison of the recorded pore pressure changes with analysis results indicated close correspondence of measured and predicted peak magnitudes for a given range of horizontal movement (for typical analysis reference points at $x = 13.7$ and 17.8 m in front of the initial rigid body position). The analysis results also implied similar rates of excess pore pressure development in relation to the individual transducer responses; however, some over - prediction of recorded magnitudes may be expected for simulation

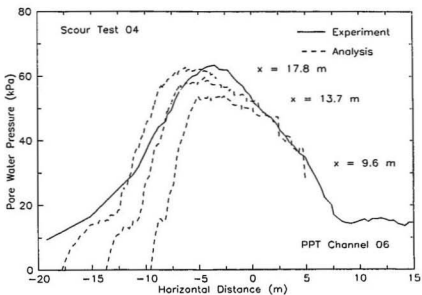
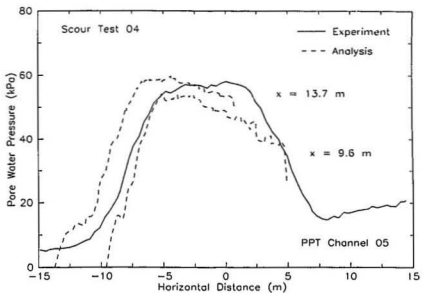


Figure 6.5 Test 04 comparison of analysis results with experimental measurements for individual pore pressure transducers

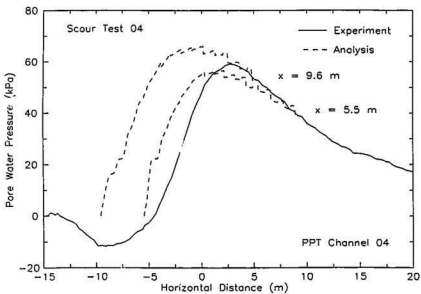
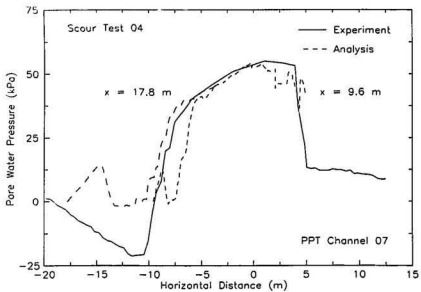


Figure 6.5 (continued) Test 04 comparison of analysis results with experimental measurements for individual pore pressure transducers

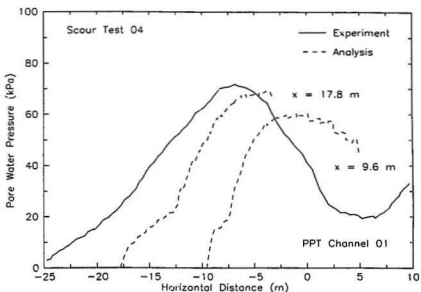


Figure 6.5 (continued) *Test 04 comparison of analysis results with experimental measurements for individual pore pressure transducers*

of an increased range of horizontal movement. The physical model loading history resulted in a more gradual initial development of excess pore pressures which may have allowed for a limited amount of dissipation and a corresponding decrease in the measured values. The apparent over-prediction of test measurements may also be partially attributable to the lateral separation of particular transducers from the scour axis. The predicted locations associated with attainment of the peak response showed reasonable agreement with the recorded values, where some experimental error was expected in determination of the relative positions of the model keel and individual transducers during the event. Comparison of computed pore pressure changes with measurements for the Channel 07 transducer, situated at a depth of 2.3 m, demonstrated that the analysis was

able to simulate the character of the response, including negative excess pore pressure development related to suppressed volumetric dilation for heavily overconsolidated soil conditions at shallow depth. In general, the test measurements showed greater variability of pore pressure magnitudes with changes in depth, in comparison with results from the analysis.

Interface Pressures

In Figure 6.6, the contact pressures for reference interface elements, acting in the direction of the normal to the surface of the rigid body, are shown plotted against horizontal position during simulation of the event. The reference elements (denoted EL 1004, 1005, 1006, and 1007) incorporated the nodes along the inclined surface of the rigid body at the initial position, as shown in Figure 6.1. The analysis results displayed the development of the normal stress with finite - sliding interaction between the rigid body and the deformable soil medium. The element responses were characterized by a build - up of compressive normal stress with movement along the inclined surface of the rigid body, to a peak value which occurred at the transition to the horizontal bottom surface; the normal stress decreased to a minimum value with further movement along the horizontal surface, although an abrupt rise in pressure was associated with the transition to loss of contact between the element and the rigid body. Computed normal stresses at the inclined and horizontal rigid surfaces may be compared with measured contact pressures acting on the model iceberg; however, no data were acquired in Test 04 due to malfunction of the inductive pressure transducers mounted on the model. The predicted reduction of normal stresses to minimum values on the horizontal surface

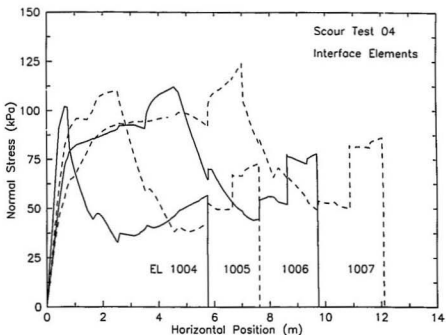


Figure 6.6 Test 04 analysis contact normal stress versus horizontal position for reference rigid surface interface elements

supported evidence from other tests in the experimental programme, from which it may be inferred that the extent of this surface had limited influence on the effects of scouring.

Resultant Forces

Figure 6.7 shows a plot of the computed horizontal and vertical components of the resultant force acting on the rigid body together with prototype forces scaled from the model test measurements presented in Figure 4.22. For the horizontal component, close agreement was obtained between computed and measured values over the complete range

of movement simulated in the analysis, to within a difference of 0.8 percent at the final horizontal position. For the vertical component, the apparent stiffness of the measured response initially exceeded the analysis result; however, correspondence between computed and measured values improved following increased movement, to within a difference of 1.3 percent at the final horizontal position. Adequate prediction of the resultant force values also served as an indication of the extent of similarity between the associated stress fields.

Several factors contributed to observed differences in computed and measured resultant force values, and to potential divergence with representation of a greater range of movement in the analysis. Measurement inaccuracies were anticipated, and values of the vertical force component, derived indirectly from the test data, were indeterminate at the inception of movement. The analysis was also unable to account for the initial separation of keel and soil and the variation of scour depth and attack angle preceding the establishment of an equilibrium vertical position and orientation. The continued build - up of failed frontal mound material represented the forces associated with the development of surcharge over a limited range of movement; however, the absence of a clearing mechanism implied an unbounded increase of the computed force and eventual over - prediction of the measured steady - state response. In addition, the analysis did not allow for interface shear forces attributable to adhesion or friction at the sides of the model keel. The expected force contribution arising from side friction was small for the practically smooth interface conditions considered relevant to the physical model study.

The influence of the interface conditions adopted in the analysis on the computed resultant force magnitudes was investigated for values of the soil / rigid surface friction

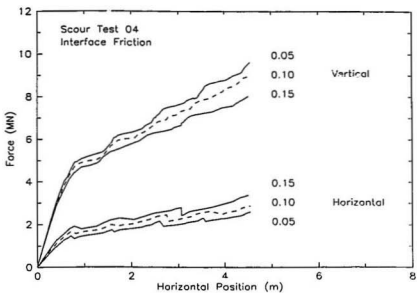
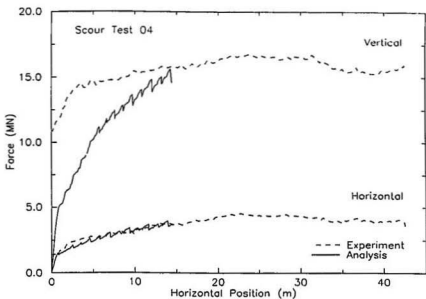


Figure 6.7 Top : Test 04 comparison of computed and measured resultant force components; Bottom : Analysis force records for different interface friction coefficients

angle of $\delta = 2.9, 5.7,$ and 8.5° corresponding to friction coefficients of $\mu = 0.05, 0.10,$ and 0.15 . Figure 6.7 shows the horizontal and vertical force components for the different interface assumptions, plotted against horizontal position for a consistent range of movement of 4.5 m. The computed horizontal force increased with greater interface friction, and a difference of 9.5 percent at the final position was associated with the 2.8° increase of the friction angle. Conversely, the computed vertical force decreased with greater interface friction, and a difference of 6.6 percent at the final position was related to the same increase of friction angle. The magnitude of the total resultant force was not altered significantly by the change in the interface condition. The use of a realistic low value of the interface friction angle in the analysis provided improved correlation with the measured responses.

Soil Deformation

Figure 6.8 shows a view of the displaced configuration of the finite element mesh and the corresponding soil displacement vectors from the analysis, following horizontal movement of 14.5 m to the final position of the rigid body. The computed displacement field exhibited discontinuities for elements adjacent to the inclined rigid surface, as may be attributable to the inadequacy of the coarse discretization to accommodate high strain gradients in this region; the large elements at the interface reflected an averaged behaviour. The available experimental data on subsurface soil displacements were derived from measurements at individual soil deformation grids, presented in Figure 4F.5. In comparison, the computed two - dimensional displacement field was qualitatively similar

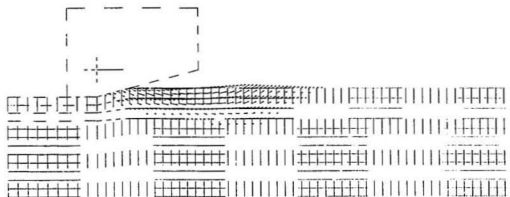
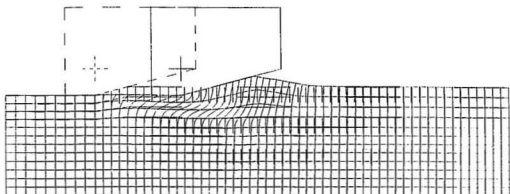


Figure 6.8 *Test 04 analysis results - final rigid body position; Top : Displaced configuration of mesh (initial shown dashed); Bottom : Displacement vectors (maximum length $x = 14.5$ m)*

to the recorded displaced configuration for an axial section through the clay specimen, as illustrated in Figure 4.26.

Displacement vectors plotted for different analysis increments displayed the development of soil deformation patterns during simulation of the event. The material points initially situated at the interface with the inclined rigid surface were displaced in a direction between the horizontal and the normal to the surface, with decreasing magnitude at greater depth. The displacement vectors rotated vertically upward with increased distance in front of the rigid surface, defining a semi-circular region of large soil displacement which extended to positions beneath the scour depth. The upward and forward displacement of soil in this region was compatible with heave of the free surface in front of the rigid body and formation of a continuous frontal mound. Small backward (negative horizontal) displacements were computed at positions below the base of the rigid body, in agreement with limited data available from other tests in the experimental programme; however, these movements were associated primarily with elastic extension which accompanied undrained compression of elements directly beneath the inclined rigid surface.

Contour plots of the horizontal and vertical components of soil displacement are presented in Figures 6.9 and 6.10, for increments 50, 100, 200, and 338, corresponding with rigid body horizontal movements of 1.8, 4.1, 8.6, and 14.5 m, respectively. The horizontal displacement field was defined by a semi-circular region of large displacement which extended well below the base of the rigid body, and diminished with distance in front of and below the scour depth at the current position of the inclined rigid surface. The plotted contours of the vertical component of displacement displayed two

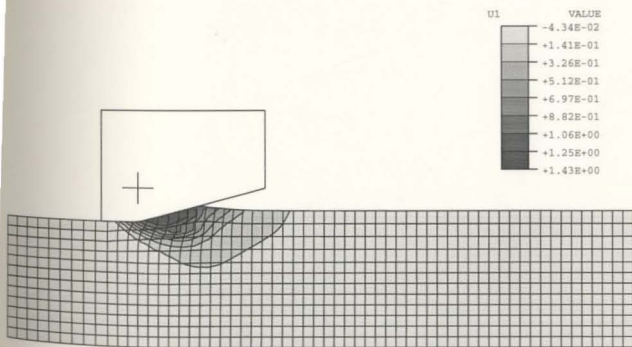
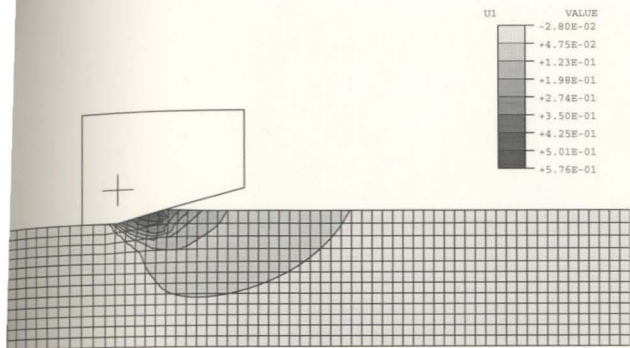


Figure 6.9 Test 04 analysis contour plots of horizontal component of soil displacement (m) for different rigid body positions. Top : $x = 1.8$ m; Bottom : $x = 4.1$ m

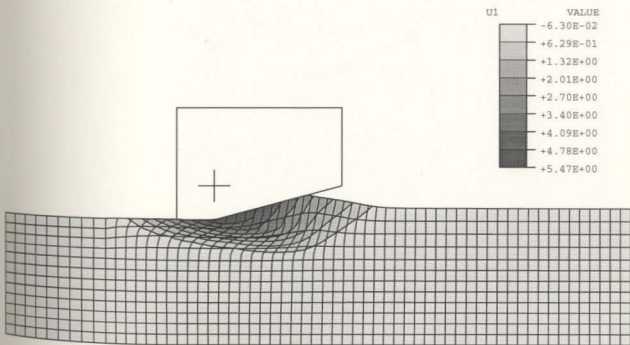
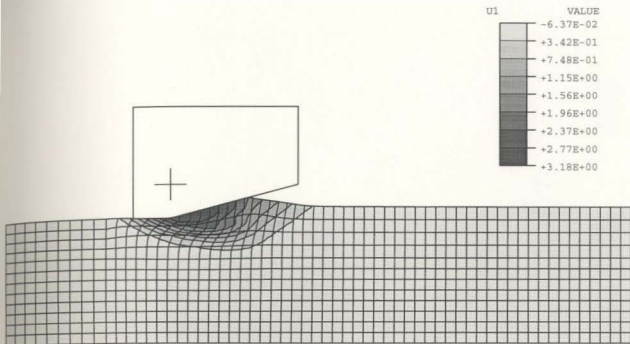


Figure 6.9 (continued) Test 04 analysis contour plots of horizontal component of soil displacement (m) for different rigid body positions. Top : $x = 8.6$ m; Bottom : $x = 14.5$ m

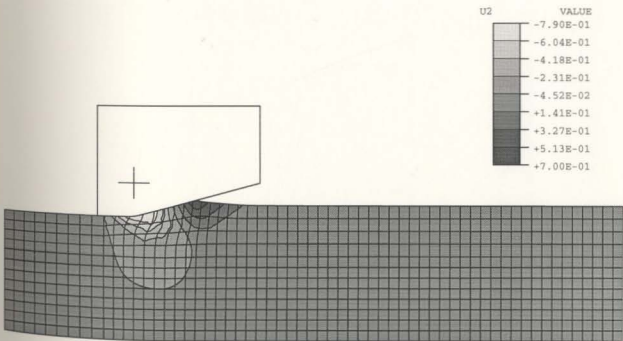
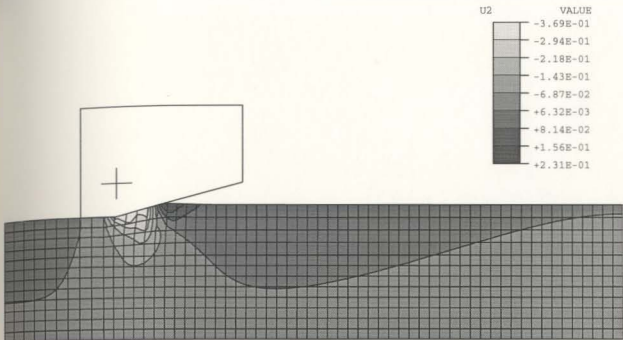


Figure 6.10 Test 04 analysis contour plots of vertical component of soil displacement (m) for different rigid body positions. Top : $x = 1.8$ m; Bottom : $x = 4.1$ m

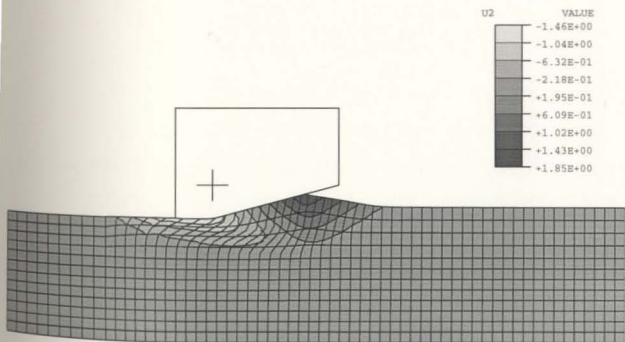
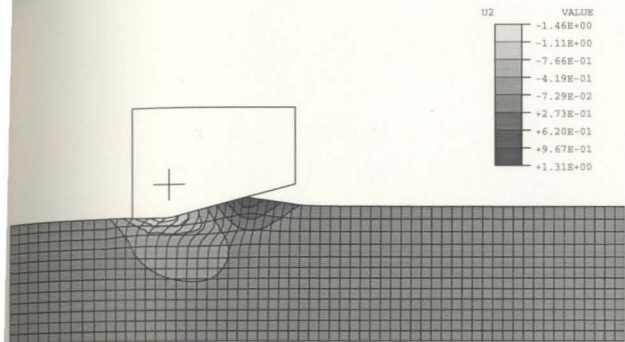


Figure 6.10 (continued) *Test 04 analysis contour plots of vertical component of soil displacement (m) for different rigid body positions. Top : $x = 8.6$ m; Bottom : $x = 14.5$ m*

distinct regions which separated upward (positive vertical) displacement, associated with formation of the frontal mound, from downward (negative vertical) displacement, related to compression beneath the rigid body, and bounded by a maximum value equal to the scour depth. A material point situated in front of the rigid body, was initially subjected to upward and forward displacement, and subsequently experienced downward and continued forward displacement with passage of the rigid body. In the assessment of analysis results, it was necessary to differentiate between the transient displacement of a material point, which was dependent upon proximity of the rigid body, and the ultimate or cumulative displacement of the same point following complete passage of the rigid body, which represented the displacement value measured in the experiment.

$$\text{The equivalent plastic strain magnitude, defined as } \bar{\epsilon}_p = \left\{ \frac{2}{3} \epsilon_{ij}^p : \epsilon_{ij}^p \right\}^{1/2}$$

in which ϵ_{ij}^p is the plastic strain tensor, served as a measure of the total accumulation of plastic strain induced during the event. Figure 6.11 shows contours of the plastic strain magnitude plotted for different increments in the analysis, in order to illustrate the propagation of a region of large (plastic) deformation during scouring. A peak magnitude of plastic strain of 110 percent was established following horizontal movement of 14.5 m to the final position of the rigid body, and values which exceeded about 15 percent were computed at a maximum depth on the order of 4.5 m or 3.0 scour depths below the base of the scour. The magnitude and extent of the region of plastic straining underwent continued growth over the complete range of movement simulated in the analysis, with decreased rate of development toward an apparent steady - state condition.

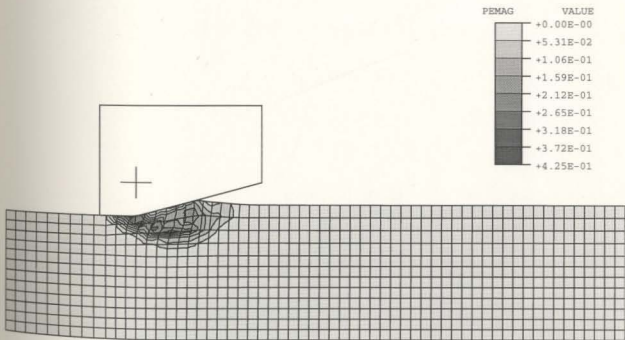
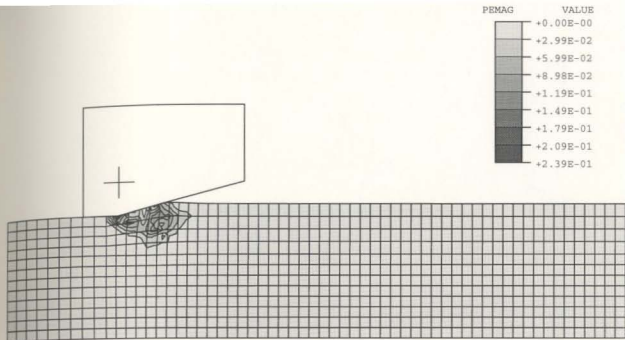


Figure 6.11 Test 04 analysis contour plots displaying magnitude of plastic strain for different rigid body positions. Top : $x = 1.8$ m; Bottom : $x = 4.1$ m

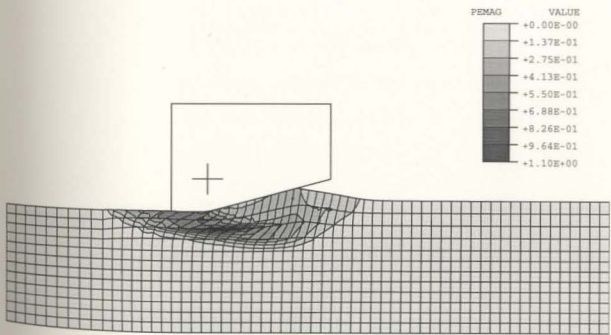
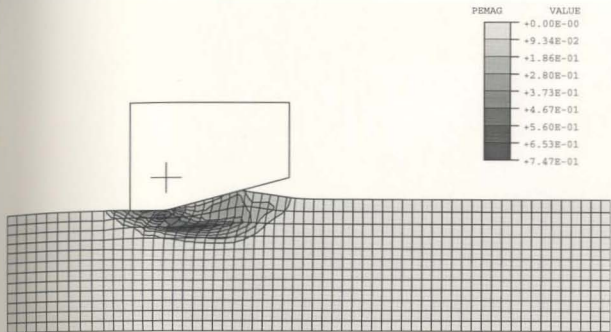


Figure 6.11 (continued) *Test 04 analysis contour plots displaying magnitude of plastic strain for different rigid body positions. Top : $x = 8.6$ m; Bottom : $x = 14.5$ m*

Figures 6.12 and 6.13 provide comparisons of computed and measured profiles of the horizontal and vertical components of soil displacement, respectively. The test values were recorded subsequent to completion of the event, as presented in Figure 4.27. The analysis results are displayed for reference Nodal Lines 27 and 29, with initial positions in front of the rigid body as depicted in Figure 6.1, selected to represent the cumulative response following complete passage of the rigid body beyond the initial positions. The computed profiles of horizontal displacement displayed increased magnitude for nodal lines at greater distance in front of the initial rigid body position; the development of an equilibrium displaced configuration was precluded by the requirement for continuity of the displacement field together with representation of a continued build - up of the frontal mound. To ensure relevant simulation of the deformed state exhibited during site investigation of the physical model, the analysis results were presented for conditions following unloading and associated elastic rebound, at the completion of the event. Figure 6.14 shows computed displacement profiles for conditions before and after elastic rebound. In comparison, the displacement results indicated negligible overall change with allowance for rebound; however, small negative horizontal displacements at depth were found to represent an elastic portion of the response which was recovered upon unloading.

The soil displacement profiles for the reference nodal lines in the analysis displayed close correspondence with the test records, in consideration of measurement inaccuracies and inherent limitations of the idealization. Some dissimilarity was also anticipated due to variation of measured results acquired from grids at different locations within the clay specimen. The horizontal component of displacement was larger in

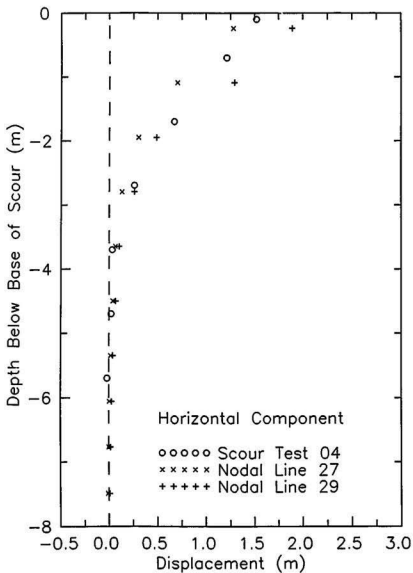


Figure 6.12 Test 04 comparison of measured and computed values of the horizontal component of soil displacement plotted against depth below the scour base

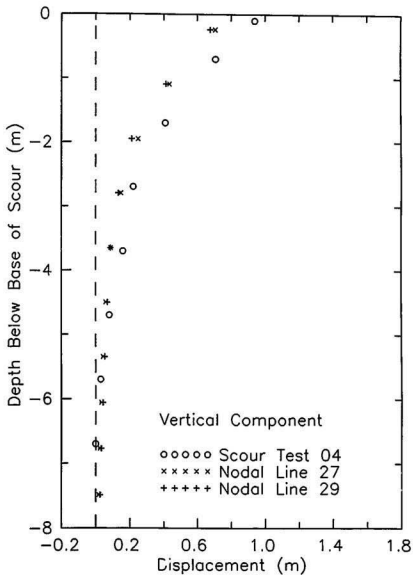


Figure 6.13 Test 04 comparison of measured and computed values of the vertical component of soil displacement plotted against depth below the scour base

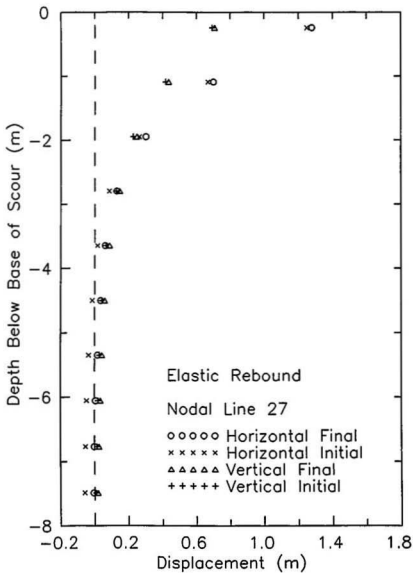


Figure 6.14 Test 04 comparison of computed displacement profiles before and after unloading and associated elastic rebound

magnitude than the associated vertical component, and decreased more abruptly with depth beneath the base of the scour. The maximum horizontal displacement of 1.52 m scaled from test measurements immediately below the scour base (interpolated at a depth below base = 0.1 m) was bounded by the computed values of 1.40 and 2.00 m for Nodal Lines 27 and 29, respectively. The depth of a region of measured large horizontal displacement below the scour base (assessed for a lower bound displacement magnitude of 0.2 m) was 3.08 m at prototype scale or 2.0 scour depths, whereas values of 2.78 and 3.12 m were established for the reference nodal lines in the analysis.

The vertical displacement profile included a maximum magnitude equal to the scour depth, and displayed more gradual reduction with distance beneath the scour than the associated horizontal component. The computed vertical displacements for Nodal Lines 27 and 29 were almost identical, and both under - predicted prototype magnitudes scaled from test records. The maximum vertical displacement of 0.94 m based on measurements immediately below the scour base (interpolated at a depth below base = 0.1 m) exceeded the value of 0.76 m derived from results of the analysis. The extent of a region of measured large vertical displacement below the scour base (assessed for a lower bound displacement magnitude of 0.2 m) was 3.21 m at prototype scale or 2.1 scour depths, which was greater than the depth of 2.60 m inferred from the computed displacement field.

The effects of changes to the interface conditions on the displacements predicted by the analysis were studied for values of the soil / rigid surface friction angle of $\delta = 2.9, 5.7, \text{ and } 8.5^\circ$ corresponding to friction coefficients of $\mu = 0.05, 0.10, \text{ and } 0.15$. Figures 6.15 and 6.16 display profiles of the horizontal and vertical components

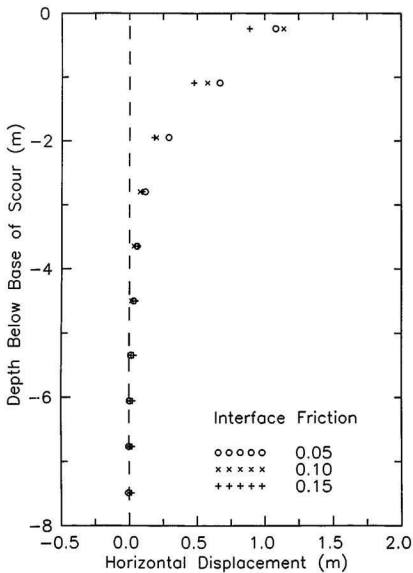


Figure 6.15 Test 04 analysis comparison of profiles of the horizontal displacement component for different interface friction coefficients

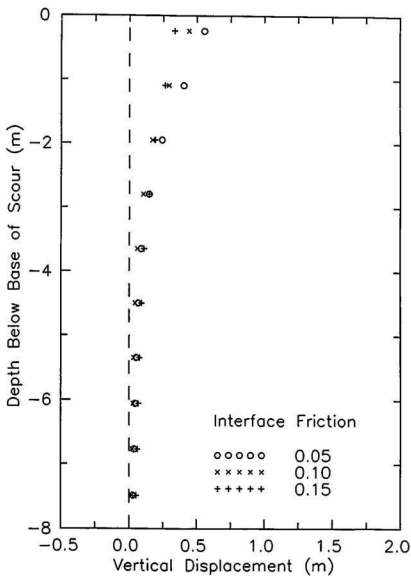


Figure 6.16 Test 04 analysis comparison of profiles of the vertical displacement component for different interface friction coefficients

of displacement computed for the different interface assumptions, based on a consistent range of horizontal movement of the rigid body of 4.5 m. Both components of displacement decreased with greater interface friction, and a 2.8° increase of the friction angle resulted in maximum differences in displacement on the order of 0.1 m for near surface positions. The variation in displacement magnitude declined with depth below the scour base, and the predicted extent of the region of large soil displacement was similar for each of the interface conditions under consideration.

6.3 Analysis of Tests 05 / 09

6.3.1 Input Conditions

Numerical analyses were also performed to study the prototype scouring event corresponding to Test 05 and related modelling of models Test 09, which were described in Sections 4.3.5 and 4.3.9, respectively. Input conditions and material parameters used in the analyses are given in Table 6.1. The initial stress state for the Test 05 clay specimen was defined through application of an increased laboratory pre - consolidation stress in relation to Test 04, with consequent reduction in the depth of scouring for similar imposed boundary conditions. A constant value of the prototype scour depth of 1.21 m was adopted in the analyses, based on the average equilibrium vertical penetration established in the experiment. The prototype rate of horizontal translation of the rigid body was specified as 0.072 m/s, as scaled directly from the average Test 05 velocity. Test 09 measurements were included in a comparative examination with results of the

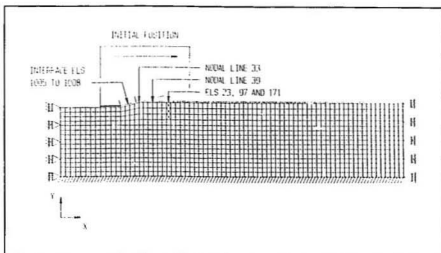


Figure 6.17 Test 05 / 09 analysis mesh configuration illustrating reference elements and nodes

analyses, both to evaluate correspondence with predicted values and to provide limited verification of the experimental techniques through correlation with the Test 05 data. The average equilibrium scour depth established in Test 09 was 1.10 m at prototype scale, and the recorded depth of scouring increased to approximately 1.25 m over the final portion of the event. The rate of scouring achieved during the experiment represented a prototype velocity of 0.078 m/s, which exceeded the corresponding Test 05 value.

The finite element mesh, shown in Figure 6.17, was adapted from the general configuration employed in the Test 04 analysis, with nominal element dimensions decreased in proportion to the reduction in scour depth. The Test 05 / 09 mesh incorporated 3776 nodes and 1176 elements, which included both rectangular 8 - noded isoparametric elements and compatible rigid surface interface elements. The total number of variables in the model was 8487, which consisted of the degrees of freedom of the

model as well as the Lagrange multiplier variables. An equivalent prototype rigid body movement of 12.8 m was established over 202 increments in the analysis, with allowance for an incremental displacement less than 10^{-6} times the total prescribed value.

6.3.2 Analysis Results

The results of numerical analyses for the Test 05 / 09 event are presented in this section, and compared with the experimental measurements reported in Chapter 4.

Local Element Behaviour

Reference Elements, EL 23, 97, and 171, selected to illustrate patterns of local behaviour, were situated at a horizontal position $x = 11.8$ m, and at average depths below surface of 0.7, 2.1, and 3.5 m, respectively, as depicted in Figure 6.17. The effective stress paths for the reference elements are displayed in Figure 6.18, together with the corresponding deviatoric stress - strain responses. In addition, excess pore pressures, generated as the simulation progressed, are shown plotted versus deviatoric strain in Figure 6.19.

The initial yield surface size, defined by the laboratory pre - consolidation stress, was increased in relation to Test 04, and reference elements in Test 05, at similar initial stresses, represented more heavily overconsolidated states. It was noted that for states which are dry of critical, the correspondence between experimental data and the predictions of Modified Cam - clay theory is less adequate, and that data of failure are better described by the equation of the Hvorslev surface (Schofield and Wroth, 1968).

The peak shear stresses computed were therefore expected to be higher than those observed to cause rupture, and over - prediction of negative excess pore pressures was also anticipated with representation of a more dilative response. While use of the Hvorslev equation provides a better fit to data in this region, Britto and Gunn (1987) suggested that, in their experience of practical application via the finite element method, significant advantages over direct use of Cam - clay (or Modified Cam - clay) theory were not apparent. The adopted numerical representation was also unable to predict discontinuous behaviour with the localization of distortion in distinct rupture planes.

The Test 05 elements exhibited comparable patterns of behaviour to Test 04 local responses, described in Section 6.2.2. The onset of yield occurred at higher levels of deviatoric stress, and the subsequent deformation was associated with an increased range of plastic softening and contraction of the yield surface. Once the soil yielded, the effective stress paths turned toward critical state and pore pressures declined so that the recoverable, elastic compression, arising from the increased mean effective stress, balanced the irrecoverable, plastic expansion, related to the changing size of the yield surface. For the elements EL 23 and 97, at near surface depths, negative excess pore pressures were induced following yield as a result of the suppressed volumetric dilation under essentially undrained conditions. In relation to Test 04, the reference elements exhibited similar pore pressure magnitudes at the completion of the simulation, following local attainment of critical states and associated positive excess pore pressure development. The range of movement was insufficient to represent unloading related to the passage of the rigid body beyond the horizontal position of the selected elements.

The cumulative shear strains established at reference element locations in Test 05

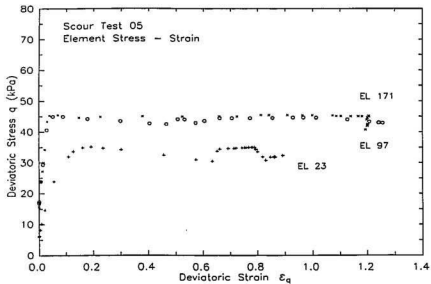
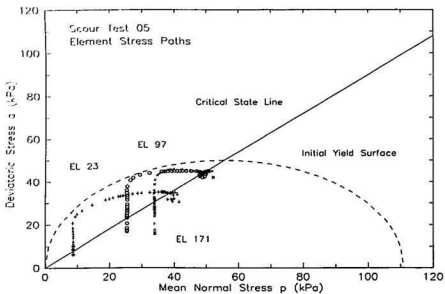


Figure 6.18 Top : Computed effective stress paths for reference elements (EL 23, 97, and 171) during event simulation; Bottom : Element deviatoric stress against strain

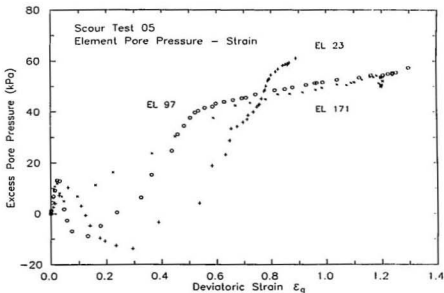


Figure 6.19 Computed excess pore pressures during event simulation plotted against deviatoric strain for reference elements (EL 23, 97, and 171)

exceeded the values computed following a larger range of movement in Test 04. The magnitudes of shear strain were higher for elements EL 97 and 171 ($\epsilon_q = 1.33$ and 1.19, respectively) below the depth of the scour cut, relative to the surface element EL 23 ($\epsilon_q = 0.90$) situated above the base of the rigid body. At high strain levels, the deviatoric stress : strain response for element EL 23 was somewhat irregular, as may be attributed to effects of severe distortion in this region.

Excess Pore Pressures

Figure 6.20 shows contour plots of computed excess pore pressures for the analysis increments 50, 100, 150, and 202, representing horizontal movements of the rigid body

of 3.0, 7.1, 9.9, and 12.8 m, respectively. The computed magnitudes exceeded Test 04 analysis values, for which a larger range of movement was simulated at a greater scour depth. The spatial distributions of the measured pore pressure responses in Tests 05 and 09, for different horizontal positions of the model, were displayed in Figures 5E.1 and 9E.1, in the corresponding sections of Appendix A. The experimentally recorded magnitudes ranged between extremes of - 44 and 108 kPa for transducers located within the apparent steady - state region of scouring, and these values were in reasonable agreement with predicted bounds given in Figure 6.20. The distribution of computed excess pore pressures also showed general correspondence with the region of measured effects of scouring, which extended to a prototype horizontal distance on the order of 25 m in front of the current model position, and to vertical positions at the bottom boundary of the soil domain. The computed negative excess pore pressures in front of and behind the current rigid body position coincided with pore suctions measured preceding and following passage of the model over a given transducer location.

Comparisons of the measured pore pressures in Test 05 with computed responses at corresponding prototype depths in the numerical model are presented in Figure 6.21 for individual transducer Channels 05, 06, 07, 04, 01, and 02, with model locations as indicated in Table 4.9. The complete range of movement of the model in relation to a particular transducer location was not simulated in the analysis, and results were therefore presented for reference integration points at different horizontal distances in front of the initial rigid body position. The computed magnitudes increased with greater initial horizontal distance from the reference point, with decreasing rate of change toward an apparent steady - state response associated with movement from a far - field initial

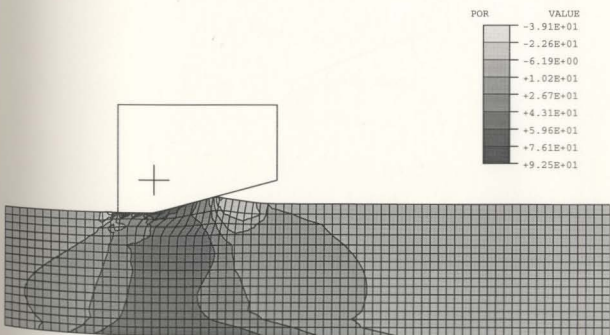
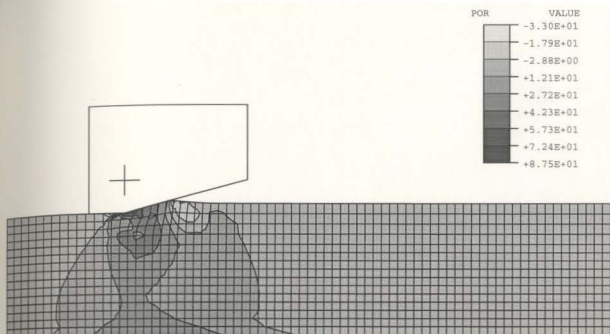


Figure 6.20 Test 05 / 09 analysis contour plots of excess pore pressure (kPa) for different rigid body positions. Top : $x = 3.0$ m; Bottom : $x = 7.1$ m

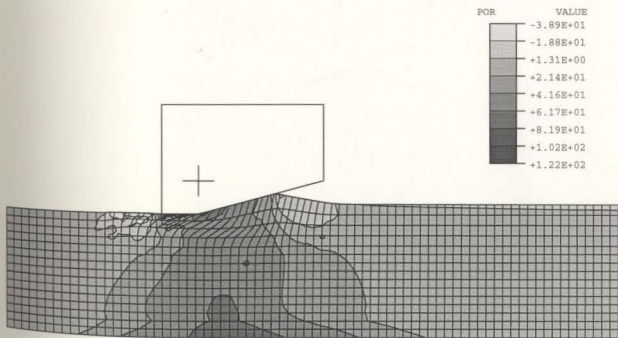
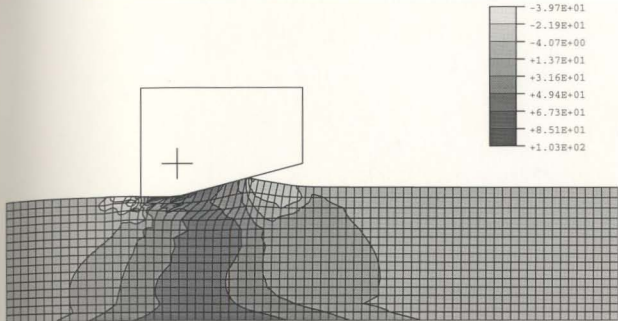


Figure 6.20 (continued) Test 05 / 09 analysis contour plots of excess pore pressure (kPa) for different rigid body positions. Top : $x = 9.9$ m; Bottom : $x = 12.8$ m

position. The measured pore pressure distribution with lateral distance from the scour axis was not accounted for in the two - dimensional analysis representation.

An assessment of the adequacy of analysis predictions based on consideration of a single transducer record was inappropriate due to the anticipated experimental error, the influence of disturbance arising during installation, and the effects of arching and stress concentration on the measured response. The analysis results did not provide detailed correlation with individual transducer records in Test 05, as exhibited for similar comparisons of computed and measured pore pressure values in Test 04. For some transducers (Channels 05, 04, and 01), reasonable correspondence of computed and measured peak magnitudes was evident for typical analysis reference points at $x = 14.7$ and 19.2 m, with slight over - prediction expected for simulation of an increased range of horizontal movement. The analysis under - predicted measured peak magnitudes in other instances (Channels 06, 07, and 02); although, computed pore pressures less than test values were anticipated for a transducer (Channel 02) situated in the unsteady region of scouring, near to the initial horizontal position in the physical model event.

In general, the under - prediction of experimental peak values in Test 05 was associated with transducer locations at shallower depth, and the analysis results displayed more uniformity of magnitude with changes in depth than the test records. The rates of computed excess pore pressure development and dissipation during passage of the rigid body were reasonably similar to measured responses for individual transducers. In the analysis, peak magnitudes were realized at horizontal positions of the rigid body preceding passage over the material point (at negative values of horizontal distance in Figure 6.21) and depended on the depth of the material point; in the experiment, the

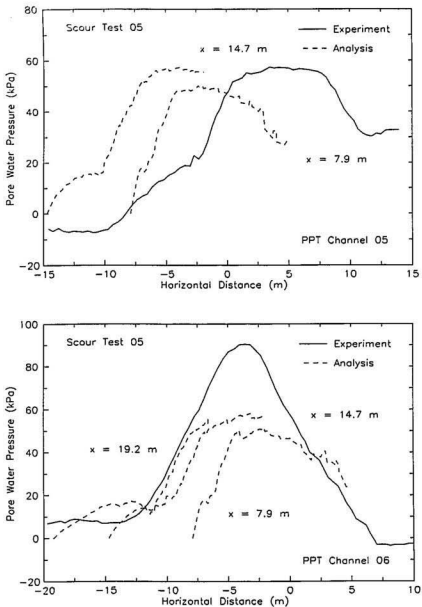


Figure 6.21 Test 05 comparison of analysis results with experimental measurements for individual pore pressure transducers

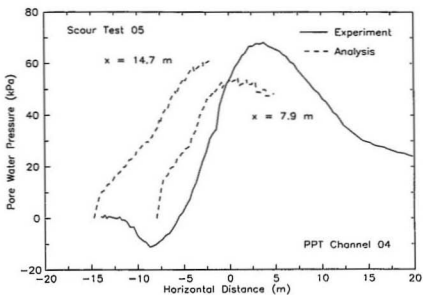
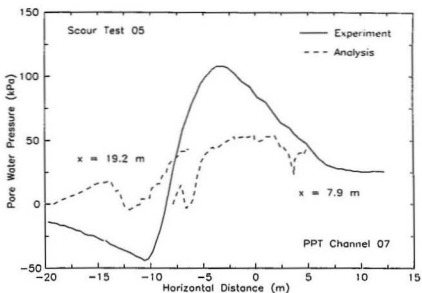


Figure 6.21 (continued) Test 05 comparison of analysis results with experimental measurements for individual pore pressure transducers

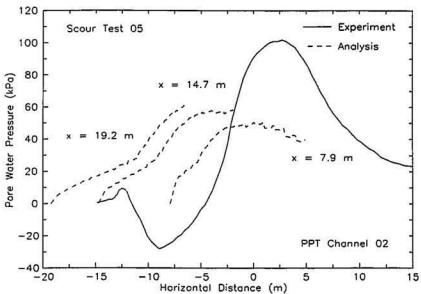
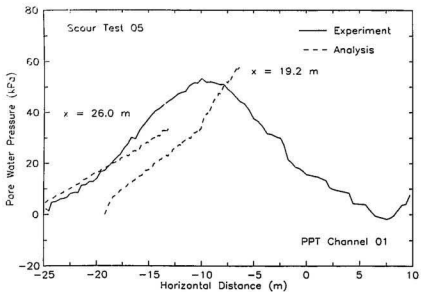


Figure 6.21 (continued) Test 05 comparison of analysis results with experimental measurements for individual pore pressure transducers

locations of peak magnitudes showed greater variability, partially attributable to anticipated experimental error in determination of the relative positions of model and transducer during the event. The development of negative excess pore pressures, for heavily over - consolidated conditions at shallow depth, was predicted qualitatively in the analysis; however, associated magnitudes and pore suctions recorded by transducers at greater depth were not adequately represented.

In comparison of computed values with Test 09 measurements some over - prediction was expected, since the constant depth of scouring adopted in the analysis exceeded the average equilibrium scour depth established in the experiment. An overall assessment of individual transducer records displayed reasonable correspondence of peak magnitudes with simulation of limited horizontal movement in the analysis, and over - prediction of experimental values for a more realistic increased range of horizontal movement. The analysis indicated a relatively uniform distribution of peak pore pressure magnitudes with changes in depth, and was unable to quantitatively represent observed attenuation of measured peak responses with increased depth.

Interface Pressures

Figure 6.22 shows contact pressures for reference interface elements along the inclined surface of the rigid body at the initial position (denoted EL 1005, 1006, 1007, and 1008 in Figure 6.17). The contact pressures are plotted versus horizontal position over the complete range of movement during simulation of the event. The Test 05 / 09 reference element responses were similar in character to the corresponding Test 04 analysis results; however, greater magnitudes were predicted at both the inclined and horizontal bottom

surfaces of the rigid body. The computed element normal stresses increased to peak values with movement along the inclined surface, and decreased to minimum values with subsequent movement along the horizontal surface; the transition to a loss of contact between the element and rigid body was associated with an abrupt rise in pressure. Test 05 inductive pressure transducer measurements at the inclined surface and horizontal base of the model are also presented in Figure 6.22, where measured peak and average pressures are superimposed on the test records. In addition, the peak and average experimental values are shown plotted in relation to the reference element responses. The average pressure magnitude at the horizontal base was less than 40 percent of the peak pressure which acted at the inclined surface of the model. The comparison of average and peak measured values with computed normal stresses indicated close correspondence with test data acquired for both the inclined and horizontal surfaces.

Resultant Forces

Figure 6.23 displays the computed horizontal and vertical components of the resultant force acting on the rigid body together with prototype forces scaled from the Test 05 and 09 measurements, which were presented in Figures 4.31 and 4.66, respectively. Comparison between resultant force records for the modelling of models Tests 05 and 09 indicated reasonable agreement, with increased correspondence over the final portion of the event, where similarity of the measured scour depths in both tests was greatest. The analysis predicted increased magnitudes of both the horizontal and vertical resultant force components relative to corresponding Test 04 computed values, and this finding was in accordance with the experimental results; however, the correlation of computed and

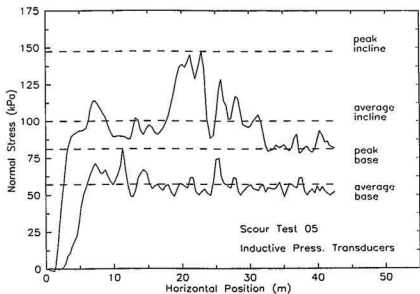
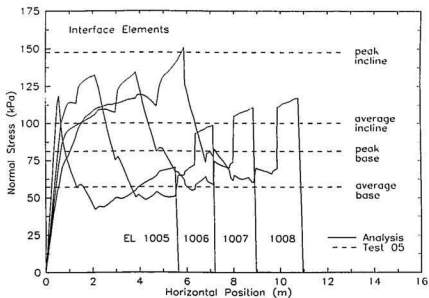


Figure 6.22 Top : Test 05 / 09 analysis normal stresses compared with measured peak and average values; Bottom : Transducer records for inclined surface and horizontal base

measured resultant force records was less satisfactory for the Test 05 / 09 analysis. For the horizontal component, the analysis results under - predicted the measured response over the extent of movement simulated in the analysis. The difference in magnitude between computed and measured horizontal forces was approximately 13 percent at the final horizontal position. Extrapolation of the computed horizontal force record implied reasonable agreement with the experimental results for an apparent steady - state scouring condition associated with representation of an increased range of movement. For the vertical component, reasonable correspondence was obtained between computed and measured values at the final horizontal position in the analysis, to within a difference of about 5 percent. The analysis predicted a progressive increase of vertical force over the simulated range of movement, without a marked tendency toward a constant magnitude consistent with the experimental results.

The dissimilarity of computed and measured forces may be attributed in part to specific limitations of the numerical representation. The analysis did not allow for the additional forces developed as a result of the increased scour depth preceding the establishment of an equilibrium vertical position and orientation of the model. Furthermore, the effects of adhesion or friction acting at the sides of the model were neglected, and this factor also contributed to under - prediction of the test measurements. The eventual divergence of computed and measured vertical forces was expected, with ongoing build - up of frontal mound material, inherent to the two - dimensional continuum idealization. The limited range of movement investigated in the analysis provided adequate approximation of the measured effects of a steady - state scouring condition associated with continued movement; however, allowance for a clearing

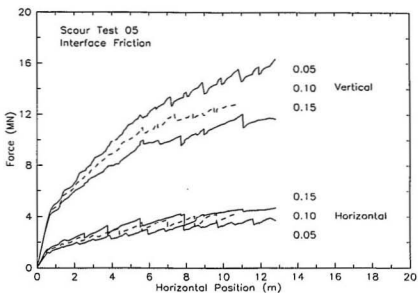
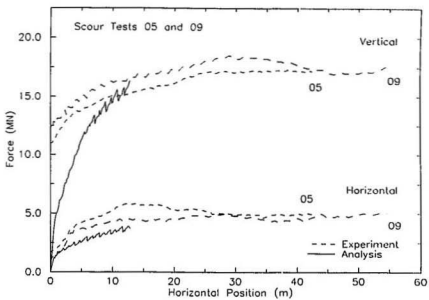


Figure 6.23 Top : Test 05 / 09 comparison of computed and measured resultant force components; Bottom : Analysis force records for different interface friction coefficients

mechanism was required as part of the numerical representation, in order to form a realistic simulation of the complete scouring episode.

The computed horizontal and vertical components of the resultant force are shown plotted in Figure 6.23 for values of the soil / rigid surface friction angle of $\delta = 2.9, 5.7,$ and 8.5° corresponding to friction coefficients of $\mu = 0.05, 0.10,$ and 0.15 . The analysis results displayed a comparable influence of changes in interface conditions in relation to the Test 04 investigation. The horizontal force component increased in magnitude and the corresponding vertical component decreased as a result of the assumption of an increased interface friction angle in the analysis, and divergence of the computed force records was enhanced over a greater range of horizontal movement. A 2.8° increase of the interface friction angle reduced the magnitude of the total resultant force by as much as 5 to 10 percent, at the completion of movement; the modest increase of friction angle, relative to the realistic low value adopted in the general Test 05 / 09 analysis, provided improved correspondence of the computed and measured force responses.

Soil Deformation

Figure 6.24 shows the displaced finite element mesh configuration at the termination of horizontal movement in the analysis, and the corresponding plot of soil displacement vectors. The computed displacement field exhibited comparable characteristics in relation to the corresponding Test 04 analysis results. The apparent discontinuity of displacements between adjacent elements below the inclined rigid surface suggested improper behaviour and some deficiency of the numerical representation at very large movement. Experimental evidence of subsurface displacements recorded at individual grid locations

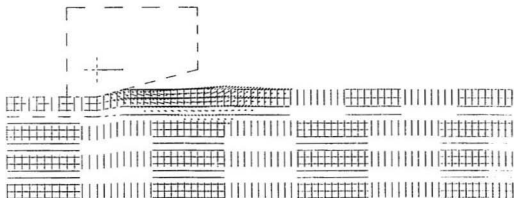
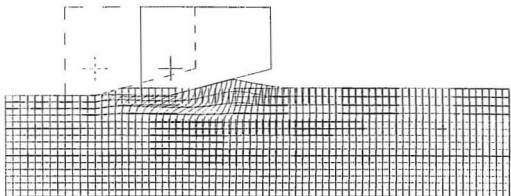


Figure 6.24 Test 04 analysis results - final rigid body position; Top : Displaced configuration of mesh (initial shown dashed); Bottom : Displacement vectors (maximum length $x = 12.8$ m)

was presented in Figures 5F.5 and 9F.5. The two - dimensional displacement field from the analysis was qualitatively similar to the displaced configuration of the axial grid at the final model position, depicted in Figures 4.35 and 4.70 for Tests 05 and 09, respectively. In comparison with computed values, the measured region of large vertical displacement extended to greater depth below the scour, attributable in part to vertical movement of the model associated with the discontinuation of scouring.

Soil displacement vectors, plotted for different horizontal positions of the rigid body during simulation of the event, also displayed similar patterns of movement in comparison with the Test 04 analysis results. The computed displacement field was characterized by a semi - circular region of large displacement, compatible with downward or negative vertical displacement of a material point beneath the current position of the inclined rigid surface, and positive vertical displacement at locations in front of the rigid surface, associated with formation of a continuous frontal mound. The region of large displacement extended below the scour depth, and the magnitude of both horizontal and vertical components of the displacement diminished with increased depth. The development of small (elastic) negative horizontal displacements below the scour depth may be attributed to lateral extension which accompanied undrained compression of elements beneath the rigid surface; cumulative displacement data for the Test 09 event provided limited experimental evidence of similar backward - directed movements at depth.

Figures 6.25 and 6.26 show contours of the horizontal and vertical components of soil displacement plotted for analysis increments 50, 100, 150, and 202, corresponding with rigid body horizontal movements of 3.0, 7.1, 9.9, and 12.8 m, respectively. The

contours of the horizontal component described a semi - circular region of large displacement, and displayed decreased magnitudes with distance in front and below the current position of the inclined rigid surface. The contours of the vertical component defined two distinct regions of transient displacement depending on proximity to the rigid body : a region of upward displacement related to heave of the free surface and frontal mound formation, and; a region of downward displacement associated with subsequent compression beneath the advancing rigid body, with maximum value equal to the scour depth. Although similar patterns of movement were exhibited in relation to results from the Test 04 analysis, the predicted displacements were different in magnitude and extent, as described below.

Contours of the equivalent plastic strain magnitude are displayed in Figure 6.27, as computed for different increments of horizontal movement of the rigid body. The development of a mechanism of general plastic failure or large deformation may be inferred from the region of yielded elements and associated high magnitudes of plastic strain during simulation of the event. In relation to the Test 04 analysis results, the computed region of plastic straining was less extensive, and maximum plastic strain magnitudes exceeded Test 04 values established over an identical range of rigid body movement. A peak plastic strain magnitude of 106 percent was computed following horizontal movement of 12.8 m, and values greater than approximately 15 percent were apparent at a maximum depth on the order of 3.7 m or 3.1 scour depths below the base of the scour. The region of plastic straining exhibited continued development with increased movement throughout the simulation, toward a constant extent representing an apparent steady - state condition.

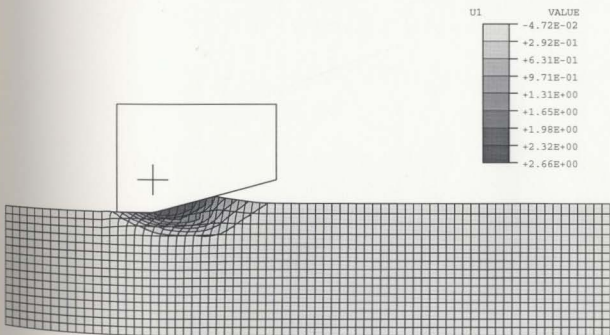
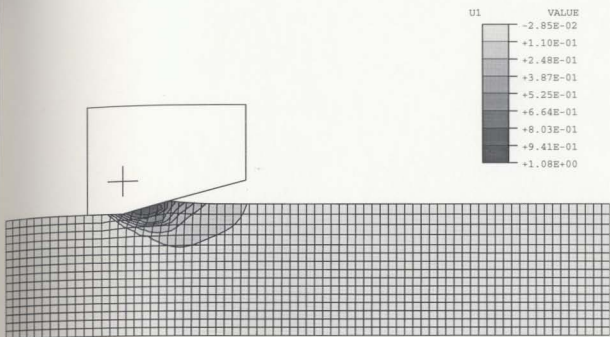


Figure 6.25 Test 05 / 09 analysis contour plots of horizontal component of soil displacement (m) for different rigid body positions. Top : $x = 3.0$ m; Bottom : $x = 7.1$ m

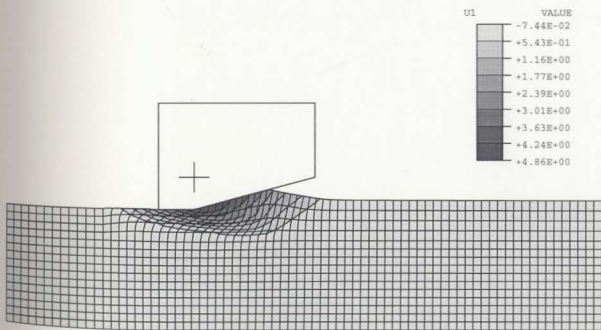
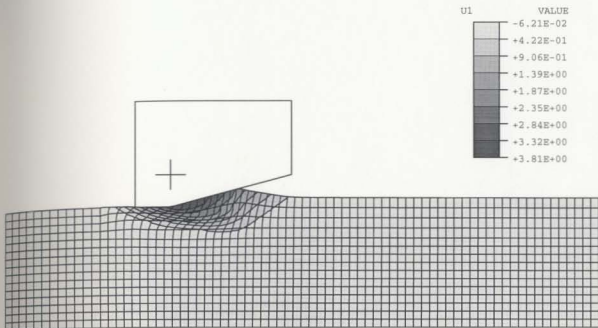


Figure 6.25 (continued) Test 05 / 09 analysis contour plots of horizontal component of soil displacement (m) for different rigid body positions. Top : $x = 9.9$ m; Bottom : $x = 12.8$ m

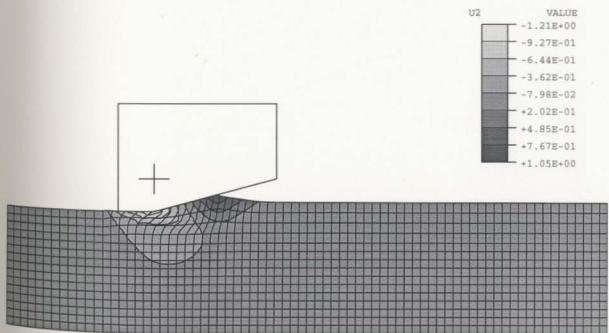
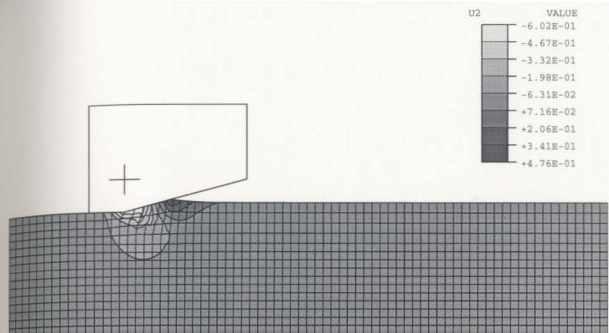


Figure 6.26 Test 05 / 09 analysis contour plots of vertical component of soil displacement (m) for different rigid body positions. Top : $x = 3.0$ m; Bottom : $x = 7.1$ m

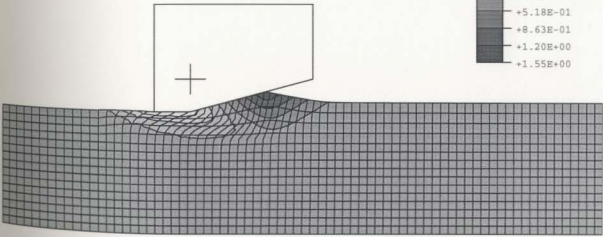
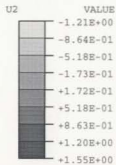
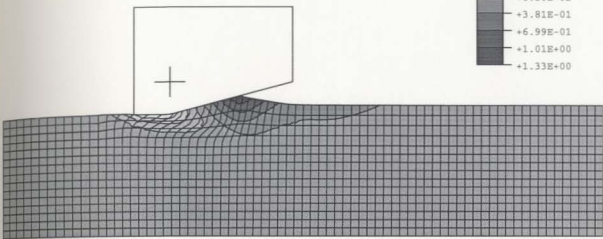
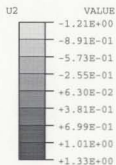


Figure 6.26 (continued) Test 05 / 09 analysis contour plots of vertical component of soil displacement (m) for different rigid body positions. Top : $x = 9.9$ m; Bottom : $x = 12.8$ m

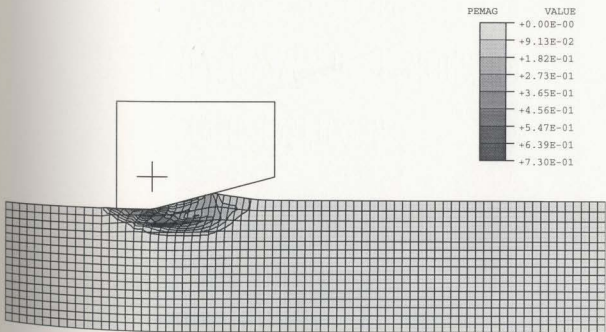
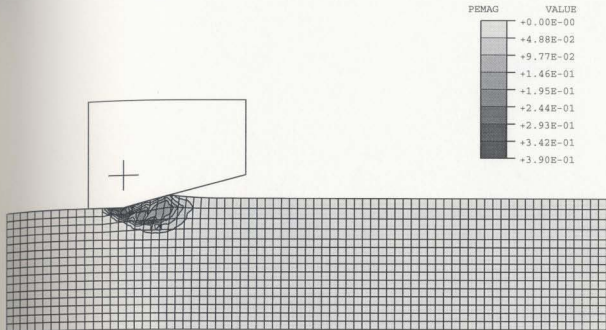


Figure 6.27 Test 05 / 09 analysis contour plots displaying magnitude of plastic strain for different rigid body positions. Top : $x = 3.0$ m; Bottom : $x = 7.1$ m

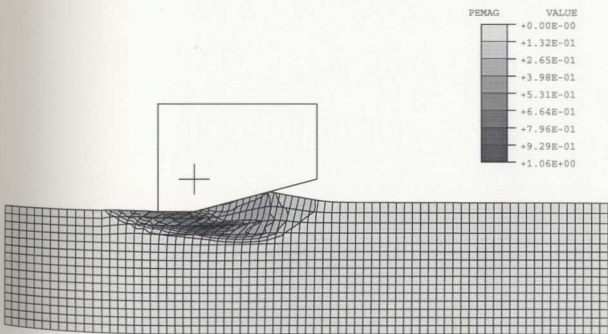
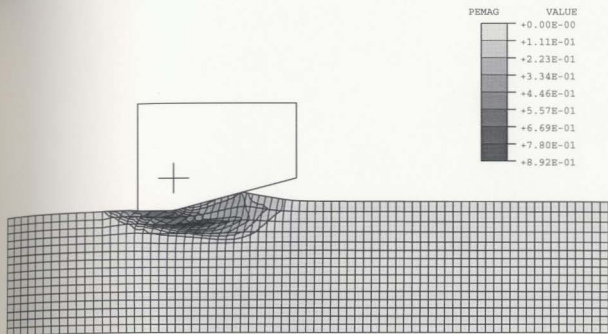


Figure 6.27 (continued) Test 05 / 09 analysis contour plots displaying magnitude of plastic strain for different rigid body positions. Top : $x = 9.9$ m; Bottom : $x = 12.8$ m

The computed and measured profiles of the horizontal and vertical components of soil displacement are presented in Figures 6.28 and 6.29, respectively. The experimental results represented the average of values derived from axial and lateral grid measurements, as given in Figures 4.36 and 4.71 for Tests 05 and 09, respectively. The test measurements were compared with the analysis results for reference Nodal Lines 33 and 39, at locations in front of the initial rigid body position, as shown in Figure 6.17. Nodal Line 33 displacement values represented the cumulative response following complete passage of the rigid body beyond the initial position, whereas Nodal Line 39 was situated below the horizontal base of the rigid body at the termination of movement in the analysis. The increased displacement magnitudes computed for individual nodal lines located at greater distance in front of the initial rigid body position may be attributed to the requirement for continuity of the displacement field together with continued build - up of the frontal mound, as imposed by constraints of the numerical representation. The computed displacement profiles included the effects of unloading and associated elastic rebound, relevant to conditions during displacement measurement in the experiment. The small (elastic) backward - directed or negative horizontal displacements, computed at depth below the scour, were recovered with the allowance for rebound.

Comparison between displacement profiles for the modelling of models Test 05 and 09 measurements indicated reasonable correspondence, with notable variation of recorded magnitudes of the vertical displacement component between tests. The differences in the computed responses for the Test 04 and 05 / 09 events represented the effects of a reduction in scour depth and a decreased range of movement, in addition to

the prescribed change of the initial soil state. The computed maximum displacement magnitudes and the depth of the region of large horizontal displacement were reduced in relation to the corresponding Test 04 analysis results, and these findings were in agreement with the experimental trends. The analysis results also exhibited diminished extent of the region of large vertical displacement, in contrast with an increased depth of influence inferred from test measurements.

The computed profiles of the horizontal component of displacement for reference Nodal Lines 33 and 39 are compared with the experimental records for Test 05 and 09 in Figure 6.28. The maximum horizontal displacement, equal to 1.12 m for Nodal Line 33 (interpolated at a depth below base = 0.1 m), was in reasonable agreement with values of 1.29 and 1.08 m scaled from the Test 05 and 09 measurements. The results for Nodal Line 39, at greater distance in front of the initial rigid body position, displayed increased horizontal displacement, and implied divergence from an equilibrium displaced configuration with simulation of continued movement in the analysis. The depth of a region of computed large horizontal displacement below the base of the scour (assessed for a lower bound displacement magnitude of 0.2 m) ranged from 1.83 to 2.80 m based on the results for Nodal Lines 33 and 39, respectively. The analysis results were compared with measured values of 2.99 m in Test 05 and 2.78 m in Test 09, or approximately 2.5 scour depths; the correlation between computed and measured depths improved with numerical representation of an increased range of movement.

The computed profiles of the vertical component of displacement for reference Nodal Lines 33 and 39 are compared with the experimental records for Test 05 and 09 in Figure 6.29. The analysis results displayed less gradual attenuation of vertical

displacement with depth below the base of the scour, and under - predicted test measurements over the complete range of depths considered. The computed maximum vertical displacement of 0.61 m (interpolated at a depth below base = 0.1 m) was lower than the corresponding values of 0.88 and 0.68 m scaled from the Test 05 and 09 measurements. The region of large vertical displacement extended to a maximum computed depth below the scour base of 1.88 m (assessed for a lower bound displacement magnitude of 0.2 m) which substantially under - predicted the depth of influence inferred from the experimental evidence. The measured profiles of vertical displacement represented an apparent upper bound for tests in the experimental programme, and were deemed less reliable due to the variation between Test 05 and 09 results, and differences in data acquired from the individual grids. The computed vertical displacement magnitudes were comparable to minimum values scaled from the test measurements.

Analyses were performed to study the effects of changes in the soil / rigid surface friction angle over the range of values $\delta = 2.9, 5.7, \text{ and } 8.5^\circ$ corresponding to friction coefficients of $\mu = 0.05, 0.10, \text{ and } 0.15$. Similar to results of the Test 04 investigation of interface conditions, the computed horizontal and vertical components of displacement decreased with specification of higher values of the friction angle, except at material points immediately adjacent to the base of the scour. An increase of the friction angle of 2.8° resulted in maximum differences in the displacement magnitudes on the order of 0.1 m for near surface positions, based on representation of a consistent range of horizontal movement of 12.8 m in the analysis. The trend of the results suggested modestly improved correlation, between the computed displacements for Nodal Line 33

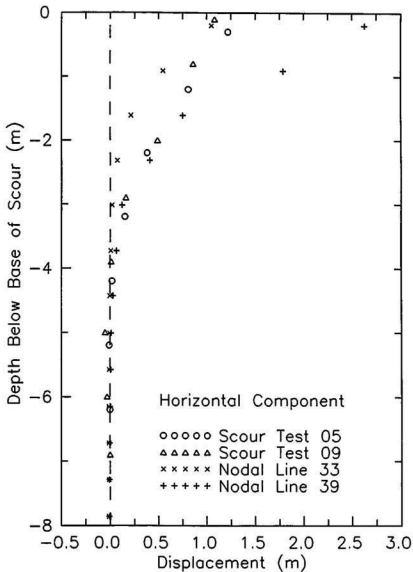


Figure 6.28 Test 05 / 09 comparison of measured and computed values of the horizontal component of soil displacement plotted against depth below the scour base

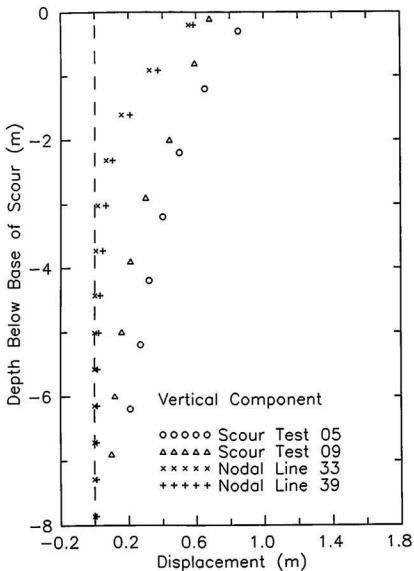


Figure 6.29 Test 05 / 09 comparison of measured and computed values of the vertical component of soil displacement plotted against depth below the scour base

and the test measurements, with use of a realistic low value of the friction angle, as adopted in the Test 05 / 09 analysis.

6.4 Soil Deformation

6.4.1 Numerical Validation

Practical Limitations

The requirement to represent large movements relevant to the physical model imposed practical constraints on implementation of the analysis and discretization of the soil domain. Severe element distortion restricted the range of movement over which convergence was attained, and limited allowable mesh refinement in the vicinity of the rigid body. Adaptive mesh rezoning algorithms may be introduced to provide more detailed and accurate information in the region of high strain gradients adjacent to the rigid body. For two - dimensional undrained deformation, volume loss in the scour path must be partially accommodated through continued upward displacement ahead of the advancing rigid body. Without allowance for a lateral clearing mechanism, a stable configuration of the frontal mound could not be established in the analysis, and divergence of the associated displacement field was anticipated with continued movement. The measured steady - state response was therefore approximated by the cumulative displacement which followed complete passage beyond a material point situated in front of the initial rigid body position, and which corresponded with the development of a realistic configuration of the frontal mound.

Analysis of Scour Tests

Comparison between the Test 04 experimental data and responses computed through simulation of the corresponding prototype scouring event, established the viability of the numerical representation. The analysis results exhibited reasonable quantitative agreement with the measured effects of scouring, including excess pore pressures, resultant forces, and soil displacements. The correspondence between computed and measured values indicated that realistic approximations of steady - state conditions may be obtained without requirement to represent the complete range of horizontal movement in the analysis. The analysis allowed for progressive development of soil failure with continued movement: from the initial elastic response to yield and plastic deformation contained by surrounding elastic regions, followed by very large deformation in regions of unrestricted plastic flow. The soil response was characterized by a semi - circular region of large displacement which extended from the base of the rigid body to the free surface, and encompassed positions beneath the scour depth. The region defined a pattern of displacement and did not represent a physical condition of shear separation or discontinuity; the computed displacement magnitudes attenuated with distance in front of and below the current rigid body position, without evidence of localized shear distortion associated with formation of distinct rupture planes.

The development of a localized soil deformation response which represented a physical discontinuity was restricted by the relatively coarse discretization which was adopted in the numerical analysis. In addition, the tendency for near surface soil elements to undergo softening upon shear was partially suppressed by drainage conditions which

limited the allowable volume change during the event. The variation of cumulative soil displacements with depth computed for reference nodal lines in the analysis provided reasonable predictions of measured values; the computed profiles were not attributed to an explicit mechanism of shear dragging adjacent to a rupture plane or rigid body sliding relative to the soil.

The Test 05 / 09 analysis permitted an assessment of the influence of a change in the initial state of the soil; although, the results also represented the effects of changes to other variables, including the scour depth and the range of horizontal movement, in relation to the Test 04 analysis. The correlation of computed and measured values was less satisfactory for the Test 05 / 09 analysis, which indicated some deficiency of the numerical representation in addition to anticipated measurement inaccuracies. The analysis defined an increased depth of soil at heavily overconsolidated initial states, associated with contraction of the yield surface and strain softening behaviour. The analysis results displayed increased magnitudes of cumulative shear strain and reduction in extent of the region of large displacement, in comparison with Test 04 computed values. The greater localization of response was consistent with an increased number of soil elements which experienced softening toward critical states under continued deformation throughout the event; strain softening behaviour was associated with development of a concentration of deformation in regions which had become weaker by comparison with the surrounding soil. In contrast, soil which underwent plastic volumetric compression and hardening, allowed for increased transmission of stresses and distribution of deformation over a greater depth of influence.

Compressible and Brittle Soil Events

In prediction of the effects of scouring, two general classes of event may be distinguished in accordance with the regimes of soil behaviour defined through concepts of critical state theory : (1) Compressible behaviour with stable yielding of initially loose or lightly overconsolidated materials on the wet side of critical state, and; (2) Brittle behaviour with rupture of initially dense or heavily overconsolidated materials on the dry side of critical state. In the compressible or wet state, an event may be characterized by continuum distortion or flow, where loss of material in the scour path is accommodated primarily through compressive deformation beneath the incision; distinct rupture planes are not formed and cumulative soil displacements attenuate with increased distance from the rigid body. In contrast, where brittle or dry behaviour represents the dominant mode of soil response, an event may be characterized by formation of a succession of rupture planes which develop from the base of the rigid body to the free surface in a repeating pattern, with related periodic variation of the resultant forces; in this instance, the bulk of material loss in the scour path may be accounted for through progressive lateral clearing of blocks of soil separated from the continuum, associated with the creation of discontinuous berm features at the sides of the scour incision.

The present study provided evidence of the applicability of the adopted numerical representation to the deformation of soft clay under essentially undrained scouring conditions, in which the integrated effect of element responses described an event dominated by compressible soil behaviour. The analysis was not applied to investigate brittle soil events, for which the development of rupture planes may be expected to invalidate the numerical representation, without specific allowance made to address the

effects of discontinuities. Comparative examination of the Test 04 and 05 / 09 analyses displayed dependency of the depth of the region of large displacement on soil behaviour, which was altered with the imposed stress history or initial state. Compressible soil events were associated with development of a relatively extensive region of large displacement, with greater stresses being transmitted through strain hardened material; this range of soil behaviour may, therefore, represent a limiting condition for which the evaluation of sub - scour effects was most relevant to ensure pipeline burial at sufficient depth below a region of large displacement. In contrast, brittle soil events, with strain softening beyond peak stresses, involved the concentration of intense shearing and volume change in very thin regions of material, and large sub - scour soil displacement was expected to be relatively localized for this range of soil behaviour.

The assessment of previous analytical investigations of mechanisms of failure developed during scouring events (see Chapter 1) indicated that, for horizontally moving ice features, rupture planes were not expected to extend below the depth of scouring, with the exception of strongly dilatant soils, for which minor sub - scour disturbance was predicted. The available experimental evidence displayed cumulative displacements at positions below the depth of rupture planes defined through the analysis of failure mechanisms. For brittle soil events, shearing may be expected to occur almost solely on the rupture planes, with eventual deformation at constant volume and constant mobilized friction under continued relative motion toward critical states. An additional region of large (plastic) soil displacement may be attributed to dragging deformations of soil immediately beneath the rupture planes or adjacent to the rigid body sliding relative to the soil; however, the softening response of the neighbouring initially dense or heavily

overconsolidated soil may also be expected to inhibit the extent of a region of large dragging displacements, as further deformation would remain concentrated in the weakened soil.

6.4.2 Effects of Parameters

Initial State and Stress Paths

In the present study, the numerical representation was not implemented to investigate the complete range of parameters which defined the effects of a scouring event. In addition, evaluation of the influence of parameters through direct comparison of the results of tests in the experimental programme, was hindered by the small number of tests performed, and by permitted variation in individual tests. Section 6.4.1 discussed the effects of initial state on the depth of the region of large scour - induced soil deformation, with comparison of the Test 04 and 05 / 09 computed values. The measured displacement profiles were inconsistent with the analysis results, in consideration of the relatively extensive region of large vertical displacement recorded for Tests 05 and 09; however, the variation in measured magnitudes of vertical displacement suggested that results presented were representative of extreme values and may be associated with unsteady conditions.

The mode of deformation and failure was not defined exclusively by the stress history or initial state of the soil; the expected response was also dependent on the total stress paths (drained or undrained) applied during the event. The influence of the stress path may be illustrated by considering an element of dense or heavily overconsolidated

soil, with initial state on the dry side of critical, situated in front of the initial position of the rigid body or ice keel. If passage of the keel imposed loading which involved increased deviatoric or shear stress at constant mean normal stress, the element would exhibit brittle soil behaviour, with strong tendency to soften and generate dilatant ruptures; however, if a large increase of mean normal stress was applied more rapidly than the corresponding deviatoric component, the stress path may reach failure on the wet side of critical, and the element would then display compressible behaviour, associated with hardening and continuum distortion. The effects of parametric variations on the soil deformation developed during scouring may, therefore, be evaluated qualitatively in accordance with anticipated changes to stress paths, which describe the relationship between mean normal and deviatoric components of stress under the applied loading.

Drainage Conditions

In the present experimental programme, Test 06 provided the most striking evidence of the contrast between the mode of soil deformation and failure exhibited for brittle soil events, in relation to events dominated by compressible soil behaviour. The input conditions for Test 06 were identical to those for the Test 05 baseline event, with the exception of the imposed stress history, which defined a more heavily overconsolidated initial soil state. Importantly, due to equipment malfunction, Test 06 involved a substantially reduced scouring velocity which, together with the enhanced rate of dissipation in the model, implied that the event represented fully or partially drained conditions. The Test 06 scour was characterized by extensive loose or discontinuous berm material, and a large amount of surcharge was built - up at the front and sides of

the advancing model. Comparison of the cumulative displacement profiles for Tests 05 and 06 (shown in Figures 4.36 and 4.45) served to illustrate dissimilarities in the measured effects of scouring. In Test 06, the magnitude of the horizontal component of displacement was very large at positions above or immediately beneath the scour base, but movements were limited to a shallow or localized region. The magnitude of the vertical component of displacement was small or negligible at all sub - scour depths. The loss of material in the scour path was therefore accommodated through frontal mound development and subsequent lateral clearing to discontinuous berm features, rather than by compressive deformation below the incision.

The drained soil conditions in Test 06 allowed for dissipation of excess pore suction by the mechanism of transient flow of pore water, which led to softening and consequent concentration of deformation in a narrow region of weakened soil. The influence of drainage conditions, also offered an explanation for the relative similarity of measured displacement patterns for other tests in the experimental programme, which indicated dominant compressible soil behaviour, despite differences in the initial soil state. For the essentially undrained conditions which were relevant in the majority of tests, the dissipation of negative excess pore pressures was restricted, such that softening behaviour and localization of the soil response in a near surface region was partially inhibited. The suppression of softening was apparent in consideration of the computed element deviatoric stress - strain responses for Test 04 and 05 / 09 analyses, shown in Figures 6.2 and 6.18, respectively. In practice, relatively compressible soil behaviour may therefore represent the most prevalent response during scouring in clay, where full - scale field conditions may be expected to be undrained for most conceivable events.

However, it should also be noted that, for events which are nominally undrained, in the sense that the overall volume does not change, there may still be local drainage of pore water from the surrounding soil, which may facilitate softening and development of thin zones of shearing or rupture planes.

Test 08 provided further substantiation of the influence of drainage conditions on soil behaviour and the effects of scouring. The displacement patterns in this test were comparable to those measured in Test 06 and both tests involved a significant reduction in the rate of model movement, which allowed for dissipation of negative excess pore pressures during the event. In addition, an increase of the interface friction angle or adhesion with decreased strain rate, may have represented a contributing factor to the localization of response which was exhibited in both tests. The effects of changes to interface conditions were investigated as part of the Test 04 and 05 / 09 analyses, and it was found that computed horizontal and vertical components of displacement decreased with specification of higher values of the interface friction angle, as illustrated in Figures 6.15 and 6.16, respectively.

Attack Angle

For brittle soil behaviour, previous analyses have suggested that rupture planes were unlikely to extend far below the depth of scouring, and this conclusion was unaffected by changes to the angle of attack; although, boundary wedges or dead zones of soil were required to establish compatibility with modification to the interface geometry. The effect of decreasing the attack angle was also to induce high or rapidly increasing mean normal stresses as the rigid body or ice keel approached a blunt configuration applicable to a

field scouring event. Therefore, while the initial soil state may define a dense or heavily overconsolidated condition, the large spherical pressures generated at low attack angles may be sufficient to direct the stress path to failure on the wet side of critical states, with resulting plastic compression of the soil. In contrast, rupture and fracture may represent the dominant mode of deformation and failure during soil cutting at low effective stress levels with sharp or positively - raked implements.

For compressible soil behaviour, decreasing the attack angle altered the pattern and extent of the expected deformation. A blunt interface geometry induced greater vertical stresses during a scouring event, with corresponding increased vertical strains and displacements. In Test 08, the attack angle of the model iceberg was increased to 25 degrees, and resulting measured vertical displacements were small or negligible, and large horizontal displacements were limited to a relatively shallow sub - scour region. The influence of a change to the angle of attack was not isolated, however, and the results of this test also reflected the effects of a substantially reduced rate of model advance, and a greater scour depth in relation to baseline conditions.

Scour Depth

The boundary conditions which served to define the two - dimensional representation of scouring included the scour depth in addition to the angle of attack. The analysis of failure mechanisms proposed for brittle soil events implied that the expected extent of rupture planes beneath the scour base was insensitive to changes to both parameters. As with reduction of the attack angle, the effect of increasing the scour depth was to generate additional mean normal stresses which may induce compressible soil behaviour

for initial states on the dry side of critical. In this manner the influence of both parameters may be expected to be interdependent, in that a limiting condition for which the dominant mode of soil deformation and failure changes from brittle to compressive, for a given initial state, may be described as a function of both the attack angle and the depth of scouring.

The scour depth also influenced the expected soil response indirectly, as increased depths were related to decreased initial vertical effective stresses, such that soil within the region of influence of the event, represented more lightly overconsolidated initial states associated with plastic compression. For compressible soil behaviour, the pattern and extent of soil deformation was dependent upon the scour depth, as the intensity of vertical stresses induced during scouring was increased for greater scour depths, leading to increased vertical strains and displacements. In addition, increased spherical pressures resulted in compression and hardening for soil elements below the scour and allowed for greater transmission of stresses, which facilitated distribution of deformation over a greater depth. The assessment of the influence of scour depth through direct comparison of the results of tests in the experimental programme was not possible; however, measurements in individual tests displayed decreased magnitude and extent of displacement for grid locations near to the end of the scour path, associated with a reduced depth of scouring at steady conditions.

Scour Width

For brittle soil behaviour, analytical descriptions of three - dimensional scouring mechanisms for narrow ice features are not available, and limited information exists by

which to define the expected lateral and vertical extent of rupture planes in exceptional cases where plane strain assumptions are invalidated. For events in which compressible soil behaviour is dominant, decreasing the scour width may be expected to diminish the extent of the induced stresses and corresponding strains and displacements below the scour. The attenuation of stresses with depth is more gradual for events which involve high scour width / depth ratios appropriate to two - dimensional representations of the field scouring process. The relatively greater depths required to realize the same reduction in stresses may be attributed to the reduced capacity for lateral distribution of the applied loads during an event : only one lateral dimension is available for large widths associated with plane strain conditions whereas, by contrast, stresses developed beneath a narrow ice keel are permitted to spread out symmetrically over the horizontal planes.

The reasonable agreement obtained between experimental data and analysis results in Test 04 provided support for a two - dimensional numerical representation, particularly as typical field scouring geometries may be expected to involve greater width / depth ratios than those investigated in the experimental programme. The analysis was, however, unable to account for edge effects due to observed near - surface lateral displacements, as well as possible dissipation of lateral sub - scour movement over an extensive area. Test 07 was intended to permit an assessment of the influence of width on the effects of scour, and input conditions were altered from the Test 05 baseline case with reduction of the scour width by half. Comparison of the distribution of measured displacements with depth for Tests 05 and 07 (shown in Figures 4.36 and 4.53) displayed similar profiles of horizontal displacement; however, in Test 07, the extent and

magnitude of the vertical displacement were decreased substantially. Measured displacement patterns also exhibited large lateral movements in the plane perpendicular to the direction of travel; although, these movements were partially attributed to lateral inclination or tilt of the model during the scouring event.

Vertical Stiffness

Whereas the vertical (hydrostatic) stiffness of the rigid body or ice feature affected its overall motion and stability for unsteady conditions at the inception of an event, the influence of vertical stiffness on the effects of scouring at an equilibrium depth and orientation may be expected to be negligible, over the range of stiffness conditions considered plausible for a full - sized iceberg or pressure ridge. The foremost effect of a change in the vertical stiffness was, therefore, to alter the boundary conditions of scour depth and angle of attack during the establishment of steady - state conditions. Test 02 provided limited experimental evidence of soil - structure interaction effects during scouring, with uplift response related to increased soil stiffness in the vicinity of a model pipeline trench; however, comparable behaviour was not apparent in remaining tests, where the model iceberg was modified to address the concern of unrealistic vertical stiffness.

Soil Type

In the present study, the effects of scouring were investigated in Speswhite kaolin clay, and experimental data were not acquired for soil of dissimilar type and mineralogy.

However, the behaviour of sand may also be fitted into the critical state framework which served to distinguish compressible and brittle soil events for clay. Inferences may, therefore, be drawn concerning the expected modes of deformation and failure, with consideration of similarity between the behaviour of loose sand and that of normally or lightly overconsolidated clay, and between that of dense sand and heavily overconsolidated clay. While the pattern of behaviour of sand is similar to that of clay, there are differences of degree, and except for situations in which mean normal stresses are very high, or the sand is unusually loose, the consolidation characteristics are much less important. The behaviour of sand is influenced most of all by its initial specific volume. The majority of sands are deposited in states which are denser than critical and, at low or modest stresses, behave as though they were heavily overconsolidated, irrespective of their stress history; although, some deposits may be sufficiently loose to compress upon shearing. Most commonly, therefore, sands may be expected to exhibit brittle soil behaviour during scouring, characterized by strain softening and localization of deformation, associated with the development of dilatant ruptures. The applicability of the continuum numerical representation is limited in such circumstances, without modification of the method of analysis to account for effects of discontinuous behaviour.

6.4.3 Summary of Experimental Data

Figures 6.30 and 6.31 present a summary of the test measurements of scour - induced soil displacement, in which magnitudes of the horizontal and vertical components are plotted against depth below the base of the scour. For compressible soil events, greater

peak values of the horizontal component were recorded at the scour base; however, large horizontal displacements were limited to shallower extent, as vertical displacements attenuated more gradually with depth below the scour base. Where brittle soil behaviour was dominant, as exhibited in Test 06 and, to a lesser degree, in Test 08, the response was characterized by an intense region of very large horizontal displacements immediately beneath the incision, together with small or negligible vertical displacement at all measured sub - scour positions. The experimental results displayed considerable variation, attributable to the effects of changes in the initial soil state, and to differences in stress paths during an event, which resulted from changes to boundary conditions such as the scour depth and the angle of attack. Scatter of the data may also be ascribed to measurement inaccuracies and variation in the grid measurements made in each test. In particular, the Test 01 horizontal displacement profile appeared to overestimate actual soil movements as a result of the limiting accuracy of the manual measurement techniques employed. Similarly, the variation in measured magnitudes of vertical displacement in Tests 05 and 09 indicated that the results presented were representative of extreme values for these events, related to unsteady scouring conditions.

The region of large sub - scour displacement was defined approximately for individual scouring events by specification of the maximum value immediately below the scour base (interpolated at depth of 0.1 m below the scour base) together with the limiting depth, below which displacement magnitudes less than a lower bound of 0.2 m were measured. A summary of results from the experimental programme is presented in Table 6.2. The magnitude of the horizontal component of displacement at the scour base ranged from 0.5 to 3.4 m, and averaged 1.6 m for all test measurements. The extreme

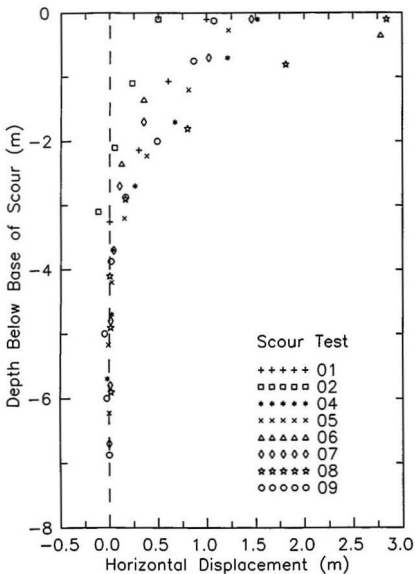


Figure 6.30 Maximum horizontal component of soil displacement plotted against depth below the scour base - summary of results from experimental programme

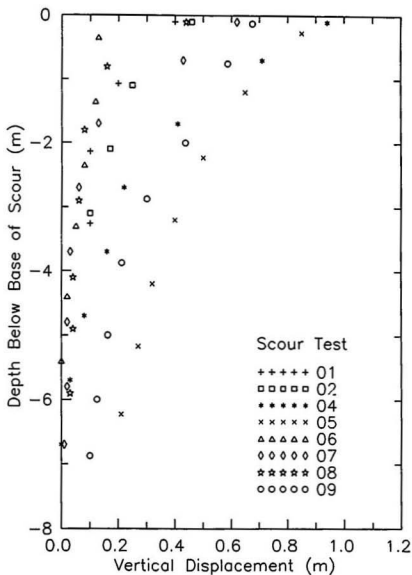


Figure 6.31 Maximum vertical component of soil displacement plotted against depth below the scour base - summary of results from experimental programme

Table 6.2 *Horizontal and vertical displacement magnitudes at scour base and limiting depths below scour base - summary of results from experimental programme*

Scour Test	Horizontal component of sub - scour displacement		Vertical component of sub - scour displacement	
	magnitude at scour base *	limiting depth below base **	magnitude at scour base *	limiting depth below base **
01	1.0	2.5	0.4	1.1
02	0.5	1.4	0.5	1.7
04	1.5	3.1	0.9	3.2
05	1.3	3.0	0.9	6.2
06	3.4	2.0	0.1	0.0
07	1.5	2.3	0.6	1.5
08	2.8	2.8	0.4	0.7
09	1.1	2.8	0.7	4.2

* magnitude (m) at depth below scour base = 0.1 m

** depth (m) at lower bound displacement magnitude = 0.2 m

values of the limiting depth of the region of large horizontal displacement were 1.4 and 3.1 m, with an average extent of 2.5 m, corresponding with a normalized value of 2.5 scour depths. The magnitude of the vertical component of displacement at the scour base ranged from 0.1 to 0.9 m, and averaged 0.6 m for all test measurements. The extreme values of the limiting depth of the region of large vertical displacement were 0.0 and 6.2 m, with an average extent of 2.3 m, corresponding with a normalized value of 2.3 scour depths. The average values may be considered relevant to compressible soil events for the particular soil type and states influenced by the range of parameters investigated in the present study. In contrast, for events which involved predominantly brittle soil behaviour, measured vertical sub - scour displacement was negligible, and the extent of the region of large horizontal displacement may be limited to less than 1.4 scour depths. The values quantifying a limiting depth of the region of large displacement were sensitive to the selected lower bound magnitude; the appropriate zero benchmark was dependent on pipeline performance, discussed in Section 6.5. In addition, inaccuracies may be expected due to interpolation between grid measurements, which were available for approximate one metre depth intervals at prototype scale.

6.5 Implications for Pipelines

6.5.1 Model Pipeline Results

The experimental programme allowed for limited direct observation of the effects of scouring on buried model pipeline segments. The scaling relationships were detailed in Section 2.4.3, and Chapter 3 provided information pertaining to model characteristics and

installation procedures. Inadequacies of the representation included the following : finite segment lengths with unknown end fixities; lack of operational internal pressure or temperature; thickness to diameter ratio which exceeded that of typical prototype geometries, and; material yield stress lower than that of commonly employed pipeline steels. These limitations suggested that measured deformations were unlikely to represent the detailed response of a typical full - scale marine pipeline. Instead, the models provided general indication of the sub - scour depths at which permanent distress of a pipeline may be induced by the effects of scouring. As indicated in Chapter 4, the nature of the distress exhibited varied from minor plastic bending in most instances, to more significant measured horizontal and vertical curvature. Model pipeline segments in the scour path experienced local denting and severe plastic bending to positions below the scour; however, the development of buckling failure and rupture or loss of integrity was inhibited by the high thickness to diameter ratio of the pipeline geometries investigated.

Table 6.3 provides a summary of model pipeline performance in the experimental programme, given as a listing of the depths for which a segment was found to be plastically deformed, and the depths for which a segment was not permanently affected by the scouring event. Two general results were evident : (1) permanent distress was displayed for some model pipelines which were initially situated at depths below the scour base, and; (2) in some instances, model pipelines subjected to large soil displacement below the scour base did not exhibit any measurable deformation. The first result was consistent with the requirement to address sub - scour soil displacement in a rational pipeline design methodology. An implication of the second result was that it may be possible to establish safe designs for pipelines buried within a region of large (plastic)

Table 6.3 Model pipeline performance for different initial depths of segments below base of scour - summary of results from experimental programme

Scour Test	Model pipeline deformed during scouring event	Model pipeline unaffected during scouring event
	Initial depth of segment below scour base (m)	Initial depth of segment below scour base (m)
01	0.1	1.1 , 3.2 , 4.5
02	0.0 , 0.2	
04	0.0 , 0.6	
05		0.6 , 1.5
06		0.4 , 1.3
07	0.6	
08	- 0.3	
09		1.5 , 2.2

soil displacement below the depth of scouring, as may also be necessary to ensure an economically viable solution.

6.5.2 Design Methodology

The primary objective of the present study was the development of models which would

allow for the evaluation of soil deformation due to ice scouring, and the relationship between theoretical and centrifuge physical approaches, in support of this objective, was depicted schematically in Figure 5.1. As illustrated in Section 6.5.1, large sub - scour soil deformations transmit loading to a buried pipeline which is stiffer or more rigid than the soil in which it is embedded. The soil - pipeline interaction must therefore be addressed in order to facilitate prediction of the pipeline response to loading imposed by soil movement, such that safe burial depths may be established in accordance with conventional design criteria. To this end, the numerical representation adopted in the present study may be extended to incorporate a model of the pipeline; however, the inherent complexity of a three - dimensional finite element analysis of the complete ice - soil - pipeline interaction, including a realistic model of the nonlinear bending of an internally - pressured pipeline, may be expected to restrict practical implementation of such an approach. Alternatively, the free field displacements, derived from numerical simulation of the ice - soil interaction, may serve as input conditions for an independent analysis of the soil - pipeline interaction. The development and verification of an engineering model of this type was recently described as part of a parallel study on the effects of ice scouring on buried pipelines (C - CORE, 1995). Some of the results of this investigation, which demonstrated the practical implementation of the design methodology implicit in the present study, are presented here for completeness.

Soil - Pipeline Interaction

An existing model of soil - pipeline interaction (PIPSOL), previously applied in simulation of the effects of differential ground movements such as frost heave and thaw

settlement (Nixon et al., 1984), was adapted for use in the analysis of the pipeline response to ice scour - induced soil deformation. The PIPSOL model (Nixon, 1994) is a numerical extension of the Winkler solution for an elastic beam on a spring foundation, in which the pipeline is represented as a nonlinear, axially loaded beam - column, and the soil is idealized as an elastic - plastic material. A nonlinear moment - bending strain relationship is used to simulate the response of the pipeline, with consideration of the biaxial stress state imposed by internal pressure. The analysis provides information on pipeline deformation in bending, axial extension, and ovalization.

Figure 6.32 illustrates the sequence of steps involved in implementation of the engineering model. These procedures may be embedded in an overall risk assessment based on seabed scour data and ice environmental information for the prescribed pipeline route, in order to address the following two conditions : (1) the probability that a particular ice keel will intersect the route during the time interval of interest, and; (2) for a given ice keel - pipeline encounter, the probability that any imposed pipeline distress will exceed design requirements for serviceability or ultimate limit states. For a given scouring event, the distribution of free field soil displacements in the vicinity of the pipeline may be defined based on information from separate numerical analyses of the ice - soil interaction, or derived directly from empirical evidence, where available.

Loads are imparted to the pipeline by relative motion between the pipeline and the surrounding soil, as will occur when the soil restricts the free movement of the pipeline or when the pipeline attempts to resist the movement of adjacent soil. This behaviour is characterized through soil resistance functions, which describe the relationship between the load per unit length of the pipeline and the relative displacement

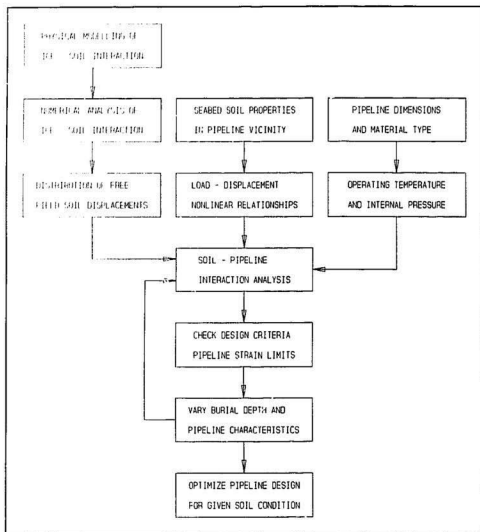


Figure 6.32 Schematic illustration of procedures involved in implementation of engineering model of ice - soil - pipeline interaction (modified after C - CORE, 1995)

between pipeline and soil. The nonlinear load - displacement relationships, also known as $p - y$ curves, may be obtained based on conventional soil mechanics principles in accordance with the recommendations provided in ASCE (1984) or other accepted industry guidelines. The final input conditions required for the analysis are the pipeline characteristics, which include the section dimensions and material type, as well as the temperature and internal pressure of the pipeline during operation. An advantage of an independent model of the soil - pipeline interaction, is to allow a series of simulations to be conducted in a rapid and computationally efficient manner, for a particular distribution of free field soil displacements. Several analyses may be performed in which the pipeline structural features and burial depth are varied, in order to optimize the design, with consideration of strain limits or other design criteria established for the pipeline section.

Verification of Engineering Model

An example investigation was carried out to demonstrate the procedures involved in implementation of the engineering model, and to illustrate the effects of changes to scour parameters on the predicted pipeline performance (C - CORE, 1995). Partial numerical verification of the model, for use in the study of ice scouring effects on buried pipelines, was also obtained through comparison of analysis results with data acquired in the present experimental programme. The analysis was conducted to predict the measured pipeline response in Test 04, where segments at two different burial depths suffered permanent distress as a result of the effects of the scouring event. The performance of

the model pipeline segment at greater depth, with an initial soil cover of 21 mm (0.6 m below the scour base at prototype scale), was simulated.

The lateral and vertical distributions of the free field soil displacements, specified as input conditions for the analysis, were derived from the experimental records presented in Section 4.3.4 and Appendix A. The measured soil displacements represented cumulative values following complete passage of the rigid body or ice keel. The maximum transient displacements during the scouring event were approximated as upper bounds for the complete data set acquired from the grid measurements. The nonlinear load - displacement relationships were based on the ASCE (1984) recommendations for soft to medium clays, where the peak load was derived from bearing capacity theory using the soil undrained shear strength at the model pipeline elevation and the interaction factor suggested by Rizkalla et al. (1992). A surcharge term was added to the bearing capacity equation to account for the high vertical stress imposed by the ice keel, such that calculated peak loads varied with lateral distance along the pipeline axis. The moment - bending strain relationship for the pipeline was estimated using a hyperbolic uniaxial stress - strain curve (Nixon, 1994). Since the experimental pipeline displacements were measured following unloading at the completion of the event, it was necessary to evaluate the relaxed strains and the corresponding displacements, with allowance for elastic rebound of the pipeline to zero bending moment.

Some aspects of the simulated pipeline response showed reasonable agreement with the experimental results, in consideration of the requirement to estimate input conditions from end of test measurements. Figure 6.33 shows a comparison of the predicted and measured displaced configuration for the pipeline. The predicted pipeline

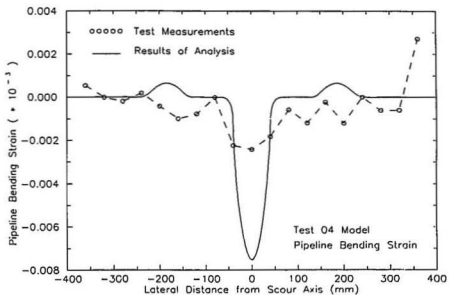
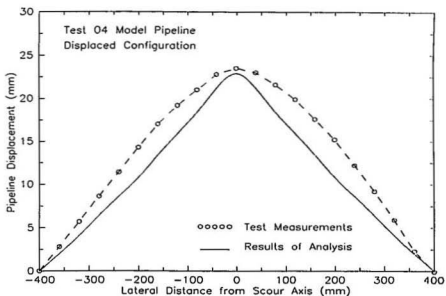


Figure 6.33 Test 04 comparison of predicted and measured values following unloading. Top : Pipeline displaced configuration; Bottom : Bending strain (C - CORE, 1995)

displacements were similar in magnitude to the measured pipeline displacements. The pipeline was deformed with the soil beneath the ice keel, and was restrained in the transverse direction by the soil outside of the scour path. With allowance for elastic rebound following unloading, the analysis predicted a high degree of straining in the central portion of the pipeline, with relaxation to a relatively uniform profile toward the ends of the segment. The measured pipeline displacements were smoother and more dispersed than the predicted values, which displayed a more pronounced plastic hinge development. The predicted displaced pipeline configuration also exhibited a slight reverse curvature adjacent to the edges of the scour path, which was not apparent from test measurements.

To allow for comparison with the analysis results, pipeline bending strains were calculated as the second derivative of the measured pipeline displacements. This approach was anticipated to introduce significant error, due to the central differencing procedure and the limiting accuracy of the test measurements. In Figure 6.33, the predicted pipeline bending strains are shown plotted against distance along the pipeline axis, together with values derived from the measured pipeline displacements. The predicted bending strains at the centre of the segment were much greater in magnitude than the corresponding experimental results, as may be partially attributed to insufficient measurement precision to permit resolution of peak values at this location.

Chapter 7

Summary and Recommendations

7.1 Introduction

The scouring of seabed sediments by a moving body of ice is a common occurrence throughout the continental shelf regions of the Arctic Ocean, the Canadian east coast, and other potential production areas for offshore hydrocarbon reserves. The effects of this phenomenon represent a critical design consideration for oil and gas pipelines planned to traverse these regions of active scouring. It has been determined that it is unlikely that an unprotected pipeline could safely withstand the large forces imposed through direct ice contact, and burial at sufficient depth to avoid this circumstance is essential. Importantly, however, large scour - induced soil deformation may also transmit loading to a pipeline buried below the maximum depth of ice intrusion, causing permanent distress which may render the structure unsafe or unserviceable. A rational pipeline design methodology must therefore incorporate a theoretical model which provides reliable quantitative predictions of the soil displacements generated during ice scouring. Following definition of the soil displacement field, the pipeline response to the scouring event may be evaluated through adapted procedures of soil - pipeline interaction analysis.

7.2 Physical Modelling

A programme of centrifuge model tests was undertaken to provide data on the effects of ice scouring, for well - defined events representative of relevant field situations, in support of the development and verification of a realistic theoretical model of the ice - soil interaction. Model design criteria or similarity requirements were satisfied such that the important physical aspects of the prototype were reproduced at specified scales. Use of the centrifuge ensured that effective stresses and pore fluid pressures in the small scale models were equivalent with corresponding full scale conditions, as required to allow for dependency of the mechanical behaviour of soil on the overall stress state.

Ice scouring is a complex phenomenon, and a variety of event scenarios may be envisaged depending upon the environmental driving forces which are acting, the characteristics of the ice feature, and the soil type and state. The assessment of field evidence provided a basis for the development of an appropriate physical model idealization. For modelling purposes, it was assumed that the ice feature moved horizontally through a uniform level seabed at constant velocity, and motion during the event was not limited by the available driving forces. Initial uplift and rotational movements were permitted prior to the achievement of steady - state conditions. The ice feature was represented by a rigid body, and the shape of the keel was chosen to reflect the equilibrium geometry, established following expected modification over the initial stages of the prototype event. The soil type investigated was reconstituted Speswhite kaolin clay; the stress history of the soil was prescribed to establish particular initial stress states, with general reference to properties of the surficial Unit A sequence of

Beaufort Sea clays, to ensure that the range of strength and stiffness modelled was relevant in practice.

Test apparatus and experimental methods were developed or adapted to simulate the idealized scouring condition, including definition of the soil stress history through laboratory preparation, establishment of the correct current effective stress levels in - flight on the centrifuge, and appropriate representation of the prototype perturbation and associated stress paths. The equipment and instrumentation also allowed for monitoring of the imposed conditions and external model responses, to ensure well - defined events which were amenable to subsequent analysis. The test measurements were intended to provide information on the contact pressures and resultant forces acting on the model ice feature, the pore water pressure changes within the soil, the scour - induced soil displacement field, and the post - event displaced configuration of model pipeline segments.

A total of nine tests was conducted, excluding proof tests which were carried out to evaluate the equipment design and system performance. In each test, a unique event applicable to a notional field situation was modelled, and accurate data on the effects of scouring were acquired. A prototype stratum of saturated clay which was 18 m deep and 85 m in diameter at Earth's gravity was investigated at 1 / 100 scale in a model specimen of equivalent soil brought into equilibrium at 100 gravities on the centrifuge. The level of pre - consolidation was selected to obtain a desired profile of overconsolidation ratio, and was altered in particular tests to examine the influence of initial soil state on the effects of scouring. The maximum vertical effective stress imposed in the laboratory ranged from 110 to 200 kPa, and a pre - consolidation stress level of 140 kPa was

selected to define the baseline test condition. The near surface clay of each specimen was in an overconsolidated state and exhibited undrained shear strengths of between 10 and 20 kPa, on average.

In addition to changes in the initial soil state, specified boundary conditions were varied in the test programme, to ascertain the effect of individual parameters on the experimental results. The vertical position of the model ice feature was unrestricted during a test, to allow for uplift movements at the inception of the event. The scour depth established for steady - state conditions included extreme values of 0.4 and 2.2 m at prototype scale, with an average magnitude of 1.2 m for the complete range of tests performed. The prototype scour width was limited to a maximum value of 10 m, which served as a baseline condition, and was reduced by half to investigate a narrow scour of 5 m width in a given test. Similarly, the attack angle of the model ice feature was set at 15 degrees to the horizontal, with a single test variation to evaluate a sharper keel geometry with an attack angle of 25 degrees. The model was advanced at a uniform rate of 0.07 m/s, which was sufficiently rapid for essentially undrained conditions to prevail, corresponding with expected field conditions for scouring in clay; however, the capabilities of the drive system were exceeded in particular tests, which resulted in movement at a substantially reduced rate, applicable to a fully or partially drained prototype event.

The centrifuge test programme demonstrated the utility of the test apparatus and experimental procedures, with exceptions where equipment malfunction resulted in unplanned changes to parameters in individual tests. The modelling of models technique provided reasonable verification of the internal consistency of the representation, and

increased confidence in extrapolation of the experimental results to full scale. The physical characteristics of the model scours were also compatible with the general morphology and structure observed in field investigations of both modern and relict features.

Excess pore pressures were measured at discrete locations throughout an area which extended over a prototype distance of 15 m, both laterally outward from the scour axis and vertically with depth. The maximum recorded increase in pore pressure in the apparent steady - state region of scouring ranged between 35 and 108 kPa, with an average value of 62 kPa. The maximum recorded pore suction in the apparent steady - state region ranged between - 16 and - 44 kPa, with an average value of - 27 kPa. The peak positive responses were typically observed at times preceding the model ice feature passage over the measurement position, whereas the negative pore pressure changes were witnessed immediately subsequent to passage of the model.

The reliability of the resultant force records was limited by the indirect measurement techniques employed in derivation of the experimental results. The test measurements did not show evidence of periodic variation of loading, apart from irregularities of the response attributed to initial unsteady conditions or measurement inaccuracies. The average magnitudes of the horizontal component of force at steady - state ranged from 2.1 to 6.0 MN in individual tests, and associated measurements of the vertical force component included values between 6.0 and 17.6 MN at prototype scale. The inclination of the resultant force vector was approximately normal to the scouring face of the model keel over the duration of most of the events investigated. The vertical / horizontal force ratio ranged between 1.9 and 3.9, and an average value of 3.0

was established for tests in the experimental programme. Contact pressures recorded at the horizontal base and inclined scouring face of the model provided some information on the stress distribution at the interface; however, the transducer responses were characterized by considerable fluctuation and the pressure measurements were subject to inaccuracies as the result of stress concentration and arching effects. The data records from bottom - mounted transducers suggested that the force contribution developed at the horizontal base of the model typically represented a smaller portion of the resultant force measured during the event.

7.3 Numerical Analysis

The finite element method was evaluated for use in the development of a theoretical model for prediction of the soil response under idealized scouring conditions. The adopted numerical representation included the following attributes : a finite strain formulation to accommodate both large deformations and strains as characteristic effects of scouring; a coupled deformation / diffusion solution for soil modelled as a two - phase nonlinear elastic - plastic material, and; a finite - sliding capability applied by means of rigid surface interface elements to allow for inherent nonlinear boundary effects. The general purpose finite element code ABAQUS provided the necessary capabilities for implementation of the analysis.

A finite strain theory was required to account for large soil movements which introduced significant changes in the geometry of the solution domain, where peak strain levels on the order of unity were developed in simulation of a scouring event. A correct

formalism of stresses and strains was established, and the constitutive relations were generalized in accordance with the revised definitions. An updated Lagrangian formulation was adopted, which allowed for appropriate representation of the soil stress history, the boundary conditions, and the stress and strain states in the current deformed configuration. Rectangular eight-noded isoparametric elements with biquadratic displacement and bilinear pore pressure descriptions were selected for use in the coupled effective stress analysis, with consideration of the incompressibility constraint imposed by essentially undrained conditions. The solid (continuum) elements used a fully nonlinear formulation to accommodate finite strain and rotation; however, a computational limit may be exceeded in local regions of high strain gradients, where severe element distortion may result in loss of accuracy and decreased rate of solution convergence.

The soil behaviour was described by the Modified Cam-clay critical state model, which is known to successfully reproduce the major deformation characteristics of soft clays. In accordance with concepts of critical state theory, the soil exhibited strain hardening or softening behaviour following initial yield, and the particular response induced was dependent upon the initial state and the applied stress paths. For yielding of lightly overconsolidated soil on the wet side of critical state, continued deformation was associated with volumetric compression or positive excess pore pressure development, whereas, for yielding of heavily overconsolidated soil on the dry side of critical state, volumetric expansion or negative excess pore pressures were anticipated. The soil underwent hardening or softening toward an ultimate or critical state, where

plastic shear distortion continued indefinitely without further changes in volume or effective stresses.

Adequate simulation of nonlinear boundary effects at the ice - soil interface was accomplished through use of rigid surface interface elements that modelled the contact between an element face, which formed part of the deformable soil medium, and a rigid body idealization of the model keel. The formulation allowed for separation and relative displacement of finite magnitude, and arbitrary rotation of the contacting surfaces. A perfectly hard contact condition was defined such that any contact pressure could be transmitted between the surfaces, with no interpenetration. The tangential shear stress tractions were related to the normal pressure stress in accordance with the standard Coulomb friction model.

The material parameters adopted in the analysis were derived from an extensive base of experimental data for Speswhite kaolin clay, acquired through accumulated experience at Cambridge University with triaxial and oedometer tests. The complete description of the constitutive model required five parameters to specify the shape and size of the yield surface at a given mean effective stress and specific volume, as well as the elastic properties of the material. The model parameters included the critical state stress ratio, the gradient of the normal consolidation lines, the gradient of the swelling lines, the critical state reference specific volume, and a constant value of the Poisson's ratio. The variation of the vertical and horizontal permeabilities with the current state was also specified through empirical relationships which described dependency on the void ratio. In addition, an appropriate value of the interface angle of friction was

required, with implementation of the friction model to define the local material response at the contacting surfaces.

A two - dimensional plane strain idealization was investigated, and full scale prototype conditions were simulated directly in the analysis. Numerical representation of a scouring event required sufficient horizontal movement of the rigid body to approximate a steady - state condition. Severe distortion of elements adjacent to the rigid body restricted allowable movement of the finite element mesh for which convergence was attained at large movements, and it was therefore necessary to adopt a relatively coarse discretization over the scour depth. Preliminary analyses were conducted to determine the maximum rigid body movement, as related to the selected mesh configuration. The boundary conditions adopted in the analysis were compatible with those imposed in containment of the physical model.

The numerical analysis was implemented through specification of the sequence of events or loadings for which the response of the model was sought. The *in situ* effective stress state and the corresponding specific volume conditions were established in the initial step of the analysis, in accordance with the prescribed stress history and assumed one - dimensional loading / unloading of the soil. The simulation of the event was imposed as a perturbation step, following a process of iteration to ensure equilibrium of the initial stress state with boundary conditions and geostatic loadings. The motion of the rigid body was idealized as a horizontal translation at a uniform scour depth, selected to represent the steady - state condition. A final unloading step followed simulation of the scouring event, to allow for direct comparison of the analysis results with data acquired through post - test site investigation of the physical model.

In the assessment of potential scouring mechanisms for essentially undrained conditions, it was necessary to balance the volume change due to loss of material in the scour path. The material included in development of a frontal mound, and berm formation through lateral clearing, was insufficient to accommodate the complete volume loss during scouring, and the remainder of the volume change involved sub - scour deformation. It was inferred that downward vertical sub - scour displacement was compensated through lateral displacement at depth, together with upward displacement across a wide lateral extent; however, a pattern of deep - seated lateral movement was not identified explicitly in the experimental study. Lateral displacements were measured at shallow depth, and associated with local heave of the surface adjacent to the edges of the scour. The lack of evidence for a characteristic mechanism of sub - scour deformation was attributed to the distribution of material movement over an extensive region. In addition, volume change related to compression below the scour depth was partially accommodated through surface drainage, as pore pressure dissipation transpired more rapidly in the centrifuge model than in the corresponding prototype.

The limitations of the two - dimensional continuum representation were evaluated in consideration of restrictions imposed on potential scouring mechanisms. Without allowance for lateral movement of failed material, the model described a progressive build - up of the frontal mound, where downward vertical displacement was insufficient to account for the complete volume loss in the scour path. The absence of a lateral clearing mechanism limited the range of motion of the rigid body over which realistic predictions of the material response were expected. In addition, the numerical representation neglected edge effects of near - surface lateral displacement and associated

local heave. Sub - scour displacements permitted opposite to the direction of motion of the rigid body did not represent a significant component of the material response, with continued upward displacement in front of the rigid body.

Preliminary verification of the numerical approach was provided through a comparative examination of the approximate solutions derived from the analysis and the experimental data acquired in representative tests. Tests 04, 05 and 09, with limited departures from idealized scouring conditions adopted in the analysis, were compared with numerical simulations of the corresponding prototype events. Correlation of measurements from Tests 05 and 09, which modelled an identical prototype event, also permitted assessment of the internal consistency of the experimental methods.

The comparison of Test 04 data and values computed through simulation of the event, indicated reasonable quantitative agreement between predicted and measured effects of scouring, including excess pore pressures, resultant forces, and soil displacements. The computed excess pore pressure field displayed overall correspondence with the range of measured pore pressure magnitudes, and the zone of influence inferred from transducer records. In addition, the analysis results provided appropriate representation of the character of the local responses including similar peak magnitudes and rates of excess pore pressure development; although, in general, measured pore pressure magnitudes exhibited greater variability with changes in depth, in relation to computed values.

Adequate prediction of the horizontal and vertical components of the resultant force also provided evidence of similarity between associated stress fields. Close agreement was obtained between computed and measured values of the horizontal force

component, over the complete range of movement simulated in the analysis. For the vertical force component, the correspondence between computed and measured values improved with increased movement; however, eventual over - prediction of the measured steady - state response was anticipated, with continued upward displacement of material in front of the rigid body and representation of a greater range of movement in the analysis. Other factors which served to inhibit realistic prediction of the resultant force included measurement inaccuracies, the effects of initial unsteady conditions, and the force contribution arising from friction at the sides of the model keel.

The computed two - dimensional displacement field was qualitatively similar to the measured displaced configuration for an axial section through the clay specimen. The analysis results displayed a semi - circular pattern of large soil displacement which extended from the base of the rigid body to the free surface, and encompassed material beneath the scour depth. The magnitudes of the computed displacements attenuated with distance in front of and below the current position of the rigid body. A material point situated in the scour path, was initially subjected to upward and forward displacement, associated with formation of a continuous frontal mound, and subsequently experienced downward and continued forward displacement, with passage of the rigid body beyond the position. Soil displacements opposite to the direction of motion were computed at positions below the scour depth, consistent with evidence from other tests in the experimental programme; however, these backward movements primarily represented an elastic portion of the response which was recovered upon unloading.

The profiles of horizontal soil displacement derived from the analysis exhibited increased magnitudes for vertical profiles at greater distance in front of the initial rigid

body position, without allowance for lateral movement of material in the scour path. The measured steady - state response was represented by the cumulative displacement of reference vertical profiles subjected to complete passage of the rigid body, and associated with development of a realistic configuration of the frontal mound. The correspondence between computed and measured horizontal and vertical displacements indicated that displacement conditions for steady - state scouring may be approximated without requirement to represent the complete range of horizontal movement in simulation of the event.

The correlation of Test 05 / 09 analysis results with experimental data was less satisfactory, and indicated deficiencies of the numerical representation in addition to expected measurement inaccuracies. The computed excess pore pressure field displayed reasonable agreement with the range of recorded magnitudes and the region of measured effects of scouring; however, the computed responses did not provide detailed correspondence with individual transducer records, as exhibited for similar comparisons of computed and measured pore pressure values for Test 04. The Test 05 / 09 analysis predicted a relatively uniform distribution of excess pore pressures, and was unable to quantitatively represent the observed attenuation of measured peak magnitudes with increased depth. The contact pressures for reference interface elements increased to maximum values with movement along the inclined surface of the rigid body, and decreased to minimum values at the horizontal bottom surface. The computed normal stresses at the interface displayed close agreement with average and peak values from measurements at the inclined and horizontal surfaces.

The Test 05 / 09 analysis predicted greater magnitudes of both the horizontal and vertical components of the resultant force in relation to corresponding Test 04 computed values, in agreement with the experimental findings; however, the analysis results provided inadequate representation of the force measurements. For the horizontal component, the computed values under - predicted the measured response, as may be partially attributed to neglect of additional forces arising from initial unsteady conditions and the effects of friction acting at the sides of the model keel. For the vertical component, reasonable correspondence was obtained between computed and measured values at the completion of movement in the simulation; however, the computed force record displayed continued increase without convergence toward the measured steady - state level.

The computed soil displacement field displayed similar patterns of movement in comparison with results from the Test 04 analysis. The region of large displacement extended below the scour depth, and both horizontal and vertical components diminished in magnitude with increased distance from the current rigid body position. The vertical profiles of horizontal displacement at reference positions in the analysis provided reasonable predictions of the measured maximum sub - scour displacement, and correlation between the computed and measured depth of large displacement improved with representation of a greater range of movement. For the vertical component, the measured displacements decreased more gradually with depth below the base of the scour, and the analysis results under - predicted the test measurements over the complete profile of depths investigated. The computed vertical displacement magnitudes were comparable to lower bounds of the experimental data.

The laboratory pre - consolidation stress applied in Tests 05 and 09 defined an increased depth of soil at heavily overconsolidated initial states in relation to Test 04 conditions. The Test 05 / 09 analysis predicted increased magnitudes of cumulative shear strain and reduction in the extent of the region of large displacement in relation to Test 04 computed values. The greater localization of the response was associated with an increased number of soil elements having tendency to soften toward critical states under continued deformation throughout the event.

7.4 Soil Deformation

In evaluation of the effects of scouring, two general classes of event were distinguished, corresponding to compressible and brittle regimes of soil behaviour, defined through concepts of critical state theory. For compressible behaviour, with stable yielding of initially loose or lightly overconsolidated materials on the wet side of critical state, an event was characterized by continuum distortion or flow. The volume change due to loss of material in the scour path was balanced primarily through compressive deformation beneath the incision, rupture planes were not formed, and scour - induced soil displacements attenuated with distance from the rigid body. Compressible soil events were associated with plastic volumetric compression and strain hardening, which allowed for increased transmission of stresses and distribution of deformation over a greater depth of influence. As a result, events dominated by compressible soil behaviour were most relevant from the point of view of pipeline design to accommodate sub - scour soil deformation.

In contrast, for brittle behaviour of initially dense or heavily overconsolidated materials on the dry side of critical state, an event was characterized by development of a succession of rupture planes, extending from the base of the rigid body to the free surface in a repeating pattern, and associated with periodic variation of the resultant force. In this instance, the material loss in the scour path was largely attributed to progressive lateral clearing of discontinuous blocks of soil, and related berm formation at the sides of the incision. For brittle soil events, with strain softening beyond peak stresses, soil deformation was concentrated in regions of weakened material, and sub - scour soil displacement was expected to be relatively localized. Previous analytical investigations indicated that rupture planes formed as mechanisms of failure during brittle events do not extend far below the depth of scouring, although minor sub - scour disturbance was predicted for strongly dilatant soils. A region of large (plastic) soil displacement was attributed to shear dragging deformations of soil immediately beneath the rupture planes or the rigid body sliding relative to the soil; however, the softening behaviour of adjacent material was also expected to limit the extent of a region of large dragging displacements.

The present study provided verification of the adopted numerical representation for prediction of the effects of scouring in soft clay under essentially undrained conditions, where the soil response was governed by compressible behaviour. Similar applicability was not demonstrated for brittle soil events, where the development of discontinuous failure mechanisms was incompatible with the continuum idealization. The analysis was not implemented to investigate a range of parametric variations, and the

evaluation of the influence of test parameters relied primarily on data acquired from the experimental programme.

The mode of soil deformation and failure exhibited during a scouring event was dependent upon the initial state of the soil, and was also influenced by changes to the applied stress paths which resulted from variation of boundary conditions described by test parameters. A substantially reduced scouring velocity in particular tests, together with drainage at the enhanced rate of dissipation in the model, allowed for softening of near surface soil and scouring effects which were characteristic of brittle soil events. The relative similarity of measured displacement patterns in other tests was attributed in part to the influence of drainage conditions. For essentially undrained conditions, the dissipation of negative excess pore pressures was suppressed, such that softening behaviour and consequent localization of the soil response was partially inhibited.

The attack angle and scour depth defined boundary conditions for the two - dimensional representation of scouring. For brittle soil events, earlier analytical studies implied that the extent of rupture planes developed during scouring was independent of changes to both parameters, and failure mechanisms were not expected to encompass positions below the depth of scouring. The effect of decreasing the attack angle or increasing the scour depth was to induce high or rapidly increasing mean normal stresses which may be sufficient to direct stress paths to failure through stable yielding on the wet side of critical states. For compressible soil behaviour, changes to the attack angle or scour depth influenced the pattern and extent of the expected soil deformation. The intensity of vertical stresses induced during scouring was increased for greater scour depths or blunter keel geometries, leading to increased vertical strains and displacements.

In addition, increased spherical pressures resulted in plastic compression and hardening for soil elements below the scour and allowed for greater transmission of stresses, and increased distribution of deformation.

The correspondence of computed and measured effects of scouring in the analysis of Test O4 provided support for a two - dimensional numerical representation, where typical field scouring geometries were anticipated to entail greater scour width / depth ratios than investigated in the experimental programme. For exceptional cases involving narrow ice features, where plane strain conditions were invalidated, analytical descriptions of three - dimensional scouring mechanisms, for events in which brittle soil behaviour was dominant, were uncertain. For compressible soil behaviour the reduction of scour - induced stresses, and corresponding strains and displacements, with depth below the scour was more gradual for two - dimensional events described by high width / depth ratios. The diminished capacity for lateral distribution of the applied loads during a plane strain event accounted for greater depths required to attain a similar reduction in stresses, resulting in a more extensive region of sub - scour deformation.

Although the present study was limited to the investigation of Speswhite kaolin clay, the critical state framework assisted in the evaluation of expected modes of deformation and failure for scouring events in soil of dissimilar type and mineralogy. The *in situ* states of sand deposits are most commonly situated on the dry side of critical. Sands therefore exhibit similar patterns of behaviour to heavily overconsolidated clays, although some deposits may be sufficiently loose to compress during shear. As a result, brittle soil behaviour, associated with localized deformation and the development of

dilatant ruptures, was expected for scouring in sand at states representative of typical field soil deposits.

A summary of test measurements of sub - scour soil displacement displayed variation due to the effects of changes to the prescribed stress history or initial state, and to differences in applied stress paths arising from changes to boundary conditions in individual scouring events. Some scatter of the experimental data was also attributed to the inaccuracies introduced by measurement techniques. In general, the measured horizontal component of displacement was larger in magnitude at the scour base than the corresponding vertical component, and the vertical component of displacement attenuated more gradually with depth below the scour. For the horizontal component, the magnitude of displacement at the scour base (interpolated at a depth of 0.1 m below the scour base) ranged from 0.5 to 3.4 m, with an average displacement of 1.6 m for all tests. The extent of the region of large displacement (estimated for a lower bound displacement magnitude of 0.2 m) ranged from 1.4 to 3.1 m below the scour base, with an average depth of 2.5 m, corresponding to a normalized value of 2.5 scour depths. For the vertical component, the magnitude of displacement at the scour base ranged from 0.1 to 0.9 m, with an average displacement of 0.6 m for all tests. The extent of the region of large displacement ranged from 0.0 to 6.2 m below the scour base, with an average depth of 2.3 m, corresponding to a normalized value of 2.3 scour depths. The average values derived from the summary of experimental data were applicable to the particular soil type and states investigated in the present study, which defined compressible soil events in the majority of tests performed. In contrast, brittle soil events were characterized by small or negligible vertical displacements, and a relatively intense region of large horizontal

displacement which extended to less than approximately 1.4 scour depths below the scour base.

7.5 Pipeline Response

A summary of model pipeline performance in the experimental programme provided an indication of the sub - scour depths at which permanent distress of a pipeline may result from the effects of scouring. The plastic deformation exhibited by pipeline segments initially located at depths below the scour base supported the requirement to account for sub - scour soil displacement in a rational pipeline design methodology. The observation of other segments which were unaffected by the event suggested that, in some instances, safe designs may be established for pipelines buried in regions of large (plastic) soil displacement below the scour depth, as may also be necessary to ensure a cost - effective solution.

For a given scouring event, the distribution of free field soil displacements was defined through complementary approaches of physical and numerical modelling of the ice - soil interaction. A design methodology (C - CORE, 1995) was described in which the measured or computed soil displacements then served as input conditions for an independent analysis of the soil - pipeline interaction. Partial verification of the approach was obtained through comparative examination of analysis results with test measurements of the displaced configuration of a model pipeline segment, acquired in the present experimental programme.

7.6 Further Research

The present study was undertaken to advance the understanding of ice scouring effects on seabed soil through observations from centrifuge model testing and related numerical analyses. Further research is recommended to address the limitations of the physical and numerical representations and to extend their range of application.

The experimental programme comprised a series of nine tests in which a particular idealization of ice scouring was investigated. The tests explored a limited range of parametric variations for model scouring events conducted in a reconstituted kaolin clay. The accurate definition of input conditions was hindered by the permitted degrees of freedom of the model ice feature, and also by equipment and instrumentation malfunction in some instances. Further testing is required, to encompass an increased range of scouring conditions, and to allow for controlled study of the effects of individual parameters on the soil response. Among the relevant parameters expected to influence the magnitude and extent of soil displacements developed during a scouring event are the stress history or initial state of the soil, the attack angle, and the scour depth. Tests should also be performed to establish the relative significance of the length of the horizontal surface of the rigid body idealization of the ice keel. Importantly, the experimental database on ice scouring effects should be extended through investigation of an increased range of known laboratory materials, in addition to layered soil deposits which may represent a relevant field soil condition.

The programme of additional tests should be planned with consideration of the requirement to provide quantitative data in support of the development and verification

of deterministic models of the ice - soil interaction. Therefore, continued emphasis should be placed on the improvement of measurement techniques to facilitate detailed evaluation of soil displacements and related mechanisms of soil failure. To allow for verification of models of the soil - pipeline interaction, more realistic pipeline representations should also be incorporated in the centrifuge tests, with appropriate instrumentation to monitor the bending strains and deformations induced by a scouring event. Subsequent testing should also address particular deficiencies of the experimental methods adopted in the present study, including design of more reliable systems for the measurement of resultant forces. Furthermore, undrained shear strength determinations were inadequate in assessment of the degree to which the preferred stress history was achieved in each test. As a result, more extensive in - flight site investigation is recommended to reduce the uncertainty in empirical relationships established between the measured resistances and the soil strength and stiffness.

In the present study, numerical analyses were restricted to two - dimensional plane strain representations of the scouring process. Preliminary verification of the approach was provided through comparison with data acquired in the experimental programme. Further analyses are necessary to demonstrate correspondence with observations for other scouring events, in consideration of the complexity of the numerical procedures adopted. Ideally, the numerical representation should be successively improved through repeated application and empirical modification of input conditions or modelling assumptions. Pending further validation, the generality of the finite element method could then be exploited to investigate the influence of parametric variations over significant or realistic ranges. Although three - dimensional

representations of ice scouring are not anticipated to provide a viable approach for similar practical application, analyses of this type should be undertaken in order to provide information on the lateral distribution of soil displacements, and also to define scouring mechanisms for extreme narrow width events.

Appropriate characterization of the effects of scouring required simulation of large movements corresponding to steady - state conditions, which imposed constraints on implementation of the analysis and discretization of the soil domain. In addition, the two - dimensional continuum representation did not allow for accommodation of volume loss in the scour path through lateral soil displacement, and this restricted the range of movement of the rigid body over which realistic predictions of scouring effects could be expected. For compressible soil events, the measured steady - state response was adequately approximated by the cumulative displacement following complete passage of the rigid body, and corresponding with the development of a realistic configuration of the frontal mound. Comparative examination of analysis results and measured soil displacements for other scouring events is recommended in order to evaluate the reliability of this approximation and to establish more accurately the required range of simulated movement. Consideration should also be given to the application of rezoning techniques, to allow for appropriate mesh refinement in the region of high strain gradients adjacent to the rigid body, and to provide increased consistency in the range of movement over which convergent solutions are attained. Adequate simulation of brittle soil events may only be achieved through element removal and the introduction of a pre - existing discontinuity at the scour base in the numerical representation.

Direct calibration against full scale field test data will ultimately be required in order to evaluate the model predictive capabilities and limitations introduced by the various simplifying assumptions adopted in both the physical and numerical representations of the scouring process. Additional field investigations are also recommended to resolve uncertainties which still exist concerning the physical characteristics and motion of ice features during scouring episodes. Continued research will also be necessary to address more complicated field conditions which may include anisotropic and heterogeneous soil deposits, irregular ice geometries, abrasion or fracture of the ice, unsteady uplift or rotational movements, and the effects of pipeline trenching.

References

- Abdelnour, R., 1988. Assessment of Effect of Length and Orientation of a Multi - Year Ridge on the Force acting on Conical Structures. *Proceedings of the IAHR Symposium on Ice Problems*, Sapporo, Japan.
- Abdelnour, R. and Graham, B., 1984. Small Scale Tests of Sea Bottom Ice Scouring. *Proceedings of the IAHR Symposium on Ice Problems*, Hamburg, Germany, Vol. III, pp. 267 - 279.
- Abdelnour, R., and Lapp, D., 1980. Model Tests of Sea Bottom Ice Scouring. *Arctic Petroleum Operators Association*, Report No. 150, submitted by Arctic Canada Limited.
- Abdelnour, R., Lapp, D., Haider, S., Shinde, S.B., and Wright, B., 1981. Model Tests of Sea Bottom Scouring. *Proceedings of the Sixth International Conference on Port and Ocean Engineering under Arctic Conditions*, Quebec City, Quebec, Vol. II, pp. 688 - 705.
- Airey, D.W., 1984. Clays in Circular Simple Shear Apparatus. *Ph.D. Thesis*, University of Cambridge, Cambridge, U.K.
- Almeida, M.S.S., 1984. Stage Constructed Embankments on Soft Clays. *Ph.D. Thesis*, University of Cambridge, Cambridge, U.K.
- Almeida, M.S.S. and Parry, R.H.G., 1983. Tests with Centrifuge Vane and Penetrometer in a Normal Gravity Field. *Cambridge University Engineering Department Technical Report*, D - Soils, TR141.
- Almeida, M.S.S. and Parry, R.H.G., 1983. Studies of Vane and Penetrometer Tests during Centrifuge Flight. *Cambridge University Engineering Department Technical Report*, D - Soils, TR142.
- Al - Tabbaa, A., 1984. Anisotropy of Clay. *M.Phil. Thesis*, University of Cambridge, Cambridge, U.K.
- Al - Tabbaa, A., 1987. Permeability and Stress - Strain Response of Speswhite Kaolin. *Ph.D. Thesis*. University of Cambridge, Cambridge, U.K., 133 p.
- Andrier, B., 1981. E.T.P.M. in Pipelaying and Burying Activities. *Proceedings of the Symposium, Production and Transportation Systems for the Hibernia Discovery*, (eds. W.E. Russell and D.B. Muggeridge), St. John's, Newfoundland.

- ASCE, 1984. *Guidelines for the Seismic Design of Oil and Gas Pipeline Systems*. Prepared by the Committee on Gas and Liquid Fuel Lifelines of the ASCE Technical Council on Lifeline Earthquake Engineering. Published by the American Society of Civil Engineers, 465 p.
- Atkinson, J.H. and Bransby, P.L., 1978. *The Mechanics of Soils - An Introduction to Critical State Soil Mechanics*. McGraw - Hill Book Company (UK) Limited, University Series in Civil Engineering, 375 p.
- Bailey, R.C., 1994. Implications of Iceberg Dynamics for Iceberg Stability Estimation. *Cold Regions Science and Technology*, Vol. 22, pp. 197 - 203.
- Baligh, M.M. and Scott, R.F., 1976. Analysis of Wedge Penetration in Clay. *Geotechnique*, Vol. 26, No. 1, pp. 185 - 208.
- Ball, P., Gaskill, H.S., and Lopez, R.J., 1981. Iceberg Motion : An analysis of two data sets collected at drill sites in the Labrador Sea. *Centre for Cold Ocean Resources Engineering (C-CORE) Technical Report*, Publication 81 - 2.
- Barnes, P.W., Reimnitz, E., and Rearic, D.M., 1982. Ice Gouge Characteristics Related to Sea - Ice Zonation, Beaufort Sea, Alaska. *National Research Council of Canada, Workshop on Ice Scouring*, Organized by the NRC Subcommittee on Snow and Ice, Montebello, Quebec, 32 p.
- Barnes, P.W., Reimnitz, E., and Ross, R., 1980. Nearshore Surficial Sediment Textures, Beaufort Sea, Alaska. *U.S. Geological Survey Open File Report*, No. 80 - 196, 41 p.
- Barrie, J.V., Collins, W.T., Clark, J.I., Lewis, C.F.M., and Parrott, D.R., 1986. Submersible Observations and Origin of an Iceberg Pit on the Grand Banks of Newfoundland. *Current Research, Part A, Geological Survey of Canada*, Paper 86 - 1A, pp. 251 - 258.
- Bass, D.W. and Peters, G.R., 1984. Computer Simulation of Iceberg Instability. *Cold Regions Science and Technology*, Vol. 9, pp. 163 - 169.
- Bass, D.W. and Woodworth - Lynas, C.M.T., 1986. Iceberg Crater Marks on the Sea Floor, Labrador Shelf. *Marine Geology*, No. 79, pp. 243 - 260.
- Been, K., 1990. Mechanisms of Failure and Soil Deformation during Scouring. *Proceedings of the Workshop on Ice Scouring and the Design of Offshore Pipelines*, Calgary, Alberta, pp. 179 - 191.

- Been, K., Conlin, B.H., Crooks, J.H.A., Fitzpatrick, S.W., Jeffries, M.G., Rogers, B.T., and Shinde, S., 1986. Back Analysis of the Nerlerk Berm Liquefaction Slides : Discussion. *Canadian Geotechnical Journal*, Vol. 24, pp. 170 - 179.
- Been, K., Kosar, K., Hachey, J., and Rogers, B.T., 1990. Ice Scour Models. *Proceedings of the Ninth International Conference on Offshore Mechanics and Arctic Engineering*, Houston, Texas, Vol. V, pp. 179 - 188.
- Berenger, D. and Wright, B.D., 1980. Ice Conditions affecting Offshore Hydrocarbon Production in the Labrador Sea. *Proceedings of Intermaritec 80*, Hamburg, Germany, pp. 390 - 402.
- Bolton, M.D., English, R.J., Hird, C.C., and Schofield, A.N., 1973. Modelling. *Proceedings of the Symposium on Plasticity and Soil Mechanics*, Cambridge University, pp. 251 - 258.
- Boyd, D.W., 1965. Climatic Information for Building Design in Canada. *Division of Building Research Report*, No. 8329, National Research Council, Ottawa, Canada.
- Britto, A.M., Kusakabe, O., and Schofield, A.N., 1981. Trench Headings in Soft Clay. *Report to the British Gas Corporation*, Cambridge University Engineering Department, Soil Mechanics Group. 92 p.
- Britto, A.M. and Gunn, M.J., 1987. *Critical State Soil Mechanics via Finite Elements*, Ellis Horwood Limited Publishers, Chichester, England, 488 p.
- Brooks, L.D., 1982. Iceberg Dimensions. *National Research Council of Canada Workshop on Ice Scouring*, Organized by the NRC Subcommittee on Snow and Ice, Montebello, Quebec.
- Brown, J.D., 1986. Geotechnical Engineering Offshore Eastern Canada. *Proceedings of the Third Canadian Conference on Marine Geotechnical Engineering*, St. John's, Newfoundland, Vol. 3, pp. 852 - 878.
- Brown, R.J., 1990. The First Arctic Pipeline and Later Developments. *Proceedings of the Workshop on Ice Scouring and the Design of Offshore Pipelines*, Calgary, Alberta, pp. 323 - 334.
- Bruce, G.C., 1991. Offshore Newfoundland : Canada's Next Major Oil Producing Region. *Newfoundland Offshore Industries Association Conf.*, St. John's, NF.
- Burland, J.B., 1967. Deformation of Soft Clay. *Ph.D. Thesis*, University of Cambridge, Cambridge, U.K.

- Canada Oil and Gas Lands Administration, 1990. *Proceedings of the Workshop on Ice Scouring and the Design of Offshore Pipelines*, Calgary, Alberta, 499 p.
- C - CORE, 1995. Pressure Ridge Ice Scour Experiment (PRISE) Phase 3 : Engineering Model Application, Draft Final Report. *C - CORE Publication 95 - C19*, 61 p.
- Chari, T.R., 1975. Some Geotechnical Aspects of Iceberg Grounding. *Ph.D. Thesis*, Memorial University of Newfoundland, St. John's, Newfoundland, 181 p.
- Chari, T.R., 1979. Geotechnical Aspects of Iceberg Scours on Ocean Floors. *Canadian Geotechnical Journal*, Vol. 16, No. 2, pp. 379 - 390.
- Chari, T.R., 1980. A Model Study of Iceberg Scouring in the North Atlantic. *Journal of Petroleum Technology*, Vol. 32, pp. 2247 - 2252.
- Chari, T.R. and Green, H.P., 1981. Iceberg Scour Studies in Medium Dense Sands. *Proceedings of the International Conference on Port and Ocean Engineering under Arctic Conditions*, Quebec City, Vol. II, pp. 1012 - 1019.
- Chari, T.R., Green, H.P., and Reddy, A.S., 1982. Some Geotechnical Aspects of Iceberg Furrows. *Proceedings of the Second Canadian Conference on Marine Geotechnical Engineering*, Preprint Volume, Halifax, Nova Scotia, 4 p.
- Chari, T.R. and Peters, G.R., 1981. Estimates of Iceberg Scour Depths. *Proceedings of the Symposium on Production and Transportation Systems for the Hibernia Discovery*, St. John's, Newfoundland, pp. 178 - 188.
- Cheah, H.C., 1981. Site Investigation Techniques for Laboratory Soil Models. *M.Phil. Thesis*, University of Cambridge, Cambridge, U.K.
- Chi, L. and Kushwaha, R.L., 1988. Finite Element Analysis of Forces on a Plane Soil Blade. *Journal of the Canadian Society of Agricultural Engineering*, Vol. 31, No. 2, pp. 135 - 140.
- Chipman, W., 1992. Oil and Gas Fields Offshore Newfoundland and Labrador : Development Potential and Scenarios. *Newfoundland Offshore Industries Association Conference*, St. John's, Newfoundland.
- Christian, H., 1985. Stress History of Surficial Beaufort Sea Sediments. *M.Sc. Thesis*, The University of Alberta, Edmonton, Alberta, 334 p.
- Christian, H. and Morgenstern, N.R., 1986. Compressibility and Stress History of Holocene Sediments in the Canadian Beaufort Sea. *Proceedings of the Third Canadian Conference on Marine Geotechnical Engineering*, St. John's, Newfoundland, Vol. 1, pp. 275 - 299.

- Clark, J.I., 1991. Design for Safety in Northern Waters. *Proceedings of Offshore Pipeline Safety, An International Workshop*, New Orleans, Louisiana.
- Clark, J.I., Chari, T.R., Landva, J., and Woodworth - Lynas, C.M.T., 1989. Pipeline Route Selection in an Iceberg - Scoured Seabed. *Marine Geotechnology*, Vol. 8, pp. 51 - 67.
- Clark, J.I. and Landva, J., 1988. Geotechnical Aspects of Seabed Pits in the Grand Banks Area. *Canadian Geotechnical Journal*, Vol. 25, pp. 448 - 454.
- Clark, J.I., Paulin, M.J., Lach, P.R., Yang, Q.S., and Poorooshab, H., 1994. Methodology for the Design of Pipelines in Ice Scoured Seabeds. *Proceedings of 13th International Conference on Offshore Mechanics and Arctic Engineering (OMAE, 1994)*, Houston, Texas, Vol. V, pp. 107 - 125.
- Clark, J.I. and Poorooshab, F., 1989. Protection of Sea Bottom Facilities in an Ice Scoured Environment. *Proceedings of the Annual Conference of the Canadian Society for Civil Engineering*, pp. 617 - 632.
- Clegg, D.P., 1981. Model Piles in Stiff Clay. *Ph.D. Thesis*, University of Cambridge, Cambridge, U.K.
- Cold Ocean Design Associates Ltd., 1994. Offshore Pipelines in Cold Regions, Course Notes. *Short Course*, presented by CODA in conjunction with Andrew Palmer and Associates and C-CORE, St. John's, Newfoundland, September.
- Comfort, G., Gilbert, G., and Ferregut, C., 1990. Analysis of Subscour Stresses and Probability of Ice Scour - Induced Damage for Buried Submarine Pipelines, Volume 1, Database of Key Ice Scour Parameters, *Contractor Report submitted by Fleet Technology Ltd. and Canadian Seabed Research Ltd. to the Canada Oil and Gas Lands Administration*.
- Comfort, G. and Graham, B., 1986. Evaluation of Sea Bottom Ice Scour Models. *Environmental Studies Revolving Funds*, Report No. 037, Ottawa, Canada, 71 p.
- Craig, W.H., 1982. Strain Rate and Viscous Effects in Physical Models. *Proceedings of the International Conference on Soil Dynamics and Earthquake Engineering*, Southampton, England, Vol. 1, pp. 351 - 365.
- Croasdale, K.R. & Associates Ltd., 1994. A Research Planning Study for Canada's Frontier Oil and Gas. Second Edition. K.R. Croasdale and J.C. McDougal (editors), *Report for OERD, Natural Resources Canada*, Ottawa, 123 p.
- Croasdale, K.R. & Associates Ltd., 1994. Environmental Research Planning Study for PERD Task 6. *Report to Federal Panel on Energy R & D*, Ottawa, 135 p.

- Crooks, J.H.A., Jefferies, M.G., Becker, D.E., and Been, K., 1986. Geotechnical Properties of Beaufort Sea Clays. *Proceedings of the Third Canadian Conference on Marine Geotechnical Engineering*, St. John's, Newfoundland, pp. 329 - 343.
- Davidson, C.S., 1980. The Shear Modulus of Clays. *Engineering Tripos. Part II Research Project Report*, University of Cambridge, Cambridge, U.K.
- Davies, M.C.R., 1981. Centrifugal Modelling of Embankments on Clay Foundations. *Ph.D. Thesis*, Cambridge University, Cambridge, England, 148 p.
- Dean, E.T.R., and Edgcombe, K., 1988. Cambridge Geotechnical Centrifuge Centre FLY14 User Manual. *Cambridge University Engineering Department Report*, D - Soils, TR 204 (V01a), 52 p.
- Dean, E.T.R. and Schofield, A.N., 1983. Two Centrifuge Model Tests : Earthquakes on Submerged Embankments. *Proceedings Atti Del XV Convegno Nazionale Di Geotecnica Spoleto*, pp. 115 - 129.
- Dempster, R.T., and Bruneau, A.A., 1973. Dangers Presented by Icebergs and Protection Against Them. *Arctic Oil and Gas : Problems and Possibilities Conference*, Le Havre, France.
- De Paoli, S., Morrison, T.B., and Marcellus, R.W., 1982. Analysis of Interaction Probabilities Between Large Ice Features and Offshore Structures in the Canadian Beaufort Sea. *Unpublished Report*.
- Desai, C.S. and Phan, H.V., 1980. Three - Dimensional Finite Element Analysis including Material and Geometric Nonlinearities. *Computational Methods in Nonlinear Mechanics*, North Holland Publishing Company, (ed. J.T. Oden), pp. 205 - 224.
- Desai, C.S., Phan, H.V., and Perumpral, J.V., 1982. Mechanics of Three - Dimensional Soil Structure Interaction. *Proceedings of the American Society of Civil Engineers, Journal of the Engineering Mechanics Division*, Vol. 108, No. EM5, pp. 731 - 747.
- Det norske Veritas, 1988. Statistical Data Analysis of New Scour Characteristics in the Beaufort Sea. *Draft Contractor Report*, submitted by Det norske Veritas (Canada) Limited to the Geological Survey of Canada.
- Det norske Veritas, 1988. Updated Statistical Data Analysis of New Scour Characteristics in the Beaufort Sea. *Draft Contractor Report*, submitted by Det norske Veritas (Canada) Limited to the Geological Survey of Canada.

- Dickins, D., Krajczar, K., Shearer, J., Bjerkelund, I., and Poulin, M., 1991. The Ice Environment Affecting the Distribution of New Scours in the Canadian Beaufort Sea. *Report prepared by D.F. Dickins and Associates Ltd. and Shearer Consulting for the Atlantic Geoscience Centre*, 111 p.
- Dickins, D.F. and Wetzel, V.F., 1981. Multi - Year Pressure Ridge Study, Queen Elizabeth Islands. *Sixth International Conference on Port and Ocean Engineering under Arctic Conditions (POAC)*, Montreal, Quebec, Vol. II and III.
- Dinsmore, R.P., 1972. Ice and its Drift into the North Atlantic Ocean. *International Commission for the Northwest Atlantic Fisheries*, Special Publication No. 8, pp. 89 - 127.
- Ebbesmeyer, C.C., Okubu, A., and Helseth, J.M., 1980. Description of Iceberg Probability between Baffin Bay and the Grand Banks using a Stochastic Model. *Deep Sea Research*, Vol. 27A, pp. 975 - 986.
- Edwards, R.Y., Comfort, G., and Arsenault, L., 1978. Ice Conditions in Viscount Melville Sound and Barrow Strait West. *ARCTEC Canada Limited*, Unpublished Report for Department of Fisheries and Environment.
- El - Tahan, M.S. and El - Tahan, H.W., 1983. Forecast of Iceberg Ensemble Drift. *Proceedings of the Offshore Technology Conference (OTC 83)*, Houston, Texas, pp. 151 - 158.
- Elmes, D.R., 1986. Creep and Viscosity of Two Kaolin Clays. *Ph.D. Thesis*, University of Cambridge, Cambridge, U.K.
- Endicott, L.J., 1970. Centrifugal Testing of Soil Models. *Ph.D. Thesis*, University of Cambridge, Cambridge, U.K.
- Fader, G.B. and King, L.H., 1981. A Reconnaissance of the Surficial Geology of the Grand Banks of Newfoundland, *Current Research, Part A, Geological Survey of Canada*, Paper 81 - 1A, pp. 45 - 56.
- Fader, G.B. and Miller, R.D., 1986. Regional Geological Constraints to Resource Development - Grand Banks of Newfoundland. *Proceedings of the Third Canadian Conference on Marine Geotechnical Engineering*, St. John's, Newfoundland, Vol. 1, pp. 3 - 40.
- FENCO Ltd., 1975. An Analytical Study of Ice Scour on the Sea Bottom. R. Pilkington and H. Iyer (editors), *Report submitted to the Arctic Petroleum Operators Association*, Project No. 69.

- Flower, E.C. and Hallquist, J.O., 1986. Computer - Aided Simulation of Metal Forming. *Lawrence Livermore Laboratory Report*, URCL - 93634, Preprint.
- Gadala M.S., Oravas, G.A., and Dokainish, M.A., 1983. A Consistent Eulerian Formulation of Large Deformation Problems in Statics and Dynamics. *International Journal of Non - Linear Mechanics*, Vol. 18. No. 1, pp. 21 - 35.
- Gadala, M.S. and Oravas, 1984. Numerical Solutions of Nonlinear Problems of Continua - Survey of Formulation Methods and Solution Techniques. *Journal of Computers & Structures*, Vol. 19, No. 5, pp. 865 - 877.
- Geonautics Ltd., 1989. Regional Ice Scour Database Update Studies. *Environmental Studies Research Funds*, Report No. 105, Ottawa, Canada, 168 p.
- Gilbert, G.R., 1990. Scour Shape and Sub - Scour Disturbance Studies from the Canadian Beaufort Sea. *Proceedings of the Workshop on Ice Scouring and the Design of Offshore Pipelines*, Calgary, Alberta, pp. 127 - 144.
- Gilbert, G.R., Blasco, S., Stirbys, A.F., and Lewis, C.F.M., 1985. Beaufort Sea Ice Scour Analysis using a Computerized Database. *Proceedings of the 17th Offshore Technology Conference*, Houston, Texas, Paper No. 4969, pp. 111 - 114.
- Gilbert, G.R., Delory, S.J., and Pedersen, K.A., 1989. Beaufort Sea Ice Scour Data Base (Scourbase) Update to 1986. *Environmental Studies Research Funds*, Report No. 097, Ottawa, Canada, 95 p.
- Gilbert, G.R. and Pedersen, K., 1986. Ice Scour Database for the Beaufort Sea. *Environmental Studies Revolving Funds*, Report No. 055, Ottawa, Canada, 99 p.
- Golder Associates Ltd., 1989. Laboratory Indentor Testing to Verify Ice - Soil - Pipe Interaction Models. *Report to Gulf Canada Resources Limited*, Proprietary Joint Industry Project, 42 p.
- Golder Associates Ltd., 1990. Analysis of Subscour Stresses and Probability of Ice Scour - Induced Damage for Buried Submarine Pipelines, Vol. II, Deterministic Model of Ice - Soil - Pipe Interaction. *Canada Oil and Gas Lands Administration*, 204 p.
- Goodwin, C.R., Finley, J.C., and Howard, L.M. (editors), 1985. Ice Scour Bibliography. *Environmental Studies Revolving Fund*, Study No. 271 - 99 - 00, Ottawa, Canada, 92 p.
- Grant, D.A., 1973. A Note on the Simulation of Iceberg Breakup. *Commander Maritime Command, Unpublished Report*, Canadian Department of National Defence, MC/ORB Staff Note 3/73.

- Green, H.P., 1984. Geotechnical Modelling of Iceberg - Seabed Interaction. *M.Eng. Thesis*, Memorial University of Newfoundland, St. John's, Newfoundland, 165 p.
- Gustajtis, K.A., 1979. Iceberg Scouring on the Labrador Shelf, Saglek Bank. *Centre for Cold Ocean Resources Engineering (C-CORE) Technical Report*, Publication No. 79 - 13, 43 p.
- Hambly, E.C., 1969. Plane Strain Behaviour of Stiff Clay. *Ph.D. Thesis*, University of Cambridge, Cambridge, U.K.
- Hamilton, J.M., Dunnivant, T.W., Murff, J.D., and Phillips, R., 1991. Centrifuge Study of Laterally Loaded Behavior in Clay. *Proceedings of the International Conference, Centrifuge 91* (ed. H.Y. Ko), Balkema, Rotterdam, pp. 285 - 292.
- Hettiaratchi, D.P.R. and Reece, A.R., 1975. Boundary Wedges in Two - Dimensional Passive Soil Failure, *Geotechnique*, Vol. 25, No. 2, pp. 297 - 320.
- Hibbitt, H.D., Karlsson, B.I., and Sorensen, E.P., 1994. User's Manuals and Theory Manual. *ABAQUS / Standard Version 5.4 Documentation*, Hibbitt, Karlsson & Sorensen Ltd., Providence, Rhode Island.
- Hivon, E., 1983. Stress History in the Beaufort Sea : An Initial Study. *Geological Survey of Canada*, Unpublished Report.
- Hnatiuk, J. and Brown, K.D., 1977. Sea - Bottom Scouring in the Canadian Beaufort Sea. *Proceedings of the Ninth Annual Offshore Technology Conference*, Houston, Texas, Vol. 3, No. 2946, pp. 519 - 528.
- Hnatiuk, J., Kovacs, A., and Mellor, M., 1978. A Study of Several Pressure Ridges and Ice Islands in the Canadian Beaufort Sea. *Journal of Glaciology*, Vol. 20, No. 84.
- Hodgson, G.J., Lever, J.H., Woodworth - Lynas, C.M.T., and Lewis, C.F.M. (editors), 1988. The Dynamics of Iceberg Grounding and Scouring (DIGS) Experiment and Repetitive Mapping of the Eastern Canadian Continental Shelf. *Environmental Studies Research Funds Report No. 094*, Ottawa, Ontario, 318 p.
- Hotzel, S.I. and Miller, J.D., 1983. Icebergs : Their Physical Dimensions and the Presentation and Application of Measured Data. *Annals of Glaciology*, International Glaciological Society, Vol. 4, pp. 116 - 123.
- Houlshy, G.T., 1981. A Study of Plasticity Theories and their Applicability to Soils. *Ph.D. Thesis*, University of Cambridge, Cambridge, U.K.

- Hughes, T.J.R. and Winget, J., 1980. Finite Rotation Effects in Numerical Integration of Rate Constitutive Equations Arising in Large Deformation Analysis. *International Journal for Numerical Methods in Engineering*, Vol. 15, pp. 1862 - 1867.
- Huetink, J., Vreede, P.T., and van der Lugt, J., 1990. Progress in Mixed Eulerian - Lagrangian Finite Element Simulation of Forming Processes. *International Journal for Numerical Methods in Engineering*, Vol. 30, pp. 1441 - 1457.
- James, R.G., 1973 a. Radiographic Techniques. *Cambridge University Engineering Department Report*, C - Soils, LN 1b, 16 p.
- James, R.G., 1973 b. Determination of Strains in Soils by Radiography. *Cambridge University Engineering Department Report*, C - Soils, LN 1a, 44 p.
- Josenhans, H.W., 1973. Evidence of Pre - Date Wisconsin Glaciations on the Labrador Shelf, Cartwright Saddle Regions. *Canadian Journal of Earth Sciences*, Vol. 20, No. 2, pp. 225 - 235.
- Josenhans, H.W., Zevenhuizen, J., and Klassen, R.A., 1986. The Quaternary Geology of the Labrador Shelf. *Canadian Journal of Earth Sciences*, Vol. 23, No. 8, pp. 1190 - 1213.
- King, E.L., and Gillespie, R.T., 1985. Regional Iceberg Scour Distribution and Variability on the Eastern Canadian Continental Shelf. In *Ice Scour and Seabed Engineering*. C.F.M. Lewis, D.R. Parrott, P.G. Simpkin, and J.T. Buckley (editors), Environmental Studies Revolving Funds Report, No. 049, pp. 172 - 181, Ottawa, Canada.
- Kiousis, P.D., Voyiadjis, G.Z., and Tumay, M.T., 1988. A Large Strain Theory and its Application in the Analysis of the Cone Penetration Mechanism. *International Journal for Numerical and Analytical Methods in Geomechanics*, Vol. 12, pp. 45 - 60.
- Knogle, D., 1979. The Influence of Pore - Water Tension on the Undrained Shear Strength of Kaolin. *Engineering Tripos Part II Research Project Report*, University of Cambridge, Cambridge, U.K.
- Kovacs, A., 1972. Ice Scoring marks floor of the Arctic shelf. *Oil and Gas Journal*, Vol. 70, No. 43.
- Kovacs, A., 1975. Multi - year pressure ridge model. *Unpublished Report*.

- Kovacs A., Dickens, D., and Wright, B., 1975. A Study of Multi - Year Pressure Ridges and Shore Ice Pile - Up. *Arctic Petroleum Operators Association Report*, Project No. 89, 45 p.
- Kovacs, A. and Gow, A.J., 1976. Some characteristics of grounded floebergs near Prudhoc Bay, Alaska. *Cold Regions Research and Engineering Laboratory*, Report 76 - 34, Hanover, New Hampshire, 10 p.
- Kovacs, A. and Mellor, M., 1971. Sea ice pressure ridges and ice islands. *Creare Technical Note*, Report TN - 122, Creare Inc., Hanover, New Hampshire.
- Kovacs, A. and Mellor, M., 1974. Sea Ice Morphology and Ice as a Geologic Agent in the Southern Beaufort Sea. *Reprint from The Coast and the Shelf of the Beaufort Sea, The Arctic Institute of North America*, Arlington, Va., pp. 113 - 164.
- Kovacs, A., Weeks, W.F., Ackley, S., and Hibler, W.D. III, 1973. Structure of a Multi - Year Pressure Ridge. *Reprint from Arctic, Journal of the Arctic Institute of North America*, Vol. 26, No. 1, pp. 22 - 31.
- Kusakabe, O., 1982. Stability of Excavations in Soft Clay. *Ph. D. Thesis*, University of Cambridge, Cambridge, U.K.
- Kutter, B.L., Sathialingam, N., and Herrmann, L.R., 1988. The Effects of Local Arching and Consolidation on Pore Pressure Measurements in Clay. *International Conference Proceedings, Centrifuge 88* (ed. J.F. Corte), Balkema, Rotterdam, pp. 115 - 118.
- Lach, P.R. and Clark, J.I., 1994. Ice Scouring of the Seabed. *Proceedings of the International Conference, Centrifuge 94*, Singapore (eds. C.F. Leung, F.H. Lee, and T.S. Tan), September, pp. 803 - 808.
- Lach, P.R., Clark, J.I., and Poorooshasb, F., 1993. Centrifuge Modelling of Ice Scour. *Proceedings of the 4th Canadian Conference on Marine Geotechnical Engineering*, St. John's, Newfoundland, Vol. 1, pp. 357 - 374.
- Langhaar, H.L., 1951. *Dimensional Analysis and the Theory of Models*. John Wiley and Sons, New York, 166 p.
- Lee, F.H., 1985. Centrifuge Modelling of Earthquake Effects on Sand Embankments and Islands. *Ph.D. Thesis*, University of Cambridge, Cambridge, U.K.
- Lever, G.V., 1991. Floating Production System Design Considerations for East Coast Canada. *Proceedings of the 13th World Petroleum Congress*, Buenos Aires, Argentina, pp. 345 - 353.

- Lever, J.H., Bass, D.W., Lewis, C.F.M., Klein, K., and Diemand, D., 1989. Iceberg / Seabed Interaction Events observed during the DIGS Experiment. *Proceedings of the Eighth International Conference on Offshore Mechanics and Arctic Engineering*, The Hague, Vol. IV, pp. 205 - 220.
- Lewis, C.F.M. and Barrie, J.V., 1981. Geological Evidence of Iceberg Grounding and Related Seafloor Processes in the Hibernia Discovery Area of Grand Bank, Newfoundland. *Proceedings of the Symposium on Production and Transportation Systems for the Hibernia Discovery*, Newfoundland Petroleum Directorate, St. John's, Newfoundland, pp. 146 - 177.
- Lewis, C.F.M. and Blasco, S.M., 1990. Character and Distribution of Sea - Ice and Iceberg Scours. *Proceedings of the Workshop on Ice Scouring and the Design of Offshore Pipelines*, Calgary, Alberta, pp. 57 - 101.
- Lewis, C.F.M. and Parrott, D.R., 1987. Iceberg Scouring Rate Studies, Grand Banks of Newfoundland. *Current Research, Part A. Geological Survey of Canada*, Paper 87 - 1A, pp. 825 - 833.
- Lewis, C.F.M., Parrott, D.R., d'Apollonia, S.J., Gaskill, H.S., and Barrie, J.V., 1988. Methods of Estimating Iceberg Scouring Rates on the Grand Banks of Newfoundland. *Port and Ocean Engineering Under Arctic Conditions*, Fairbanks, Alaska, Vol. III, pp. 229 - 254.
- Liu, W.K., Chang, H., Belytschko, T., and Chen, J.S., 1987. Arbitrary Lagrangian - Eulerian Stress Update Procedures for Forming Simulations. In : *Advances in Inelastic Analysis*, presented at the Winter Annual Meeting of The American Society of Mechanical Engineers, Boston, Massachusetts, pp. 153 - 175.
- Lowrings, M.G. and Banke, E.G., 1983. Consolidation of Pressure Ridges in First - Year Landfast Ice, Eastern Beaufort Sea, Winter 1981 - 82. *Martec Limited Report*, prepared for Gulf Canada Resources Inc., Calgary, Alberta.
- Lyon, W., 1967. Under Surface Profiles of Sea Ice Observed by Submarine. In *Physics of Snow and Ice, International Conference on Low Temperature Science*, Institute of Low Temp. Sci., Sapporo, Japan, Vol. 1, pp. 701 - 711.
- Mair, R.J., 1979. Centrifuge Modelling of Tunnel Construction in Soft Clay. *Ph.D. Thesis*, Cambridge University, Cambridge, England, 142 p.
- Manson, S.M., 1980. An Investigation of the Strength and Consolidation Properties of Speswhite Kaolin. *Engineering Tripos Part II Research Project Report*, University of Cambridge, Cambridge, U.K.

- McGonigal, D. and Wright, B.D., 1978. Beaufort Sea Ice Movement from Rams Buoy Data Analysis, 1975 - 77. *Gulf Canada Resources Report*.
- McKeehan, D.S., 1990. Construction Strategies for Arctic Offshore Pipelines. *Proceedings of the Workshop on Ice Scouring and the Design of Offshore Pipelines*, Calgary, Alberta, pp. 335 - 346.
- Meagher, L., 1978. Compilation of the Thickness of Recent Soft Sediment and Ice - Related Features in the Beaufort Sea, Northwest Territories, Canada. *Geological Survey of Canada Report*, Terr. Sci. Division, Project No. 77 - 30.
- Mobil Oil Canada Ltd., 1985. *Hibernia Development Project, Environmental Impact Statement*, VI IIIa, Biophysical Assessment, 258 p.
- Murray, A., Ferregut, C., and Ritch, R., 1990. Analysis of Subscour Stresses and Probability of Ice Scour - Induced Damage for Buried Submarine Pipelines, Volume 3, Probabilistic Modelling, *Contractor Report submitted by Fleet Technology Ltd. to the Canada Oil and Gas Lands Administration*, 42 p.
- Murray, J.E., 1969. The Drift, Deterioration, and Distribution of Icebergs in the North Atlantic Ocean. *Canadian Institute of Mining and Metallurgy, The Ice Seminar*, Special Volume 10, pp. 3 - 18.
- Nadarajah, V., 1973. Stress - Strain Properties of Lightly Overconsolidated Clays. *Ph.D. Thesis*, University of Cambridge, Cambridge, U.K.
- Nagtegaal, J.C., 1982. On the Implementation of Inelastic Constitutive Equations with Special Reference to Large Deformation Problems. *Computer Methods in Applied Mechanics and Engineering*, North Holland Publishing, Vol. 33, pp. 469 - 484.
- Nagtegaal, J.C., Parks, D.M., and Rice, J.R., 1974. On Numerically Accurate Finite Element Solutions in the Fully Plastic Range. *Computer Methods in Applied Mechanics and Engineering*, North Holland Publishing, Vol. 4, pp. 153 - 177.
- Nagtegaal, J.C. and De Jong, J.E., 1981. Some Computational Aspects of Elastic - Plastic Large Strain Analysis. *International Journal for Numerical Methods in Engineering*, Vol. 17, pp. 15 - 41.
- Nevel, D.E., 1965. A Semi - Infinite Plate on an Elastic Foundation. *U.S. Army Corps of Engineers, Cold Regions Research and Engineering Laboratory*, CRREL Report No. 221.
- Nixon, J., 1994. *User Manual and Program Verification for Pipsol Stress Analysis Program for Pipes Subjected to Ground Displacements - Version 94 - 1*. Prepared by Nixon Geotech Limited, Calgary, Alberta, 23 p.

- Nixon, J., Stuchly, J., and Pick, A., 1984. Design of Norman Wells Pipeline for Frost Heave and Thaw Settlement. *Proceedings of the 3rd International Conference on Offshore Mechanics and Arctic Engineering*, New Orleans, LA.
- Nunez, I.L., 1989. Centrifuge Model Tension Piles in Clay. *Ph.D. Thesis*, University of Cambridge, Cambridge, U.K., 150 p.
- Nunez, I.L., Phillips, R., Randolph, M.F., and Wesselink, B.D., 1988. Modelling Laterally Loaded Piles in Calcareous Sand. *Proceedings of the International Conference on Centrifuge Modelling*, Centrifuge 88, Paris, France, pp. 371 - 381.
- O'Connor, M.J. and Associates Ltd., 1980. Development of a Proposed Model to Account for the Surficial Geology of the Southern Beaufort Sea. *Report prepared for the Geological Survey of Canada*, 128 p.
- O'Connor, M.J. and Associates Ltd., 1982. An Evaluation of the Regional Surficial Geology of the Southern Beaufort Sea. *Report prepared for the Geological Survey of Canada*, 187 p.
- Oden, J.T. and Pires, E.B., 1983. Nonlocal and Nonlinear Friction Laws and Variational Principles for Contact Problems in Elasticity. *Journal of Applied Mechanics*, Vol. 50, pp. 67 - 73.
- Ovesen, N.K., 1985. The Application of the Theory of Modelling to Centrifuge Studies. State of the Art Review on Geotechnical Centrifuge Modelling. *Proceeding of the 11th International Conference on Soil Mechanics and Foundation Engineering*, San Francisco, Balkema, Rotterdam.
- Palmer, A.C., 1990. Design of Marine Pipelines in Seabed Vulnerable to Ice Scour. *Proceedings of the Workshop on Ice Scouring and the Design of Offshore Pipelines*, Calgary, Alberta, Session 2, Ice / Soil / Pipeline Interactions, pp. 167 - 178.
- Palmer, A.C., 1994. *Personal Communication*.
- Palmer, A.C., Kenny, J.P., Perera, M.R., and Reece, A.R., 1979. Design and Operation of an Underwater Pipeline Trenching Plough. *Geotechnique*, Vol. 29, No. 3, pp. 305 - 322.
- Palmer, A.C., Konuk, I., Love, J., Been, K., and Comfort, G., 1989. Ice Scour Mechanisms. *Proceedings of the 10th International Conference on Port and Ocean Engineering under Arctic Conditions*, Lulea, Sweden, Vol. 1, pp. 123 - 132.

- Palmer, A. C., Konuk, I., Been, K., and Comfort, G., 1990. Ice Gouging and the Safety of Marine Pipelines. *Proceedings of the 22nd Annual Offshore Technology Conference*, Houston, Texas, pp. 235 - 244.
- Paulin, M.J., 1992. Physical Model Analysis of Iceberg Scour in Dry and Submerged Sand. *M. Eng. Thesis*, Memorial University of Newfoundland, St. John's, Newfoundland, 183 p.
- Paulin, M.J., Lach, P.R., Poo-roo-shab, F., and Clark, J.I., 1991. Preliminary Results of Physical Model Tests of Ice Scour. *Proceedings of the 11th International Conference on Port and Ocean Engineering under Arctic Conditions*, St. John's, Newfoundland.
- Phillips, R., 1982. Trench Excavations in Clay. *MPhil. Thesis*, University of Cambridge, Cambridge, U.K., 43 p.
- Phillips, R., 1988. Centrifuge Lateral Pile Tests in Clay. *Tasks 2 and 3 - Final Report*, Prepared for Exxon Production Research Company, Houston Texas, 39 p.
- Phillips, R., 1990. *Personal Communication*.
- Phillips, R., 1991. Film Measurement Machine User Manual. *Cambridge University Engineering Department Report*, D - Soils, TR 246, 40 p.
- Phillips, R., 1992. Centrifuge Modelling : Practical Considerations. In : *Geotechnical Centrifuge Technology*, edited by R.N. Taylor, Blackie Academic & Professional Publishers, Glasgow, UK, pp. 34 - 60.
- Phillips, R., Paulin, M.J., Clark, J.I., and Lach, P.R., 1993. Centrifuge Modelling for Offshore Development. *Newfoundland Ocean Industries Association Conference*, St. John's, Newfoundland.
- Pilkington, G.R., and Marcellus, W., 1981. Methods of Determining Pipeline Trench Depths in the Canadian Beaufort Sea. *Proceedings of the International Conference on Port and Ocean Engineering under Arctic Conditions*, Vol. 2, pp. 674 - 687.
- Pokrovsky, G.I. and Fyodorov, I.S., 1968. *Centrifugal Modelling in the Construction Industry*. Moscow : Stroiedat, English Translation, Building Research Establishment Library, Vol. 1.
- Pokrovsky, G.I. and Fyodorov, I.S., 1969. *Centrifugal Modelling in the Mining Industry*. Moscow : Niedra, English Translation, Building Research Establishment Library, Vol. 2.

- Poorooshasb, F., 1989. Large Scale Laboratory Tests of Seabed Scour. *Contract Report for Fleet Technology Limited, C - CORE Contract No. 89 - C15.*
- Poorooshasb, F. and Clark, J.I., 1990. On Small Scale Ice Scour Modelling. *Proceedings of the Workshop on Ice Scouring and the Design of Offshore Pipelines*, Calgary, Alberta, pp. 193 - 236.
- Poorooshasb, F., Clark, J.I., and Woodworth - Lynas, C.M.T., 1989. Small Scale Modelling of Iceberg Scouring of the Seabed. *Proceedings of the 10th International Conference on Port and Ocean Engineering under Arctic Conditions*, Lulea, Sweden, Vol. 1, pp. 133 - 134.
- Poorooshasb, H.B. and Q.S. Yang, 1993. Finite Element Analysis of Seabed Sub - Scour Deformation. In : Pressure Ridge Ice Scour Experiment (PRISE) Phase II Progress Report. *C - CORE Contract Report*, No. 93 - C4, 105 p.
- Powrie, W., 1986. The Behaviour of Diaphragm Walls in Clay. *Ph.D. Thesis*, University of Cambridge, Cambridge, U.K., 196 p.
- Prasad, K.S.R., 1985. Analytical and Experimental Modelling of Iceberg Scours. *M.Eng. Thesis*, Memorial University of Newfoundland, St. John's, Newfoundland, 170 p.
- Prasad, K.S.R. and Chari, T.R., 1986. Some Factors Influencing Iceberg Scour Estimates. *Proceedings of the 4th International Conference on Offshore Mechanics and Arctic Engineering*, Dallas, Texas, pp. 302 - 309.
- Rizkalla, M., Poorooshasb, F., and Clark, J.I., 1992. Centrifuge Modelling of Lateral Pipeline / Soil Interaction. *Proceedings of the 11th International Conference on Offshore Mechanics and Arctic Engineering*, Calgary, Alberta.
- Rogers, B.T., 1990. Influence of the Burial Trench and Subsurface Soil Conditions on the Stability of the Proposed Offshore Pipeline for Amauligak Development. *Proceedings of the Workshop on Ice Scouring and the Design of Offshore Pipelines*, Calgary, Alberta, pp. 303 - 317.
- Roscoe, K.H., and Burland, J.B., 1968. On the Generalized Stress - Strain Behaviour of Wet Clay. *Engineering Plasticity*, (eds. J. Heyman and F.A. Leckie), Cambridge University Press, pp. 535 - 609.
- Sanderson, T.J.O., 1989. *Ice Mechanics : Risks to Offshore Structures*. Graham and Trotman, London, U.K.
- Savvidou, C., 1984. Effects of a Heat Source in Saturated Clay. *Ph.D. Thesis*, University of Cambridge, Cambridge, U.K.

- Segall, M.P., Barrie, J.V., Lewis, C.F.M., and Maher, M.L.J., 1985. Clay Minerals Across the Tertiary - Quaternary Boundary, Northeastern Grand Banks of Newfoundland : Preliminary Results. *Current Research, Part B, Geological Survey of Canada*, Paper 85 - 1B, pp. 63 - 68.
- Scott, R.F., 1988. Physical and Numerical Models. *Centrifuges in Soil Mechanics*, W.H. Craig, R.G. James, and A.N. Schofield, eds., Balkema, Rotterdam, pp. 103 - 118.
- Schofield, A.N., 1980. Cambridge Geotechnical Centrifuge Operations. *Geotechnique*, Vol. 30, pp. 227 - 268.
- Schofield, A.N. and Wroth, C.P., 1968. *Critical State Soil Mechanics*, McGraw - Hill, London, U.K.
- Sharp, J.J., 1981. *Hydraulic Modelling*. Butterworth & Co. (Publishers) Ltd., London, U.K., 242 p.
- Shearer, J.M., Laroche, B., Fortin, G., 1986. Canadian Beaufort Sea 1984 Repetitive Mapping of Ice Scour. *Environmental Studies Revolving Funds Report No. 032*, Ottawa, Canada, 43 p.
- Shi, A.J.M., Chandrasakar, S., and Yang, H.T.Y., 1990. Finite Element Simulation of Metal Cutting Process with Strain - Rate and Temperature Effects. *Fundamental Issues in Machining*, presented at the Winter Annual Meeting of the American Society of Mechanical Engineers, Dallas, Texas, pp. 11 - 24.
- Skurihin, V.A., Surkov, G.A., and Truskov, P.A., 1992. Selection of the Subsea Pipeline Route for the Offshore Chaivo Field. *Proceedings of the 2nd International Offshore and Polar Engineering Conference*, Vol. II, San Francisco, U.S.A.
- Sloan, S.W. and Randolph, M.F., 1982. Numerical Prediction of Collapse Loads Using Finite Element Methods. *International Journal for Numerical and Analytical Methods in Geomechanics*, Vol. 6, pp. 47 - 76.
- Sodhi, D.S., and El - Tahan, M., 1980. Prediction of an Iceberg Drift Trajectory during a Storm. *Annals of Glaciology*, International Glaciological Society, Vol.1, pp. 77 - 82.
- Sokolovski, V.V., 1965. *Statics of Granular Media*. Pergamon Press, New York, N.Y.
- Springman, S.M., 1989. Lateral Loading on Piles due to Simulated Embankment Construction. *Ph.D. Thesis*, University of Cambridge, Cambridge, U.K.

- Springman, S.M., 1993. Centrifuge Modelling in Clay : Marine Applications. *Proceedings of the 4th Canadian Conference on Marine Geotechnical Engineering*, St. John's, Newfoundland, Vol. 3, pp. 853 - 895.
- Stewart, D.I., 1989. Groundwater Effects on In - Situ Walls in Stiff Clay. *Ph.D. Thesis*, University of Cambridge, Cambridge, U.K., 135 p.
- Taylor, D.W., 1948. *Fundamentals of Soil Mechanics*. Wiley, New York.
- Taylor, R.N., 1984. Ground Movements Associated with Tunnels and Trenches. *Ph.D. Thesis*, University of Cambridge, Cambridge, U.K.
- Terzaghi, K., 1936. The Shearing Resistance of Saturated Soil and the Angle between the Planes of Shear. *Proceedings of the First International Conference on Soil Mechanics and Foundation Engineering*, Harvard, Mass., Vol. 1, pp. 54 - 56.
- Terzaghi, K., 1943. *Theoretical Soil Mechanics*. John Wiley and Son, New York, N.Y., 510 p.
- Thompson, G.R. and Long, L.G., 1989. Hibernia Geotechnical Investigation and Site Characterization. *Canadian Geotechnical Journal*, Vol. 26, pp. 653 - 678.
- Truskov, P.A. and Surkov, G.A., 1991. Scour Depths Distribution on the Northern Sakhalin Offshore. *Proceedings of the First International Offshore and Polar Engineering Conference*, Vol. II, Edinburgh, United Kingdom.
- van den Berg, P., 1991. Numerical Model for Cone Penetration. *Proceedings of the International Conference on Computer Methods and Advances in Geomechanics*. Cairns, Australia, Vol. 3, pp. 1777 - 1782.
- van den Berg, P., Teunissen, J.A.M., and Huetink, J., 1992. Cone Penetration in Layered Media, an ALE Finite Element Formulation. *Proceedings of the International Conference on Computer Methods and Advances in Geomechanics*. Morgantown, West Virginia, Vol. 2, pp. 1957 - 1962.
- Vermeer, P.A., and Verruijt, A., 1981. An Accuracy Condition for Consolidation by Finite Elements. *International Journal of Numerical and Analytical Methods in Geomechanics*, Vol. 5, pp. 1 - 14.
- Voelker, R.P., 1981. Winter 1981 Trafficability Tests of Polar Sea. *U.S. Department of Transportation Report*, Maritime Administration, Office of Research and Development, Report No. MA-RD-940-82018, Volume II, Environmental Data.
- Wood, D.M., 1990. *Soil Behaviour and Critical State Soil Mechanics*. Cambridge University Press, Cambridge, U.K., 462 p.

- Woodworth - Lynas, C.M.T., 1990. Observed Deformations Beneath Relict Iceberg Scours. *Proceedings of the Workshop on Ice Scouring and the Design of Offshore Pipelines*, Calgary, Alberta, pp. 103 - 125.
- Woodworth - Lynas, C.M.T., 1992. The Geology of Ice Scour. *Ph.D. Thesis*, University of Wales, U.K., 269 p.
- Woodworth - Lynas, C.M.T., Bass, D.W., and Bobbitt, J., 1986. Inventory of Upslope and Downslope Iceberg Scouring. *Environmental Studies Revolving Funds Report No. 039*, Ottawa, Ontario, 103 p.
- Woodworth - Lynas, C.M.T. and Guigne, J.Y., 1989. Iceberg Scours in the Glaciological Record. *Proceedings of the International Conference on Glacimarine Environments : Processes and Sediments*, Geological Society, London, United Kingdom.
- Woodworth - Lynas, C.M.T. and Guigne, J.Y., 1990. Iceberg Scours in the Glaciological Record : Examples from Glacial Lake Agassiz. *Glacimarine Environments : Processes and Sediments*, (eds. J.A. Dowdeswell and J.D. Scourse), Geological Society Special Publication No. 53, pp. 217 - 233.
- Woodworth - Lynas, C.M.T., Josenhans, H.W., Barrie, J.V., Lewis, C.F.M., and Parrott, D.R., 1991. The Physical Processes of Seabed Disturbance during Iceberg Grounding and Scouring. *Continental Shelf Research*, Vol. 11, Nos. 8 - 10, pp. 939 - 961.
- Woodworth - Lynas, C.M.T., Simms A., Rendell, C.M., 1985. Iceberg Grounding and Scouring on the Labrador Continental Shelf. *Cold Regions Science and Technology*, Vol. 10, pp. 163 - 186.
- Wadhams, P., 1975. Sea Ice Morphology in the Beaufort Sea. *Beaufort Sea Project Technical Report*, Number 36, Canada Dept. of the Environment, Victoria, B.C., 66 p.
- Wadhams, P., 1982. The Prediction of Extreme Keel Depths from Sea Ice Profiles. *Cold Regions Science and Technology*, Vol. 6, pp. 257 - 266.
- Waggett, P., 1989. The Effect of Lubricants on the Interaction Between Soil and Perspex, *Engineering Tripos Part II Research Project Report*, University of Cambridge, Cambridge, U.K.
- Wahlgren, 1979. Ice Scour Tracks in Eastern Mackenzie Bay and North of Pullen Island, Beaufort Sea. In *Current Research, Part B, Geological Survey of Canada*, Paper 70 - 1B, pp. 51 - 62.

- Weaver, J.S., Johnson, B.M., and Thibeaux, J.F., 1988. A Large Scale Model Facility to Study Ice Gouge - Soil - Pipeline Interactions. *Proceedings of the Seventh International Conference on Offshore Mechanics and Arctic Engineering*, Houston, Texas, pp. 317 - 326.
- Wright, B., Hnatiuk, J., and Kovacs, A., 1979. Multi - Year Pressure Ridges in the Canadian Beaufort Sea. *Proceedings of the International Conference on Port and Ocean Engineering under Arctic Conditions*, Norwegian Institute of Technology, Vol. 1, pp. 107 - 126.
- Wright, B., Hnatiuk, J., and Kovacs, A., 1981. Multi - Year Pressure Ridges in the Canadian Beaufort Sea. *Coastal Engineering*, Vol. 5, pp. 125 - 145.
- Wroth, C.P., 1975. In Situ Measurement of Initial Stresses and Deformation Characteristics. *Proceedings of the Conference on In Situ Measurement of Soil Properties*, ASCE Geotechnical Engineering Division, Raleigh, North Carolina, Vol. II, pp. 181 - 230.
- Wroth, C.P., Randolph, M.F., Houlsby, G.T., and Fahey, H., 1979. A Review of the Engineering Properties of Soils with Particular Reference to the Shear Modulus. *Cambridge University Engineering Department Report, D - SOILS / TR 75*.
- Yang, Q.S., Poorooshasb, F., and Poorooshasb, H.B., 1993. Analysis of Sub - Scour Deformation by Finite Element Method. *Proceedings of the 4th Canadian Conference on Marine Geotechnical Engineering*, St. John's, Newfoundland, Vol. 2, pp. 738 - 754.
- Yang, Q.S., Lach, P.R., Clark, J.I., and Poorooshasb, H.B., 1994. Comparisons of Physical and Numerical Models of Ice Scour. *Proceedings of the Eighth International Conference on Computer Methods and Advances in Geomechanics*, Morgantown, West Virginia, (eds. H.J. Siriwardane and M.M. Zaman), Vol. 2, pp. 1795 - 1801.
- Yong, R.N. and Hanna, A.W., 1977. Finite Element Analysis of Plane Soil Cutting. *Journal of Terramechanics*, Vol. 14, No. 3, pp. 103 - 125.
- Zytynski, M., Randolph, M.F., Nova, R., and Wroth, C.P., 1978. Short Communication : Modelling the Unloading - Reloading Behaviour of Soils. *International Journal of Numerical and Analytical Methods in Geomechanics*, Vol. 2, pp. 87 - 94.

Appendix A

Experimental Results

Scour Test 01

Test Number	σ_{v0} KPa	Attack Angle degrees	Width mm	Vertical Stiffness N / mm	Test Variable
1	140	15	100	26	soil state

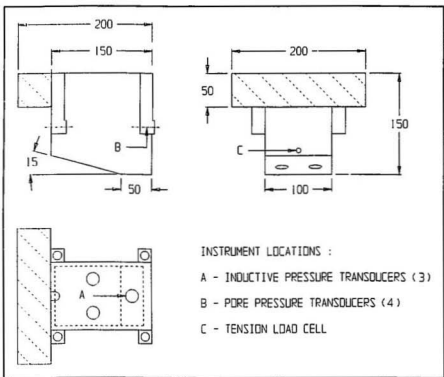


Figure 1A.1 Test 01 input parameters and model iceberg configuration

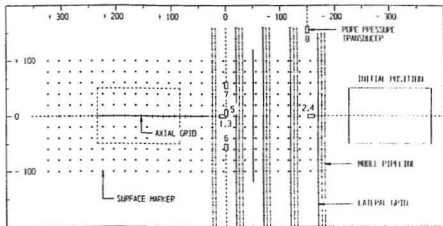
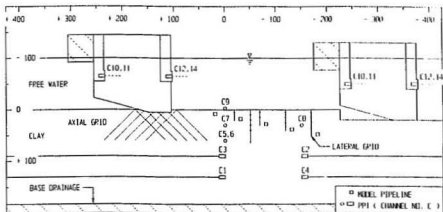


Figure 1A.2 Test 01 layout of instrumentation, deformation markers, and model pipeline segments shown in elevation and plan view (scales in mm)

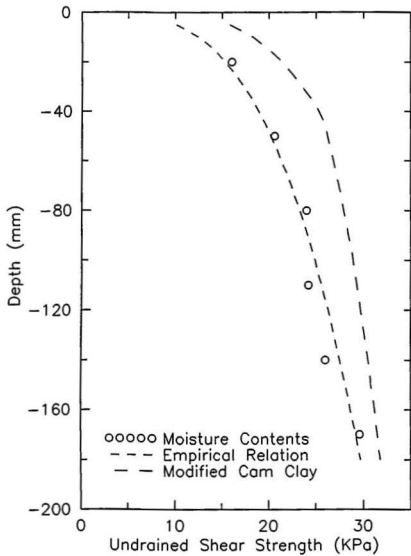


Figure 1B.1 Test 01 estimated undrained shear strength profiles based on post - test moisture content measurements and stress history of clay specimen

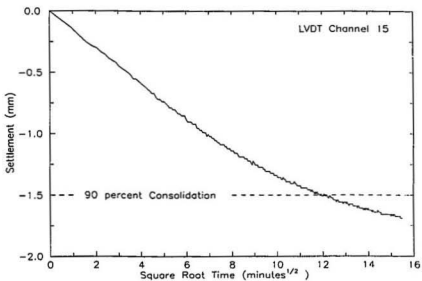
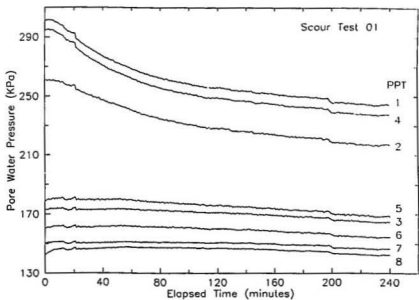


Figure 1C.1 Test 01 consolidation records. Top : Pore water pressure versus time for eight transducers; Bottom : Clay surface settlement versus square root of time

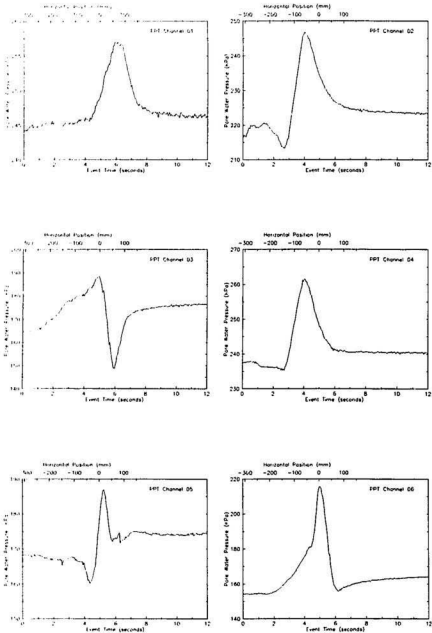


Figure 1C.2 Test 01 instrumentation data measured during scouring event

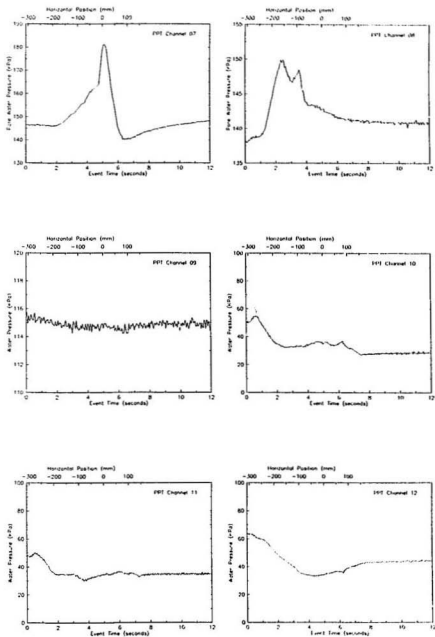


Figure 1C.2 Test 01 instrumentation data measured during scouring event

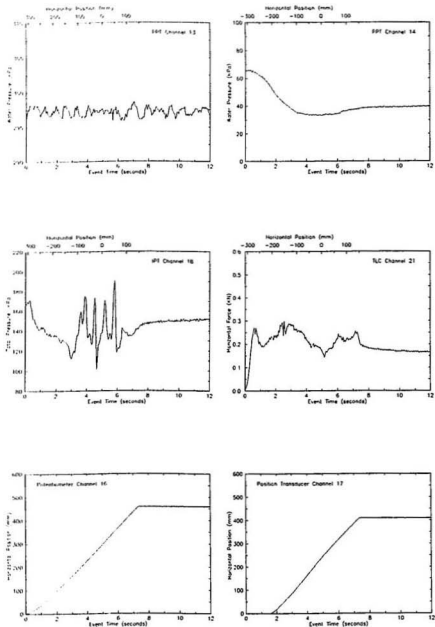


Figure 1C.2 Test 01 instrumentation data measured during scouring event

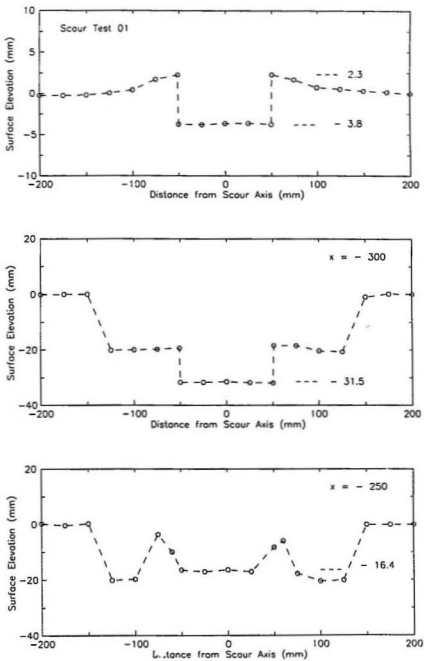


Figure 1D.1 Test 01 cross-sectional plots of clay surface profile measurements

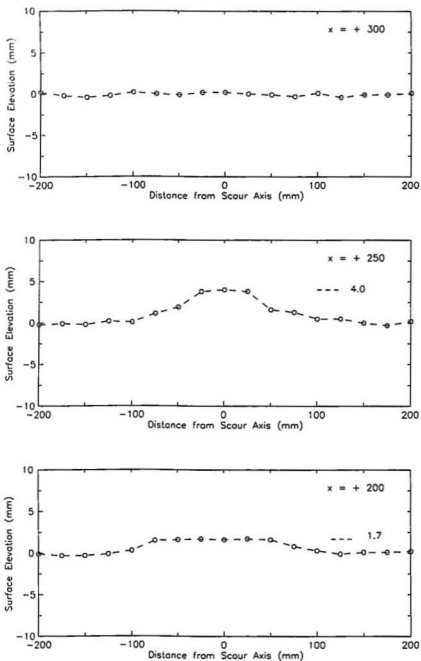


Figure 1D.1 Test 01 cross-sectional plots of clay surface profile measurements

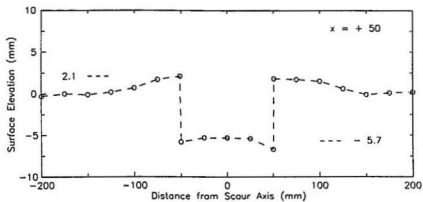
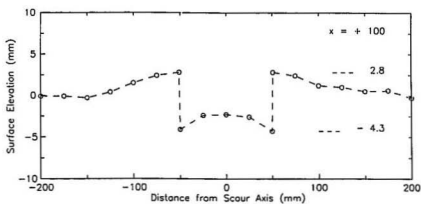
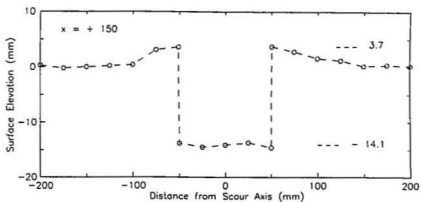


Figure 1D.1 Test 01 cross-sectional plots of clay surface profile measurements

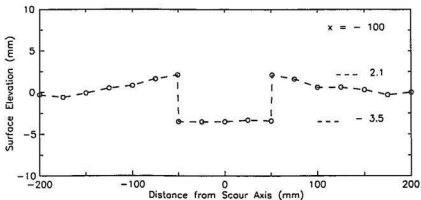
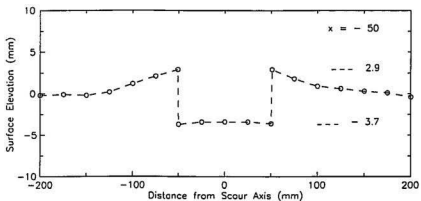
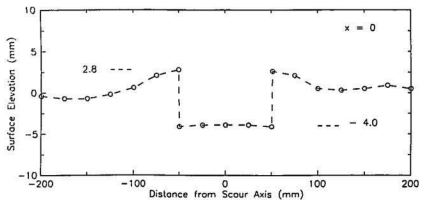


Figure 1D.1 Test 01 cross-sectional plots of clay surface profile measurements

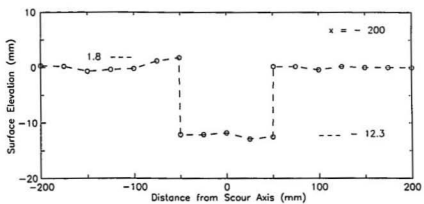
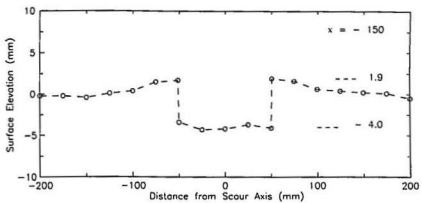


Figure 1D.1 Test 01 cross - sectional plots of clay surface profile measurements

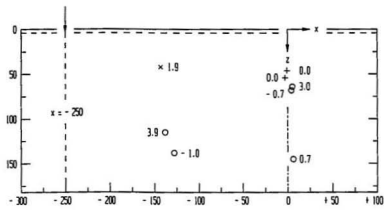
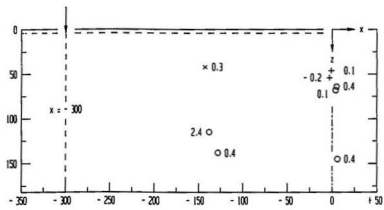
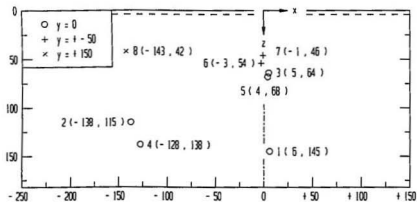


Figure 1E.1 Test 01 pore pressures (kPa) shown for different model horiz. positions

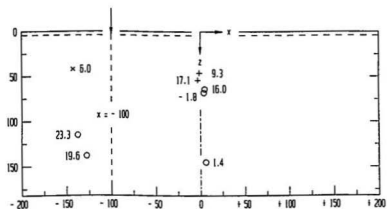
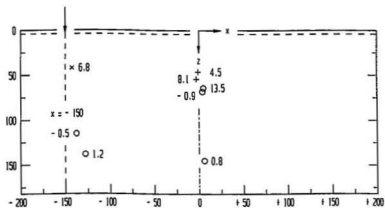
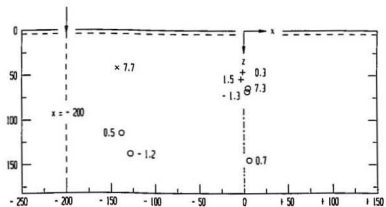


Figure 1E.1 Test 01 pore pressures (kPa) shown for different model horiz. positions

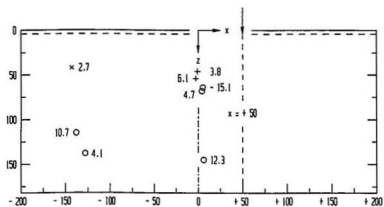
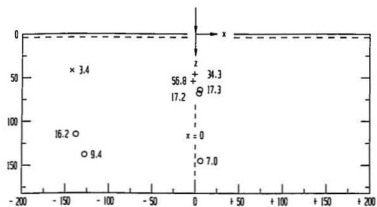
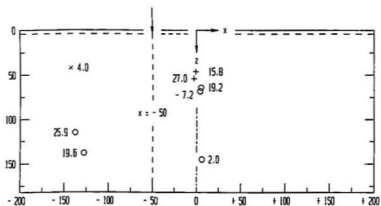


Figure 1E.1 Test 01 pore pressures (kPa) shown for different model horiz. positions

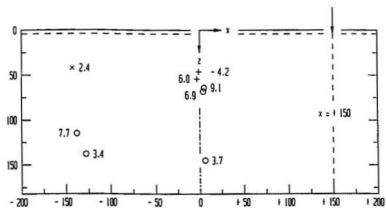
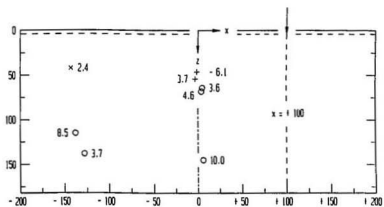


Figure 1E.1 Test 01 pore pressures (kPa) shown for different model horiz. positions

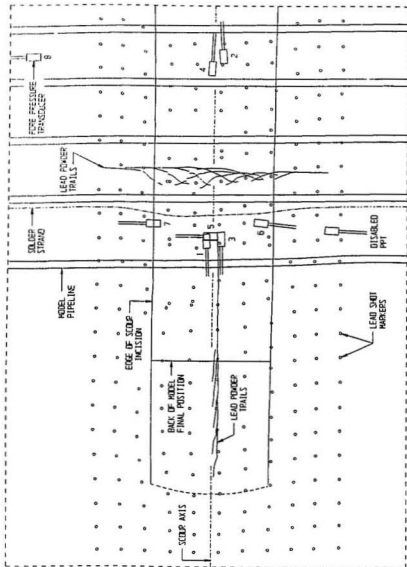


Figure 1F.1 Test 01 trace compiled from plan view radiographs of the clay specimen

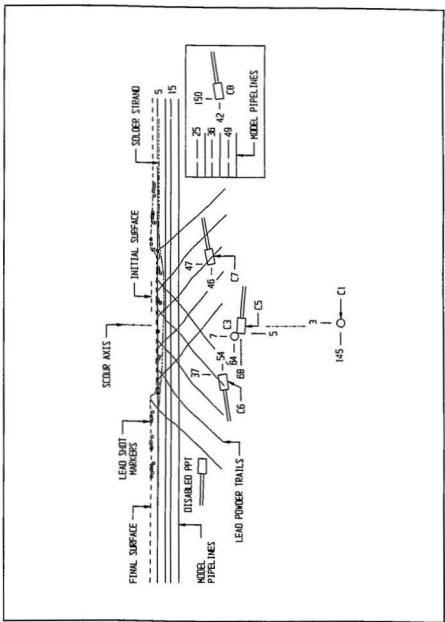


Figure 1F.2 Test O1 trace of cross-sectional radiograph showing displaced lateral grid of lead powder trails and locations of instrumentation and model pipelines (units mm)

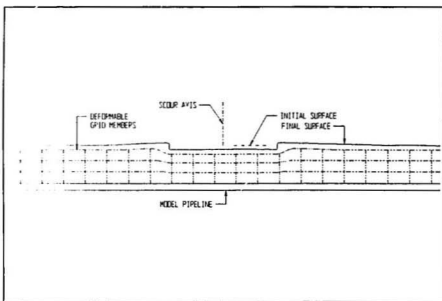
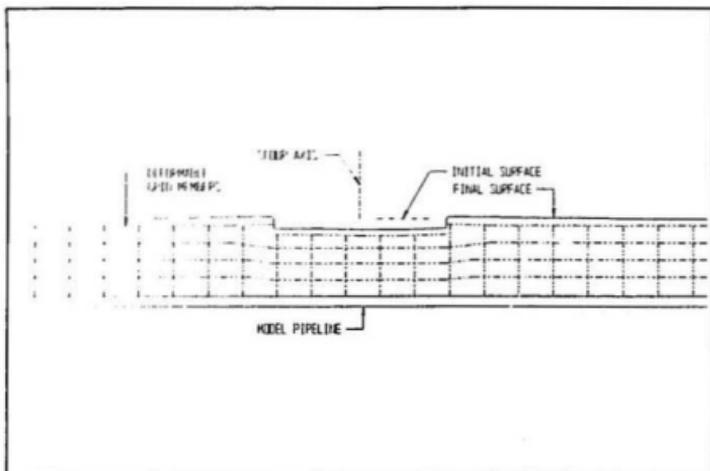


Figure 1F.3 Test 01 displaced configuration of initial lateral grids; Top : Cross - sectional view of grid at $x = -170$; Bottom : Cross - sectional view of grid at $x = -120$

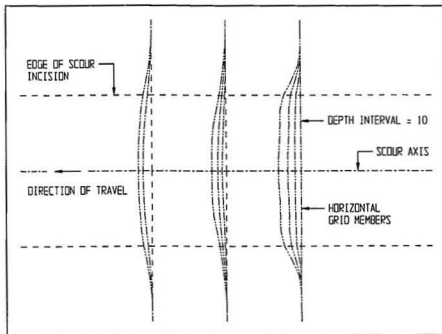
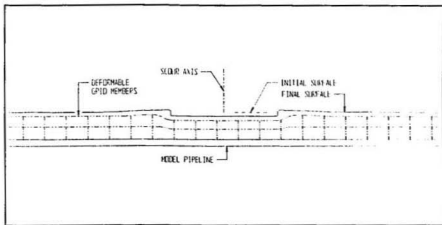


Figure 1F.3 Test 01 displaced configuration of initial lateral grids; Top : Cross-sectional view of grid at $x = -70$; Bottom : Plan view of initial lateral grids

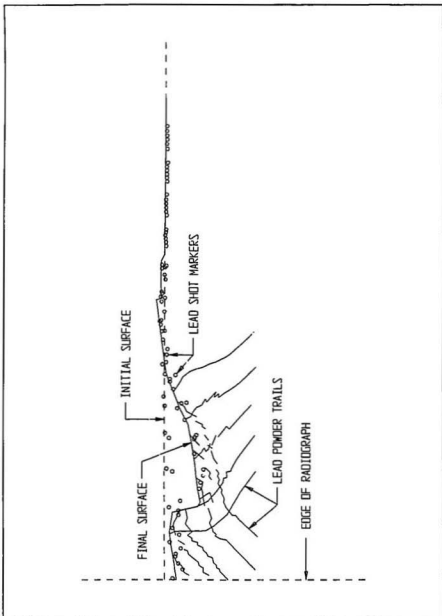


Figure 1F.4 Test 01 trace of axial section radiograph showing displaced configuration of grid of lead powder trails located at the final position of the model iceberg

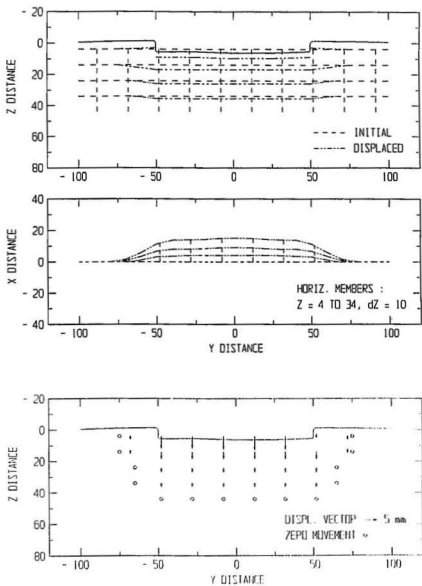


Figure 1F.5 Test 01 sub - surface soil displacement records. Top : Initial / displaced plot for lateral grid at $x = -170$; Bottom : Displacement vector plot (scales in mm)

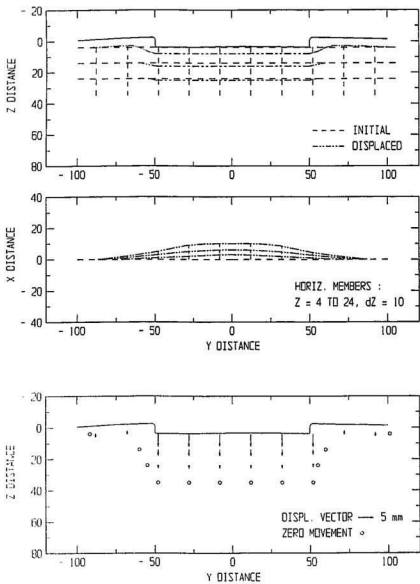


Figure 1F.5 Test 01 sub - surface soil displacement records. Top : Initial / displaced plot for lateral grid at $x = -120$; Bottom : Displacement vector plot (scales in mm)

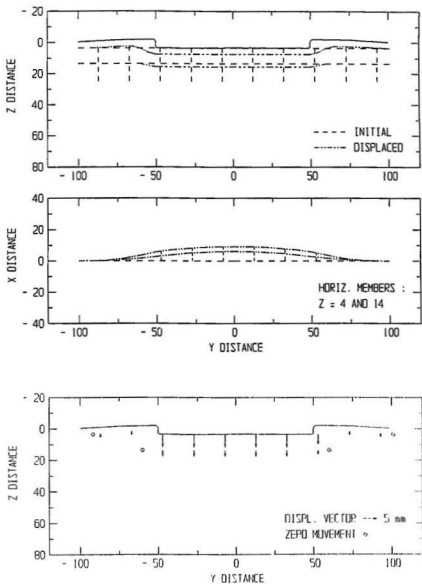


Figure 1F.5 Test 01 sub - surface soil displacement records. Top : Initial / displaced plot for lateral grid at $x = -70$; Bottom : Displacement vector plot (scales in mm)

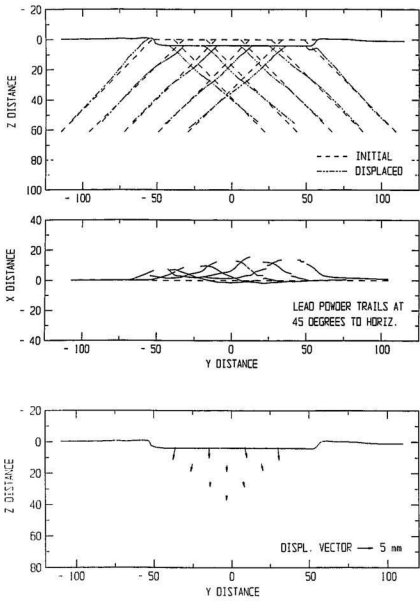


Figure 1F.5 Test 01 sub - surface soil displacement records. Top : Initial / displaced plot for lateral grid at $x = -50$; Bottom : Displacement vector plot (scales in mm)

Scour Test 02

Test Number	σ_{vo} KPa	Attack Angle degrees	Width mm	Vertical Stiffness N / mm	Test Variable
2	110	15	100	26	baseline

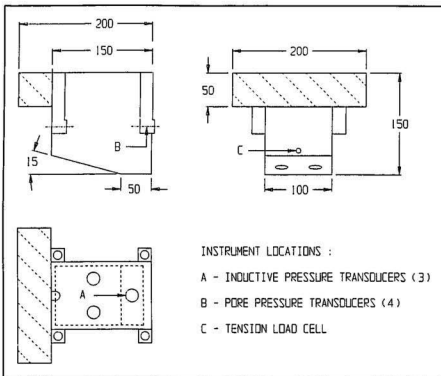


Figure 2A.1 Test 02 input parameters and model iceberg configuration

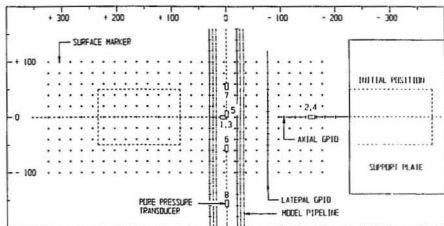
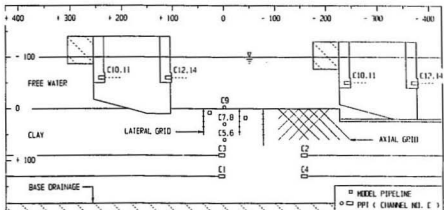


Figure 2A.2 Test 02 layout of instrumentation, deformation markers, and model pipeline segments shown in elevation and plan view (scales in mm)

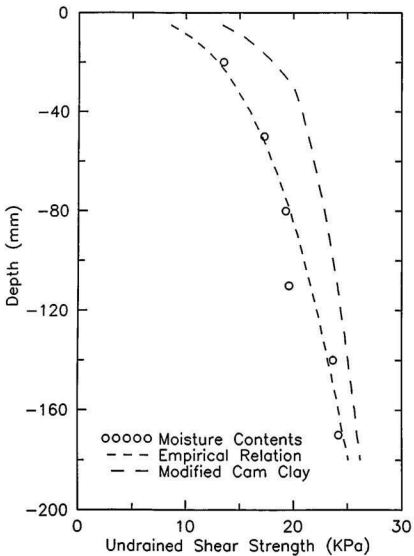


Figure 2B.1 Test 02 estimated shear strength profiles based on post - test moisture content measurements and stress history of clay specimen

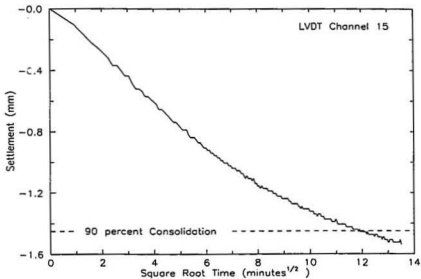
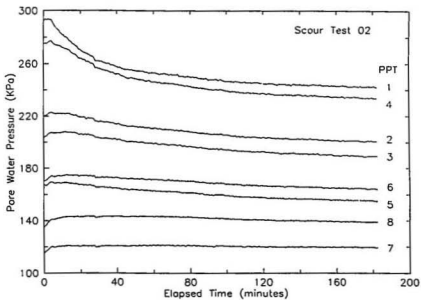


Figure 2C.1 Test 02 consolidation records. Top : Pore water pressure versus time for eight transducers; Bottom : Clay surface settlement versus square root of time

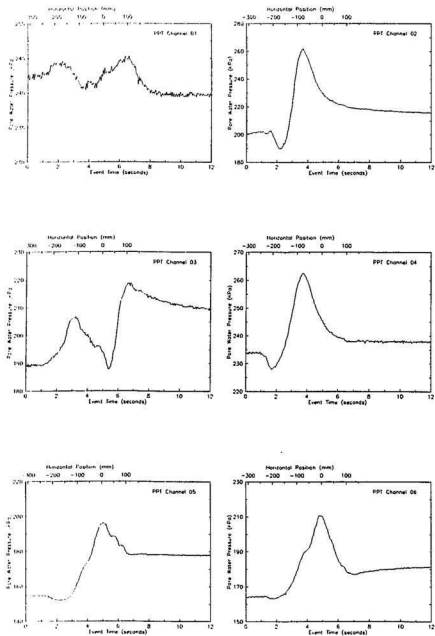


Figure 2C.2 Test 02 instrumentation data measured during scouring event

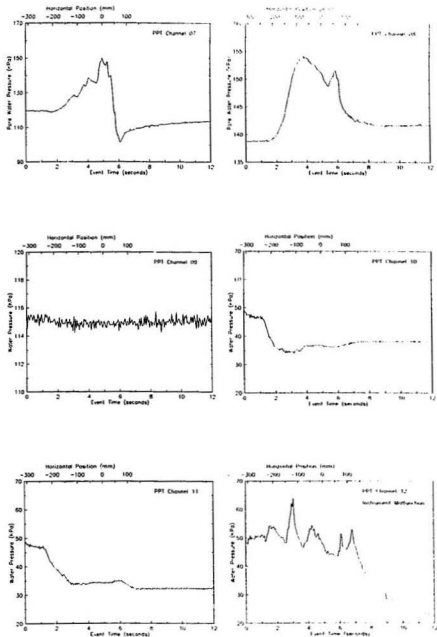


Figure 2C.2 Test 02 instrumentation data measured during scouring event

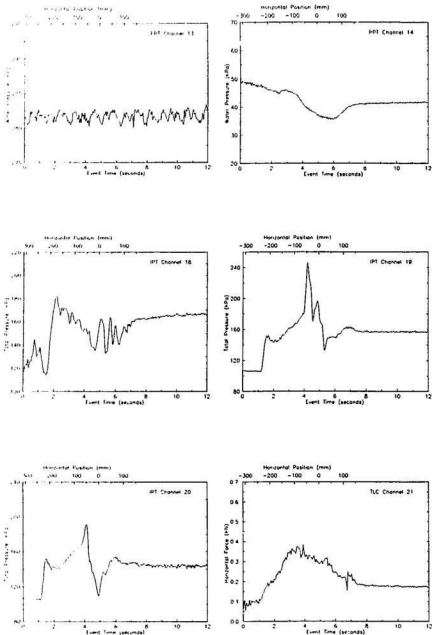


Figure 2C.2 Test 02 instrumentation data measured during scouring event

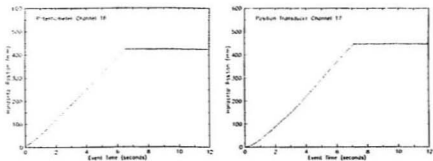


Figure 2C.2 Test 02 instrumentation data measured during scouring event

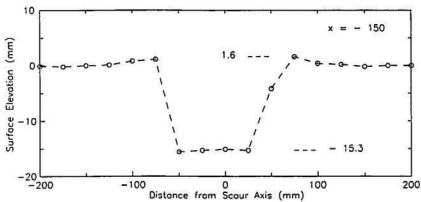
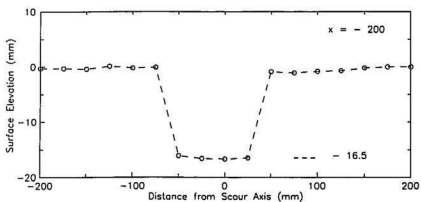
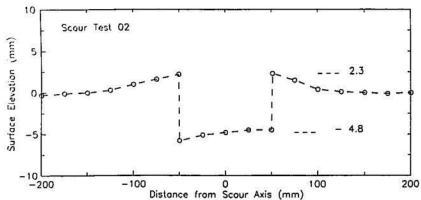


Figure 2D.1 Test 02 cross-sectional plots of clay surface profile measurements

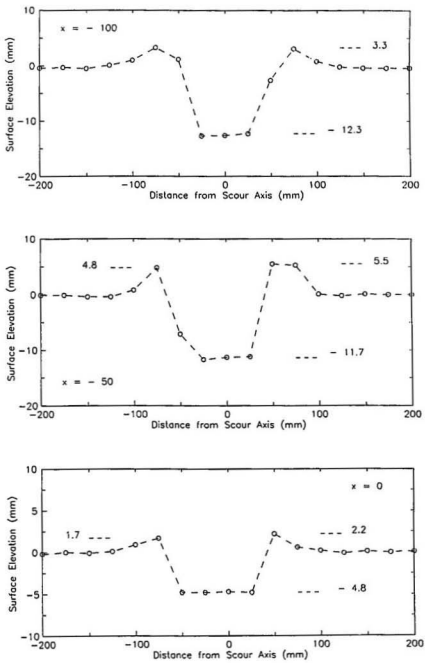


Figure 2D.1 Test O2 cross - sectional plots of clay surface profile measurements

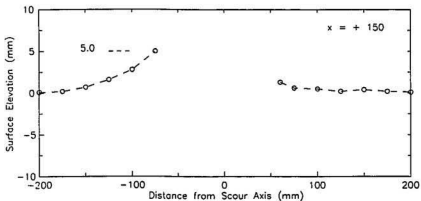
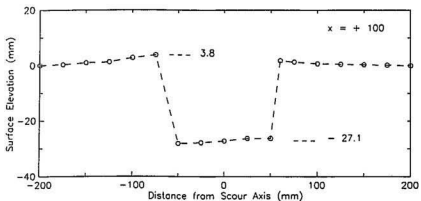
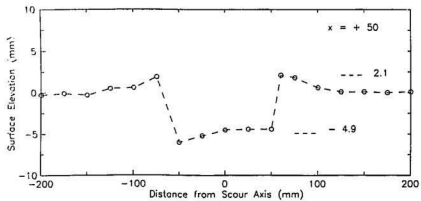


Figure 2D.1 Test 02 cross - sectional plots of clay surface profile measurements

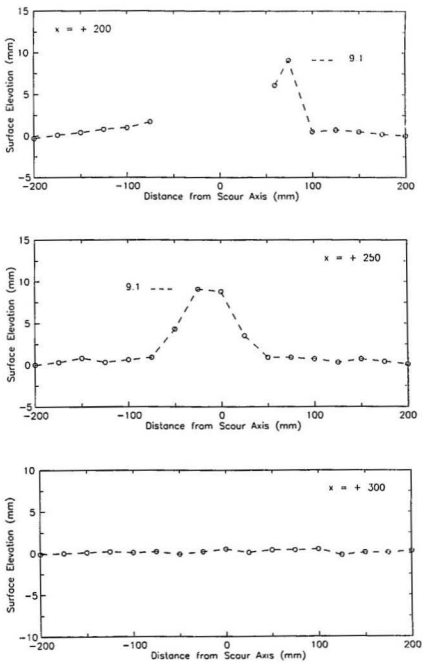


Figure 2D.1 Test 02 cross - sectional plots of clay surface profile measurements

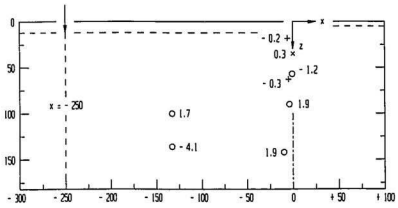
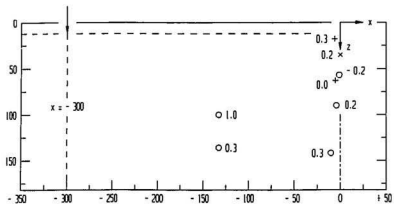
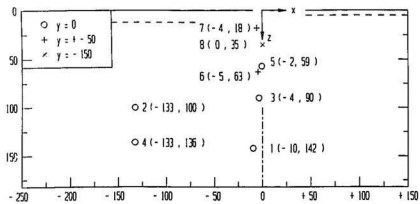


Figure 2E.1 Test 02 pore pressures (kPa) shown for different model horiz. positions

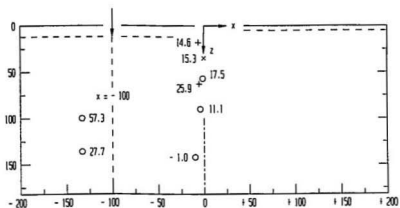
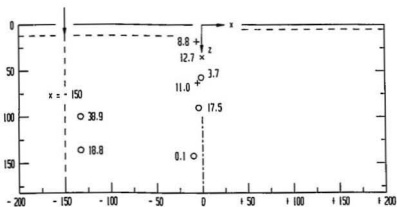
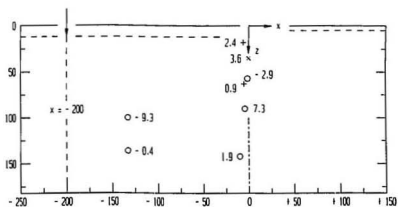


Figure 2E.1 Test 02 pore pressures (kPa) shown for different model horiz. positions

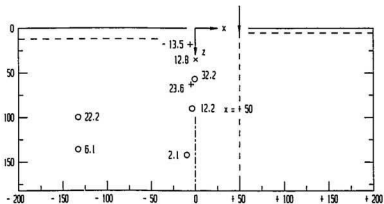
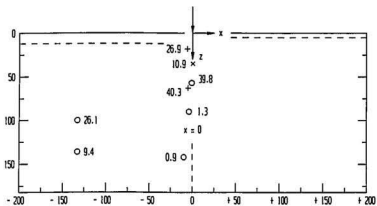
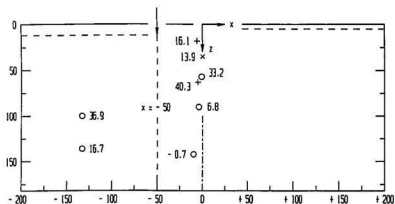


Figure 2E.1 Test O2 pore pressures (kPa) shown for different model horiz. positions

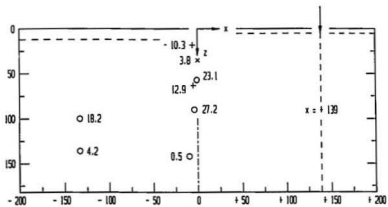
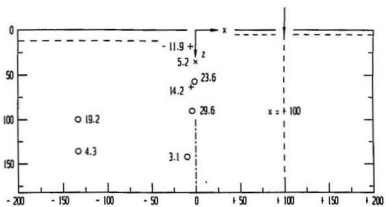


Figure 2E.1 Test 02 pore pressures (kPa) shown for different model horiz. positions

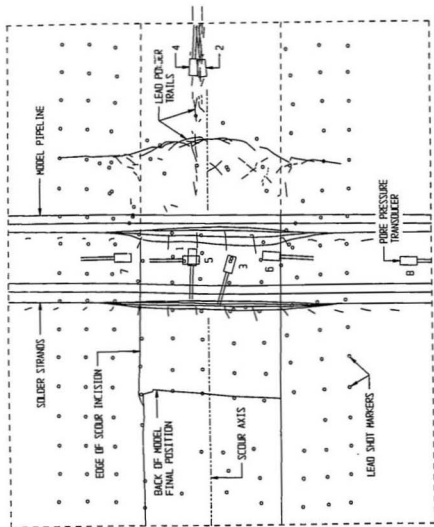


Figure 2F.1 Test 02 trace compiled from plan view radiographs of the clay specimen

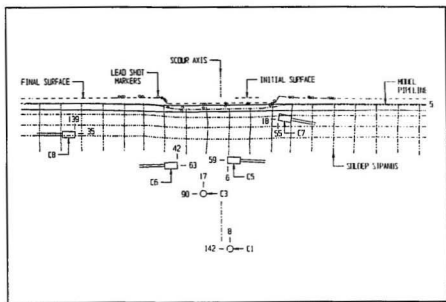
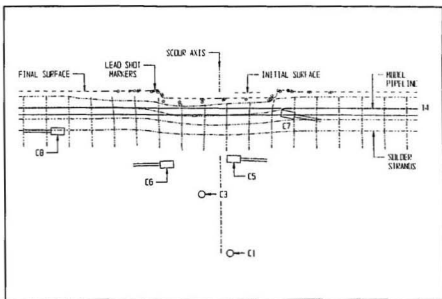


Figure 2F.2 Test 02 traces of cross - sectional radiographs showing displaced configuration of lateral grids. Top : $x = -25$; Bottom : $x = +25$ (units mm)

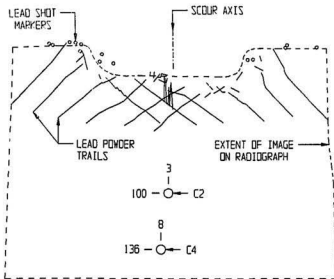


Figure 2F.3 Test 02 radiograph trace of lateral grid of lead powder trails at $x = -75$

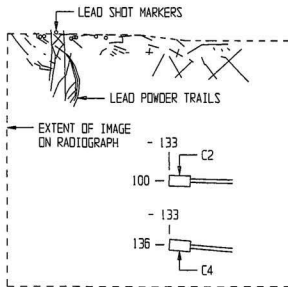


Figure 2F.4 Test 02 radiograph trace of lead powder trail axial grid; $x \approx -200$ to -75

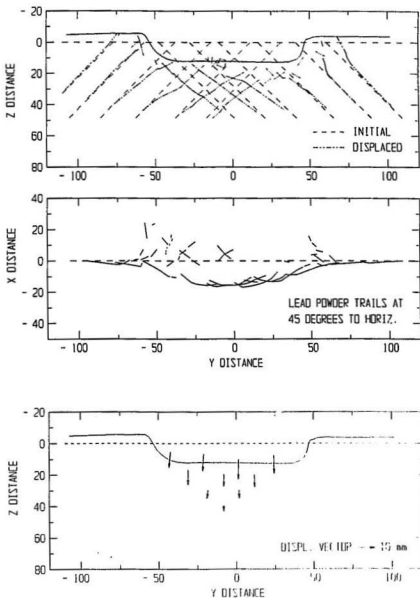


Figure 2F.5 Test O2 sub - surface soil displacement records. Top : Initial / displaced plot for lateral grid at $x = -75$; Bottom : Displacement vector plot (scales in mm)

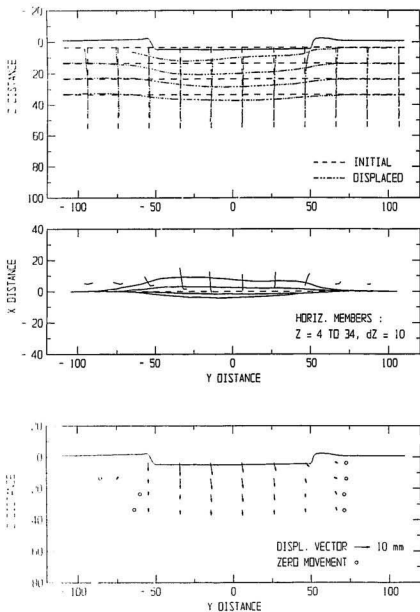


Figure 2F.5 Test 02 sub - surface soil displacement records. Top : Initial / displaced plot for lateral grid at $x = -25$; Bottom : Displacement vector plot (scales in mm)

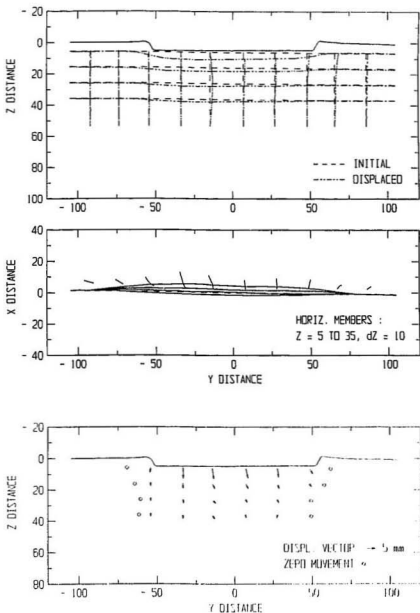


Figure 2F.5 Test 02 sub - surface soil displacement records. Top : Initial / displaced plot for lateral grid at $x = + 25$; Bottom : Displacement vector plot (scales in mm)

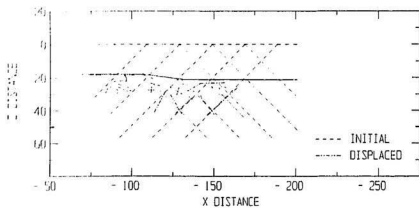


Figure 2F.5 Test 02 sub - surface soil displacement records. Initial / displaced plot for axial grid at $x \approx -200$ to -75

Scour Test 04

Test Number	σ_{v0} KPa	Attack Angle degrees	Width mm	Vertical Stiffness N / mm	Test Variable
4	110	15	100	61	soil state

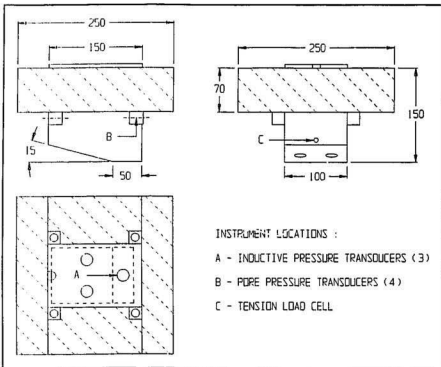


Figure 4A.1 Test 04 input parameters and model iceberg configuration

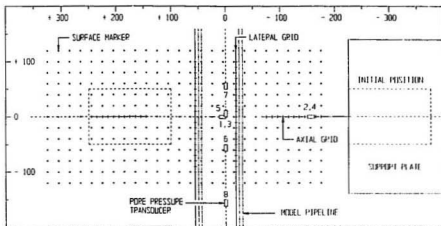
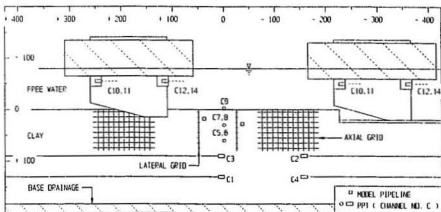


Figure 4A.2 Test 04 layout of instrumentation, deformation markers, and model pipeline segments shown in elevation and plan view (scales in mm)

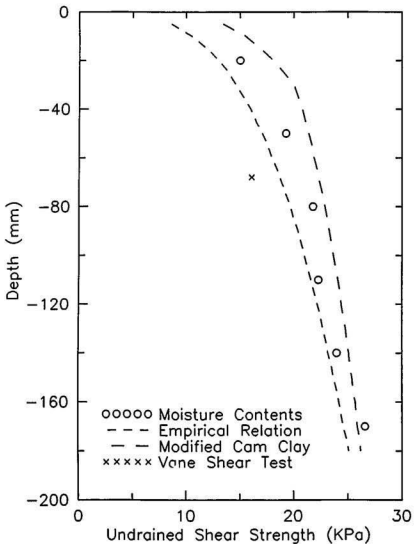


Figure 4B.1 Test 04 estimated undrained shear strength profiles based on post - test moisture content measurements, clay stress history, and in - flight vane shear tests

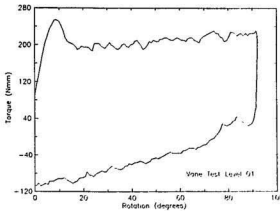
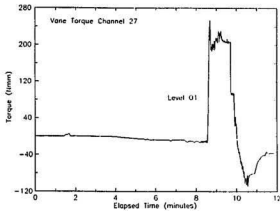
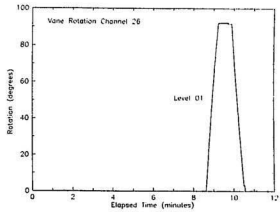


Figure 4B.2 Test 04 in - flight vane shear test for Level 01 at 6.8 m prototype depth : Vane rotation and torque against time, and torque versus rotation curve

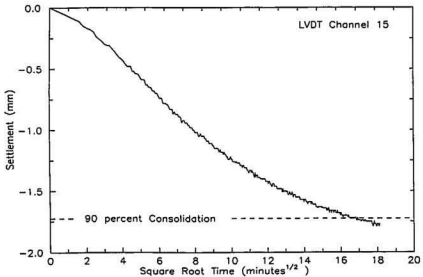
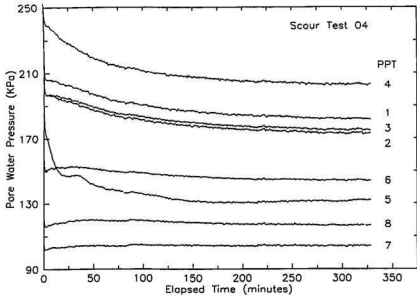


Figure 4C.1 Test 04 consolidation records. Top : Pore water pressure versus time for eight transducers; Bottom : Clay surface settlement versus square root of time

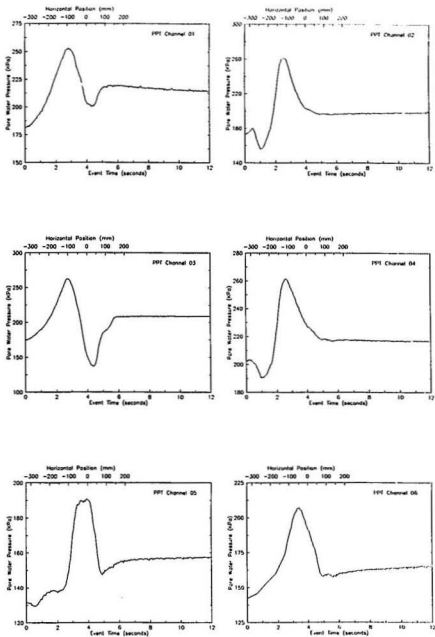


Figure 4C.2 Test 04 instrumentation data measured during scouring event

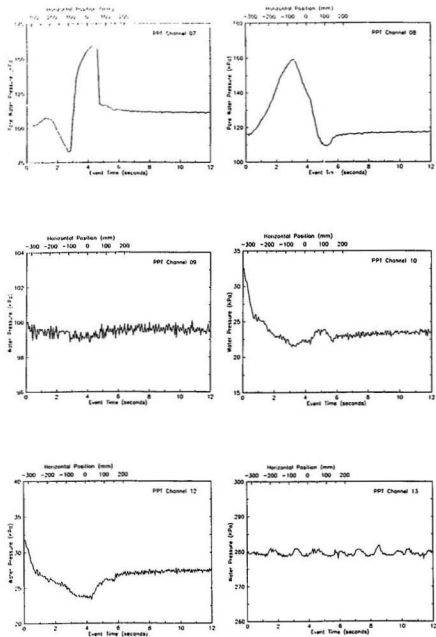


Figure 4C.2 Test 04 instrumentation data measured during scouring event

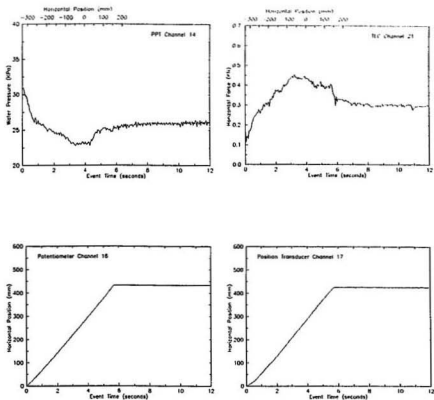


Figure 4C.2 Test 04 instrumentation data measured during scouring event

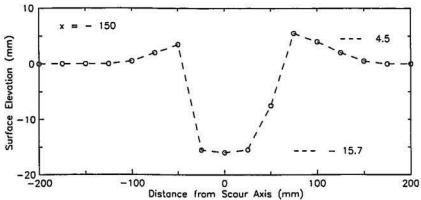
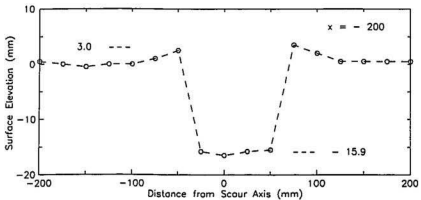
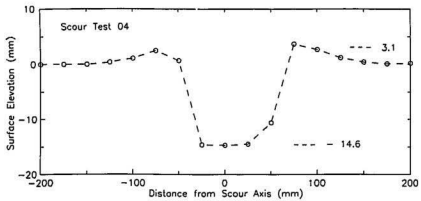


Figure 4D.1 Test 04 cross-sectional plots of clay surface profile measurements

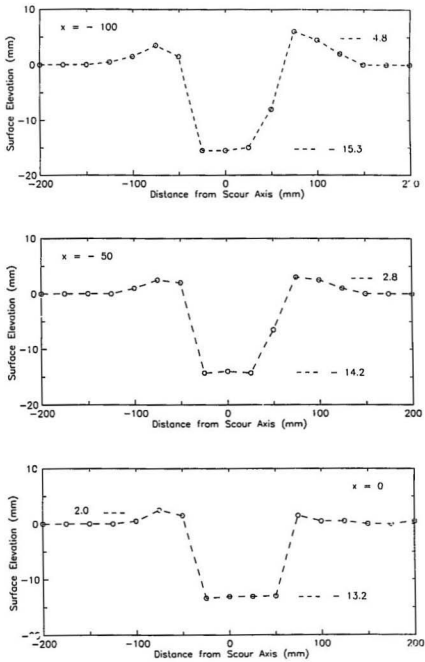


Figure 4D.1 Test 04 cross - sectional plots of clay surface profile measurements

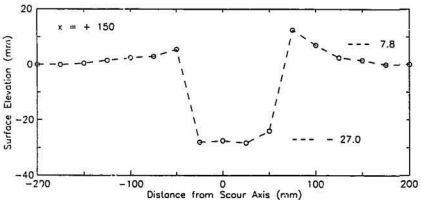
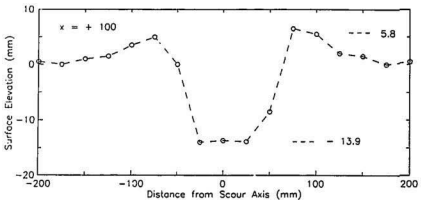
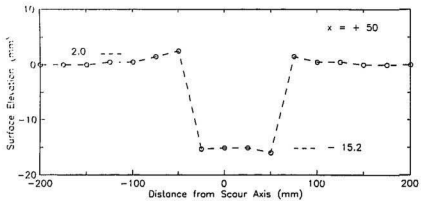


Figure 4D.1 Test 04 cross - sectional plots of clay surface profile measurements

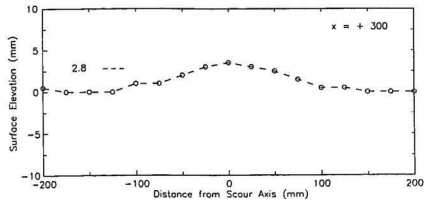
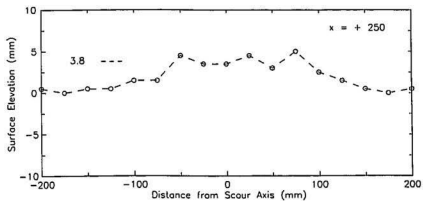
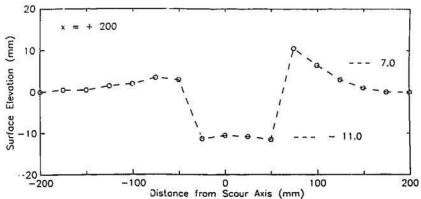


Figure 4D.1 Test 04 cross - sectional plots of clay surface profile measurements

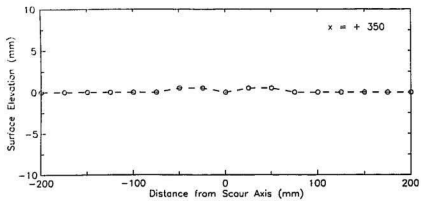


Figure 4D.1 Test 04 cross - sectional plots of clay surface profile measurements

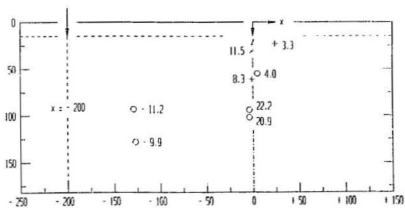
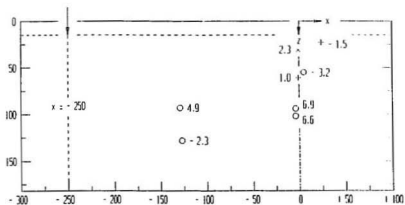
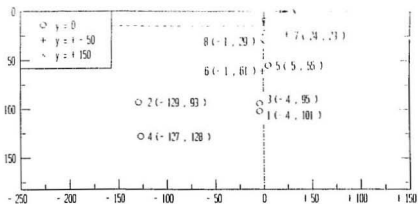


Figure 4E.1 Test 04 pore pressures (kPa) shown for different model horiz. positions

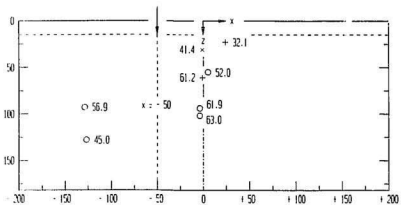
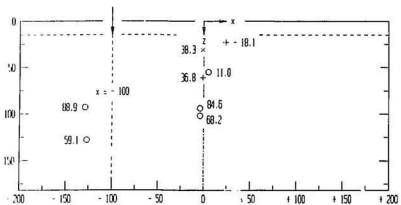
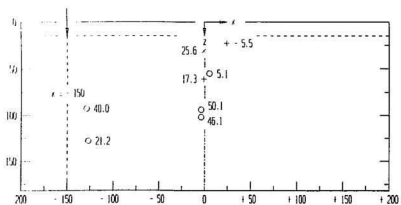


Figure 4E.1 Test 04 pore pressures (kPa) shown for different model horiz. positions

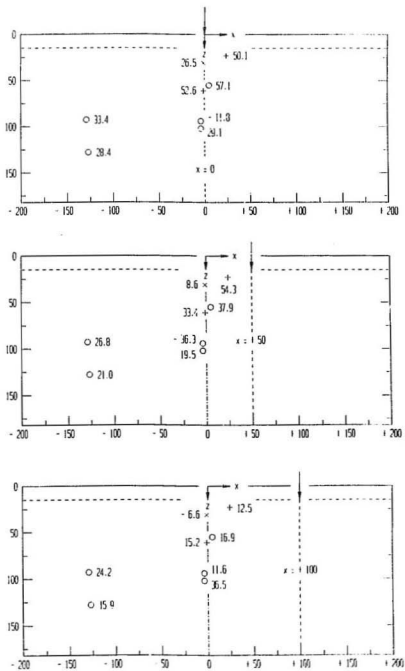


Figure 4E.1 Test 04 pore pressures (kPa) shown for different model horiz. positions

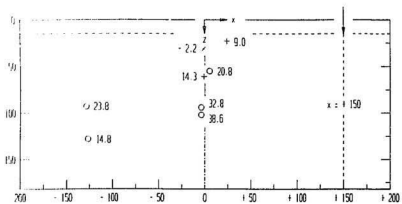


Figure 4E.1 Test 04 pore pressures (kPa) shown for different model horiz. positions

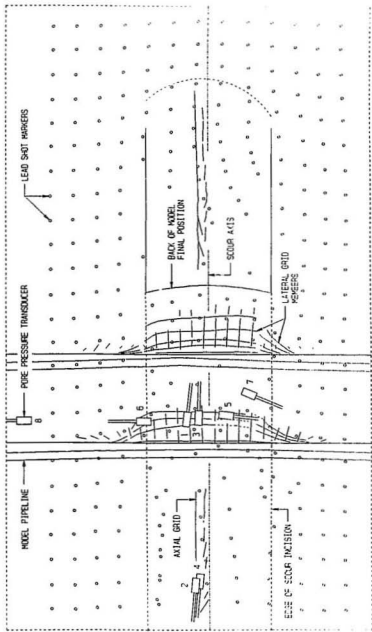


Figure 4F.1 Test 04 trace compiled from plan view radiographs of the clay specimen

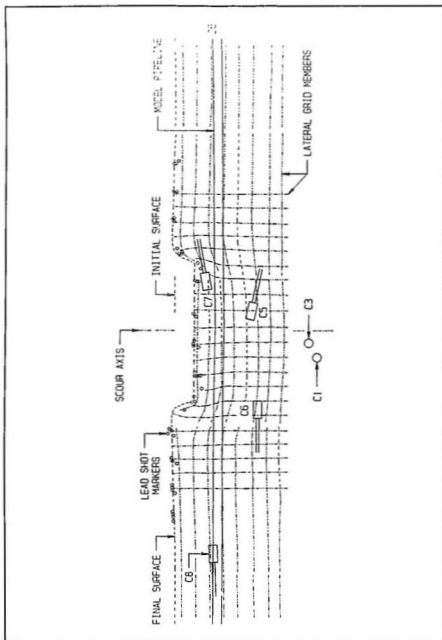


Figure 4F.2 Test 04 trace of cross - sectional radiograph showing displaced configuration of lateral grid at $x = -19$

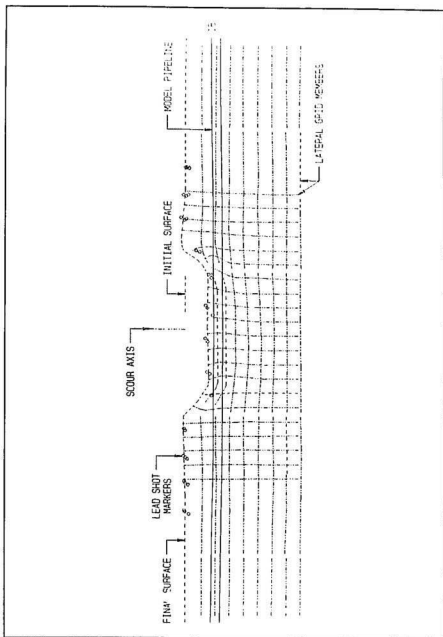


Figure 4F.2 Test 04 trace of cross - sectional radiograph showing displaced configuration of lateral grid at $x = + 54$

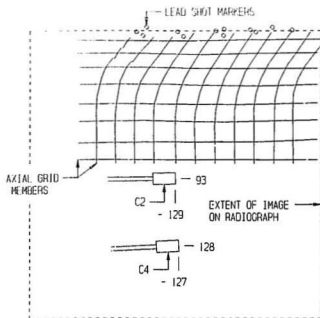


Figure 4F.3 Test 04 radiograph trace of axial grid; $x = -175$ to -50

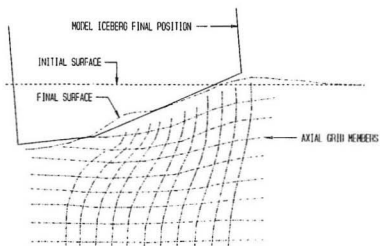
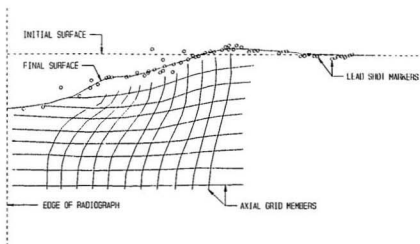


Figure 4F.4 Test 04 radiograph trace of axial grid located at $x \approx +125$ to $+275$. Bottom view depicts apparent final position of model iceberg in relation to grid

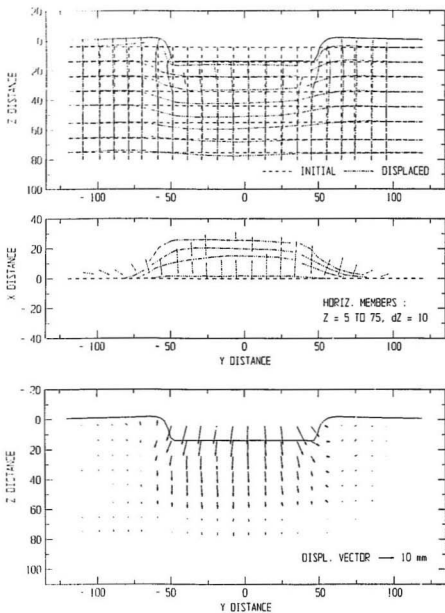


Figure 4F.5 Test 04 sub - surface soil displacement records. Top : Initial / displaced plot for lateral grid at $x = -19$; Bottom : Displacement vector plot (scales in mm)

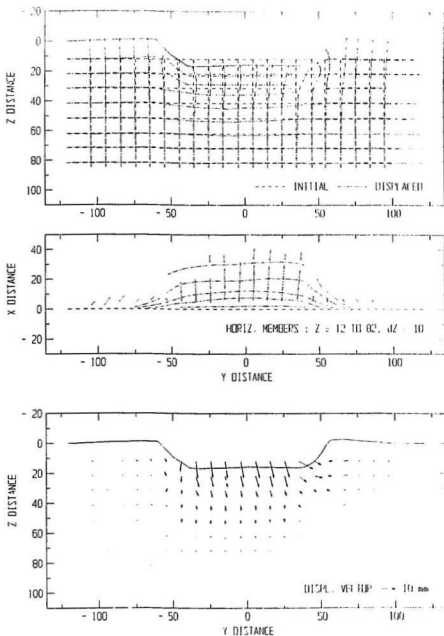


Figure 4F.5 Test 04 sub - surface soil displacement records. Top : Initial / displaced plot for lateral grid at $x = -54$; Bottom : Displacement vector plot (scales in mm)

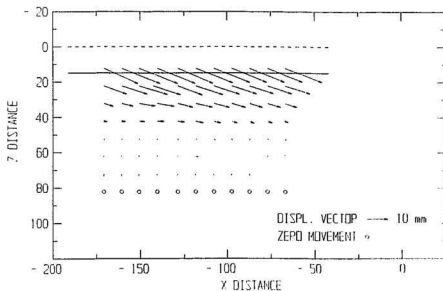
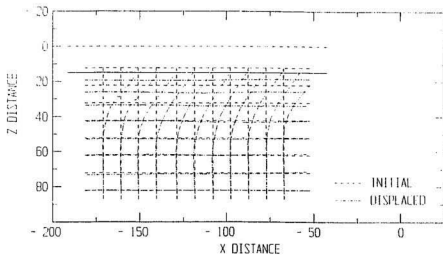


Figure 4F.5 Test 04 sub - surface soil displacement records. Top : Initial / displaced plot for axial grid at $x = -175$ to -50 ; Bottom : Displacement vector plot (scales in mm)

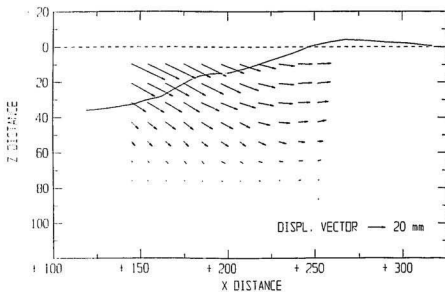
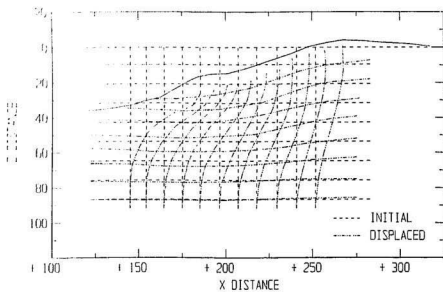


Figure 4F.5 Test 04 sub - surface soil displacement records. Top : Initial / displaced plot for axial grid at $x \approx +125$ to $+275$; Bottom : Displacement vector plot (scales in mm)

Scour Test 05

Test Number	$\sigma_{v,u}$ KPa	Attack Angle degrees	Width mm	Vertical Stiffness N / mm	Test Variable
5	140	15	100	61	baseline

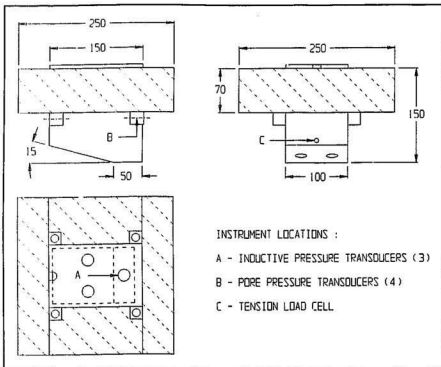


Figure 5A.1 Test 05 input parameters and model iceberg configuration

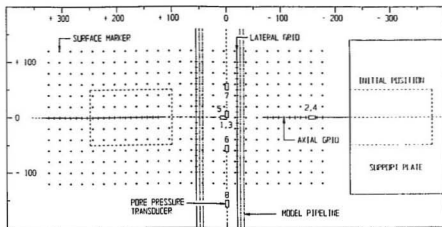
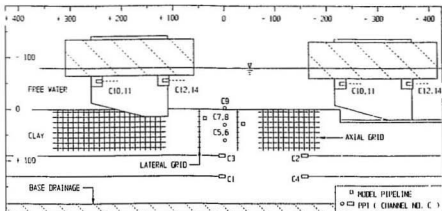


Figure 5A.2 Test 05 layout of instrumentation, deformation markers, and model pipeline segments shown in elevation and plan view (scales in mm)

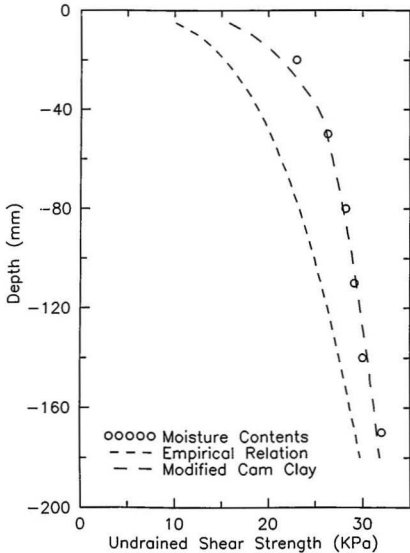


Figure 5B.1 Test 05 estimated undrained shear strength profiles based on post - test moisture content measurements and stress history of clay specimen

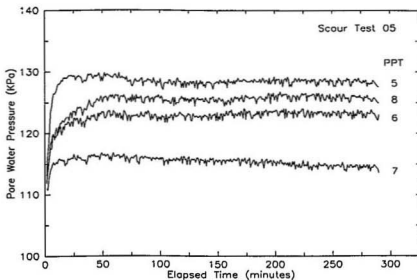
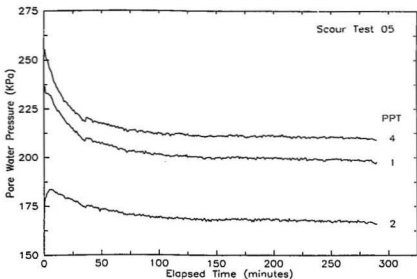


Figure 5C.1 Test 05 consolidation records. Top : Pore water pressure versus time for transducer Channels 01, 02, and 04; Bottom : Channels 05 to 08

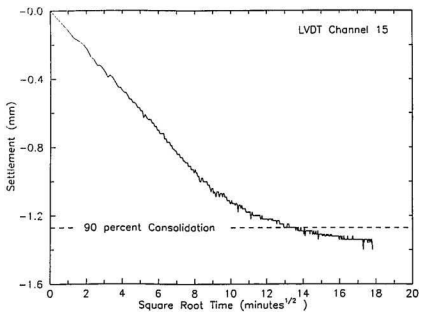


Figure 5C.1 Test 05 consolidation records. Clay surface settlement plotted versus square root of time

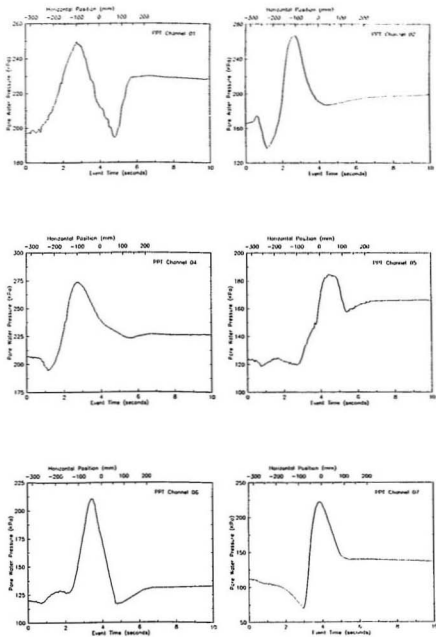


Figure SC.2 Test 05 instrumentation data measured during scouring event

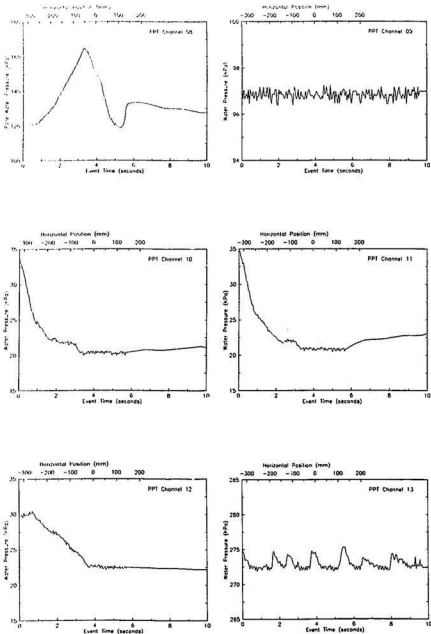


Figure 5C.2 Test 05 instrumentation data measured during scouring event

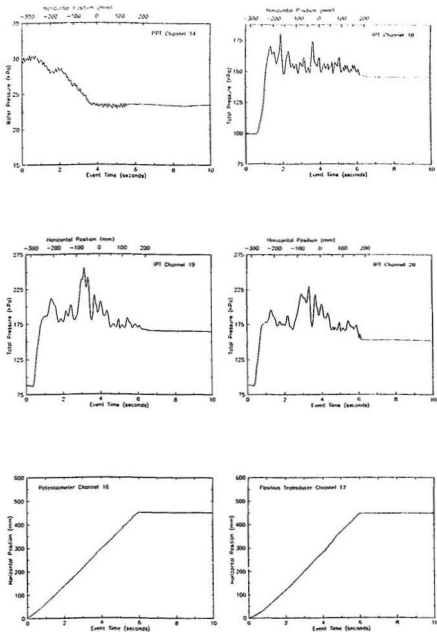


Figure 5C.2 Test 05 instrumentation data measured during scouring event

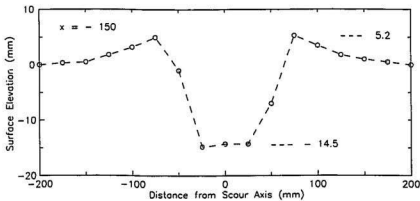
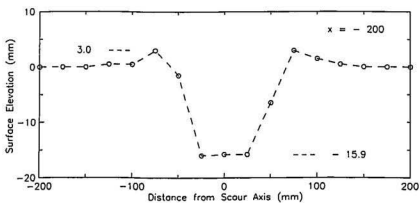
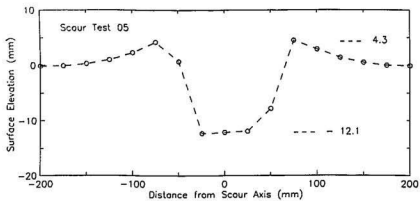


Figure 5D.1 Test 05 cross - sectional plots of clay surface profile measurements

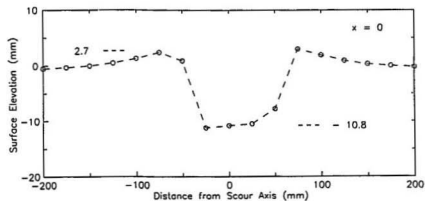
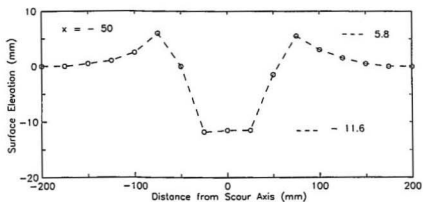
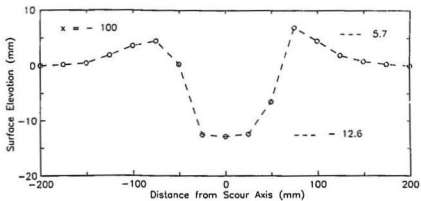


Figure 5D.1 Test 05 cross - sectional plots of clay surface profile measurements

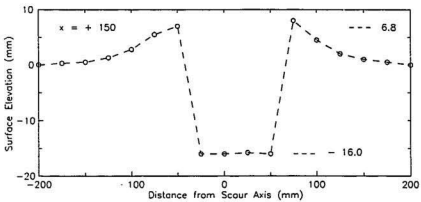
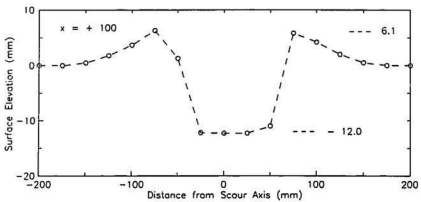
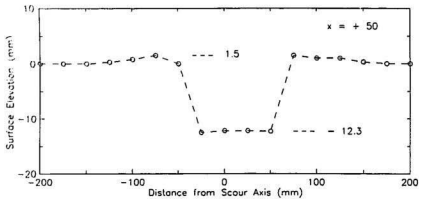


Figure 5D.1 Test 05 cross - sectional plots of clay surface profile measurements

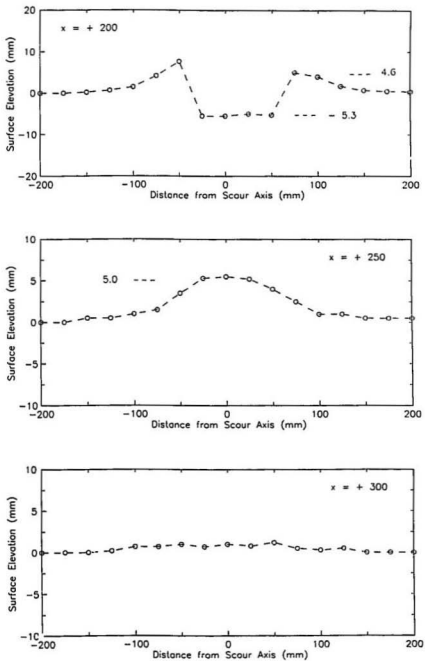


Figure SD.1 Test 05 cross - sectional plots of clay surface profile measurements

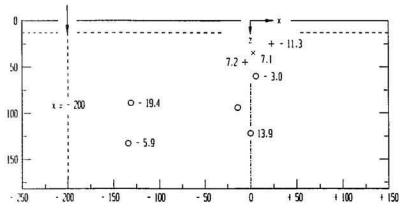
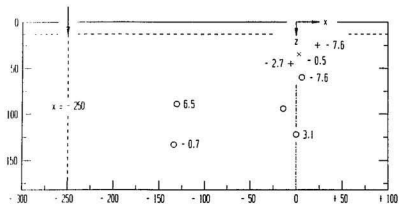
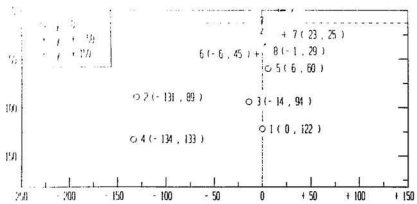


Figure SE.1 Test 05 pore pressures (kPa) shown for different model horiz. positions

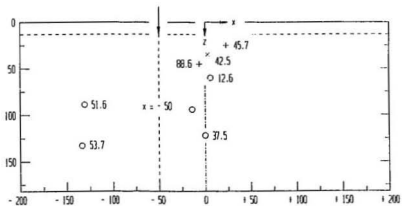
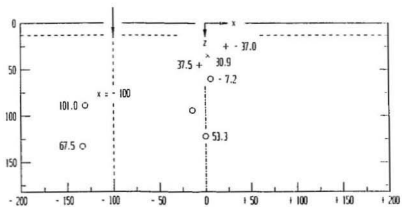
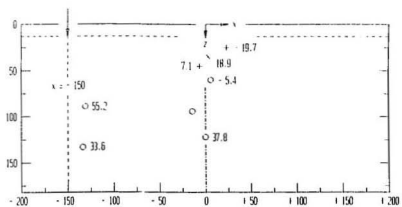


Figure SE.1 Test 05 pore pressures (kPa) shown for different model horiz. positions

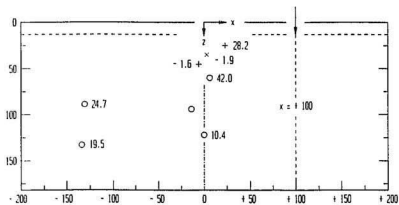
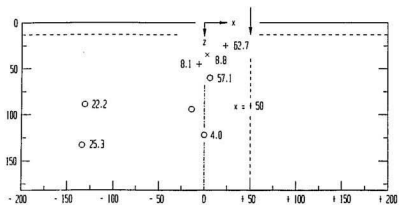
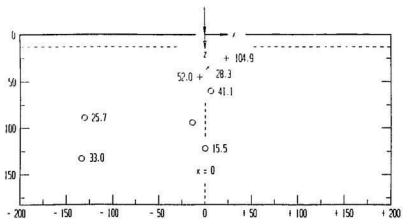


Figure 5E.1 Test 05 pore pressures (kPa) shown for different model horiz. positions

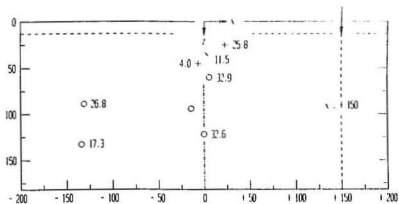


Figure 5E.1 Test 05 pore pressures (kPa) shown for different model horiz. positions

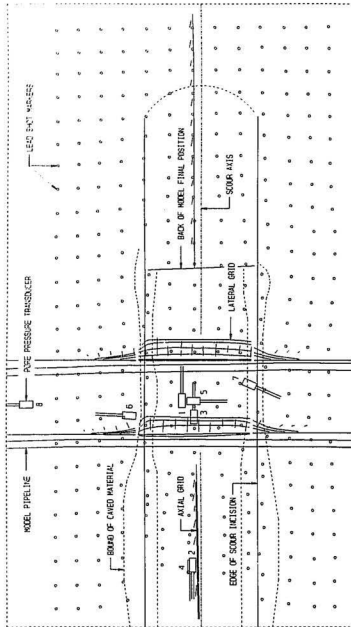


Figure 5F.1 Test 05 trace compiled from plan view radiographs of the clay specimen

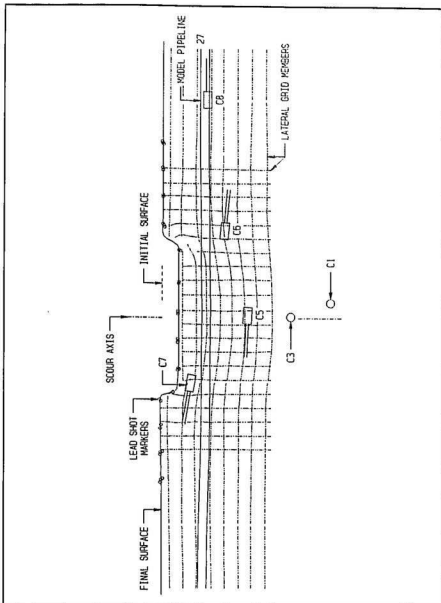


Figure 5F.2 Test 05 trace of cross - sectional radiograph showing displaced configuration of lateral grid at $x = -25$

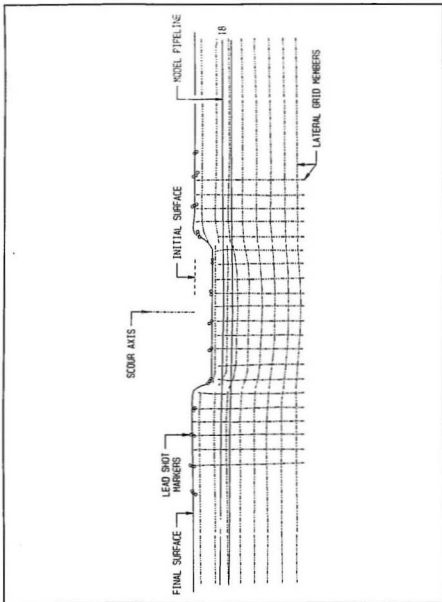


Figure 5F.2 Test 05 trace of cross - sectional radiograph showing displaced configuration of lateral grid at $x = +41$

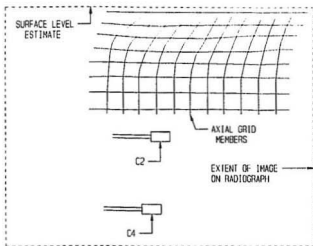


Figure 5F.3 Test 05 radiograph trace of axial grid; $x \approx -220$ to -95

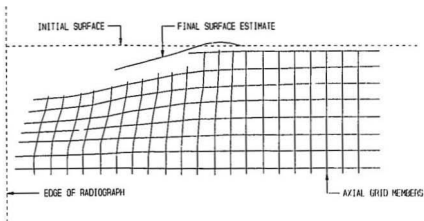


Figure 5F.4 Test 05 radiograph trace of axial grid; $x \approx +125$ to $+350$

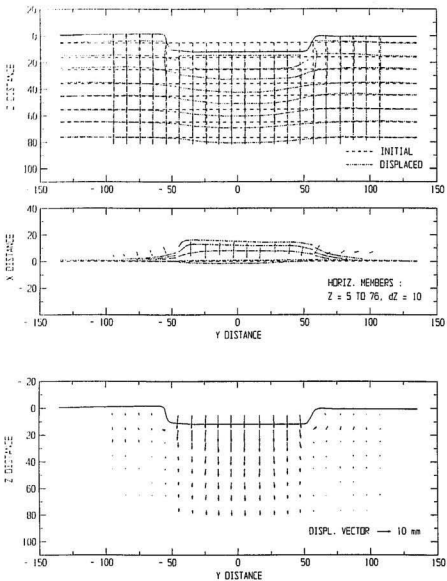


Figure 5F.5 Test 05 sub - surface soil displacement records. Top : Initial / displaced plot for lateral grid at $x = -25$; Bottom : Displacement vector plot (scales in mm)

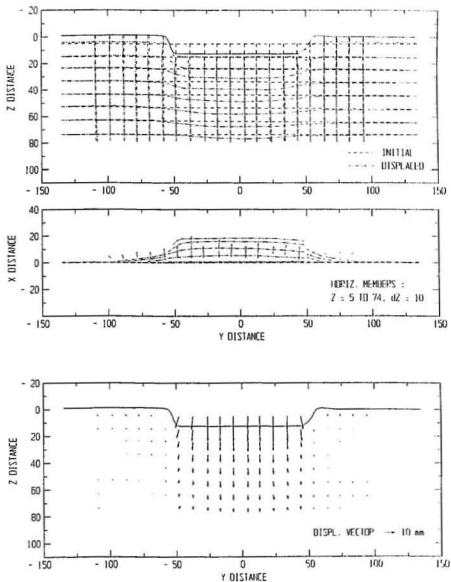


Figure 5F.5 Test 05 sub - surface soil displacement records. Top : Initial / displaced plot for lateral grid at $x = +41$; Bottom : Displacement vector plot (scales in mm)

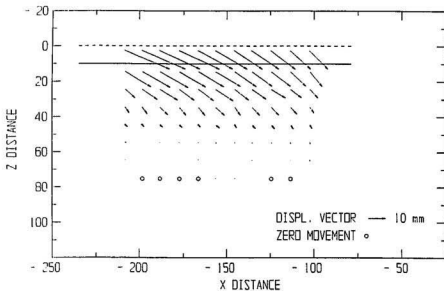
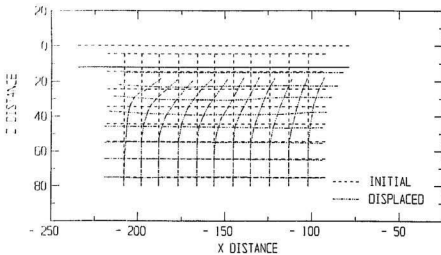


Figure 5F.5 Test 05 sub - surface soil displacement records. Top : Initial / displaced plot for axial grid at $x = -220$ to -95 ; Bottom : Displacement vector plot (scales in mm)

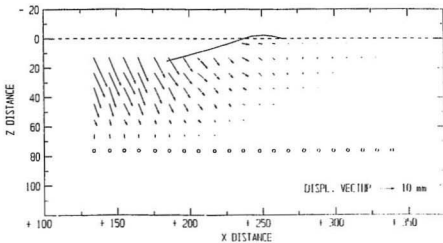
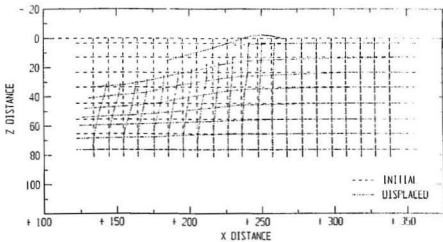


Figure 5F.5 Test 05 sub - surface soil displacement records. Top : Initial / displaced plot for axial grid at $x = +125$ to $+350$; Bottom : Displacement vector plot (scales in mm)

Scour Test 06

Test Number	$\sigma_{v,0}$ KPa	Attack Angle degrees	Width mm	Vertical Stiffness N / mm	Test Variable
6	200	15	100	61	soil state

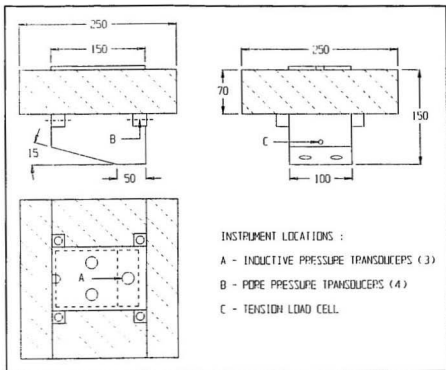


Figure 6A.1 Test 06 input parameters and model iceberg configuration

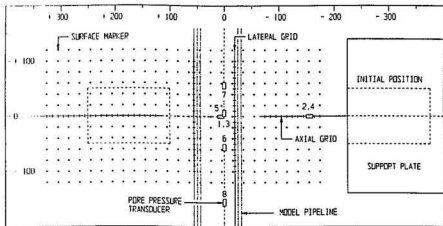
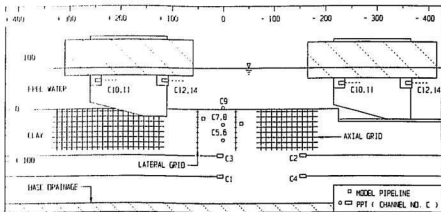


Figure 6A.2 Test 06 layout of instrumentation, deformation markers, and model pipeline segments shown in elevation and plan view (scales in mm)

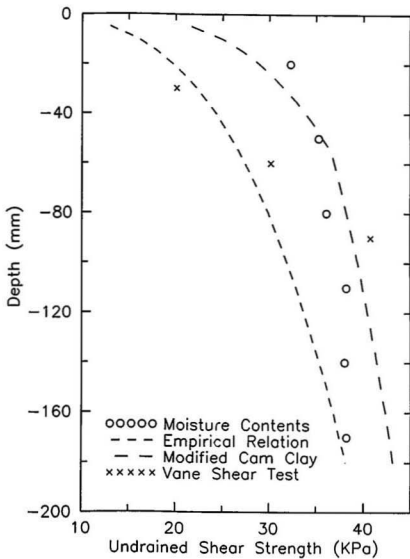


Figure 6B.1 Test 06 estimated undrained shear strength profiles based on post - test moisture content measurements, clay stress history, and in - flight vane shear tests

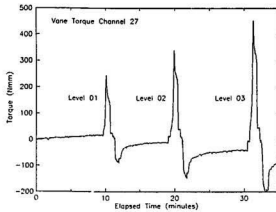
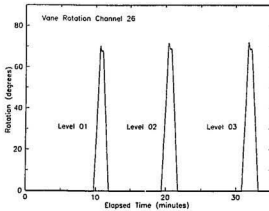
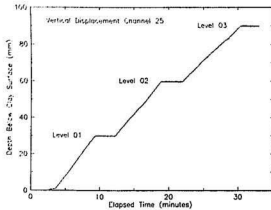


Figure 6B.2 Test 06 in - flight vane shear test results : Vane vertical displacement, rotation, and torque plotted against time

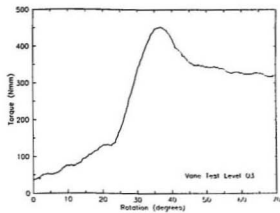
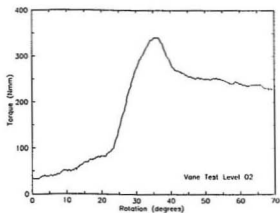
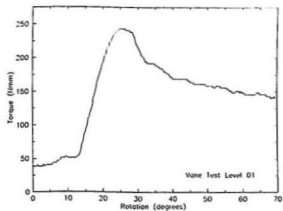


Figure 6B.2 Test 06 in - flight vane shear test results : Torque versus rotation curves at three levels within clay specimen

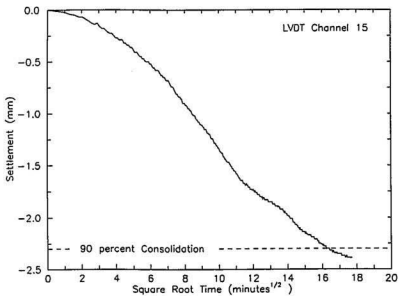
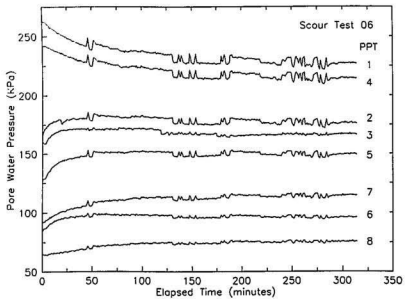


Figure 6C.1 Test 06 consolidation records. Top : Pore water pressure versus time for eight transducers; Bottom : Clay surface settlement versus square root of time

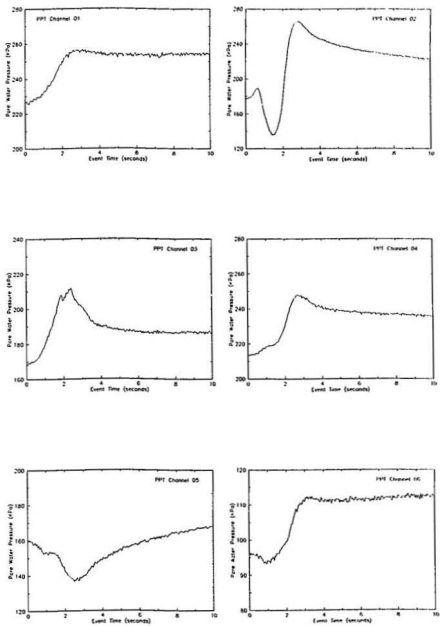


Figure 6C.2A Test 06 instrumentation data measured during initial section of event

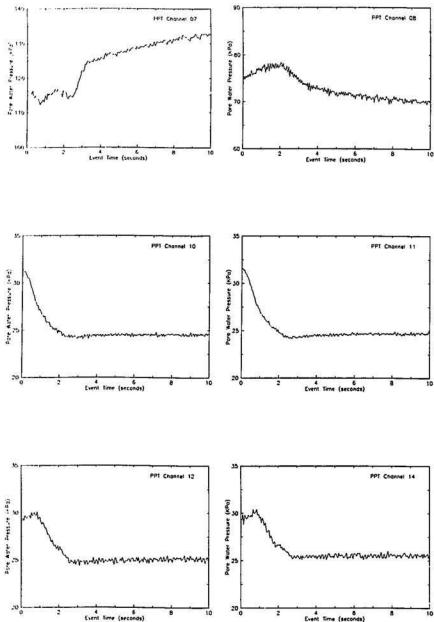


Figure 6C.2A Test 06 instrumentation data measured during initial section of event

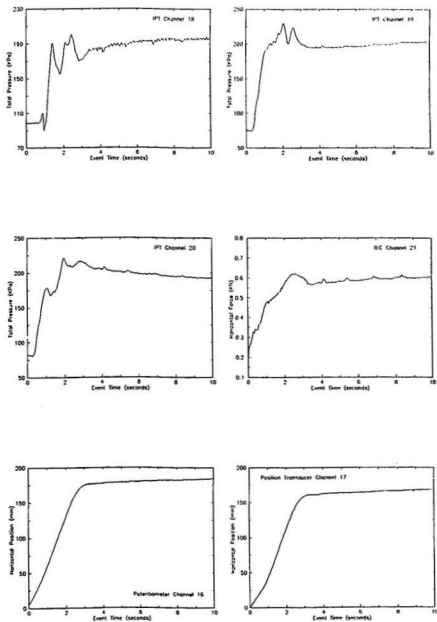


Figure 6C.2A Test 06 instrumentation data measured during initial section of event

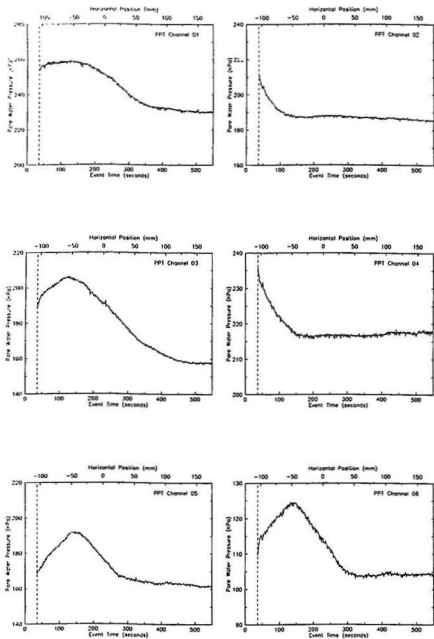


Figure 6C.2B Test 06 instrumentation data measured during final section of event

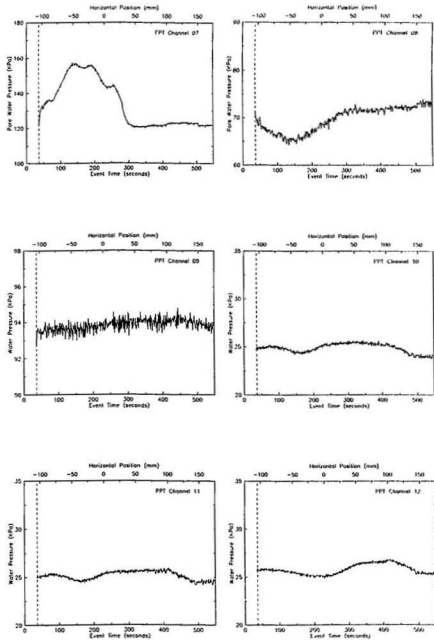


Figure 6C.2B Test 06 instrumentation data measured during final section of event

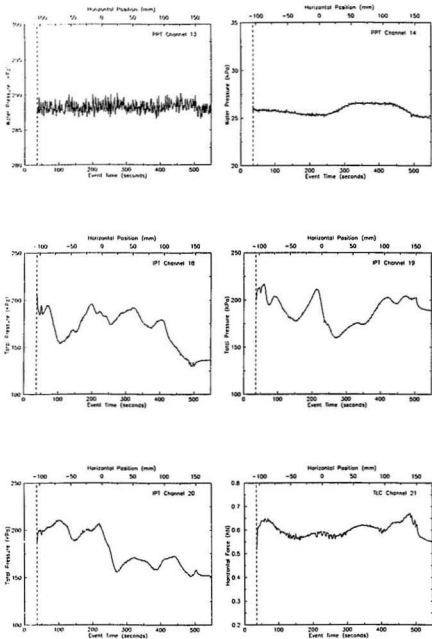


Figure 6C.2B Test 06 instrumentation data measured during final section of event

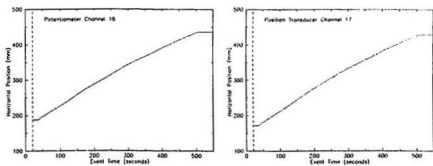


Figure 6C.2B Test 06 instrumentation data measured during final section of event

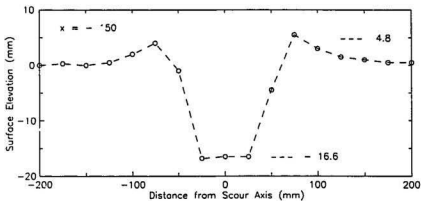
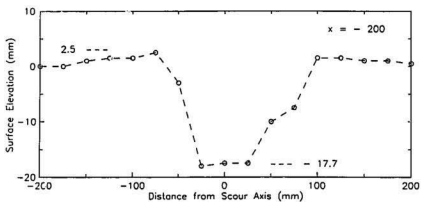
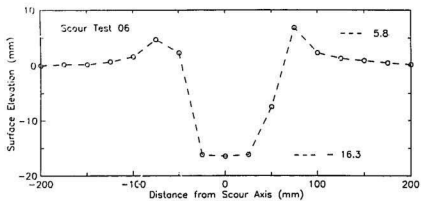


Figure 6D.1 Test 06 cross-sectional plots of clay surface profile measurements

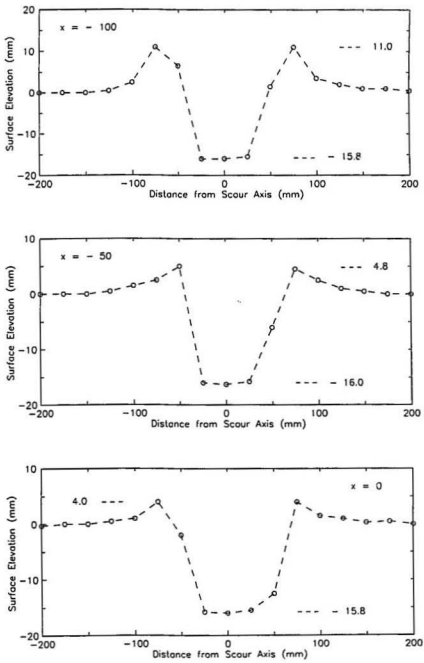


Figure 6D.1 Test 06 cross - sectional plots of clay surface profile measurements

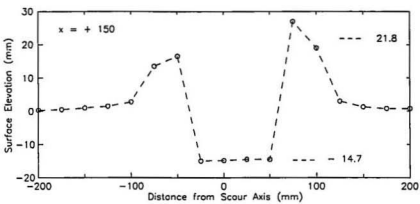
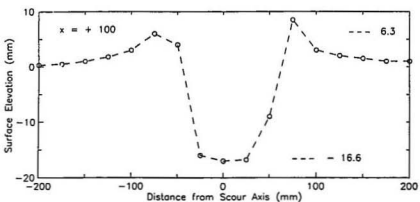
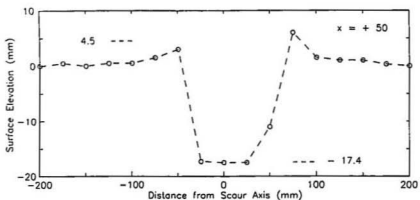


Figure 6D.1 Test 06 cross - sectional plots of clay surface profile measurements

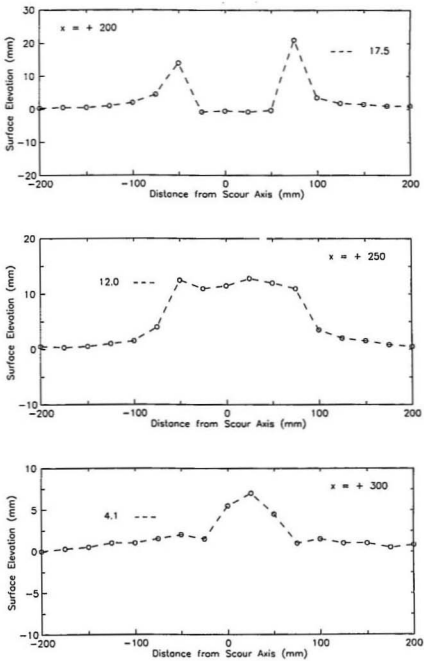


Figure 6D.1 Test 06 cross - sectional plots of clay surface profile measurements

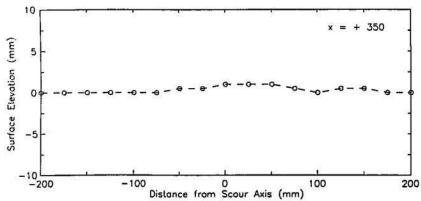


Figure 6D.1 Test 06 cross - sectional plots of clay surface profile measurements

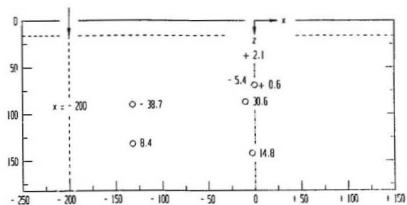
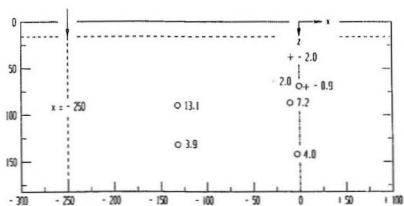
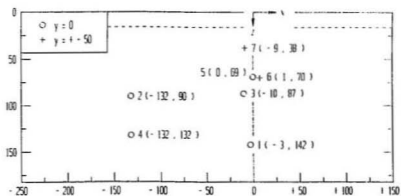


Figure 6E.1 Test 06 pore pressures (kPa) shown for different model horiz. positions

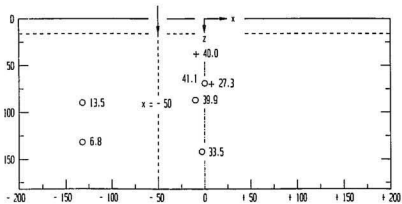
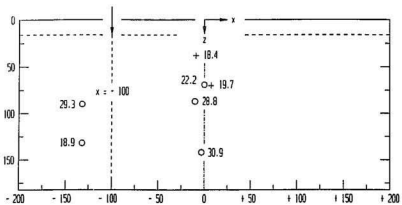
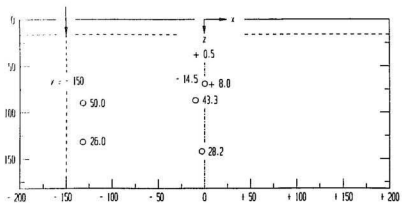


Figure 6E.1 Test 06 pore pressures (kPa) shown for different model horiz. positions

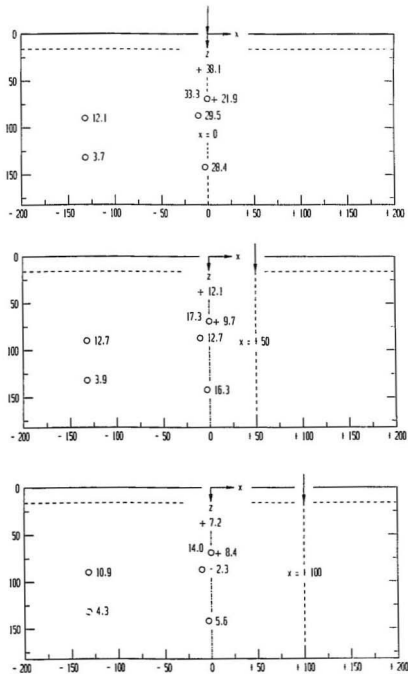


Figure 6E.1 Test 06 pore pressures (kPa) shown for different model horiz. positions

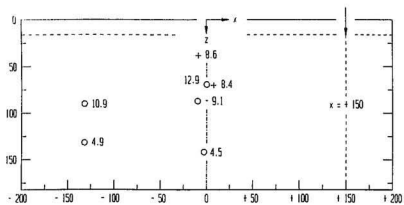


Figure 6E.1 Test 06 pore pressures (kPa) shown for different model horiz. positions

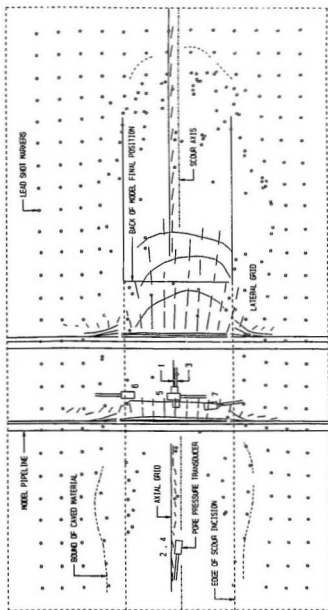


Figure 6F.1 Test 06 trace compiled from plan view radiographs of the clay specimen

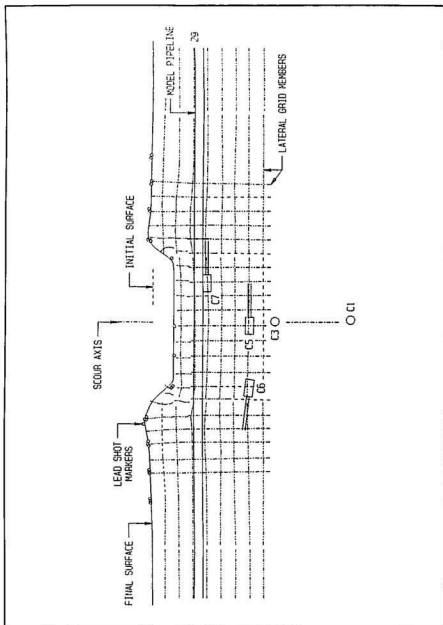


Figure 6F.2 Test 06 trace of cross - sectional radiograph showing displaced configuration of lateral grid at $x = -23$

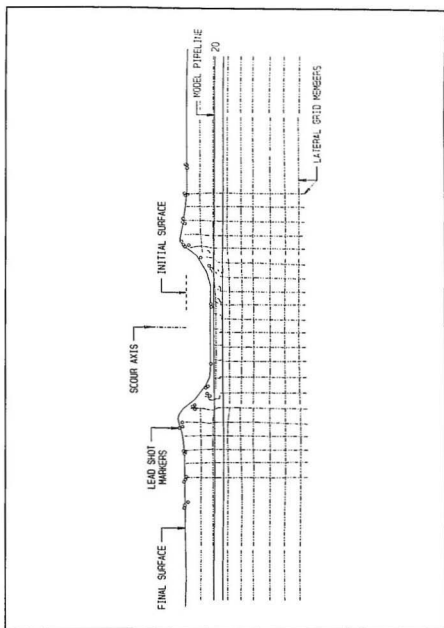


Figure 6F.2 Test 06 trace of cross - sectional radiograph showing displaced configuration of lateral grid at $x = +54$

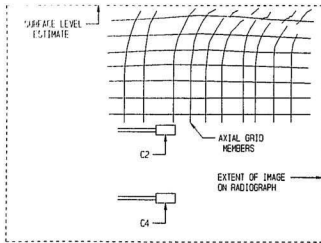


Figure 6F.3 Test 06 radiograph trace of axial grid; $x \approx -180$ to -45

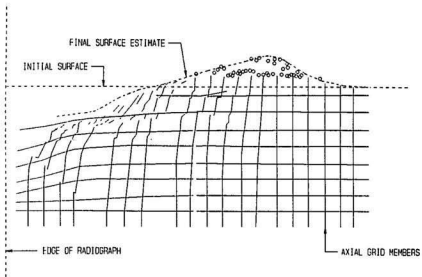


Figure 6F.4 Test 06 radiograph trace of axial grid; $x \approx +120$ to $+345$

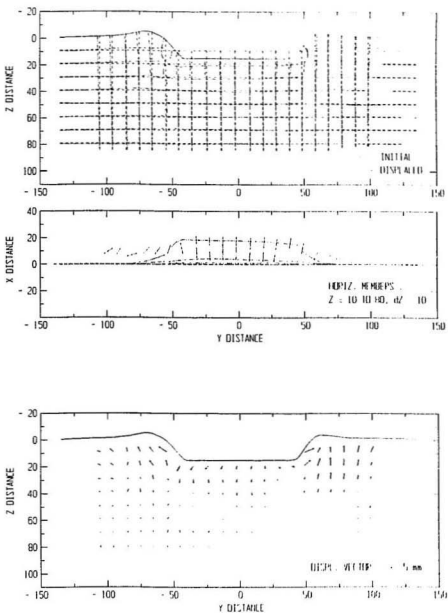


Figure 6F.5 Test 06 sub - surface soil displacement records. Top : Initial / displaced plot for lateral grid at $x \approx -23$; Bottom : Displacement vector plot (scales in mm)

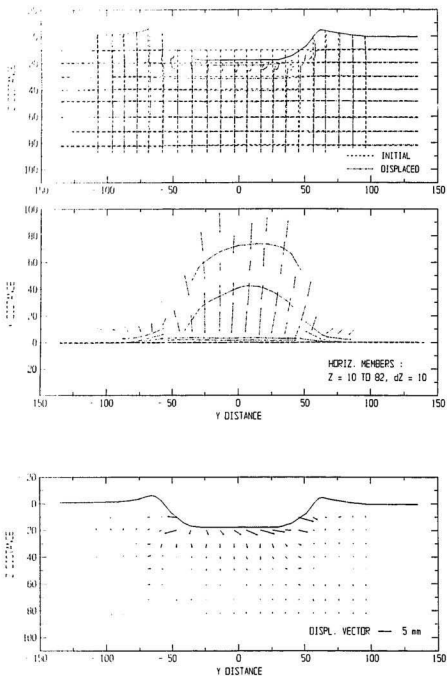


Figure 6F.5 Test 06 sub - surface soil displacement records. Top : Initial / displaced plot for lateral grid at $x = +54$; Bottom : Displacement vector plot (scales in mm)

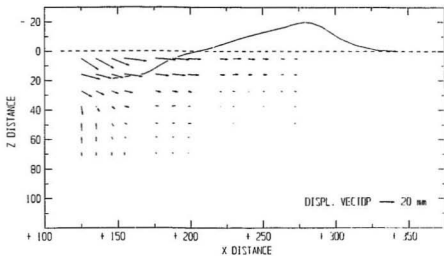
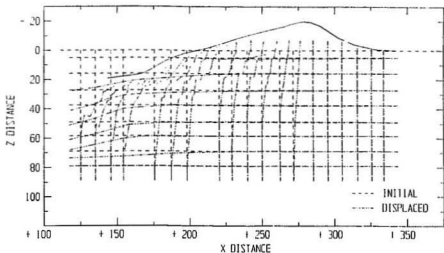


Figure 6F.5 Test 06 sub - surface soil displacement records. Top : Initial / displaced plot for axial grid at $x \approx +120$ to $+345$; Bottom : Displacement vector plot (scales in mm)

Scour Test 07

Test Number	σ_{v_0} KPa	Attack Angle degrees	Width mm	Vertical Stiffness N / mm	Test Variable
7	140	15	50	31	model width

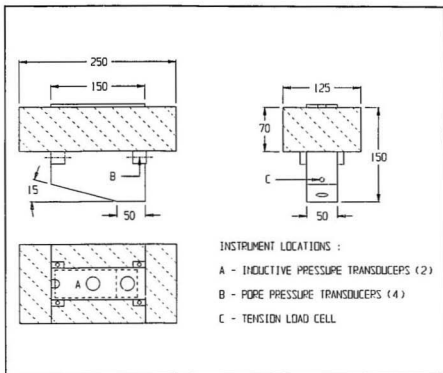


Figure 7A.1 Test 07 input parameters and model iceberg configuration

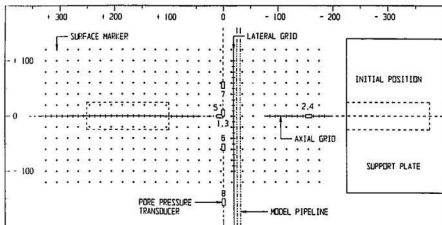
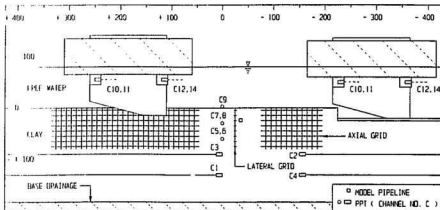


Figure 7A.2 Test 07 layout of instrumentation, deformation markers, and model pipeline segments shown in elevation and plan view (scales in mm)

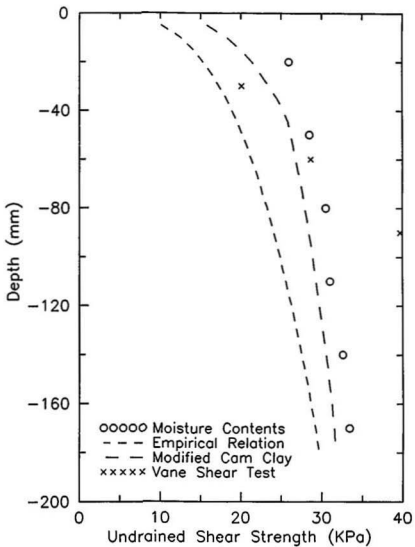


Figure 7B.1 Test 07 estimated undrained shear strength profiles based on post - test moisture content measurements, clay stress history, and in - flight vane shear tests

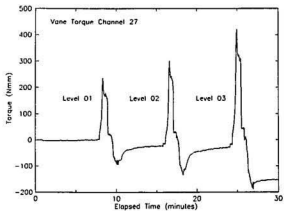
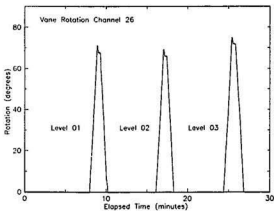
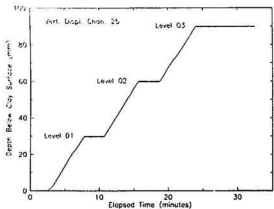


Figure 7B.2 Test 07 in - flight vane shear test results : Vane vertical displacement, rotation, and torque plotted against time

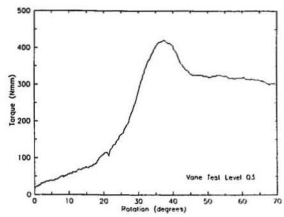
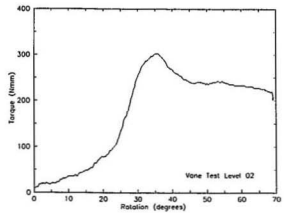
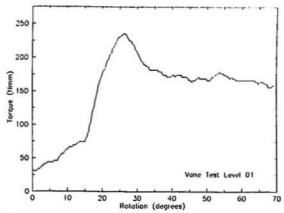


Figure 7B.2 Test 07 in - flight vane shear test results : Torque versus rotation curves at three levels within clay specimen

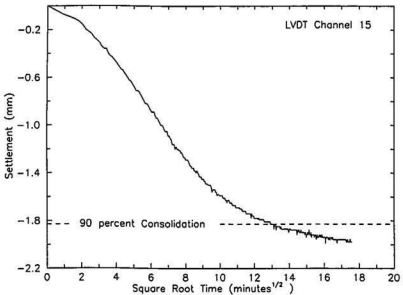
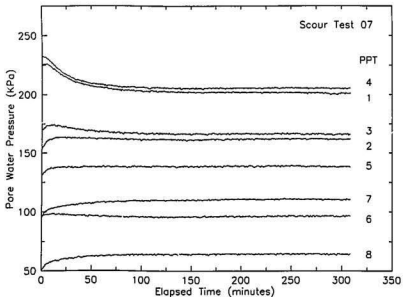


Figure 7C.1 Test 07 consolidation records. Top : Pore water pressure versus time for eight transducers; Bottom : Clay surface settlement versus square root of time

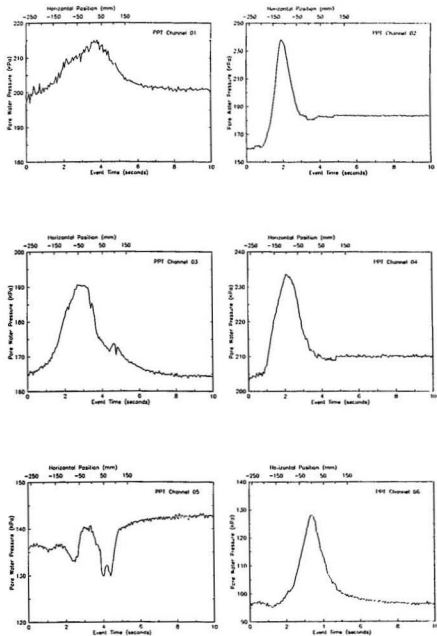


Figure 7C.2 Test 07 instrumentation data measured during scouring event

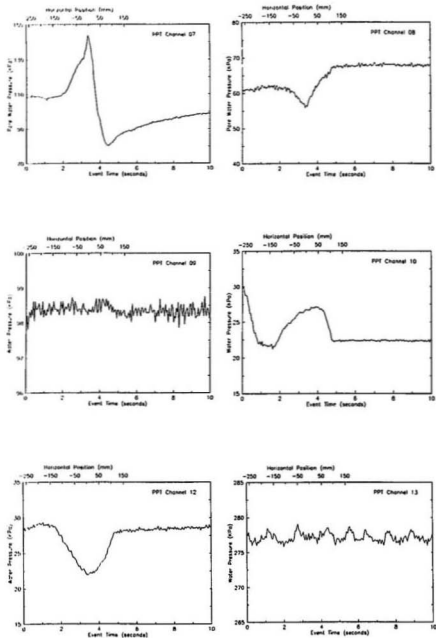


Figure 7C.2 Test 07 instrumentation data measured during scouring event

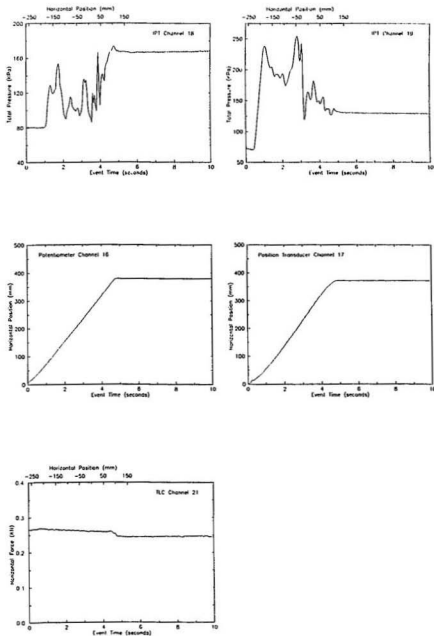


Figure 7C.2 Test 07 instrumentation data measured during scouring event

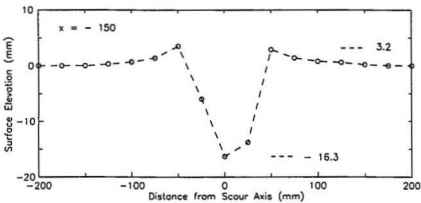
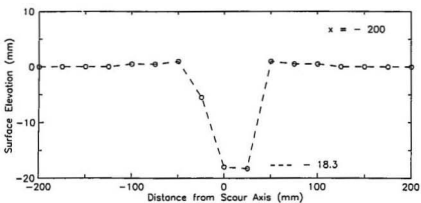
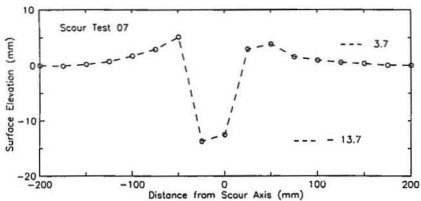


Figure 7D.1 Test 07 cross-sectional plots of clay surface profile measurements

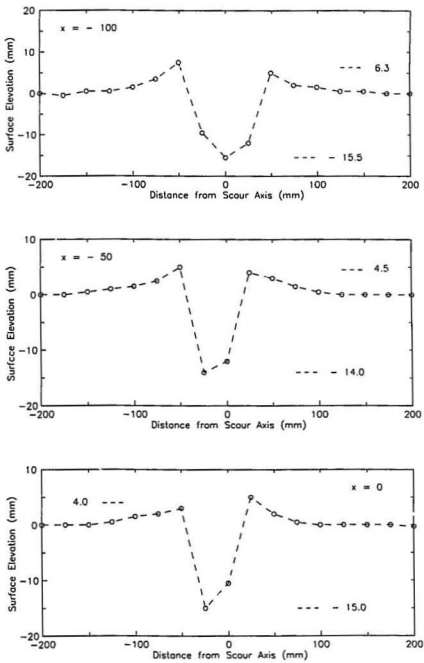


Figure 7D.1 Test 07 cross - sectional plots of clay surface profile measurements

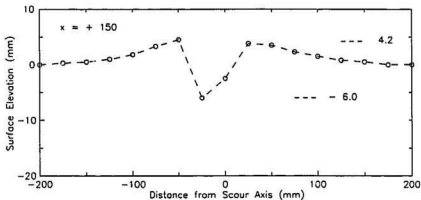
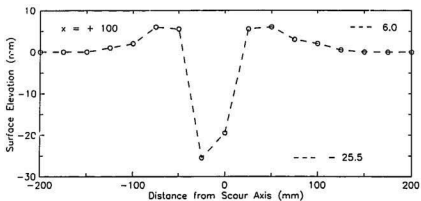
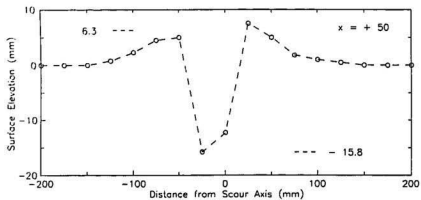


Figure 7D.1 Test 07 cross - sectional plots of clay surface profile measurements

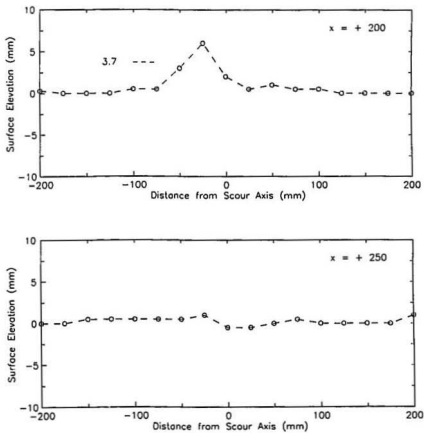


Figure 7D.1 Test 07 cross - sectional plots of clay surface profile measurements

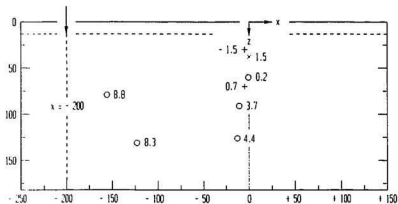
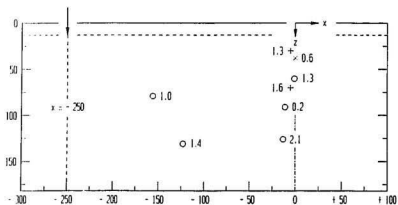
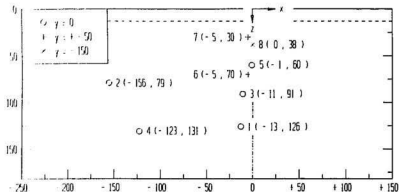


Figure 7E.1 Test 07 pore pressures (kPa) shown for different model horiz. positions

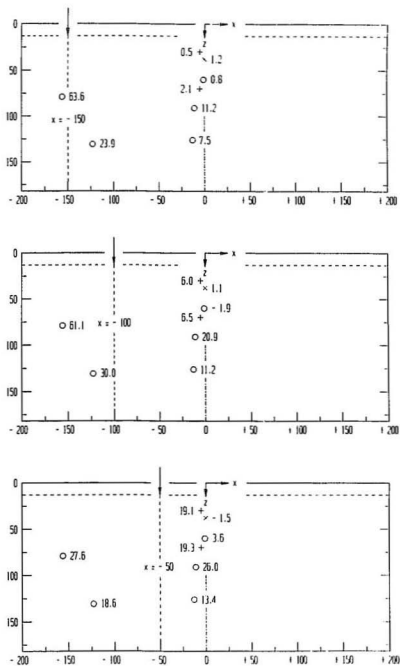


Figure 7E.1 Test 07 pore pressures (kPa) shown for different model horiz. positions

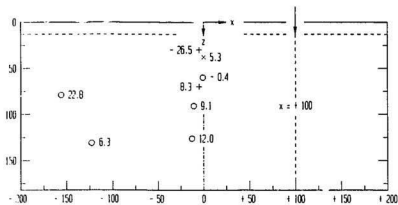
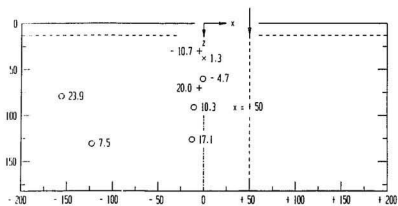
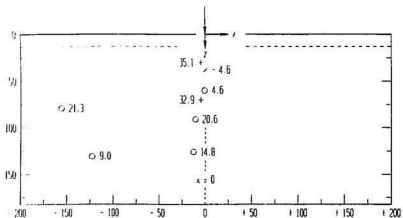


Figure 7E.1 Test 07 pore pressures (kPa) shown for different model horiz. positions

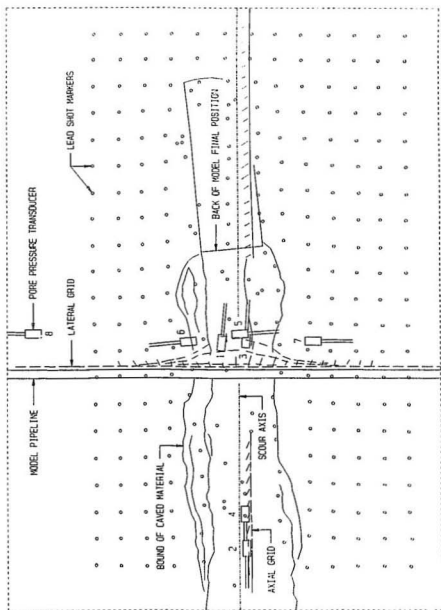


Figure 7F.1 Test 07 trace compiled from plan view radiographs of the clay specimen

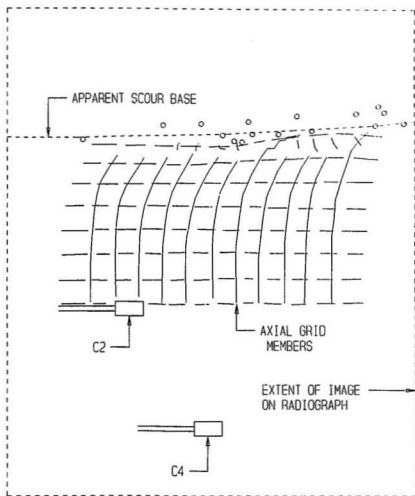


Figure 7F.3 Test 07 radiograph trace of axial grid; $x \approx -190$ to -60

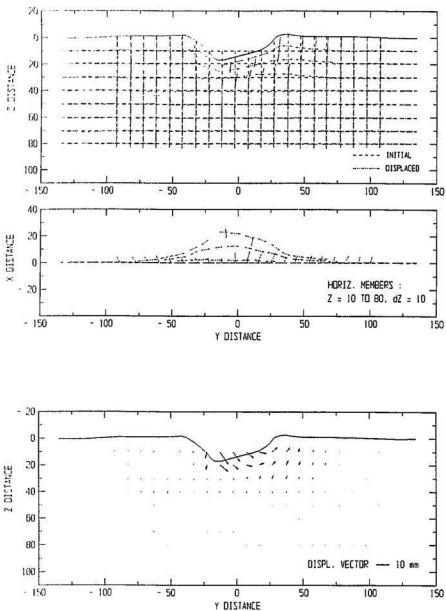


Figure 7F.4 Test 07 sub - surface soil displacement records. Top : Initial / displaced plot for lateral grid at $x = -25$; Bottom : Displacement vector plot (scales in mm)

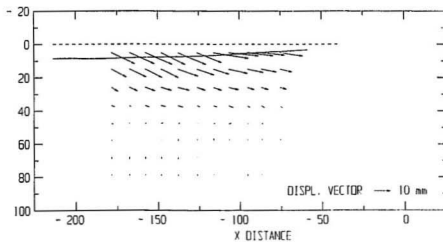
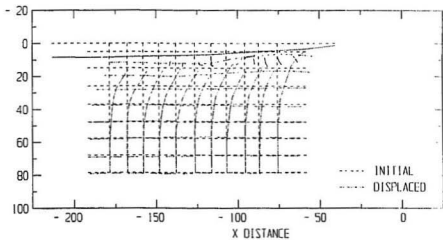


Figure 7F.4 Test 07 sub - surface soil displacement records. Top : Initial / displaced plot for axial grid at $x = -190$ to -60 ; Bottom : Displacement vector plot (scales in mm)

Scour Test 08

Test Number	$\sigma_{v,0}$ KPa	Attack Angle degrees	Width mm	Vertical Stiffness N / mm	Test Variable
8	140	25	100	61	attack angle

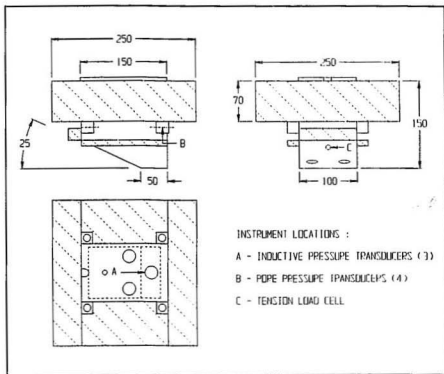


Figure 8A.1 Test 08 input parameters and model iceberg configuration

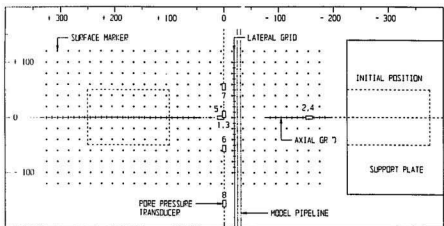
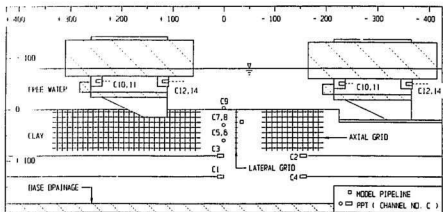


Figure 8A.2 Test 08 layout of instrumentation, deformation markers, and model pipeline segments shown in elevation and plan view (scales in mm)

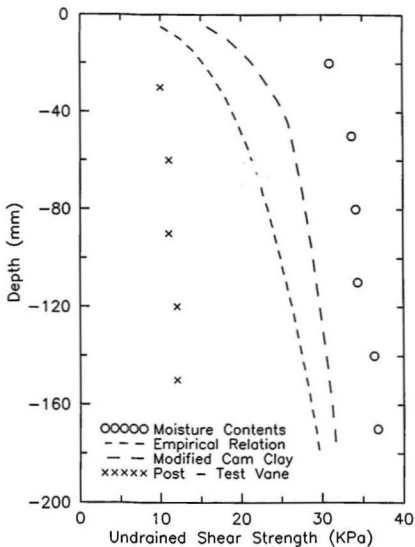


Figure 8B.1 Test 08 estimated undrained shear strength profiles based on post - test moisture content measurements, clay stress history, and Pilcon vane test

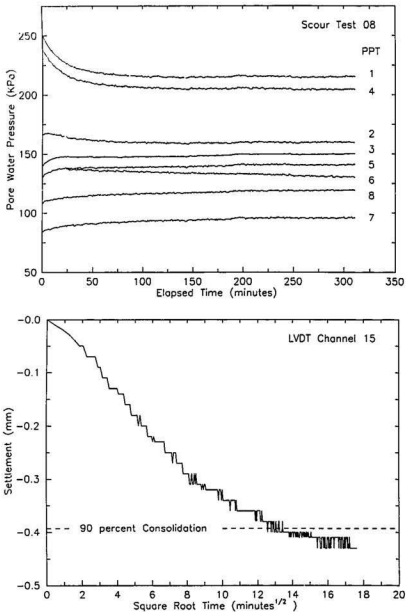


Figure 8C.1 Test 08 consolidation records. Top : Pore water pressure versus time for eight transducers; Bottom : Clay surface settlement versus square root of time

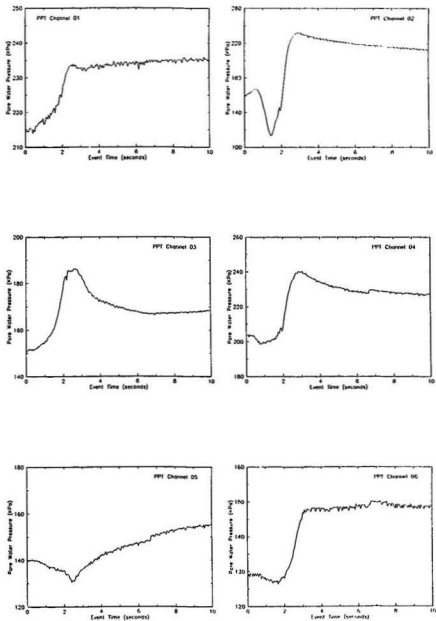


Figure 8C.2A Test 08 instrumentation data measured during initial section of event

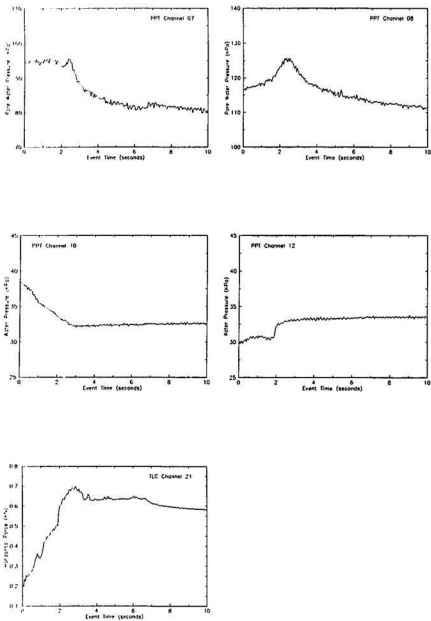


Figure 8C.2A Test 08 instrumentation data measured during initial section of event

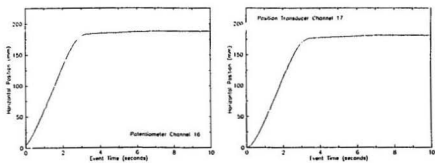


Figure 8C.2A Test 08 instrumentation data measured during initial section of event

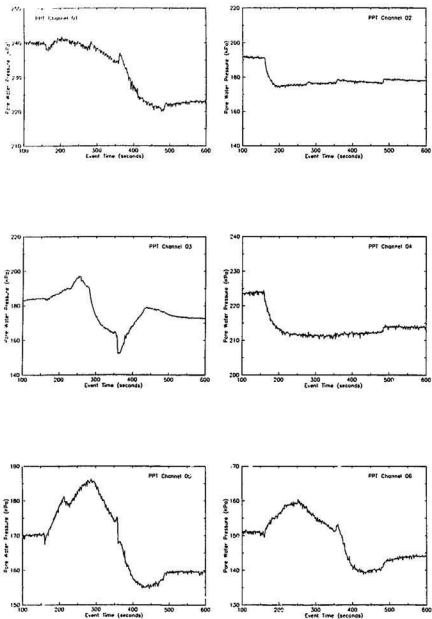


Figure 8C.2B Test 08 instrumentation data measured during final section of event

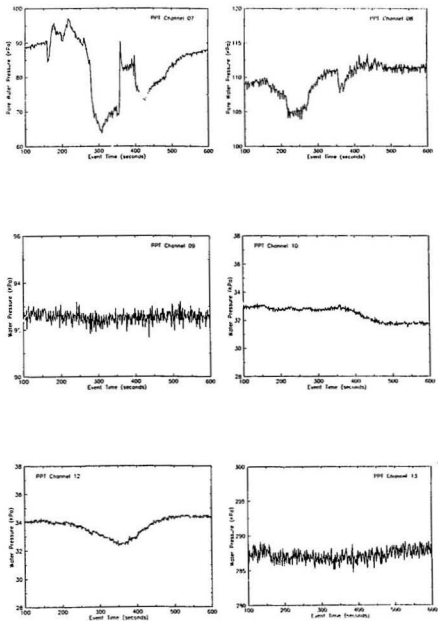


Figure 8C.2B Test 08 instrumentation data measured during final section of event

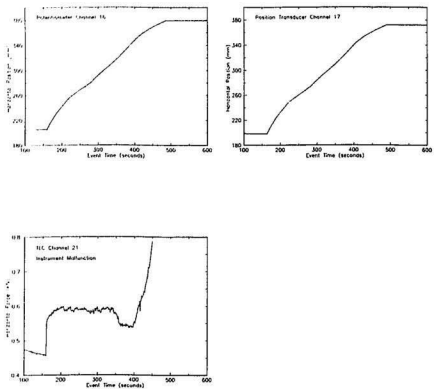


Figure 8C.2B Test 08 instrumentation data measured during final section of event

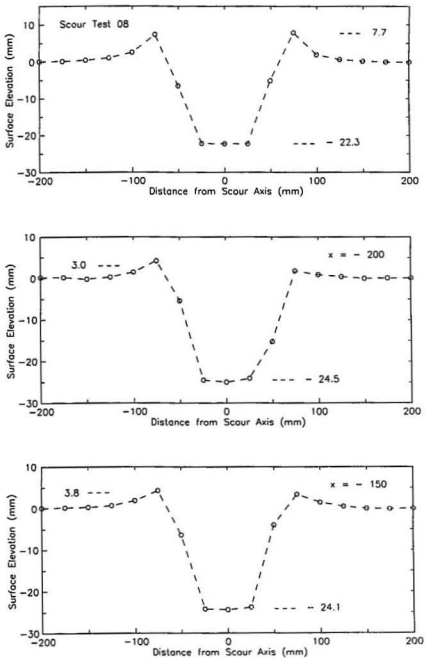


Figure 8D.1 Test 08 cross-sectional plots of clay surface profile measurements

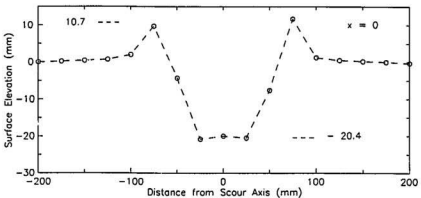
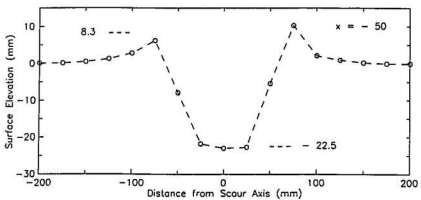
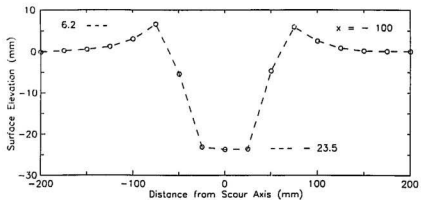


Figure 8D.1 Test 08 cross-sectional plots of clay surface profile measurements

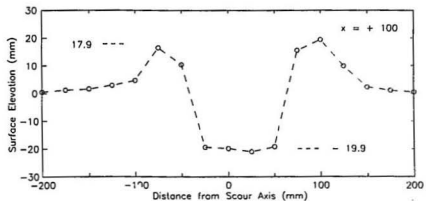
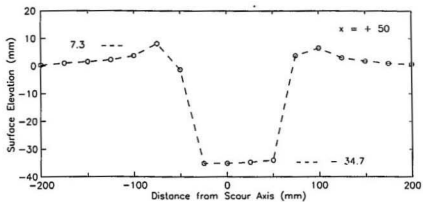
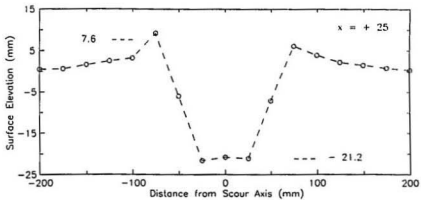


Figure 8D.1 Test 08 cross - sectional plots of clay surface profile measurements

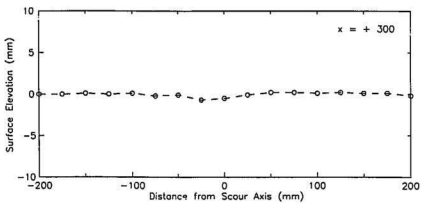
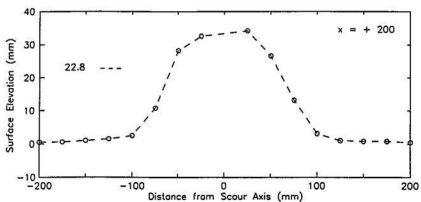
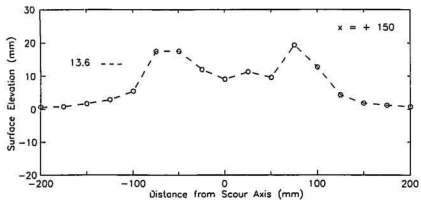


Figure 8D.1 Test 08 cross-sectional plots of clay surface profile measurements

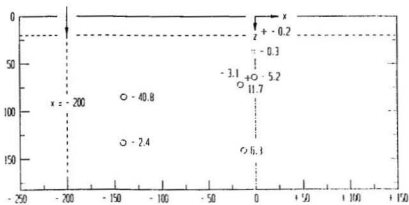
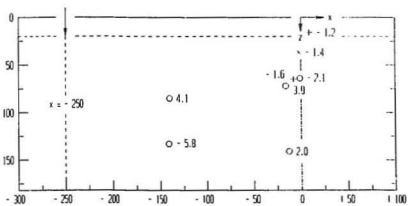
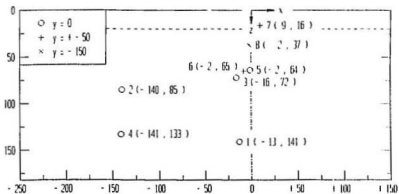


Figure 8E.1 Test 08 pore pressures (kPa) shown for different model horiz. positions

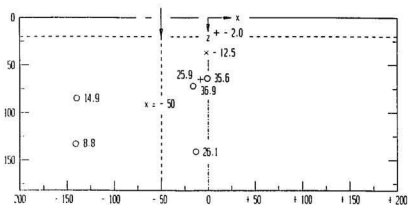
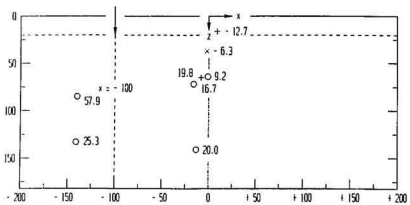
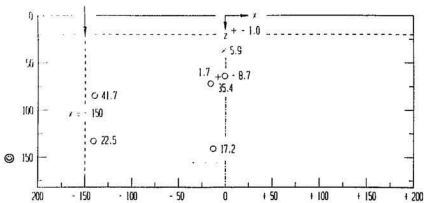


Figure 8E.1 Test 08 pore pressures (kPa) shown for different model horiz. position:

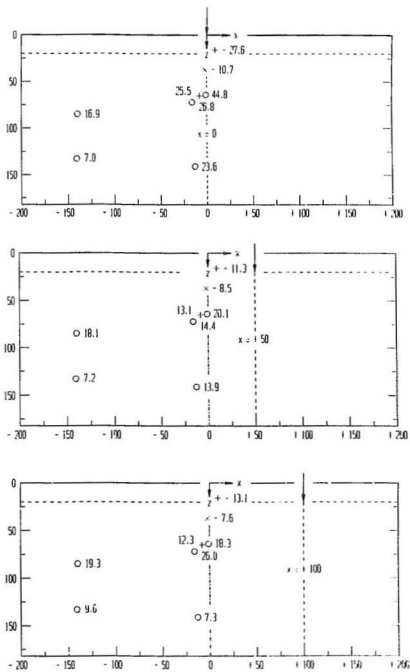


Figure 8E.1 Test 08 pore pressures (kPa) shown for different model horiz. positions

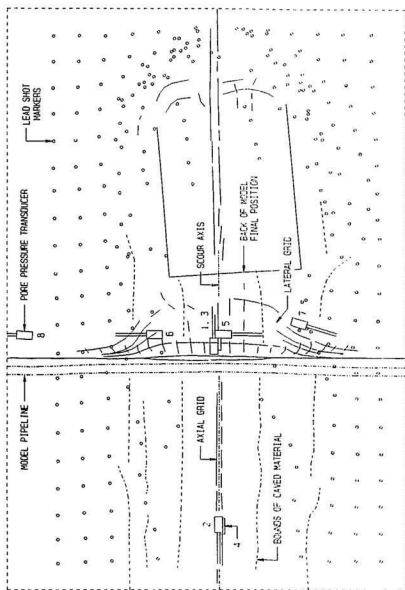


Figure 8F.1 Test 08 trace compiled from plan view radiographs of the clay specimen

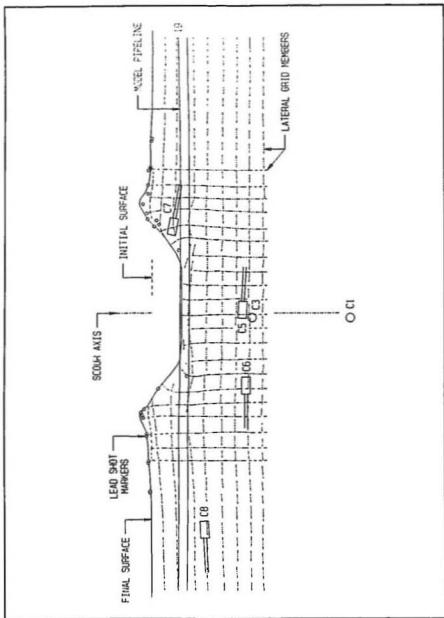


Figure 8F.2 Test 08 trace of cross - sectional radiograph showing displaced configuration of lateral grid at $x = -20$

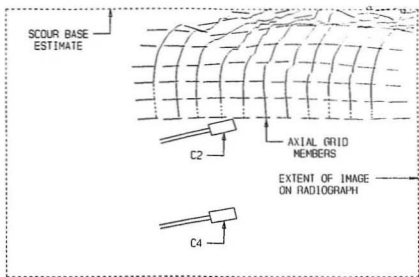


Figure 8F.3 Test 08 radiograph trace of axial grid; $x = -185$ to -55

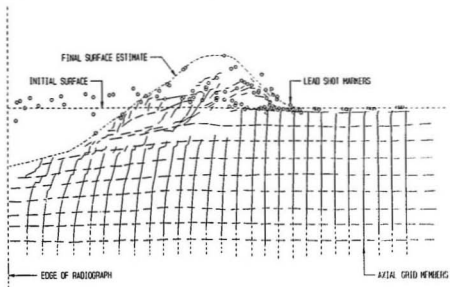


Figure 8F.4 Test 08 radiograph trace of axial grid; $x = +55$ to $+360$

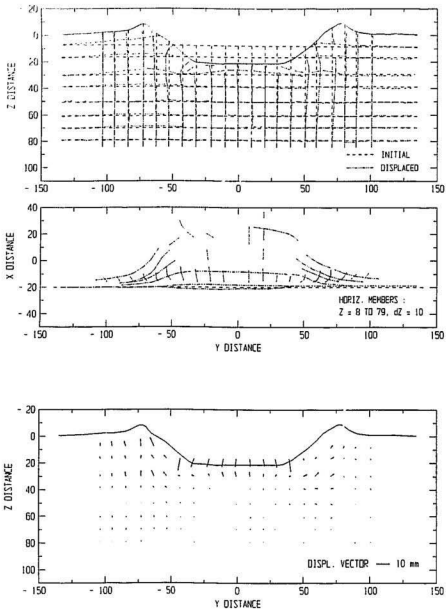


Figure 8F.5 Test 08 sub - surface soil displacement records. Top : Initial / displaced plot for lateral grid at $x = -20$; Bottom : Displacement vector plot (scales in mm)

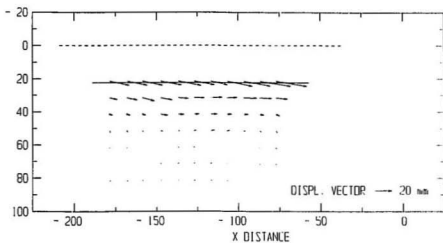
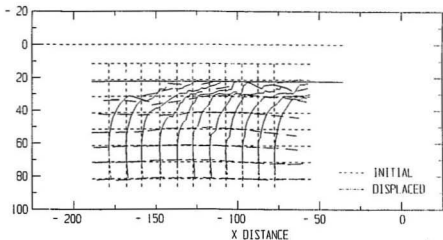


Figure 8F.5 Test 08 sub - surface soil displacement records. Top : Initial / displaced plot for axial grid at $x = -185$ to -55 ; Bottom : Displacement vector plot (scales in mm)

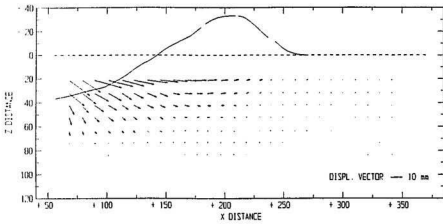
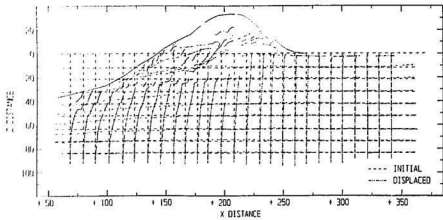


Figure 8F.5 Test 08 sub - surface soil displacement records. Top : Initial / displaced plot for axial grid at $x \approx + 55$ to $+ 360$; Bottom : Displacement vector plot (scales in mm)

Scour Test 09

Test Number	$\sigma_{v,0}$ KPa	Attack Angle degrees	Width mm	Vertical Stiffness N / mm	Test Variable
9	140	15	80	49	125 g test

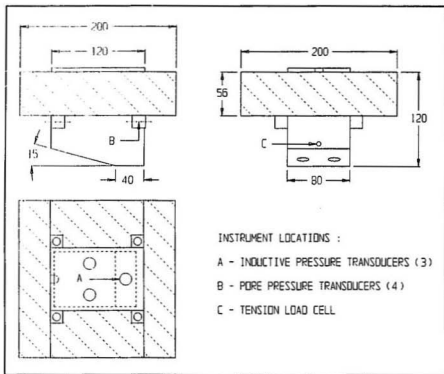


Figure 9A.1 Test 09 input parameters and model iceberg configuration

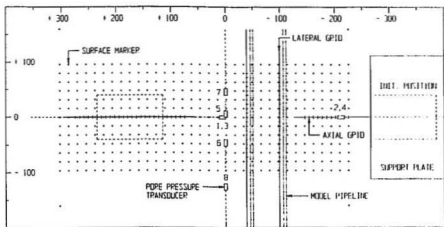
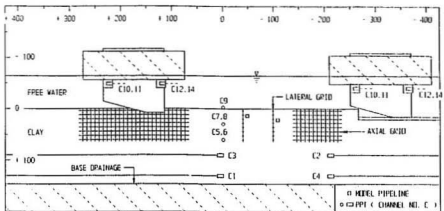


Figure 9A.2 Test 09 layout of instrumentation, deformation markers, and model pipeline segments shown in elevation and plan view (scales in mm)

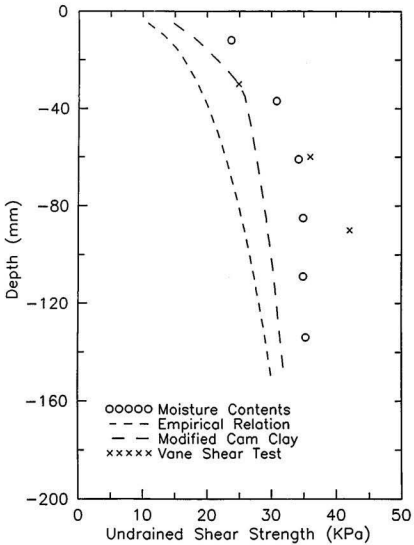


Figure 9B.1 Test 09 estimated undrained shear strength profiles based on post - test moisture content measurements, clay stress history, and in - flight vane shear tests

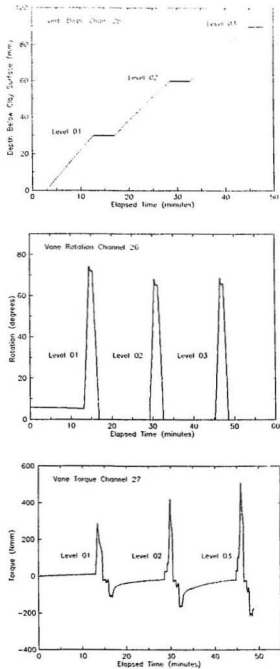


Figure 9B.2 Test 09 in - flight vane shear test results : Vane vertical displacement, rotation, and torque plotted against time

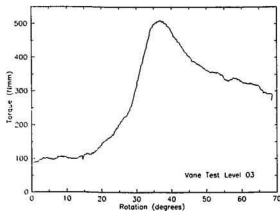
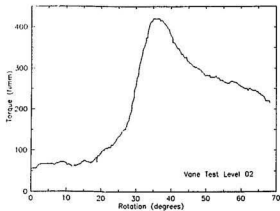
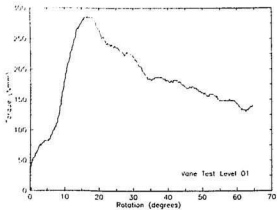


Figure 9B.2 Test 09 in - flight vane shear test results : Torque versus rotation curves at three levels within clay specimen

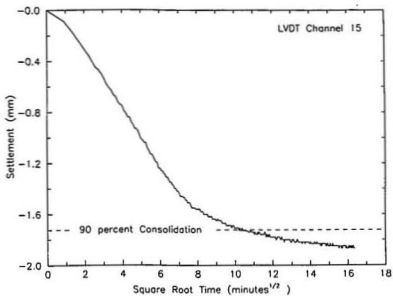
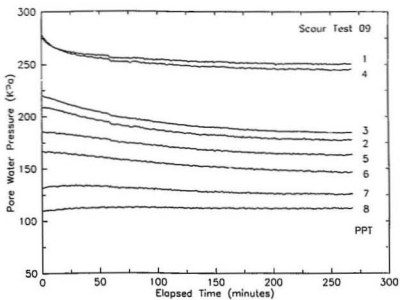


Figure 9C.1 Test 09 consolidation records. Top : Pore water pressure versus time for eight transducers; Bottom : Clay surface settlement versus square root of time

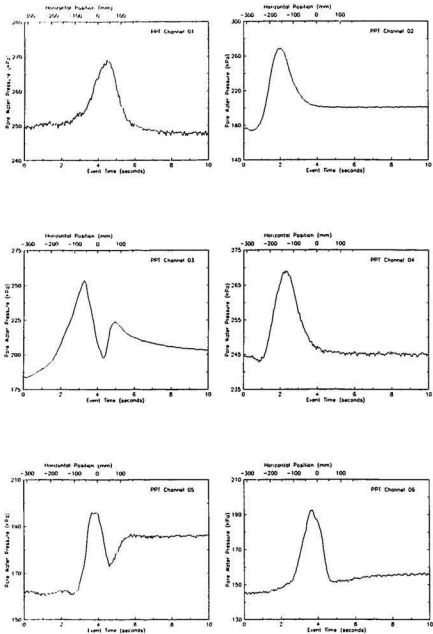


Figure 9C.2 Test 09 instrumentation data measured during scouring event

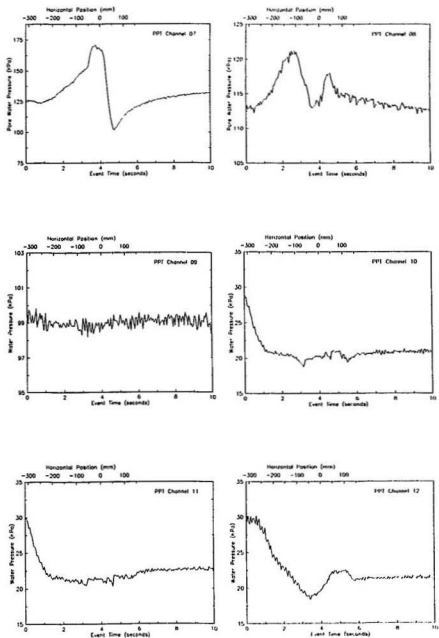


Figure 9C.2 Test 09 instrumentation data measured during scouring event

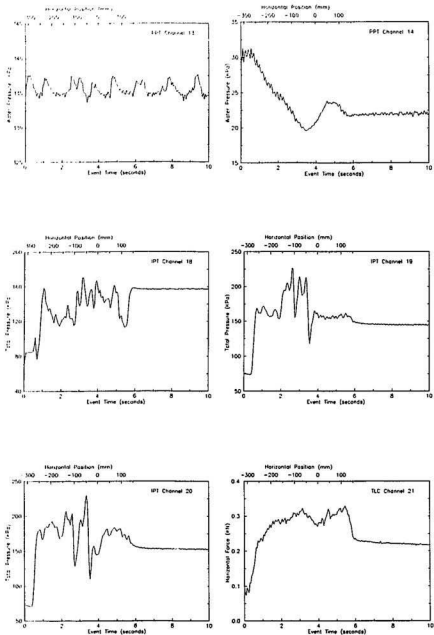


Figure 9C.2 Test 09 instrumentation data measured during scouring event

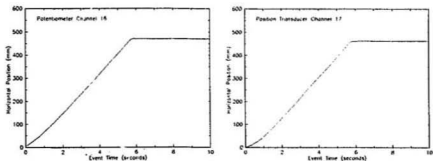


Figure 9C.2 Test 09 instrumentation data measured during scouring event

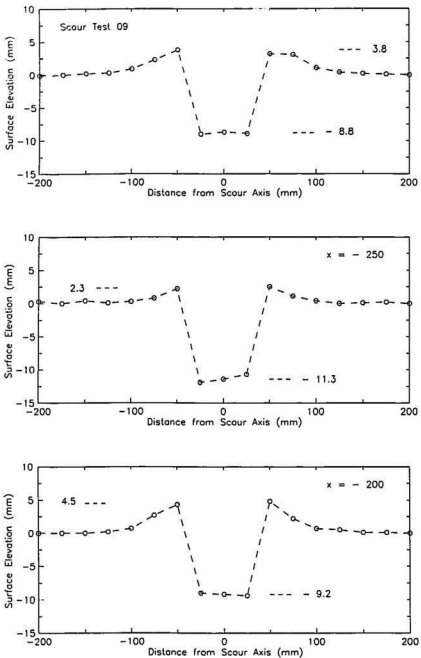


Figure 9D.1 Test 09 cross - sectional plots of clay surface profile measurements

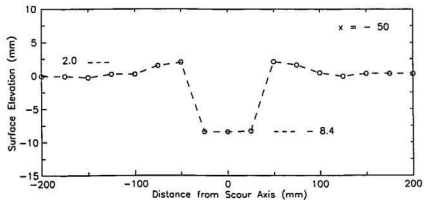
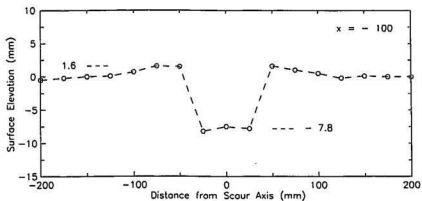
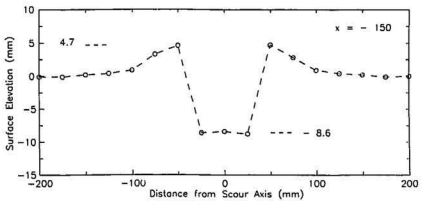


Figure 9D.1 Test 09 cross - sectional plots of clay surface profile measurements

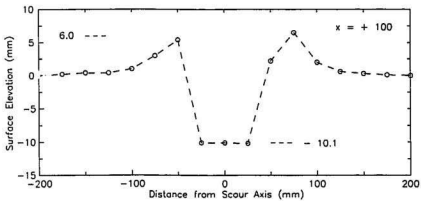
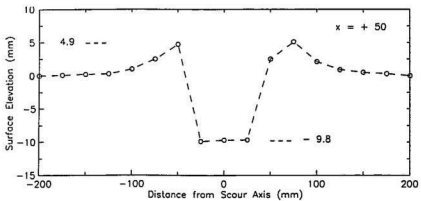
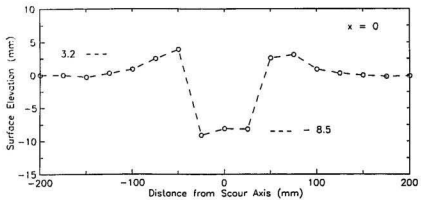


Figure 9D.1 Test 09 cross - sectional plots of clay surface profile measurements

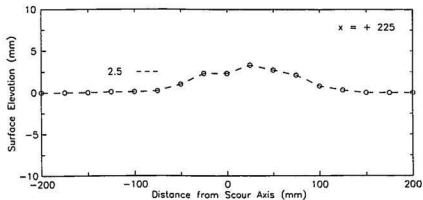
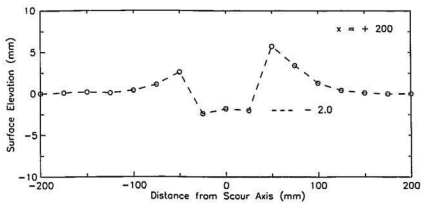
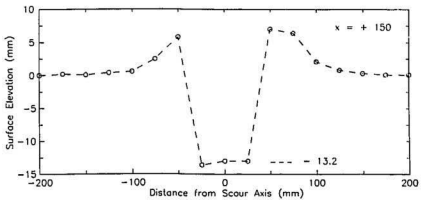


Figure 9D.1 Test 09 cross - sectional plots of clay surface profile measurements

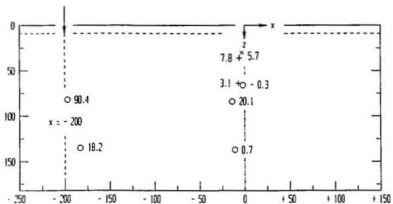
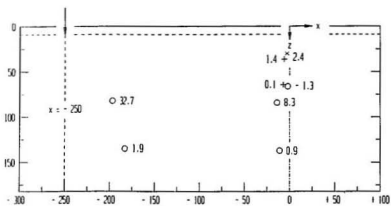
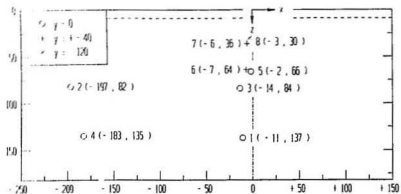


Figure 9E.1 Test 09 pore pressures (kPa) shown for different model horiz. positions

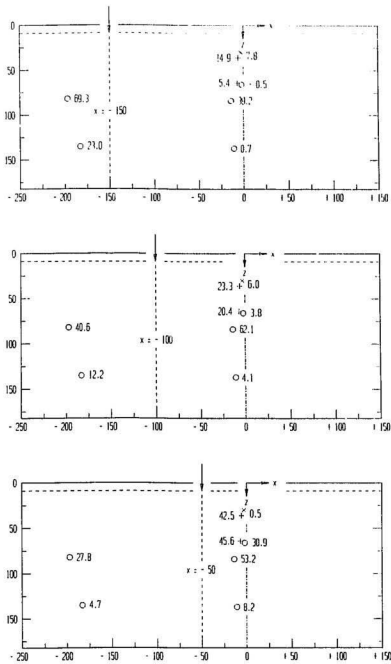


Figure 9E.1 Test 09 pore pressures (kPa) shown for different model horiz. positions

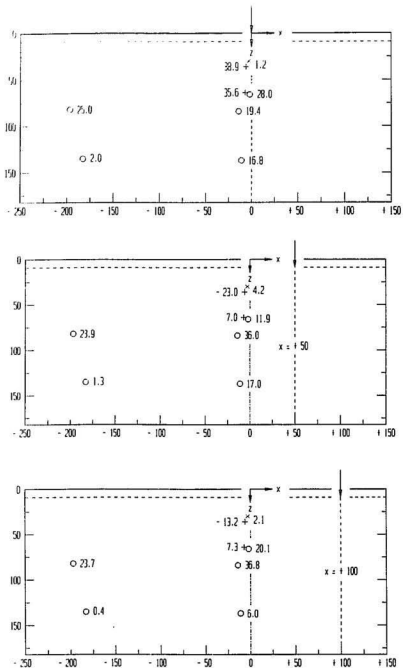


Figure 9E.1 Test 09 pore pressures (kPa) shown for different model horiz. positions

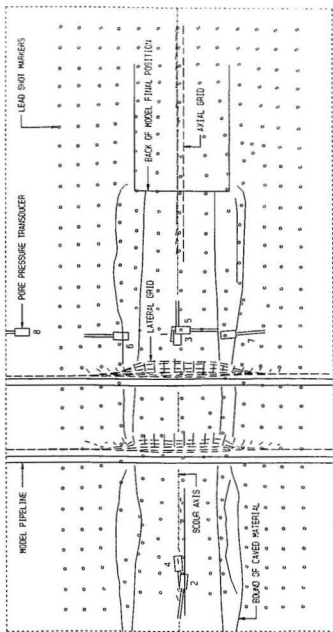


Figure 9F.1 Test 09 trace compiled from plan view radiographs of the clay specimen

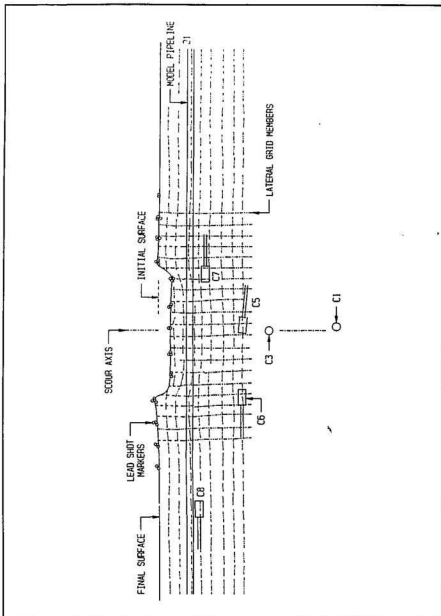


Figure 9F.2 Test 09 trace of cross - sectional radiograph showing displaced configuration of lateral grid at $x = -97$

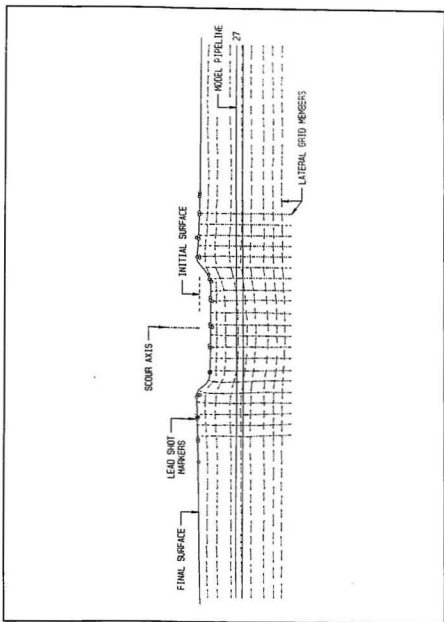


Figure 9F.2 Test 09 trace of cross - sectional radiograph showing displaced configuration of lateral grid at $x = -40$

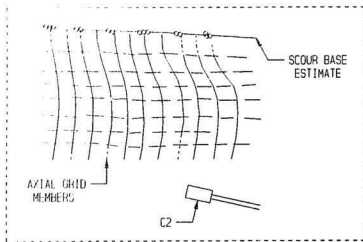


Figure 9F.3 Test 09 radiograph trace of axial grid; $x \approx -230$ to -125

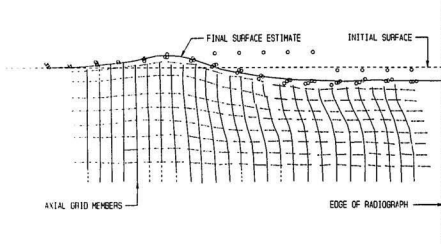


Figure 9F.4 Test 09 radiograph trace of axial grid; $x \approx +55$ to $+285$

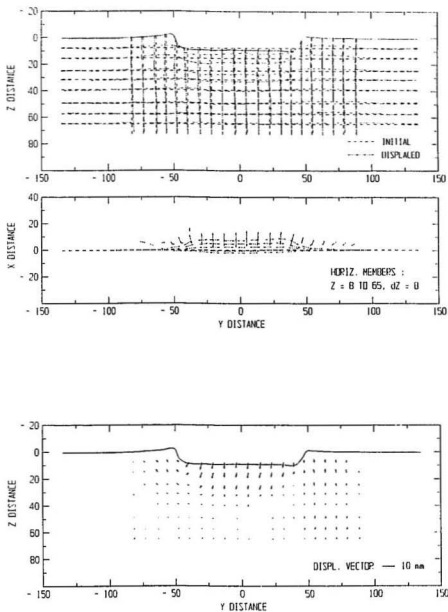


Figure 9F.5 Test 09 sub - surface soil displacement records. Top : Initial / displaced plot for lateral grid at $x = -97$; Bottom : Displacement vector plot (scales in mm)

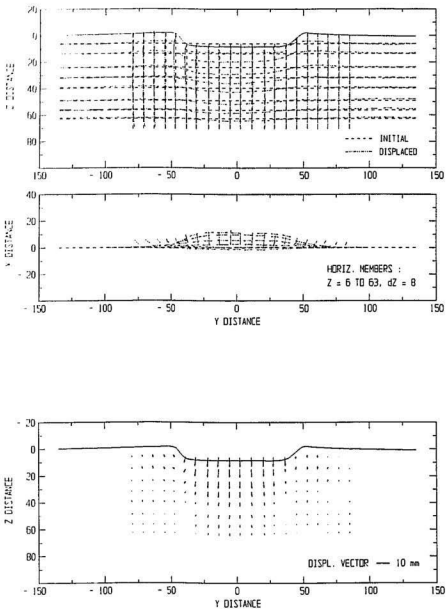


Figure 9F.5 Test 09 sub - surface soil displacement records. Top : Initial / displaced plot for lateral grid at $x = -40$; Bottom : Displacement vector plot (scales in mm)

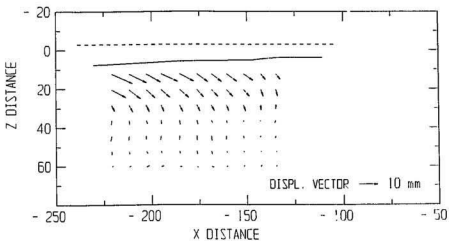
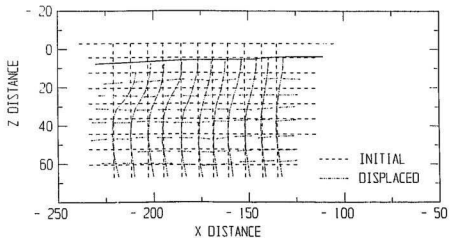


Figure 9F.5 Test 09 sub - surface soil displacement records. Top : Initial / displaced plot for axial grid at $x \approx -230$ to -125 ; Bottom : Displacement vector plot (scales in mm)

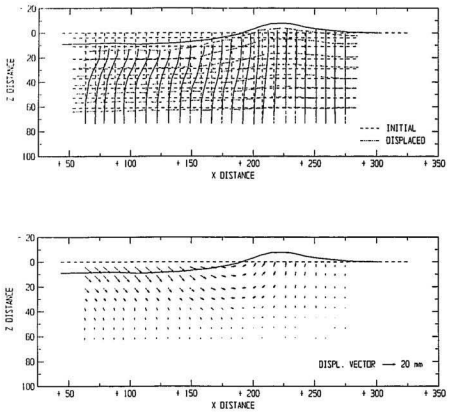


Figure 9F.5 Test 09 sub - surface soil displacement records. Top : Initial / displaced plot for axial grid at $x = +55$ to $+285$; Bottom : Displacement vector plot (scales in mm)

Appendix B

Resultant Force Calculation

This appendix describes the computational procedure used in the assessment of the resultant forces acting at the model iceberg - soil interface. An example of the resultant force calculation is presented for a specific time and model position during the baseline Test 05 scouring event. The model vertical position and orientation were established in two - dimensional space using water pressure measurements from pore pressure transducers installed at fixed elevations at the front and rear of the model. The effect of small out - of - plane model rotational movements was accounted for through use of the average of transducer measurements acquired from each side of the model.

Identification and Measured Input Data :

Scour Test 05

Event Time = 4.00 s

Horizontal Position = 0.0 mm

PPT average front = 20.6 kPa

PPT average rear = 23.2 kPa

Load Cell Horizontal Force, TLC = 499.8 N

Figure B.1 depicts the submerged model geometry with respect to a local coordinate system, as well as the force components acting during the scouring event. The elevation values E_i were calculated from the measured water pressures, and served to define the free water surface relative to an arbitrary datum at the base of the model float attachment. In this manner, the model orientation (pitch angle) and vertical position were established in relation to the known surface water level.

Model Vertical Position and Orientation :

elevation at PPT front = 11.0 mm

elevation at PPT rear = 13.6 mm

$E_1 = 10.8$ mm; $E_2 = 13.8$ mm; $E_3 = 11.2$ mm; $E_4 = 13.4$ mm; $E_5 = 9.8$ mm;

$E_6 = 14.9$ mm.

model pitch angle, $\theta = 0.020$ radians or 1.2 degrees

scour depth calculated at model inflection line, $Z_1 = 12.9$ mm

scour depth calculated at model rear, $Z_2 = 13.8$ mm

The horizontal force component was ascertained directly from the tension load cell record during the scouring event. The vertical force component was evaluated indirectly from data on the current vertical position and orientation of the model iceberg in free surface water, together with detailed information on the mass and submerged geometry of the model. The simplified force system shown in Figure B.1 included the total weight force W_t , the individual components comprising the buoyancy force B_i , and the horizontal and vertical components of the resultant force, F_h and F_v , acting on the

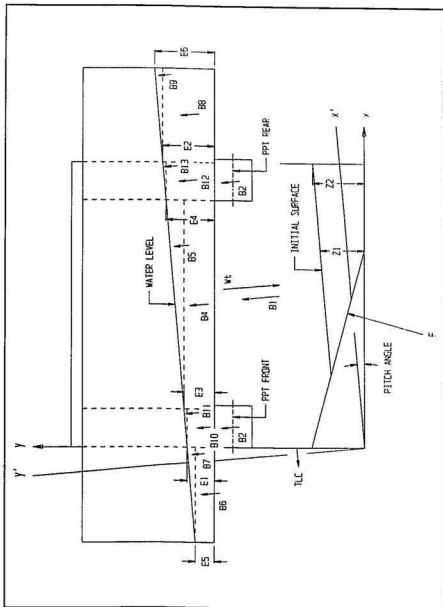


Figure B.1 Sketch showing submerged model geometry and force components acting during scouring event (exaggerated pitch angle)

inclined face of the model. In the following, the position of the point of action of each force component was established in relation to the x - y coordinate system for the initial model orientation, prior to the inception of rotational movement.

Force Magnitudes and Positions - Initial Coordinate System :

Component	x (mm)	y (mm)	Force (N) at 1 g	Force (N) at 100 g
Wt	83.3	79.8	- 35.022	3502.2
B1	80.0	44.2	10.279	1027.9
B2	10.0	70.0	0.107	10.7
B3	139.0	70.0	0.107	10.7
B4	74.5	85.6	2.997	299.7
B5	92.7	92.0	0.298	29.8
B6	- 25.0	84.9	1.200	120.0
B7	- 16.7	90.1	0.063	6.3
B8	174.0	86.9	1.698	169.8
B9	182.3	94.2	0.063	6.3
B10	10.0	85.4	0.503	50.3
B11	13.3	90.9	0.010	1.0
B12	139.0	86.7	0.626	62.6
B13	142.3	93.6	0.010	1.0
TLC	0.0	36.0	-----	- 499.8

In order to allow for the rotation of the model iceberg about a transverse axis (pitch adjustment) at the current position, the force components were transformed to the x' - y' coordinate system. The x' - axis is directed parallel to the free water surface, and

the y' - axis is directed parallel to the resultant centrifuge acceleration vector (or normal to the free water surface) such that the following relationships may be written :

$$x' = x \cos \theta + y \sin \theta \text{ and } y' = -x \sin \theta + y \cos \theta$$

Force Magnitudes and Positions - New Coordinate System :

Component	Force (N) at 100 g	x' (mm)	y' (mm)	Moment (Nmm)
Wt	- 3502.2	84.9	78.1	- 297378.0
B1	1027.9	80.9	42.6	83173.4
B2	10.7	11.4	69.8	122.6
B3	10.7	140.4	67.1	1505.8
B4	299.7	76.2	84.1	22850.2
B5	29.8	94.5	90.0	2813.8
B6	120.0	- 23.3	85.4	- 2790.3
B7	6.3	- 14.8	90.4	- 92.8
B8	169.8	175.7	83.4	29843.5
B9	6.3	184.2	90.4	1153.9
B10	50.3	11.7	85.2	590.8
B11	1.0	15.2	90.6	14.5
B12	62.6	140.7	83.9	8808.0
B13	1.0	144.2	90.6	137.2
TLC	- 499.8	0.7	36.0	17987.7

Sum of Forces in + y' - direction = - 1706.2 N

Sum of Forces in + x' - direction = - 499.8 N

Sum of Moments about Origin = - 131260 Nmm

The equations of equilibrium may be used to calculate the magnitude of the vertical and horizontal components of the resultant force, and the location of the point of action of the resultant force on the inclined face of the model.

Vertical Equilibrium :

$$F_v \text{ (positive } y' \text{ direction)} = 1706.2 \text{ N}$$

Horizontal Equilibrium :

$$F_h \text{ (positive } x' \text{ direction)} = - 499.8 \text{ N}$$

Resultant Force $F = 1777.9 \text{ N}$

Inclination of Resultant Force Vector = 73.7 degrees (measured from + x' - axis)

Location of Resultant Force $x' = 78.4 \text{ mm}$ $y' = 5.1 \text{ mm}$

Summary of Forces acting on Model Iceberg :

Component	Force (N)	x' (mm)	y' (mm)
Wt	- 3502.2	84.9	78.1
B	1796.0	82.5	60.3
F_h	- 499.8	78.4	5.1
F_v	1706.2	78.4	5.1
TLC	499.8	0.7	36.0

The resultant force calculation was implemented using a spreadsheet macro program to obtain solutions at other times and model horizontal positions during the

scouring event. To check the validity of the calculation, the results were compared with vertical force estimates based on the post - event measured profile of scour depths.



